Scenarios and Phenomena Affecting Risk of Containment Failure and Release Characteristics

Weimin Ma[1], Walter Villanueva[1], Sevostian Bechta[1], Qiang Guo[1]
Andrei Komlev[1], Mohsen Hoseyni[1], Peng Yu[1]

Anna Korpinen[2], Veikko Taivassalo[2], Tero Tyrväinen[2]
Ilkka Karanta[2]

Anders Riber Marklund[3], Sergey Galushin[3], Ola Bäckström[3]

[1]Royal Institute of Technology (KTH), Sweden

[2]Technical Research Centre of Finland Ltd (VTT)

[3]Lloyd´s Register Consulting Energy AB (LRC), Sweden

October 2019

Abstract

Objective of the project "Scenarios and Phenomena Affecting Risk of Containment Failure and Release Characteristics", dubbed SPARC, is to produce new data, and to develop models and methodologies for addressing severe accident scenarios and phenomena which are important to assess the risk of containment failure and radioactivity release in a postulated severe accident of Nordic nuclear power plants.

During 2018 substantial advances in experimental and analytical capabilities as well new insights into physical mechanisms were gained at KTH, VTT and LRC for: (i) development of experimental facilities of SIMECO-2, MRSPOD and POMECO-Q for studies of melt pool convection as well as remelting and quenching of debris beds; (ii) validation of the MEWA code for coolability analysis of particulate beds, and its applications to reactor-scale debris beds; (iii) experimental investigations on quenching of a hot sphere in a seawater pool and single molten droplet steam explosion in sea water; (iv) modeling of melt infiltration through particulate beds, and its validation against the REMCOD experiment; (v) coupled thermal-mechanical analysis approach and its validation against the FOREVER-EC2 experiment; (vi) study of a dynamic containment event tree modelling particularly focusing on the modelling of timings of events and uncertainty analysis; (vii) the comparison of MEWA and DECOSIM simulations for the post-dryout conditions of the same idealized particulate beds; and (viii) the application of a dynamic approach (such as ROAAM+) to PSA for an enhanced probabilistic risk analysis.

Key words

IDPSA, Severe Accident, Deterministic Analysis, ROAAM+

Scenarios and Phenomena Affecting Risk of Containment Failure and Release Characteristics

Final Report from the NKS-R activity (Contract: AFT/NKS-R(18)122/4)

Weimin Ma[1], Walter Villanueva[1], Sevostian Bechta[1], Qiang Guo[1], Andrei Komlev[1], Mohsen Hoseyni[1], Peng Yu[1]

Anna Korpinen[2], Veikko Taivassalo[2], Tero Tyrväinen[2], Ilkka Karanta[2]

Anders Riber Marklund[3], Sergey Galushin[3], Ola Bäckström[3]

[1]Royal Institute of Technology (KTH)
[2]Technical Research Centre of Finland Ltd (VTT)
[3]Lloyd´s Register Consulting Energy AB (LRC)

Table of contents

Executive Summary

Objective of the project "Scenarios and Phenomena Affecting Risk of Containment Failure and Release Characteristics", dubbed SPARC, is to produce new data, and to develop models and methodologies for addressing severe accident scenarios and phenomena which are important to assess the risk of containment failure and radioactivity release in a postulated severe accident of Nordic nuclear power plants.

During 2018 substantial advances in experimental and analytical capabilities as well new insights into physical mechanisms were gained at KTH, VTT and LRC for: (i) development of experimental facilities of SIMECO-2, MRSPOD and POMECO-Q for studies of melt pool convection as well as remelting and quenching of debris beds; (ii) validation of the MEWA code for coolability analysis of particulate beds, and its applications to reactor-scale debris beds; (iii) experimental investigations on quenching of a hot sphere in a seawater pool and single molten droplet steam explosion in sea water; (iv) modeling of melt infiltration through particulate beds, and its validation against the REMCOD experiment; (v) coupled thermal-mechanical analysis approach and its validation against the FOREVER-EC2 experiment; (vi) study of a dynamic containment event tree modelling particularly focusing on the modelling of timings of events and uncertainty analysis; (vii) the comparison of MEWA and DECOSIM simulations for the post-dryout conditions of the same idealized particulate beds; and (viii) the application of a dynamic approach (such as ROAAM+) to PSA for an enhanced probabilistic risk analysis.

More achievements and detailed descriptions can be found in the related publications [1-14].

1. Introduction

The goal of this project is to produce new data, and to develop models and methodologies for addressing severe accident scenarios and phenomena which are important to assess the risk of containment failure and radioactivity release in a postulated severe accident of Nordic nuclear power plants. The experimental studies and deterministic modelling at KTH and VTT provide necessary insights and data for scenarios definition and tools development which are important to PSA studies at LRC. Therefore, this joint research project enables the three Nordic partners to leverage their ongoing projects, so as to maximize the research outcomes and spread the excellences to each other. The collaborative project also helps establish/enhance the informal Nordic networks for information exchange on severe accident research.

The research tasks were originally proposed as in the following four work packages, which were slightly adapted to co-supporting projects during implementation of the project.

WP1: Experimental study of severe accident phenomena and modeling development for assessment of core melt risk and corium stabilization in a Nordic BWR.

    1.1 In-vessel debris/molten pool behavior and RPV failure, in order to gain insights into complex in-vessel phenomena, including remelting of a debris bed to a molten pool, heat and mass transfer to the vessel wall and penetrations, failure of RPV penetrations (e.g., CRGTs, IGTs), and melt release scenarios including breach ablation/clogging issues.

    1.2 Ex-vessel debris bed coolability, in order to produce new data to address the following critical issues: post dry-out heat and mass transfer of a debris bed, and corium oxidation and debris remelting.

    1.3 FCI and steam explosion, involving large and small scale experiments to study molten fuel coolant interactions (FCI), using various oxides mixture and metal compositions to address material effects on melt fragmentation, Zircaloy and steel oxidation and hydrogen generation, and triggered and spontaneous steam explosion and its suppression.

    1.4 Modelling development for deterministic analysis.

    1.5 Further development and application of ROAAM+ framework.

WP2: Development of methods for coupling of Integrated Deterministic Probabilistic Safety Analysis tools such as ROAAM+ developed by KTH with PSA in general and PSA-L2 in particular.

    2.1 Development of IDPSA generated data processing techniques for informing PSA about importance of (i) timing of events and (ii) epistemic uncertainty.

    2.2 Different approaches will be considered in collaboration with KTH and VTT to addressing of dynamic events and physical phenomena in (i) cut sets; (ii) success and failure paths; (iii) connections to PSA-L3.

WP3: Deterministic modelling of debris bed coolability and threats for the containment integrity including steam and hydrogen explosions.

    3.1 Establishing a temperature-based coolability criteria for debris beds to evaluate the coolability of a multi-dimensionally flooded conical debris bed less conservatively. Assessing more thoroughly the effect of heat transfer models to the evolution of temperature in time. Modelling a truncated cone case with MEWA. Comparing results with the DECOSIM analyses done by KTH. This task is performed in close collaboration with task 1.2 to find out the origin of the differences in the debris bed post-dryout temperature behavior noticed in previous analyses by VTT and KTH.

3.2 MELCOR analyses on hydrogen explosions. Examining accident scenarios that may lead to hydrogen explosions in the Nordic BWR containment and reactor hall.

3.3 MC3D analysis on the effect of vessel breaking mode to dynamic pressure loads on cavity wall induced by steam explosion. Assessing steam explosion loads in Nordic BWR geometry and examining the sensitivity of the results to key input parameters. Also assessing the effect of break location.

WP4: Level 2 PSA modelling of phenomena and factors affecting containment failure probability and release characteristics.

4.1 PSA-L2 analysis with the focus on factors affecting source term characteristics. The factors to be considered are: (i) plant damage states (from PSA level 1), (ii) plant design and (iii) accident progression phenomena. Generic BWR model utilizing dynamic containment event trees is developed further, with special consideration of uncertainties.

4.2 Consideration of the factors affecting the probability and magnitude of relevant phenomena such as (i) steam explosions and (ii) non-coolable debris bed formation and core-concrete interaction.

2. Activities at KTH

2.1. Development of experimental capabilities

In order to address the behavior of core melt (corium) in the lower head of a light water reactor (LWR) during postulated severe accidents, the SIMECO-2 facility was developed at KTH for experimental studies on heat and mass transfer in a molten pool of oxidic and metallic corium simulants, as well as remelting of debris bed and molten pool formation. In addition, two other new facilities MRSPOD and POMECO-Q [1][2] are being developed for studies on melt penetration in debris beds and quench of debris beds, respectively.

The test section of SIMECO-2 has a slice of semi-circular geometry, representing the lower head of the reactor vessel, as shown in Figure 1. The internal diameter, height, and width of the test section are 1000×500×120 mm, respectively. The two side walls were made of transparent quartz glass to provides visual observation of melt pool behavior. The following key phenomena can be investigated on the SIMECO-2 facility:

  a) heat and mass transfer to the vessel wall in stratified pool;
  b) effect of the crust and its formation on the interface of layers;
  c) influence of top metallic layer thickness on the focusing effect; and
  d) remelting of corium debris bed simulants representing the volumetric decay heat.

A lot of efforts, including small-scale tests with molten salts, have been devoted to selection of simulant materials for corium, which should satisfy the requirements as summarized in the

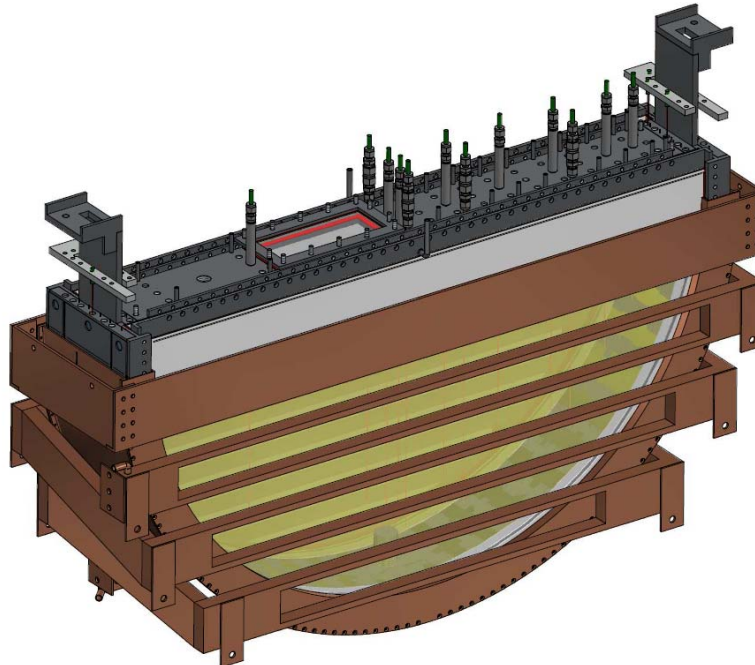Table, in order to reach the objectives and specific conditions of the experiment.

Figure 1: Schematic of SIMECO-2 test section.

Table 1: Requirements to simulant materials for SIMECO-2 experiment

Objective	Requirement
Formation of stratified configuration of molten pool	Metal (upper layer) and oxide (bottom layer) simulants are immiscible liquids with different densities.
Oxide debris bed simulant material remelting	Possibility to volumetric heat release in solid state of simulant material (coupled with the heating methods).

Inversion of oxide and metal simulants layers	Possibility of metal/oxide simulant composition change to control density of layer.
Effect of the crust formation on the layers interface	Temperature difference between solidus and liquidus of oxide layer simulant. Higher melting temperature of oxide layer simulants compared to the metal layer simulants.
Visual observation on the pool behavior	Full or partially transparency of oxide layer simulant in visible spectrum.
Other	Low toxicity.
	Absence of chemical interaction between simulants and construction materials of test section.
	Low maintenance cost.
	Reliable data about properties and phase equilibria of selected materials.

Based on the available data in literature on physical properties, the phase equilibria as well as the small-scale tests, the mixture of salts CsCl-KCl-LiCl and that of metals Al-Mg were selected as an oxidic and metallic simulant materials, respectively.

The phase diagrams of CsCl-KCl-LiCl and Al-Mg systems are shown in Figure 2. The exact compositions of salt and metallic components are variable parameters which can be adjusted according to the specific experimental needs.
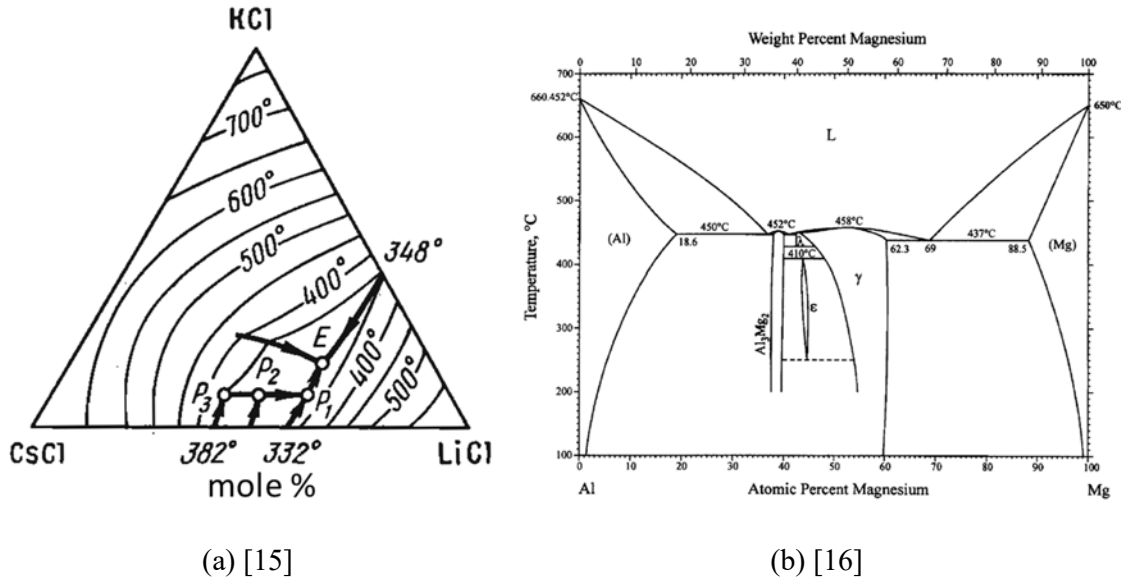

(a) [15]   (b) [16]
Figure 2: Phase diagrams of CsCl-KCl-LiCl (a) and Al-Mg (b) systems

The pre-test simulation of SIMECO-2 stratified molten pool has been performed in order to provide analytical support for the design of the facility, instrumentation, experimental test matrix and test procedures. Based on the pre-test simulation of the pool performed using the Phase-change Effective Convectivity Model (PECM) implemented in FLUENT [17], the effect of internal radiation on natural convective heat transfer in a volumetrically heated molten pool was also investigated [2].

For selection of heating methods for the SIMECO-2 facility, three experimental approaches of pool heating were considered and evaluated: immersed cartridge heating, joule (direct resistive) heating, and induction heating. Based on a number of small-scale tests as well as

numerical simulations have, the choice of heating method was made in favor of induction heating, which is contactless method and can provide melt natural convection similar to the melt convection with volumetric heat. In order to confirm a potential applicability of current method for SIMECO-2 pool heating, a numerical simulation of induction heating has been performed [18] for design of an encircling inductor (Figure 3a) with the most uniform power distribution in the salt pool (Figure 3c).
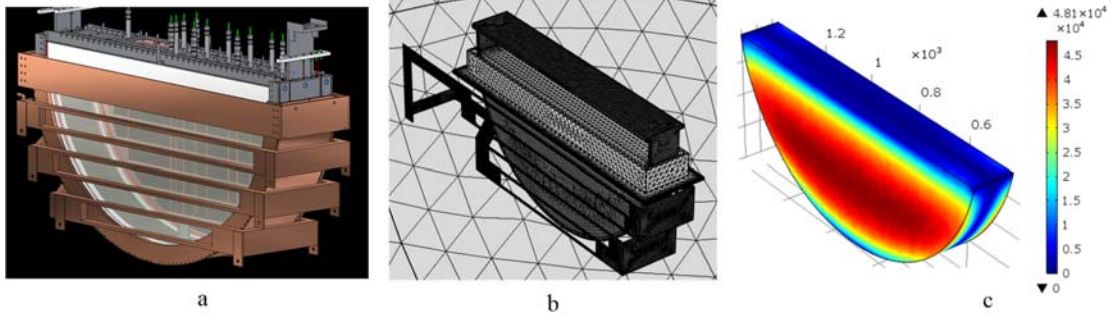

Figure 3: The general view of the inductor (a), numerical mesh (b) and resulting volumetric current density distribution in the salt pool, A·m^{-2} (c)

In addition to the present investigation on melt pool heat transfer, the SIMECO-2 facility is also suitable for studies on debris remelting process and formation of molten pool, under several important configurations as illustrated in Figure 4. The transparent quartz walls of the SIMECO-2 test section provides visual observation of fusible particles remelting, and the induction heating allows to study phenomena: (i) boiling, dryout and post dryout heat transfer in debris beds; (ii) rearrangement of molten fusible fraction in refractory debris; and (iii) Influence of penetration tubes on the infiltration of fusible particles in refractory debris.
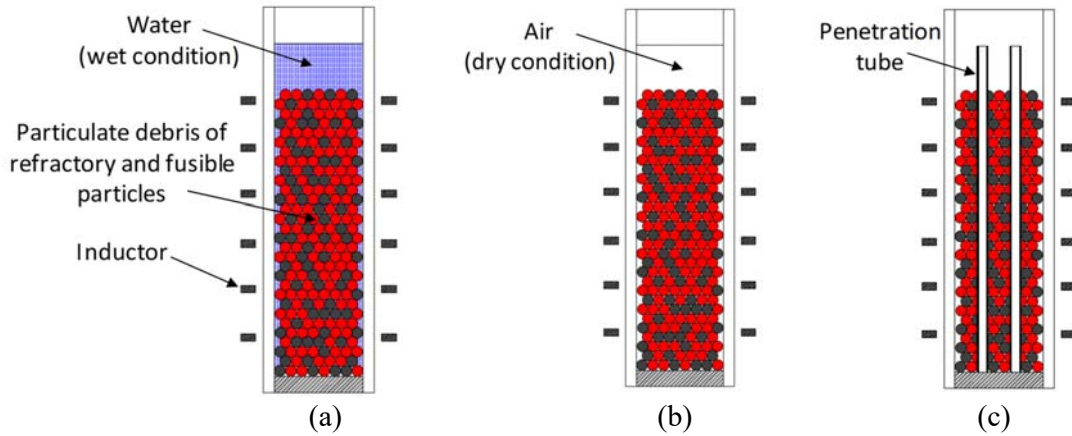

Figure 4: Schematic of central cross section of SIMECO-2 facility under different conditions of debris bed remelting.

2.2. Analysis of ex-vessel debris bed coolability

A study was performed at KTH to validate the MEWA code [19][20] against experiments for two-phase flow and dryout in particulate beds, and then investigating the coolability of ex-vessel debris beds with cylindrical, conical and truncated conical shapes assumed to form under severe accident scenarios of a boiling water reactor. The experiments chosen in the present validation are POMECO-FL [21] and POMECO-HT [22] carried out at KTH to investigate frictional laws and coolability limit (dryout) of particulate beds, respectively. The comparisons of the experimental and numerical results show that the MEWA code is capable

of predicting both the pressure drop of two-phase flow through porous media and the dryout condition of various stratified beds. While the coolability of a one-dimensional homogeneous debris bed is bounded by counter-current flow limit (CCFL), the coolability of a heap-like debris bed can be improved due to lateral ingression of coolant in a multi-dimensional geometry. After the validation work, the code was employed to simulate the coolability of prototypical debris beds of the cylindrical, conical and truncated conical shapes. The simulations showed that the dryout power density of a prototypical debris bed was roughly inversely proportional to the bed's height regardless of the bed's shape. The impacts of a debris bed's features on coolability are manifested in three aspects: multidimensionality and contour surface area of the bed, as well as the uniformity of its shape. The contour surface area is defined as the interface between debris bed and water pool, and its effective value depends on the surface orientation that determines the amount of water ingress and vapor escape. The perfect uniformity in bed's shape as cylindrical bed results in even distributions of temperature and void fraction. The dryout power density was also predicted to be strongly correlated to the uniformity of bed's shape. The MEWA simulation also predicted that coolability was improved by an downcomer embedded in the center of debris bed. The efficiency of such enhancement was largely determined by the downcomer's length, whose optimal value was obtained in simulation. The details of the study can be found in [3].

Another study is concerned with the quench of a heap-like debris beds formed in the lower drywell of a Nordic-type boiling water reactor (BWR) during a postulated severe accident. A numerical simulation using the MEWA code was performed to investigate the quenching process of the ex-vessel debris bed at post-dryout condition upon its formation. To qualify the simulation tool, the MEWA code was first employed to calculate the quenching tests recently conducted on the PEARL facility [23][24]. Comparisons of the simulation results with the experimental measurements show a satisfactory agreement. The simulation for the debris bed of the reactor scale shows that the heap-like debris bed flooded from the top is quenched in a multi-dimensional manner. The upper region adjacent to the centerline of the bed is the most difficult for water to reach under the top-flooding condition, and thus is subject to a higher risk of remelting. The oxidation of the residual Zr in the corium has a great impact on the coolability of the debris bed due to (i) large amount of reaction heat and the subsequent positive temperature feedback, (ii) the local accumulation of the produced H_2 which may create a "steam starvation" condition and suppresses the oxidation. As possible mitigation measures of oxidation, the effects of bottom-flooding and bypass on quench were also investigated. It is predicted that the debris bed becomes more quenchable with water injected from the bottom, especially for the case with the floor partially flooded in the center. A bypass channel embedded in the center of the debris bed can also promote the quenching process by providing a preferential path for both steam escape and water inflow. The details of the study can be found in [4].

2.3.   Quench of hot spherical particles in seawater

During the Fukushima nuclear accidents, raw seawater has been used to cool the reactor cores [25]. After the accidents, attention was paid to the effects of impurities in the seawater on core degradation, chemistry and fuel coolant interactions (FCI).

An experimental study was carried out at KTH to investigate the effect of seawater on FCI and steam explosion [5], using the MISTEE platform [6]. Since a steam explosion occurs when the vapor films surrounding the melt droplets collapse, it is important to understand the instability of the vapor films. For this purpose, quenching of a hot stainless-steel sphere was also investigated in the MISTEE platform [7].
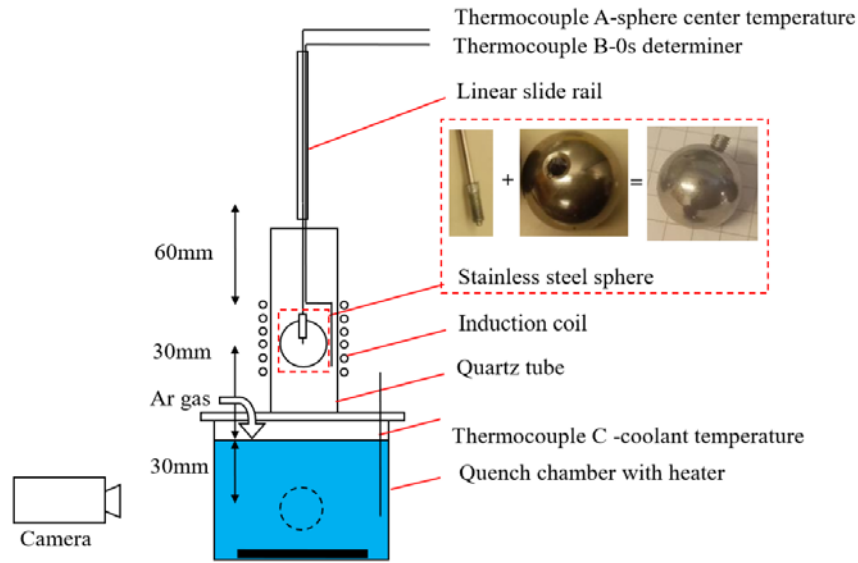
Figure 5: quenching of stainless-steel sphere in the MISTEE facility.

The experimental setup (Figure 5) consists of an induction furnace and a water pool bath filled with deionized (DI) water or seawater. A 10mm stainless-steel sphere was heated to a prescribed temperature in the induction furnace enclosed within a quartz tube, and then inserted into a transparent chamber filled with subcooled sea water (salinity is 35g/kg). The dynamics of the vapor film during the quenching process was recorded by a high-speed camera, and the sphere's temperature history was acquired by a thermocouple located in the center of the sphere. The sheathe of the thermocouple serves as the holding of the sphere in the water pool.

As shown in Figure 6, during the insertion of a 1000℃ sphere into the 30-mm depth of the 55℃ seawater pool, rapid formation of void channel, bubble detachment and vapor film oscillation were observed. The film boiling became stable at the time of 4.14s when the temperature of sphere was cooled down till 941℃.
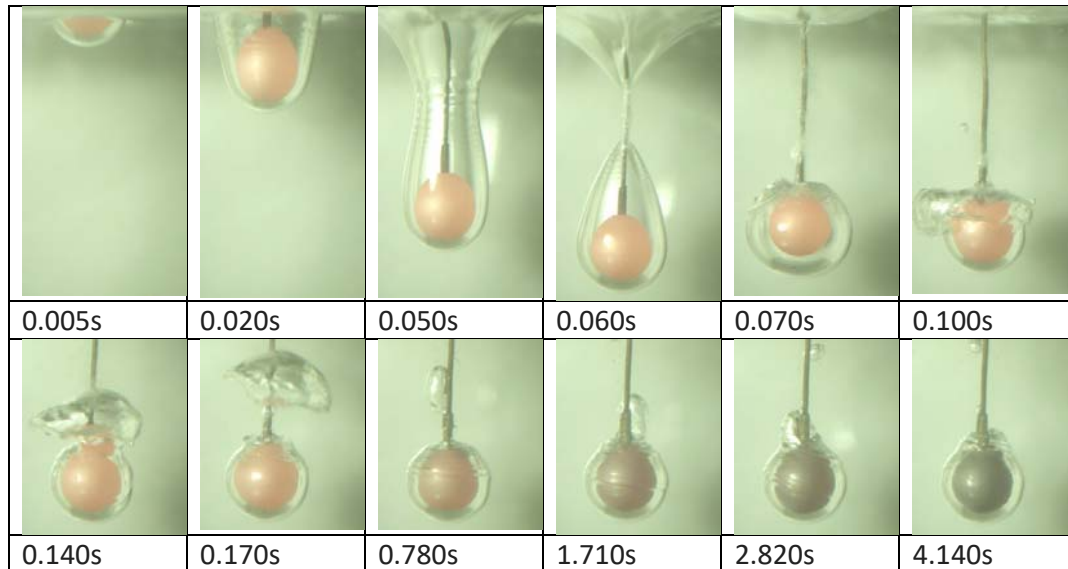

Figure 6: Immerging process of 1000℃ sphere and stable vapor film formation in seawater at 55 ℃.
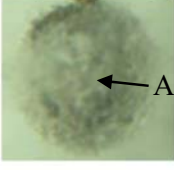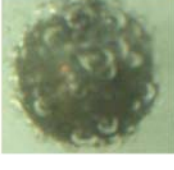
The transition of boiling modes on the hot sphere during its quenching in seawater is similar to that in fresh (DI) water (as shown in Figure 7), but the duration of each boiling mode was remarkably shorter, especially for the process of vapor film collapse, which had completed within 0.001s.
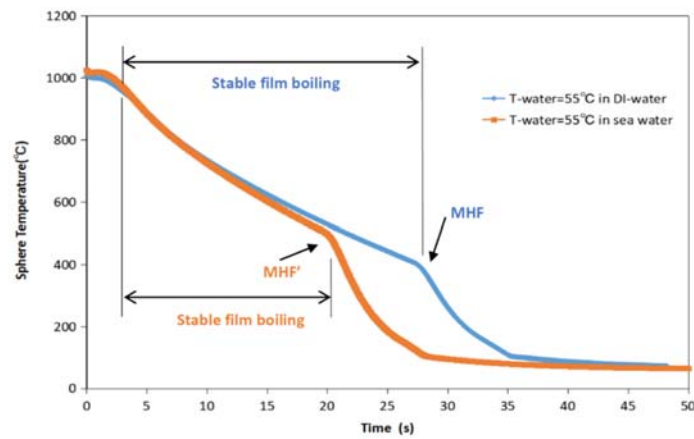
(a) temperature history curves and time of vapor film collapse
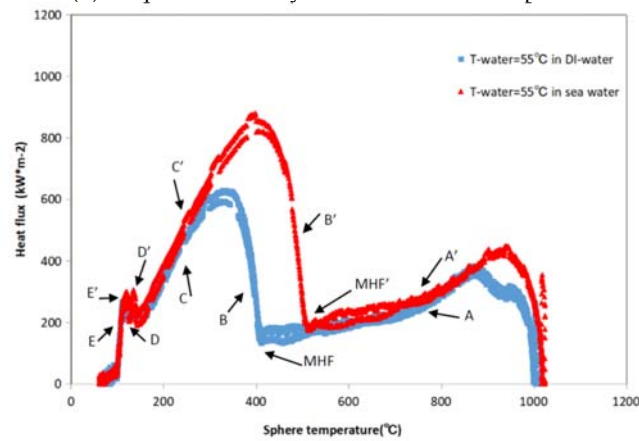
(b) heat flux curves in term of sphere temperature

Marker	Boiling modes	Present test in DI water			Present test in Sea water	
A/A'	Film boiling					
MHF/MHF'	Vapor film collapse	26.903s	27.090s	27.121s	19.120s	19.121s
B/ B'	Expansion wave		← A			
C/ C'	Golf boiling					
D/ D'	Transition boiling					
E/ E'	Nucleate boiling					

(c) images of typical boiling modes

Figure 7: Transition of boiling modes during quenching of sphere in seawater.

Based on the experimental data obtained under different coolant temperature, the minimum film boiling temperatures ($T_{MHF'}$) in seawater, as an important characteristic parameter of boiling transition, were plotted in Figure 8, whose values were about 100 ℃ more than those (T_{MHF}) in fresh water by average. The linear trend of $T_{MHF'}$ with coolant temperature can be correlated as follow.

$$T_{MHF'} = -5.7479 T_{water} + 833.37 \tag{1}$$
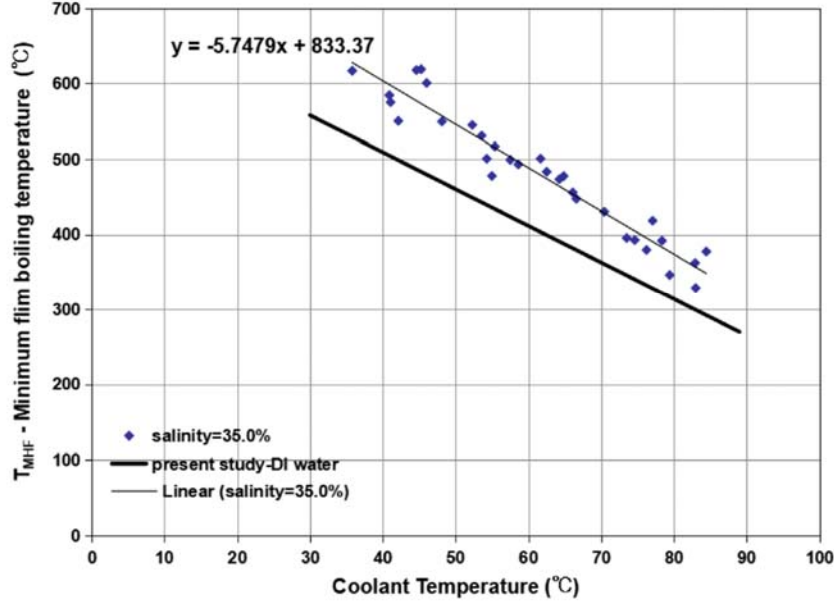
Figure 8: Minimum film boiling temperature.

2.4 Modelling of melt infiltration through particulate beds

Severe accident progression in nuclear power plants may be dependent on the metallic melt infiltration through an oxidic porous debris bed which may form in both in- and ex-vessel phases of the accident. Motivated to understand the relevant phenomena, the REMCOD experiment is being carried out to explore the effects of wettability, melt superheat and debris temperature, as well as particle size and morphology on the melt infiltration through particulate beds.

Given the experimental observation and data, model development is required to characterize the metallic melt filtration through porous oxidic debris to meet the following objectives:

- deep understanding of competing mechanisms;
- identification of governing parameters for scaling rules;
- proper definition of relevant time and length scales;
- definition of needs for further experiments with different range of affecting parameters.

Challenges in this area is the need to define the proper regime(s) according to combination of the hydrostatics and viscous forces as well as capillary forces. For vertical infiltration of melt into a porous medium, when both the gravitational and interfacial forces are important.

Consider the sketch in Figure 9 where at time zero, a liquid of fixed volume and initial height of h_0 is placed on top of a deep and dry porous medium with uniform porosity ε and permeability k. As the time passes, the liquid elevation above the top surface (h (t)) will decrease while the liquid penetration depth into the porous medium ($l(\mathrm{t})$) will increase. Differentiating the liquid pressure above and inside the porous medium with respect to the vertical direction and combining it with Darcy's law, one can easily determine the equation representing time-dependent drainage velocity as:

$$v = -\frac{k}{\mu}\left(\rho g\left(\frac{h}{l} + 1\right) + \frac{2\sigma\cos\theta}{Rl}\right), \qquad \text{for } -l(t) \leq z \leq 0 \tag{2}$$

13
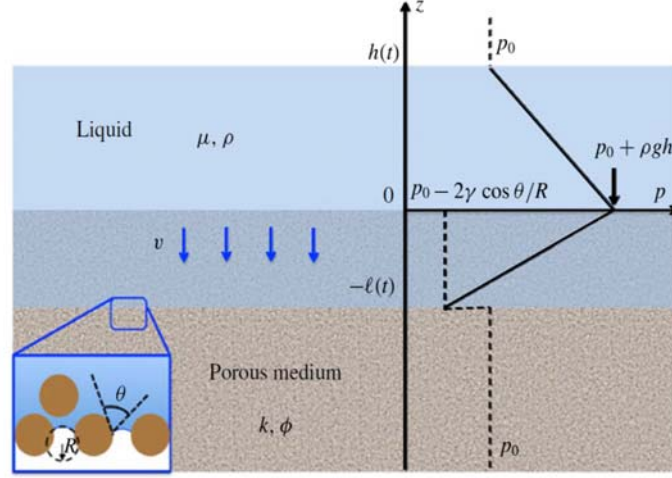
Figure 9: Vertical infiltration of melt into porous medium [26].

It means that the drainage dynamics is governed by gravity and capillary forces as emerged in the first and second terms of the above equation. The term v could be eliminated to represent the equation as function of the liquid penetration depth inside the porous media (l), by considering that the relationship between the change of the liquid volume inside the porous medium and above it. Considering a fixed volume (fixed initial height h_0), the flow dynamics is obtained by the following differential equations:

$$\varepsilon \frac{dl}{dt} = \frac{k}{\mu}\left(\rho g \left(\frac{h}{l} + 1\right) + \frac{2\sigma\cos\theta}{Rl}\right) \tag{1}$$

$$h(t) + \varepsilon l(t) = h_0 \tag{2}$$

Substituting the following dimensionless parameters into the above equations:

$$H = \frac{h}{h_0}, \quad L = \frac{l}{h_0}, \quad T = \left(\frac{k\rho g}{\varepsilon\mu h_0}\right)t, \quad H^* = \frac{h^*}{h_0} = \frac{2\sigma\cos\theta}{Rl}$$

One can obtain two dimensionless equations for the dynamics of liquid drainage into the porous medium caused by gravity & capillary effects:

$$\frac{dL}{dT} = \underbrace{\left(\frac{H}{L} + 1\right)}_{gravity} + \underbrace{\frac{H^*}{L}}_{capillary} \tag{3}$$

$$H + \varepsilon L = 1 \tag{4}$$

It is possible to combine the above equations and represent it as a single equation for L such that:

$$\frac{dL}{dT} = \left(\frac{H^*+1}{L}\right) + 1 - \varepsilon, \quad \{I.C. \quad L(0) = 0\} \tag{5}$$

Interpretation of the governing equations could be summarized as follows:

- For early time periods ($T \ll 1$), the term $\left(\frac{H^*+1}{L}\right)$ dominates, i.e. the capillary forces are important and the penetration depth is correlated with time as $L \propto T^{1/2}$.
- For late time periods ($T \gg 1$), the term $(1 - \varepsilon)$ dominates, i.e. the capillary forces vanish and the penetration depth is correlated with time as $L?T$.
- The transition between these two distinct dynamics occurs near $T^* = O(1)$.
- $L \in [0, 1/\varepsilon]$ because when $L = 1/\varepsilon$, all of the liquid has drained into the porous medium. There exists a critical drain-out time T_d, which corresponds to $L(Td) = 1/\varepsilon$.

14

For longer times, $?p = 0$ and $u \equiv -\frac{\rho g k}{\mu}$ thus L increases linearly with T.

The model has been coded using ODE solver of MATLAB software. The first calculations showed that the same trend exists in the numerical and experimental results meaning that the drainage is governed by capillary forces at the beginning and interfacial forces at later times. However, the results do not collapse with experiment. Therefore, we first study the effect of length scale and time scale to see if the problem could be resolved by following other scaling approaches. For that, we have developed 6 other scaling approaches.

A large number of Monte Carlo (10^6) simulations is performed in order to provide required statistical data for the quantification of first order and total order uncertainty importance measures [27]. The results are summarized in Table 2 with the highest rank given to the most important parameter.

The percentage of interaction terms is not relevant in each of the parameter's importance. $\sum_{i=1}^{7} s_i = 93\%$, confirms that the significant portion of the output variance is explainable by individual effect of the parameters. From Table 2, it is observed clearly that permeability gives the greatest impact on the output uncertainty (83% single effect & 90% total effect contribution). In the case we need to invest in uncertainty reduction, this parameter has a higher priority. If the uncertainty in both "permeability" and "porosity" parameters is eliminated, then the output parameter uncertainty will be reduced by almost 90%.

Table 2: Summary results of uncertainty importance analysis

Input Parameter		$S_1(X_J)$	$S_T(X_J)$	Ranking
permeability		8.32E-1	9E-1	1
porosity		5.62E-2	1.01E-1	2
contact angle		2.86E-2	4.61E-2	3
melt density		7.4E-3	1.38E-2	4
melt viscosity		3.60E-3	6.8E-3	5
Initial height		4e-4	6.48E-4	6
pore radius		~0	3.59E-4	7
acceleration of gravity g		1.42E-4	2.66E-4	8
melt surface tension		~0	4.52E-5	9

For the problem of melt infiltration in the REMCOD experiment, an appropriate value of the permeability is required to provide the best fit of our scaling model to the experimental data. Based on literature survey on the available correlations with the aim of testing each model's applicability to the problem of REMCOD experiment, it was showed that for particles with hydraulic diameter of the pores less than 0.5 mm, the permeability is best predicted by the Coelho's correlation [28]:

$$K = 0.117 \times \varepsilon^{4.57} \times R^2 \tag{8}$$

where R is the pore radius. For the hydraulic diameters in the range of 0.5 mm to 1mm the best predictions belong to Tan's suggested correlation [29]:

$$K = 0.08127 \times \varepsilon^{3.06} \times R^{1.64} \tag{9}$$

If the pores hydraulic diameter is greater than 1mm, the best choice would be Rahli's correlation [30]:

$$K = 0.0606 \times \pi/4 \times \frac{\varepsilon^{5.1}}{1-\varepsilon} \times R^2 \tag{10}$$

Figure 10 summarizes the predictions by the developed model by using new permeability correlations implemented in the simulation process. It is observed that not only the same trend exists in both experiment and simulation results but also they coincide very well, once the proper value is selected for the permeability.
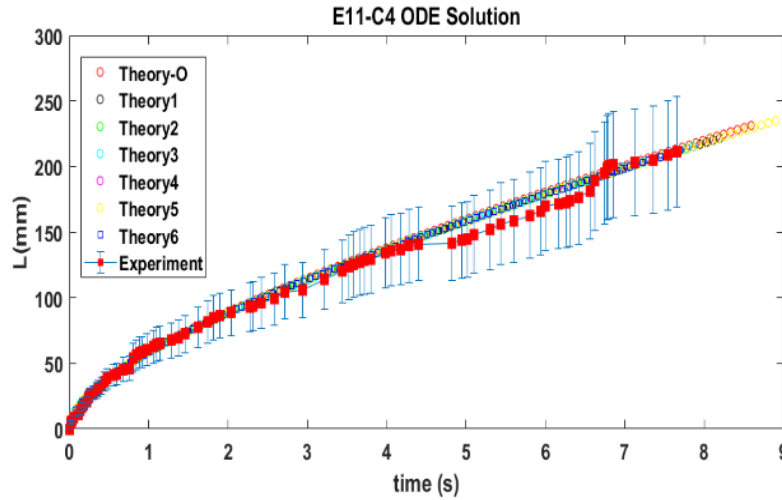

Figure10: Model predictions versus Experimental data for REMCOD experiment.

2.5 Coupled thermal-mechanical simulation of vessel failure

In the in-vessel progression of a hypothetical severe accident, core melt would relocate into the lower head and impose significant thermal loads on the reactor pressure vessel (RPV). If the cooling methods can not sufficiently remove the decay heat, the RPV would fail under the thermal attack.

The RPV failure issue is a transient thermal fluid-structural interaction (FSI) problem which involves molten pool heat transfer and creep deformation of the RPV. The modelling of this issue should address three aspects: (1) molten pool heat transfer which would determine the thermal load on the vessel; (2) creep deformation due to thermal and stress loads, which plays a dominant role in vessel failure; (3) coupling of heat transfer and vessel deformation. The FSI problem is therefore a problem involving coupled analysis per se. It is important to develop a coupling method to perform the FSI simulation.

A two-way tight coupling method considering both the transient thermal load from molten pool on vessel and the influence of vessel deformation on molten pool heat transfer is still full of challenge, due to implementation of too much information exchange. In the present study, we assume that the influence of vessel deformation on molten pool heat transfer can be ignored and only consider the thermal load from molten pool to vessel. Compared to two-way coupling, one-way coupling approach is computationally efficient, especially when turbulence, heat transfer, large scale and structural non-linearity are involved. Thereby a one-way thermo-mechanical coupling approach based on the ANSYS platform was explored here. The general procedures can be summarized as follows:

(a) heat transfer simulations of the molten pool and vessel in ANSYS Fluent where special attention was paid on turbulence modelling of molten pool;
(b) transient thermal loads transformation from ANSYS Fluent to ANSYS Structural in ANSYS Workbench with use of an extension tool;
(c) structural analysis of the vessel in ANSYS Structural where special attention was paid on creep modelling of vessel steel.

The dominant phenomena in molten pool heat transfer is the turbulent natural convection driven by internal heat source. Direct numerical simulation and large eddy simulation are too computationally expensive to be practical, because of the large scale and long failure time. The SST model is employed in current application, which is a combination of k-ε and k-ω equations. It uses a k-ω formulation in the inner parts of the boundary layer and switches to a k-ε behavior in the free-stream. It is highly recommended by ANSYS for most industrial heat transfer problems.

Creep deformation is an important phenomenon for structural materials when they are subjected to high temperature and high stress. Creep is characterized by a three-stage process, namely the primary stage when creep strain rate is decreasing with time, the secondary stage when creep strain rate is almost constant and the tertiary stage when the creep strain rate increases with time before it fails. Commercial codes such as ANSYS Structural and SIMULIA in default embed simple creep models which contain only primary or/and secondary stage(s) since for most engineering applications creep in tertiary stage is not of interest and important structural components would be safely replaced before going to tertiary stage. Since the vessel failure means that RPV would experience the tertiary stage, modelling tertiary stage is necessary. Therefore, a three-stage creep model is developed and implemented in the coupling approach through the user-programmable functions supported by ANSYS Structural. The modified theta projection method, which agrees with experiment data, was used as the creep model of vessel steel:

$$\varepsilon = \theta_1(1 - e^{-\theta_2 t}) + \theta_m t + \theta_3(e^{\theta_4 t} - 1) \tag{11}$$

where ε is the creep strain, t is time and θ_i (i=1, 2, 3, 4, m) are non-negative model parameters. In this expression, the first term decays with time, suitable to describe the primary creep stage, the second term linearly increases with time, suitable to describe the second stage and the third term increases exponentially with time, suitable to describe the tertiary stage. The model parameters are temperature- and stress-dependent and are interpolated from parameters of experimental creep curves.

Modelling and coupling details are can be found in [10].

The FOREVER-EC2 experiment [31][32] was used to validate this coupling approach. The experiment was conducted at KTH to investigate the phenomena of melt pool convection, vessel creep, possible failure processes and failure modes which occurred during the late phase of in-vessel progression by heating up a molten pool in the vessel. As shown in Figure 11, a 1:10 scaled RPV was employed in the experiment which had an outer diameter of 406 mm and wall thickness of 15 mm. French reactor steel (16MND5) was used for the lower head while upper cylindrical part was made of German Steel (15Mo3). A binary mixture of 30% CaO-70% B_2O_3 was used as melt simulant of corium. During the experiment, the melt pool was heat by a specially designed heater, to maintain a maximum t pool temperature up to 1300 °C. No external cooling was applied. The pressure in the vessel was maintained at 25 bar during the experiment.
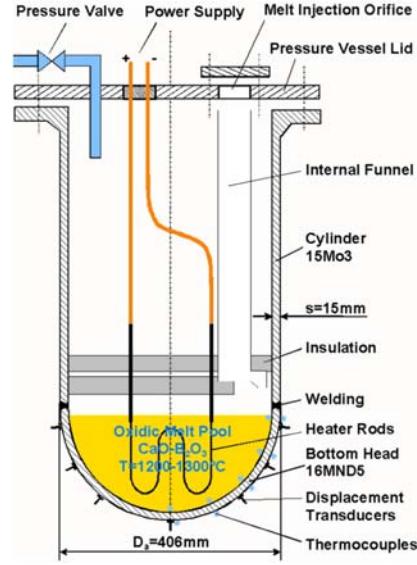
Figure 11: Schematic of FOREVER-EC2 experiment.

As one of the simulation results, Figure 12 shows the temperature fields with and without melt pool. A thermal stratification (Figure 12a) is seen in the molten pool, which is an expected phenomenon of natural convection driven by volumetric heat source. The highest temperature is 1609 K. Meanwhile, the area with a bulk temperature is small, indicating a weak convection resulting from a low Rayleigh number (~8.7834×10^9). In the lower head region covered by melt as in Figure 12b, temperature generally increases with polar angle and decreases when the polar angle is approaching 90°. It further decreases with the height in the cylindrical part. The highest temperature of the vessel is 1364 K.
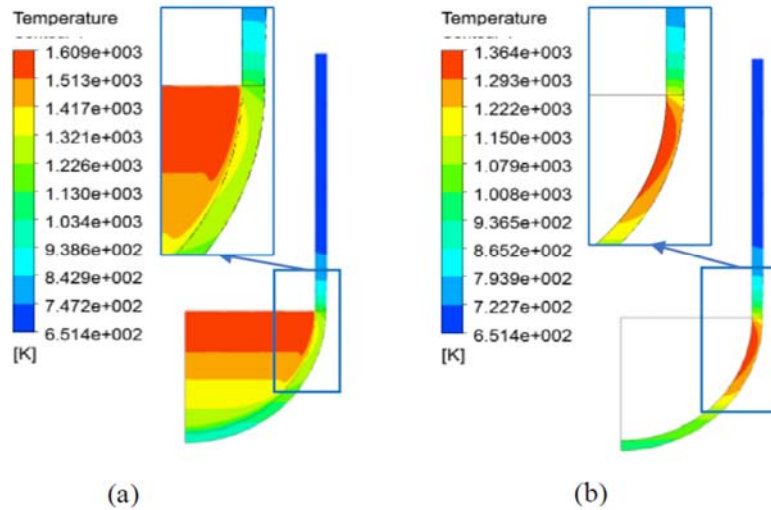
Figure 12: Temperature distribution: (a) global, (b) local vessel.

Figure 13 shows the temperature distribution along the vessel wall. In the lower head part, the temperatures of both internal and external vessel surfaces increase with polar angle, and reach respective peak values of 1280 K and 1364 K at the polar angle 80°. The predicted ex-vessel temperature profile generally agrees with the experimental data (the orange dots in Figure 13) in trend but is slightly higher than the measured. The discrepancy is mainly due to the installation method of the sheathed thermocouples. The effect of the thermocouple's thickness on the measurement error was estimated in a separate calculation, and the results show that the

18

difference between thermocouple's reading and real ex-vessel temperature is quite pronounced at high temperature. Based on the calculation, the corrected ex-vessel temperatures can be obtained as the green dots in Figure 13, which fit well to the simulated profile (the grey curve) in the range of 40°- 90°. In the bottom part (<30°), the simulated temperatures are slightly higher than the experimental data. The main reason may be crust formation and evolution in the bottom along the lower head, which is hardly accounted in the up-to-date modeling capabilities.

The predicted in-vessel temperature (the yellow curve) is higher than the ex-vessel temperature at the same angle, because heat is continuously transferred from inner surface to outer surface. The temperature difference varies from 30 K at 0° to 100 K at 80°.

Figure 13: Temperature profiles along internal and external vessel.

More validation results and discussions can be found in [10]. The validated coupling approach can be applied to reactor safety analysis cases in the next step.

3. Activities at VTT

3.1. Probabilistic and deterministic analyses at VTT

3.1.1. Introduction

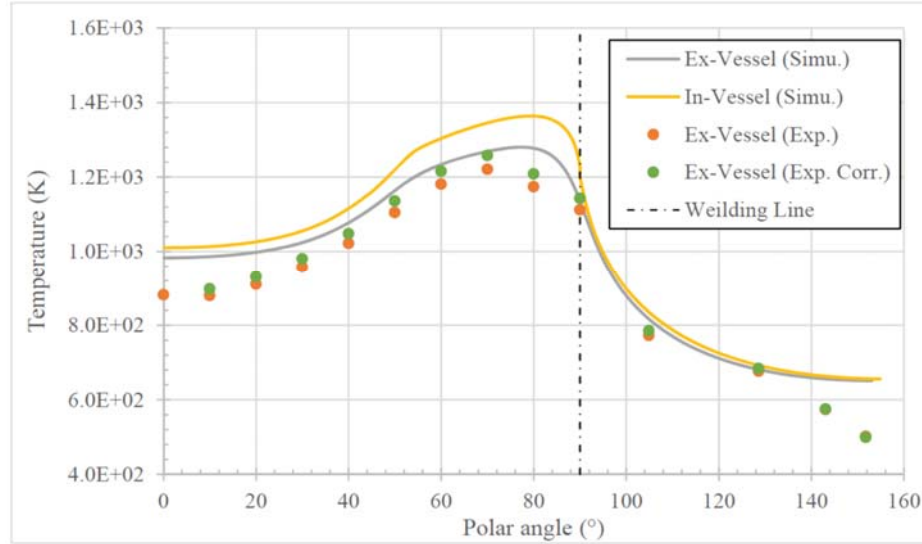To minimize potential source term to the environment during an unlikely event of severe accident, each Nuclear Power Plant (NPP) has a Severe Accident Management (SAM) strategy that should be justified by suitable means including typically both probabilistic and deterministic analyses.

Level 2 Probabilistic Risk Assessment (PRA) studies NPP accident progression after core damage, and the frequency, size and composition of radioactive releases [33]. These results are used in formulating the SAM strategy, but also for other purposes such as verification of the achievement of safety goals set by the regulator. Here some refinements to the level 2 part of a generic Boiling Water Reactor (BWR) model are made. In particular, dynamic modelling of timings of depressurization, emergency feedwater system recovery, emergency core cooling system recovery and lower drywell flooding is implemented. In addition, a two-phase uncertainty analysis procedure is presented and implemented in small and simple case studies.

The SAM strategy of the Nordic BWRs relies on cooling the corium in the flooded drywell. During corium discharge to the flooded drywell, the molten material fragments into droplets and subsequently solidifies into particles that settle on the floor of the containment forming a porous debris bed, of which coolability has to be ensured. Instead of the dryout heat flux, that might be overly conservative, it has been proposed that the coolability limit of a debris bed should be based on the increase of the particle temperature. Here MEWA simulations for debris bed behaviour in post-dryout conditions are compared to KTH's DECOSIM simulation results.

The above mentioned probabilistic and deterministic analyses are summarized as follows. More details can be found in the respective research reports in Appendix A and B.

3.1.2. Dynamic PRA modelling

The Level 2 modelling in the FinPSA software tool [34] is based on dynamic Containment Event Trees (CET) and script files behind the event tree sections [35]. The script files define functions to calculate conditional probabilities of event tree branches, timings of accident progression, and amounts of releases. Dynamic CETs provide a good alternative to analyze the effects of different timings and timing combinations. PRA modelling is more realistic when timings are explicitly included in the model and affect accident sequences in the model.

Two-phase uncertainty analysis

The purpose of a two-phase uncertainty analysis method is to separate the treatment of aleatoric and epistemic uncertainties. Aleatoric uncertainty represents uncertainty resulting from inherent randomness and epistemic uncertainty is the uncertainty related to our lack of knowledge about a system or phenomenon. The two-phase uncertainty analysis method is demonstrated by a Emergency Core Cooling System (ECCS) case study.

The two-phase uncertainty analysis approach is based on that Monte Carlo simulation of the event tree is conducted on two layers. On the epistemic layer, model parameter values are randomly varied at each iteration. For the set of parameter values thus obtained, several iterations on the aleatoric layer are performed. Each iteration on the aleatoric layer consists of randomly assigning values to random variables ("noise terms") of the event tree model based on the parameter values from the epistemic layer, and calculating the accident progression and end result variables in each branch of the event tree based on these random variable values. Based on the results from the aleatoric layer, uncertainty distributions for the accident

progression and end result variables (conditioned on the parameter values) are calculated on the epistemic layer. Finally, unconditional uncertainty distributions of the accident progression and end result variables are calculated based on the results from the epistemic layer.

One- and two-phase uncertainty analyses were performed (Appendix A) for the three different ECCS recovery event trees illustrated in Figure 14. The two-phase uncertainty analysis was performed in Excel, because the two-phase procedure has not been implemented in FinPSA yet. In the traditional one-phase uncertainty analysis the model was simulated 10 000 times to have the mean probability of vessel failure. In the two-phase uncertainty analysis, variables representing aleatoric uncertainties were simulated 200 times in each simulation block, and variables representing epistemic uncertainties were simulated 100 times, thus amounting to a total of 20 000 iterations on the aleatoric layer. The mean vessel failure probability was calculated for each of the 100 simulation blocks, and an uncertainty distribution was drawn for the vessel failure probability based on those 100 points.
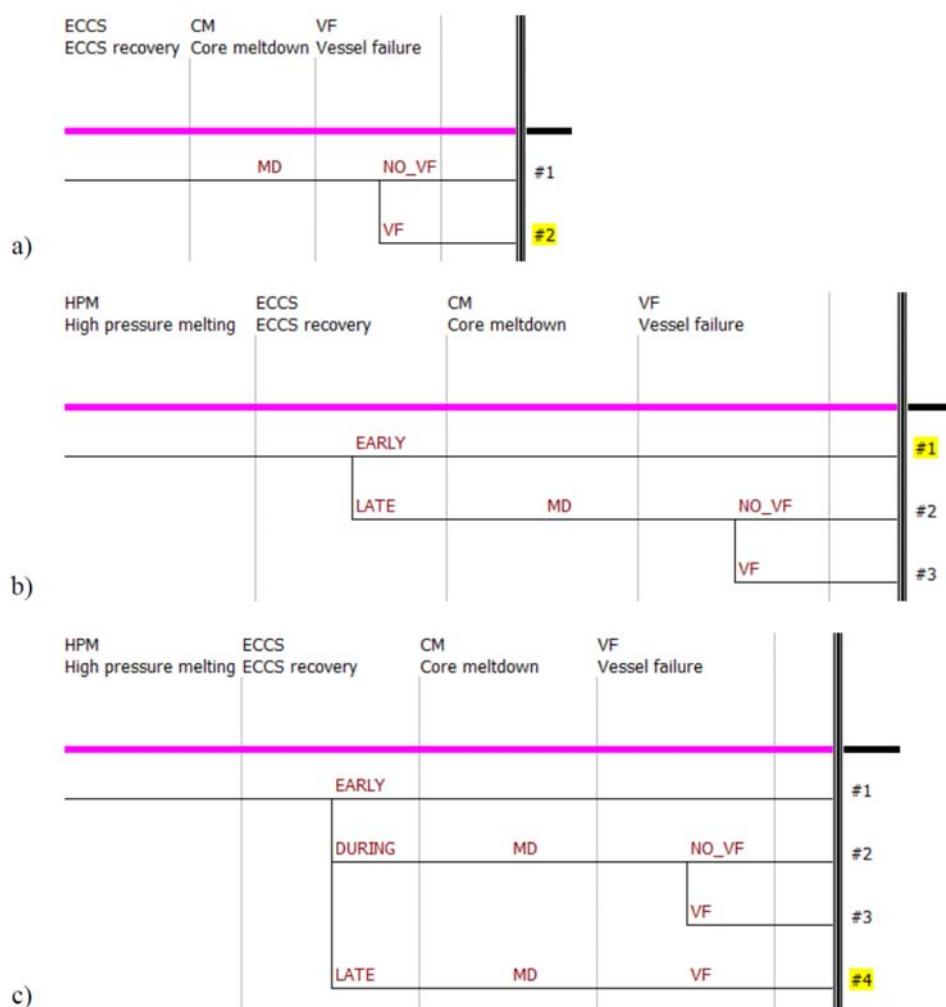
Figure 14: Different ECCS recovery event trees: a) one branch covering all recovery timings (MD means meltdown distribution), b) division to early and late recovery and c) early recovery, late recovery and recovery during core melting.

The results illustrate why aleatoric and epistemic uncertainties need to be separated to perform the uncertainty analysis in a consistent manner. Using one-phase uncertainty analysis procedure, the three models produced totally different uncertainty distributions for vessel failure probability as can be seen in Figure 15, even though they all represent the same problem

and give approximately same mean result. This shows how the resulting uncertainty distribution depends on the modelling decisions if aleatoric and epistemic uncertainties are not separated. On the other hand, the two-phase uncertainty analysis procedure produced approximately similar uncertainty distribution in each case as can be seen in Figure 16. It was also demonstrated how the accuracy of the results increases when more event tree branches are added to analyse different recovery time ranges separately, i.e. with model c, a smaller number of simulations related to aleatoric uncertainties will produce results with the same accuracy as for models a and b.
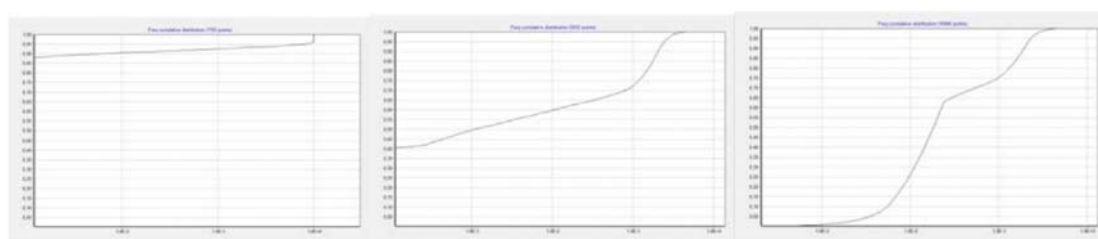
Figure 15: Cumulative uncertainty distributions of vessel failure probabilities from models a, b and c produced using one-phase uncertainty analysis.
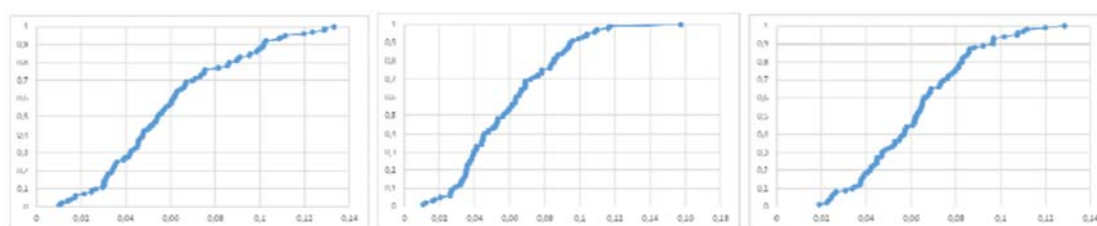
Figure 16: Cumulative uncertainty distributions of vessel failure probabilities from models a, b and c produced using two-phase uncertainty analysis.

High-pressure melting analyses

A new version of the high pressure melting CET of the BWR model [36] has been prepared utilising dynamic modelling of timings of depressurisation, emergency feedwater system (EFWS) recovery, ECCS recovery and lower drywell (LDW) flooding. Only one-phase uncertainty analysis was performed for the full CET to calculate the mean frequencies of accident sequences. In addition, a limited two-phase uncertainty analysis is performed for a small part of the CET.

The upper part of the CET is presented in Figure 17. Compared with the previous model, a new section for the EFWS recovery has been added (branches not shown in the figure because the high pressure part of the tree has been cut off). Some parts of the CET structure have also changed and some new CET functions have been introduced. The details are presented in Appendix A.
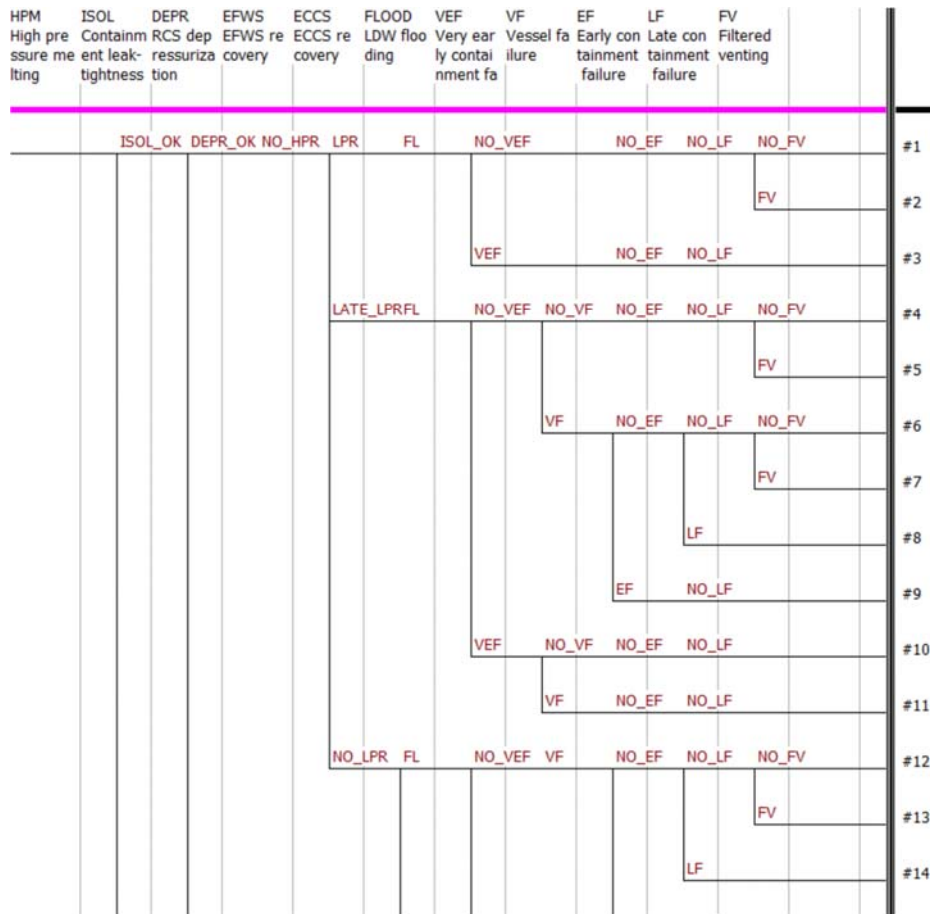
Figure 17: The upper part of the high pressure melting containment event tree.

The model was simulated 1000 cycles. Calculated release category frequencies are presented in Table 3. Release frequencies are smaller than in the previous study, because the conservative assumption of core melting in the case of successful ECCS recovery was removed. On the other hand, ex-vessel steam explosion and basemat melt-through probabilities were increased, which compensated the direction of the core melting modelling. Hydrogen explosion causing very early containment failure dominates the risk, because it is the only way for the containment to fail if core cooling is recovered early in addition to isolation failure. Hydrogen explosion modelling is also likely very conservative.

Table 3. Release category frequencies. Release categories are: no containment failure of filtered venting (OK), Isolation failure (ISOL), Very Early containment Failure (VEF), Early containment Failure (EF), Late containment Failure (LF) and Filtered Venting (FV)**.**

Release category	OK	ISOL	VEF	EF	LF	FV
Frequency	2.82E-7	9.29E-9	1.35E-7	1.66E-8	1.24E-8	4.66E-7
Frequency computed with the old model	2.60E-7	1.20E-8	2.29E-7	3.08E-8	2.51E-8	7.01E-7

A limited two-phase uncertainty analysis was performed, and based on those results, a simplified version of the model was created to remove the impacts of aleatoric variables from uncertailty analysis enabling the use of one-phase procedure for some accident sequences. The results of the one-phase uncertainty analysis are presented in Table 4. The mean frequencies are generally relatively close to the original values, which gives confidence that the model simplifications were successful. It can be noticed that the 2000 simulation cycles performed are

not sufficient for the frequencies to converge to the "accurate" values, which means that the results naturally vary a bit between simulation runs. New frequencies are systematically a bit larger because of such variation, but the model simplifications have also increased the frequencies of some sequences.

Table 4: Uncertainty analysis results for sequences 4-11 in **Figure 17**.

Sequence	Release category	Original frequency	New mean frequency	5th percentile	Median	95th percentile
#4	OK	7.40E-10	7.60E-10	3.38E-12	1.31E-10	3.34E-9
#5	FV	1.26E-9	1.35E-9	7.80E-12	2.43E-10	5.80E-9
#6	OK	1.92E-11	2.78E-11	7.61E-14	4.00E-12	9.75E-11
#7	FV	3.10E-11	4.92E-11	1.63E-13	7.79E-12	1.83E-10
#8	LF	1.09E-10	1.73E-10	7.10E-13	2.85E-11	6.53E-10
#9	EF	1.13E-10	1.93E-10	6.31E-13	3.20E-11	8.26E-10
#10	VEF	3.93E-10	4.29E-10	1.78E-12	6.75E-11	1.81E-9
#11	VEF	4.29E-11	9.23E-11	3.17E-13	1.31E-11	3.58E-10

3.1.3. Deterministic analyses on ex-vessel debris bed behaviour

Previously the effects of the debris bed geometry and flooding mode on the dryout heat flux were analysed experimentally and analytically to evaluate the coolability of an ex-vessel debris bed [37][38][39]. However, the coolability limit based on the minimum dryout heat flux might be overly conservative, since the temperature may remain on an acceptable level even in the dry zone. Instead of the dryout heat flux, it has been proposed that the coolability limit should be based on the increase of the particle temperature.

Post-dryout conditions

The post dryout behaviour of conical debris beds was studied by performing MEWA [19] [20] simulations examining the influence of bed particle size, heating power and porosity [40]. Due to the lack of experimental data that could be directly used for code validation, the MEWA results were compared to the DECOSIM results [41]. The simulation results were not in agreement. The transient behaviour of the maximum particle temperature was in most cases nearly similar, but the maximum temperatures stabilized to different levels.

The effect of heat transfer models available in MEWA did not explain the differences compared to the KTH's DECOSIM results and therefore the influence of the friction model in post-dryout conditions was analysed [42]. As MEWA does not feature the Schmidt [43] version of the modified Tung and Dhir [44] friction model used in DECOSIM, it was added into the Fluent implementation of the debris bed coolability models. The usage of the same friction model improved the agreement with the DECOSIM results.

Now the friction model applied in DECOSIM was implemented in the MEWA code and MEWA simulations were performed for the same conical and truncated-cone-shaped particle beds as in [41] including three different particle sizes: 1 mm, 2 mm, and 3 mm and three different heating powers: 100 W/kg, 200 W/kg, and 250W/kg. The details are presented in Appendix B.

Conical beds

The MEWA and DECOSIM results for the time evolution of the maximum particle temperature are compared in Figure 18. For the 1 mm particles, the agreement is good. A small difference in the maximum particle temperature curves originates mainly from the differences in the initial temperature for the first 200 s where the maximum particle temperature is in the MEWA calculations somewhat lower. For larger particles, there are significant differences. Steady states

are achieved in the MEWA simulations in all 2 and 3 mm particle cases and the maximum particle temperature stabilises to reasonably low values. In the DECOSIM results for 2 and 3 mm particles, the maximum particle temperature increases to significantly higher values and a steady state is actually achieved only for 3 mm particles with the specific heating power equal to 200 W/kg.

Figure 18: Comparison of the time evolution of the maximum solid particle temperature for the conical debris beds in the MEWA simulations of this study and in the DECOSIM simulation [41].

Truncated-cone-shaped beds

The time evolutions of the maximum particle temperature computed for the truncated-cone-shaped beds in the MEWA simulations are compared in Figure 19 to the corresponding results from the DECOSIM simulations. In the 1 mm cases, the influence of cooling is small and the agreement is again good at least for the first 5 000 s. In the MEWA simulations, the maximum particle temperature is somewhat larger. In the other cases, the maximum particle temperature is however lower in the MEWA simulations. In some cases the difference is hundreds of degrees.

Figure 19: Comparison of the time evolution of the maximum solid particle temperature for the truncated-cone debris beds in the MEWA simulations and in the DECOSIM simulations [41].

Speculative simulations for 1.3 bar

There are some obvious inconsistencies between the MEWA results and the DECOSIM results [29]. Furthermore, the saturation temperature seems to be different in the MEWA and DECOSIM simulations: the saturation temperature in the MEWA simulations is significantly higher. Figure 20 shows the saturation temperature in a MEWA simulation in which the pressure on the top surface is 1.3 bar (p_top = 1.3 bar curve). This curve meets the points for the saturation temperature in the DECOSIM simulations. The 1.3 bar curve is in agreement with the values of the NIST Chemistry WebBook [45]. The values for the topmost cells (381 K) are also the same as the lower limits of the temperature ranges in the plots for the DECOSIM results. It was therefore decided to repeat the MEWA simulations for the top surface pressure of 1.3 bar.

The time evolution of the maximum particle temperature in the MEWA simulations for the top surface pressure of 1.3 bar is presented in Figure 21 and Figure 22 for the conical and truncated-cone-shaped beds, respectively, together with the DECOSIM results [41] for the top surface pressure of 3 bar. The shapes of the time evolution curves are also similar and the steady-state conditions are obtained in the same case and not in any other case. The agreement is better for the truncated-cone-shaped beds.

When comparing the result of the DECOSIM results and the MEWA results computed with the Schmidt [43] version of the modified Tung and Dhir [44] friction model, possible differences in the model implementations should also be recalled. For instance, Schmidt [43] does not give formulas for the transition zones. There can also be other implementation differences and differences in numerics. In addition, there are still some differences in the boiling models between MEWA and DECOSIM.
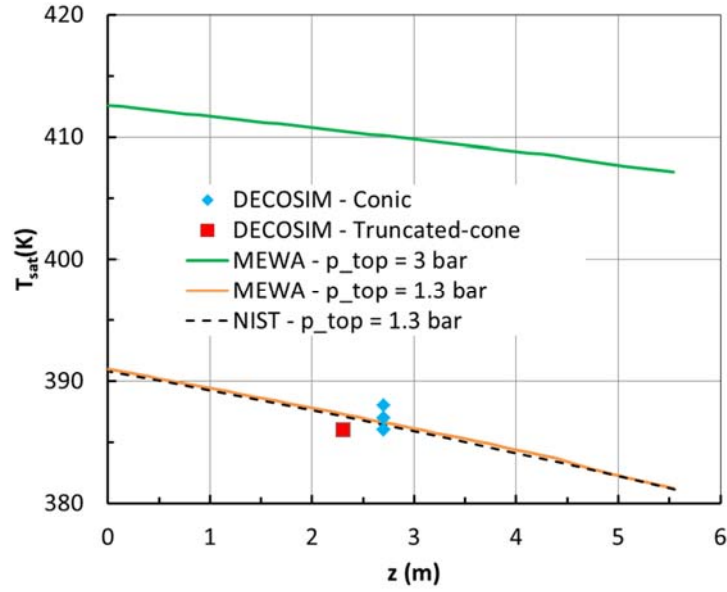
Figure 20: Saturation temperature as a function of the height in the DECOSIM simulations and in the MEWA simulations for the cases of the top surface pressure equal to 3 and 1.3 bar. The "NIST - ptop = 1.3bar" values are from [45].
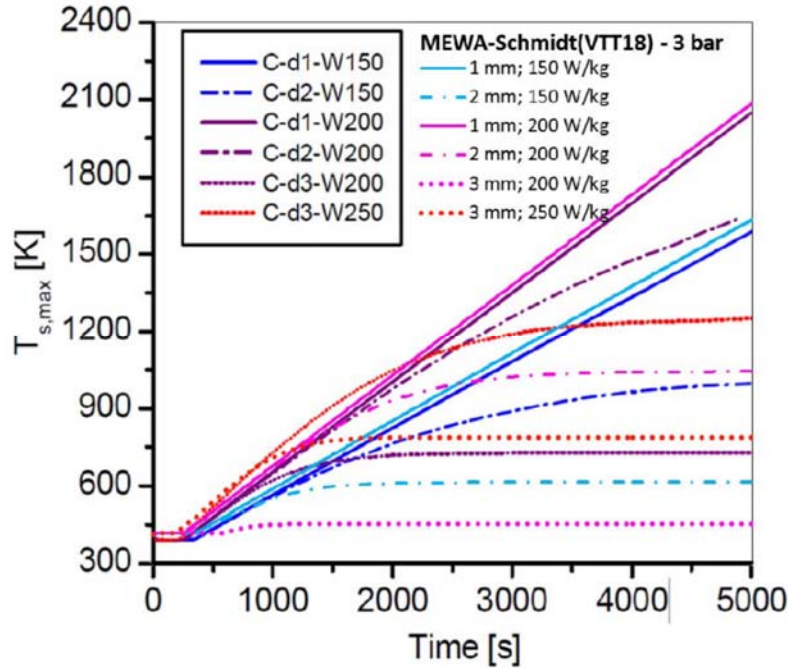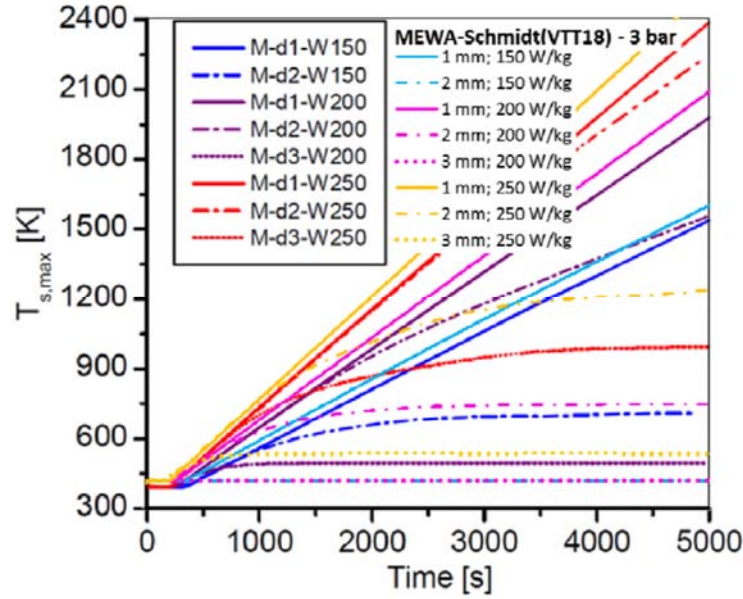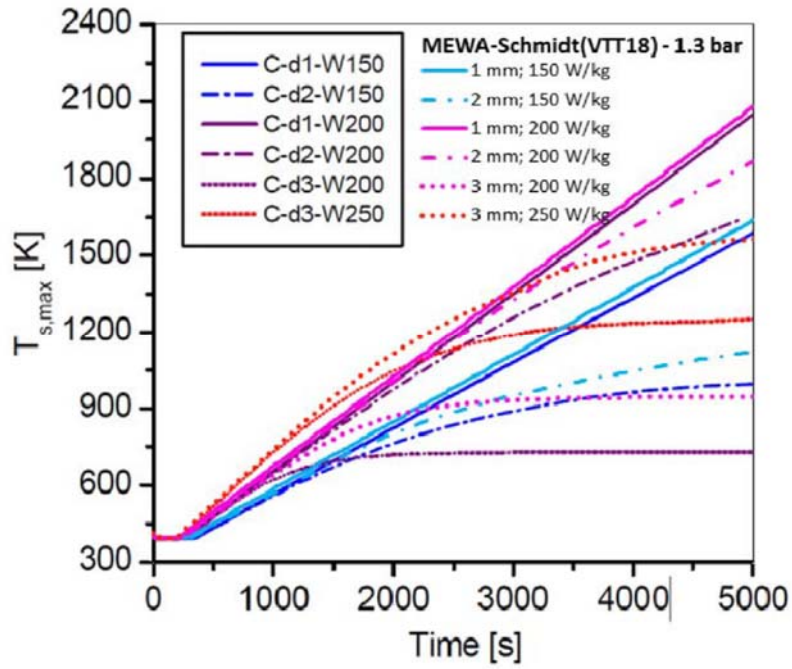

Figure 21: Comparison of the time evolution of the maximum solid particle temperature for the conical debris beds in the MEWA simulations of this study and in the DECOSIM simulations [41]. In the MEWA simulations, the top surface pressure is 1.3 bar.
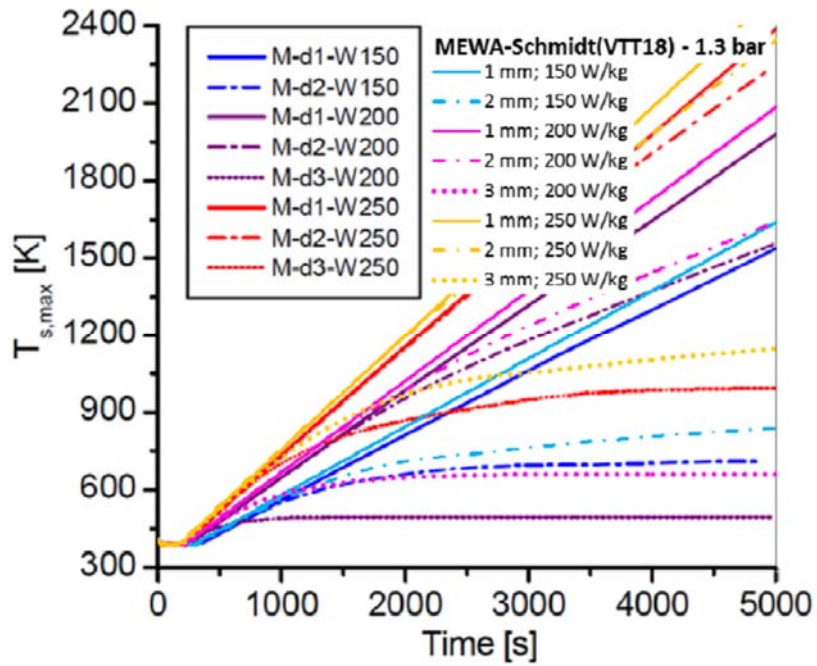
Figure 22: Comparison of the time evolution of the maximum solid particle temperature for the truncated-cone debris beds in the MEWA simulations of this study and in the DECOSIM simulations [41]. In the MEWA simulations, the top surface pressure is 1.3 bar.

4. Activities at LRC

4.1. Developing uncertainty analysis for PSA from ROAAM+

A further development of approaches for integration of dynamic methodologies (such as ROAAM+) and PSA Level 2 has been pursued by LRC to improve the scope and quality of risk analysis results and evaluate the relevance of a currently used level of detail in current PSA L2 phenomena modelling. Below is a summary of the research activity at LRC. The details can be found in the report [14] and Appendix C.

A full-scale RiskSpectrum PSA model of Nordic BWR reference plant design was used in this work as basis to select important initiating events and risk significant sequences in the severe accident progression. These scenarios were then analyzed using ROAAM+ tool for Nordic BWR, yielding information about (i) which uncertain parameters in the PSA model that are of the highest importance for the development of the accident progression and the risk of containment failure; and (ii) uncertainty in the risk by employing "knowledge-based treatment" of epistemic uncertain parameters.

The ROAAM+ [46] is a risk analysis framework for assessment of the effectiveness of Severe Accident Management (SAM) strategy in Nordic BWRs. The ROAAM+ consist of a probabilistic framework, implemented as a stand-alone computerized tool with a graphical user interface, and a set of casual relationships that represent severe accident progression.

The analysis demonstrated that the probability of containment failure due to ex-vessel steam explosion and ex-vessel debris coolability strongly depends on debris ejection mode from the vessel (Solid debris ejection option – IDEJ1 vs IDEJ0 in MELCOR). In case of solid debris ejection – off (IDEJ1) containment failure due to ex-vessel phenomena cannot be considered as physically unreasonable (for both threats). In case of solid debris ejection – on (IDEJ0), containment failure due to ex-vessel steam explosion can be considered as physically unreasonable only in case of modified design (with reinforced hatch door)). On the other hand, containment hatch door reinforcement does not affect the probability of containment failure due to basemat melt-through and this threat cannot be considered as physically unreasonable in case of IDEJ0. The ROAAM+ analysis results show that the probability of phenomena damaging the containment significantly depend on the depth of the pool in the lower drywell, e.g. coolability increases with the depth of the pool, however the opposite is true for steam explosion (i.e. higher energetics in a water deep pool). This information was used in development of enhanced PSA model of Nordic BWR.

The results obtained with the enhanced PSA model suggest that the non-contained release frequency depends on the mode of debris ejection from the vessel (IDEJ). In case of IDEJ1, it results in ~5.6 times larger value of non-contained release frequency when compared to the results obtained with reference model. Reinforcement of the hatch door in case of IDEJ1 results in reduction of the non-contained release frequency from ~5.6 to 4.2 times the value obtained with the reference PSA model. In case of IDEJ0 (both reinforced and non-reinforced design) enhanced PSA modelling results show relatively low increase of non-contained release frequency, from ~8 to 13% for non-reinforced and reinforced hatch door respectively.

The overall results show that the values of probabilities of phenomena damaging the containment used in the reference PSA model can be underestimated, judged by the respective values predicted by ROAAM+ framework. On the other hand, if it can be demonstrated that the vessel LH failure will be limited to IGTs failure and ablation of the opening will be limited, then the reference PSA model values of probabilities of phenomena damaging the containment can be considered as valid.

Present results show the dominant effect of the mode of debris ejection (IDEJ) on the results.

However, given current state of knowledge about these phenomena, it should be treated as "phenomenological splinters" scenarios in PSA, that is, it should be demonstrated that non-contained release frequency is below regulatory requirements for all splinter scenarios considered.

It should be noted that current modelling approaches used in MELCOR code, for prediction of penetrations failure and melt and debris ejection, might be over-simplified in some aspects and lack the necessary validation database. Furthermore, recent evidences from the Fukushima Daiichi Unit 2 and 3 primary containment vessel investigation, provided evidences that challenge ability of existing severe accident analysis tools to adequately predict transition of SA progression from in-vessel to ex-vessel phases in BWRs. Therefore, the results presented in this report should be considered as bounding estimates.

From a PSA stand point, the project has demonstrated that:

- It is both possible, achievable and desirable to increase the interaction between the deterministic and probabilistic assessment with regard to especially PSA level 2.
- Probabilities for phenomena can be estimated using the physical models in the thermal-hydraulic codes.
- The uncertainty can be assessed, and correlation between phenomena can be managed.
- There is room for improvement in current modelling in PSA level 2 (sequence parameters).

The implementation made in a large-scale PSA model shows that the integration of the ROAAM+ results in the PSA model is not only feasible, but could potentially lead to a considerable change of the frequency for non-acceptable release. The results show that the parameters indicated by the ROAAM+ approach as being of high importance to the quantitative results. It also emphasizes the need to distinguish between different probabilities of phenomena depending on different scenario, physical and intangible parameters (e.g. pool depth, that significantly affect coolability and steam explosion).

The approach has demonstrated that the vision, to develop the sequence from core melting, and to understand what are the important factors, is possible to meet. The integrated approach has the ability to give a more comprehensive estimation of the uncertainty compared to the standard approach. The uncertainty related to phenomena will consider the interdependency between phenomena (all the way back to relevant deterministic and intangible, boundary conditions and scenario parameters).

The dynamic approach used in the project requires extensive work regarding building the deterministic model. Once built, this model can however be modified to evaluate different initiating events and sequences. The changes in the enhanced PSA-model on the other hand are limited and easy to implement.

The integrated approach requires improvement in especially scenario definition, which practically leads to more plant damage states. The PDS should consider all necessary scenario parameters, that may affect the calculation of phenomena and hence consider also the system availability normally represented within CETs.

5. Concluding Remarks

Significant progress was made and important findings were obtained in the SPARC project carried out by KTH, VTT and LRC during 2018 The focus of this project is to produce new data and to develop models and methodologies for addressing severe accident scenarios and phenomena which are important to assess the risk of containment failure and radioactivity release in postulated severe accidents of Nordic NPPs. The main achievements obtained so far are as follows.

At KTH, the SIMECO-2 facility has been developed to investigate heat transfer in 2- and 3-layered stratified molten pool formed by oxide and metal simulants of corium with different densities. Commissioning of the facility and relevant experiments will be carried out in the end of 2019. Meanwhile, other two new facilities named MRSPOD and POMECO-Q are being developed for studies on melt penetration in debris beds and quench of debris beds, respectively.

For qualification of a coolability analysis tool, the MEWA code was validated against the POMECO-FL, POMECO-HT and PEARL experiments for two-phase flow and dryout and quench in particulate beds, and then employed to investigate the coolability of prototypical ex-vessel debris beds with cylindrical, conical and truncated conical shapes assumed to form under severe accident scenarios of a boiling water reactor. The simulations showed that the dryout power density of a prototypical debris bed was roughly inversely proportional to the bed's height regardless of the bed's shape, and the dryout power density of the debris bed was predicted to be strongly correlated to the uniformity of the bed's shape. The MEWA code was also employed to simulate the quenching process of a heap-like debris bed of the reactor scale, and the results show that the bed flooded from the top is quenched in a multi-dimensional manner, with the upper region adjacent to the centerline of the bed difficult to quench.

To address the effect of seawater on fuel coolant interactions and steam explosion, an experimental study was carried out in the MISTEE platform at KTH to investigate the quenching process of a hot stainless-steel sphere, with focus on the dynamics and instability of the vapor films surrounding the melt droplets Based on the experimental data obtained under different coolant temperature, the minimum film boiling temperatures in seawater, as an important parameter characterizing vapor film collapse , were obtained, whose values were about 100 ºC more than those in fresh water. The minimum film boiling temperature decreases linearly with coolant temperature.

Infiltration through porous media was modeled at KTH to help interpret the REMCOD experiment which was carried out to explore the effects of wettability, melt superheat and debris temperature, as well as particle size and morphology on the melt infiltration through particulate beds. Based on comparisons between the experimental data and the predictions of the model, it was observed that not only the same trend exists in both experiment and simulation results but also they coincide very well, once the proper value is selected for the permeability.

To predict the failure of reactor pressure vessel (RPV) during a severe accident of light water reactors, the multi-physics platform of ANSYS encompassing Fluent and Structural capabilities was employed to simulate the fluid dynamics and structural mechanics in a coupled manner. The FOREVER-EC2 experiment was chosen to validate the coupling approach. The results demonstrated the well-posed capability of the coupling approach for prediction of key parameters of interest, including temperature profile, total displacement of vessel bottom point and the evolution of wall thickness profile in the experiment.

Notably, one PhD thesis [6] related to steam explosion exegetics was defended at KTH in December 2018.

At VTT a dynamic containment event tree modelling particularly focusing on the modelling of timings of events and uncertainty analysis was studied. The dynamic CET provided a good alternative to analyze the effects of different timings and timing combinations. PRA modelling is more realistic when timings are explicitly included in the model and affect accident sequences in the model. A two-phase uncertainty analysis procedure has been proposed and demonstrated in a limited case study to treat epistemic and aleatoric uncertainties separately, resulting in consistent uncertainty estimates.In addition to the probabilistic study, a deterministic study of corium debris bed coolability was studied by performing numerical simulations with the MEWA code and analysing the post-dryout conditions for the hypothetical idealized particulate beds studied at KTH by utilising the DECOSIM code. The results from MEWA and DECOSIM were compared and potential reasons for the differences were discussed and tested. By implementing the friction model applied in DECOSIM into MEWA improved the correspondence of the results notably. In order to obtain the same saturation temperature reported to be in the DECOSIM simulations, the pressure on the top surface was reduced from 3 bar (documented to be used in the DECOSIM simulations) to 1.3 bar. The MEWA results for the reduced pressure agree reasonably with the DECOSIM results in all analysed cases.

At LRC the application of dynamic approach (such as ROAAM+) to PSA was demonstrated through an example. In this approach PSA was used as a basis to select important initiating events and sequences in the severe accident progression. These sequences are then analyzed with deterministic models, yielding information about which parameters that are of the highest importance for the development of the accident progression. The results from the deterministic analysis are used in PSA to improve sequence definition and the estimation of phenomena depending on the sequence and varied parameters. The ROAAM+ framework provides an assessment of the effect of epistemic (knowledge) uncertainty on the results by employing "knowledge-based treatment" of those epistemic uncertain parameters, i.e. no probability distributions of epistemic uncertain parameters are assumed if there is no available knowledge about them. The results obtained with the enhanced PSA model suggest that the non-contained release frequency depends on the mode of debris ejection from the vessel. The values of probabilities of phenomena damaging the containment used in the reference PSA model can be underestimated, judged by the respective values predicted by ROAAM+ framework. On the other hand, if it can be demonstrated that the vessel failure will be limited to failure of instrument guide tubes and ablation of the opening will be limited, the reference PSA model values of probabilities of phenomena damaging the containment can be considered as valid. Present results show the dominant effect of the mode of debris ejection on the results. However, given current state of knowledge about these phenomena, it should be treated as "phenomenological splinters" scenarios in PSA, that is, it should be demonstrated that non-contained release frequency is below regulatory requirements for all splinter scenarios considered.

More achievements and detailed descriptions can be found in the related publications [1-14].

ACKNOWLEDGEMENTS

DISCLAIMER

The views expressed in this document remain the responsibility of the author(s) and do not necessarily reflect those of NKS. In particular, neither NKS nor any other organization or body supporting NKS activities can be held responsible for the material presented in this report.

References

[1]   W. Ma, S. Bechta, et al., *Proceeding of the 46th Review Meeting for Project "Melt-Structure-Water Interactions in a Severe Accident*", KTH, Stockholm, Sweden, June 14, 2018.

[2]   W. Ma, S. Bechta, et al., *Proceeding of the 47th Review Meeting for Project "Melt-Structure-Water Interactions in a Severe Accident*", KTH, Stockholm, Sweden, December 18, 2018.

[3]   Z. Huang, W. Ma, Validation and application of the MEWA code to analysis of debris bed coolability, *Nuclear Engineering and Design* 327: 22-37, 2018

[4]   Z. Huang, W. Ma, Numerical investigation on quench of an ex-vessel debris bed at prototypical scale, *Annals of Nuclear Energy* 122: 47-61, 2018.

[5]   Q. Guo, L. Manickam, W. Ma, S. Bechta, Effects of salinity in coolant on steam explosion, *Proceedings of 18th International Topical Meeting on Nuclear Reactor Thermal Hydraulics*, Portland, USA, August 18-22, 2019.

[6]   L. Manickam, *An Experimental Study on Melt Fragmentation, Oxidation and Steam Explosion during Fuel Coolant Interactions*, Doctoral Thesis, KTH Royal Institute of Technology, 2018.

[7]   Q. Guo, L. Manickam, W. Ma, S. Bechta, Investigation on quenching of a high-temperature spherical particle in sea water, *Proc. of the 12th International Topical Meeting on Nuclear Thermal-Hydraulics, Operation and Safety*, Qingdao, China, October 14-18, 2018.

[8]   J.A. Zambaux, L. Manickam, R. Meignen, W.M. Ma, S. Bechta, S. Picchi, Study on thermal fragmentation characteristics of a superheated alumina droplet, *Annuals of Nuclear Energy* 119: 252-362, 2018.

[9]   L. Manickam, Q. Guo, W. Ma, S. Bechta, An experimental study on the intense heat transfer and phase change during melt and water interactions, *Experimental Heat Transfer,* DOI: 10.1080/08916152.2018.1505786, 2018.

[10] P. Yu, W. Ma, W. Villanueva, A. Karbojian, S. Bechta, Validation of a thermo-fluid-structure coupling approach for RPV creep failure analysis against FOREVER-EC2 experiment, *Annuals of Nuclear Energy* 133: 637-648, 2019.

[11] P. Yu, W. Villanueva, S. Galushin, W. Ma, S. Bechta, Coupled thermo-mechanical creep analysis for A Nordic BWR lower head using non-homogeneous debris bed configuration from MELCOR, *Proc. of NUTHOS-12,* Qingdao, China, October 14-18, 2018.

[12] T. Tyrväinen, I. Karanta, *Dynamic containment event tree modelling techniques and uncertainty analysis,* Research Report VTT-R-06892-18, VTT, Espoo, 2019.

[13] V. Taivassalo, *Comparison of simulations for debris bed behaviour in post-dryout conditions*, Research Report VTT-R-00223-19, VTT, Espoo, 2019.

[14] S.E. Galushin, A.R. Marklund, Developing uncertainty analysis for PSA from ROAAM+, Report no: PRJ11084933_R001, Lloyd's Register Consulting - Energy AB, 2019.

[15] B.G. Korshunov, V.V. Safonov, D.V. Drobot. Phase equilibria in halide systems. Moscow, *Metallurguya* (in Russian), pp.182. 1979.

[16] H. Okamoto, Al-Mg (Aluminum-Magnesium). *Journal of Phase Equilibria* 19 (6): 598, 1998.

[17] P. Yu, A. Komlev, W. Villanueva, Y. Li, W. Ma, S. Bechta, Pre-test simulation of SIMECO-2 experiments on stratified melt pool heat transfer. *Proceedings of the 11th International topical meeting on nuclear reactor thermal-hydraulics, operation and safety*, Gyeongju, Korea. October 9-13, 2016.

[18] D. Lopukh, I. Skrigan, A. Vavilov, A. Martynov, S. Bechta, A. Komlev, Numerical simulation of induction heating for molten pool heat transfer experiments in slice geometry, *International Multi-Conference on Industrial Engineering and Modern Technologies (FarEastCon)*, pp.1-6, 2018.

[19] S. Rahman*, Coolability of corium debris under severe accident conditions in light water reactors.* Insitut für Kernenergetik und Energiesysteme, University of Stuttgart, 2013.

[20] M. Bürger, M. Buck, W. Schmidt, Validation and application of the WABE code: Investigations of constitutive laws and 2D effects on debris coolability, *Nuclear Engineering and Design* 236: 2164-2188, 2006.

[21] L. Li, W. Ma, S. Thakre, An experimental study on pressure drop and dryout heat flux of two-phase flow in packed beds of multi-sized and irregular particles *Nuclear Engineering and Design* 242: 369-378, 2012.

[22] S. Thakre, L. Li, W. Ma. An experimental study on coolability of a particulate bed with radial stratification or triangular shape, *Nuclear Engineering and Design* 276 54-63, 2014.

[23] N. Chikhi, F. Fichot, Experimental and theoretical study of large scale debris bed reflood in the PEARL facility, *Nuclear Engineering and Design* 312, 48-58, 2017.

[24] N. Chikhi, F. Fichot, A. Swaidan, Effect of water entrainment on the coolability of a debris bed surrounded by a by-pass: Integral reflood experiments and modelling, *Annual Nuclear Energy* 110: 418-437, 2017.

[25] *Fukushima Nuclear Accident Update Log*, https://www.iaea.org/newscenter/news/fukushima-nuclear-accident-update-log-34, 2011.

[26] Y. Liu, Z. Zheng, H. Stone, The influence of capillary effects on the drainage of a viscous gravity current into a deep porous medium, *Journal of Fluid Mechanics* 817: 514-559, 2017.

[27] A. Saltelli, *Sensitivity analysis in practice: a guide to assessing scientific models*, John Wiley & Sons, 2004.

[28] D. Coelho, J. Thovert, P. M. Adler, Geometrical and transport properties of random packings of spheres and aspherical particles, *Physical Review* E 55 (2): 1959-1978, 1997.

[29] X. Tan, L. Jiang, X. Li, Y. Li, K. Zhang, A complex model for the permeability and porosity of porous media, *Chemical Engineering Science* 172: 230-238, 2017.

[30] O. Rahli, L. Tadrist, M. Miscevic, R. Santini, Fluid flow through randomly packed monodisperse fibers: The Kozeny-Carman parameter analysis, *Journal of Fluids Engineering* 119 (1): 188-192, 1997.

[31] B. R. Sehgal, R. R. Nourgaliev, T. N. Dinh, A. Karbojian, J. A. Green, and V. A. Bui, FOREVER experiments on thermal and mechanical behavior of a reactor pressure vessel during a severe accident, *Proceedings of the Workshop on in-vessel core debris retention and coolability*, Garching, Germany, March 3-6, 1998.

[32] A. Theerthan, A. Karbojian, B.R. Sehgal, EC-FOREVER experiments on thermal and mechanical behavior of a reactor pressure vessel during a severe accident Technical report-1: FOREVER-EC2 test, Technical Report SAM-ARVI-D008, March 2001.

[33] IAEA the International Atomic Energy Agency, *Development and application of level 2 probabilistic safety assessment for nuclear power plants: Specific safety guide No: SSG-4*, Vienna, 2010.

[34] VTT Technical Research Centre of Finland Ltd., *FinPSA – Tool for promoting safety and reliability*, https://www.simulationstore.com/finpsa (link accessed 29.8.2019).

[35] T. Tyrväinen, T. Silvonen, T. Mätäsniemi, Computing source terms with dynamic containment event trees. *13th International conference on probabilistic safety assessment and management (PSAM13)*, Seoul, Korea, October 2-7, 2016.

[36] T. Tyrväinen, I. Karanta, *Level 2 studies – Steam explosions and integration of PRA levels 1 and 2*, Research Report VTT-R-00191-18, VTT, Espoo, 2018.

[37] E. Takasuo, *Coolability of porous core debris beds: Effects of bed geometry and multi-dimensional flooding*. VTT Science 108. Teknologian tutkimuskeskus VTT Oy. Juvenes Print, ISBN 978-951-38-8344-7, 2015

[38] E. Takasuo, An experimental study of the coolability of debris beds with geometry variations, *Annals of Nuclear Energy* 92: 251-261, 2016.

[39] E. Takasuo, *A summary of studies on debris bed coolability and multidimensional flooding*, VTT Research Report VTT-R-00432-16, VTT, Espoo, 2016.

[40] V. Taivassalo, E. Takasuo, *Predicting debris bed behaviour in post-dryout conditions*, Research Report VTT-R-00762-17. 28 p, VTT, Espoo, 2017.

[41] S. Yakush, P. Kudinov, A model for prediction of maximum post-dryout temperature in decay-heated debris bed, *22nd International Conference on Nuclear Engineering,* Prague, Czech Republic, July 7-11, 2014.

[42] V. Taivassalo, *Comparison of friction models for debris beds in post-dryout conditions*, Research Report VTT-R-01003-18, VTT, Espoo, 2018.

[43] W. Schmidt, Interfacial drag of two-phase flow in porous media, *Int. J. Multiphase Flow* 33: 638–657, 2007.

[44] V.X. Tung, V.K. Dhir, A hydrodynamic model for two-phase flow through porous media, *International Journal of Multiphase Flow* 14: 47-65, 1998.

[45] P.J. Linstrom, W.G. Mallard, NIST Chemistry WebBook, NIST Standard Reference Database Number 69, National Institute of Standards and Technology, Gaithersburg MD, 20899, https://doi.org/10.18434/T4D303 (retrieved February 8, 2019).

[46] P. Kudinov, S. Galushin, et al., Application of integrated deterministic-probabilistic safety analysis to assessment of severe accident management effectiveness in Nordic BWRs, The 17th International Topical Meeting on Nuclear Reactor Thermal Hydraulics (NURETH-17) , Xi'an, China, September 3-8, 2017.

Dynamic containment event tree modelling techniques and uncertainty

Dynamic containment event tree modelling techniques and uncertainty analysis

Authors: Tero Tyrväinen, Ilkka Karanta

Confidentiality: Public

Report's title		
Dynamic containment event tree modelling techniques and uncertainty analysis		
Customer, contact person, address		Order reference
VYR		SAFIR 4/2018
Project name		Project number/Short name
Probabilistic risk assessment method development and applications		110223/PRAMEA
Author(s)		Pages
Tero Tyrväinen, Ilkka Karanta		31/
Keywords		Report identification code
Probabilistic risk analysis, severe accident, uncertainty		VTT-R-06892-18

Summary

VTT has developed a probabilistic risk analysis (PRA) model of a generic boiling water reactor nuclear power plant for PRA levels 1 and 2. The model can be used in research, training, education and demonstration. In this report, some refinements to the level 2 (severe accidents) part of the model are described. Particularly, dynamic modelling of timings of depressurization, emergency feedwater system recovery, emergency core cooling system recovery and lower drywell flooding is implemented.

Different techniques to model emergency core cooling system recovery time and its effects are presented in a simplified case study. The techniques are evaluated concerning uncertainty analysis.

A two-phase method of uncertainty analysis is presented. The purpose is to separate the treatment of aleatoric and epistemic uncertainties, to get rid of certain issues and inconsistencies in more traditional one-phase uncertainty analysis. The method is demonstrated by the emergency core cooling system case study. A drawback of the two-phase uncertainty analysis is that it is computationally very demanding. Therefore, it is proposed that first limited dynamic models would be constructed and analysed by the two-phase procedure; this would give input to a simplified full-scope model, allowing one-phase uncertainty analysis.

Confidentiality	Public

Espoo 4.1.2019

Written by	Reviewed by	Accepted by
Tero Tyrväinen Research Scientist	Kim Björkman Research Scientist	Eila Lehmus Research Team Leader

VTT's contact address
Box 1000, FI-02044 VTT, Finland

Distribution (customer and VTT)
SAFIR reference group 2

Contents

1. Introduction

Level 2 probabilistic risk assessment (PRA) studies nuclear power plant accident progression after core damage, and frequency, size and composition of radioactive releases [1]. Severe accident phenomena, e.g. hydrogen explosions, and timings of events, such as cooling system recovery, play an important role in such analyses. Information on severe accident progression provided by deterministic analyses is crucial to the construction of proper level 2 PRA. Integrated deterministic and probabilistic safety analysis (IDPSA) aims to bring the two types of analysis closer and improve their co-operation.

In the previous research report [2], a simplified boiling water reactor (BWR) plant PRA model including levels 1 and 2 was developed based on earlier models [3-5]. This report continues the development of the level 2 part of the model, and particularly focuses on modelling techniques and uncertainty analysis. A two-phase uncertainty analysis procedure, outlined in the previous report, is presented and implemented in limited case studies. Modelling of core cooling system recovery time is studied. The core cooling system case is used to demonstrate dynamic containment event tree modelling and the benefits of the two-phase uncertainty analysis.

Section 2 briefly describes dynamic containment event trees of FinPSA [6]. Section 3 discusses modelling techniques and uncertainty analysis. Core cooling system recovery time modelling is studied with a simple example model in Section 4, and dynamic modelling of high pressure melting case is studied more comprehensively in Section 5. Section 6 concludes the study.

2. Dynamic containment event trees

The level 2 modelling in the FinPSA software tool [6] is based on dynamic containment event trees (CETs) and containment event tree programming language (CETL). CETL is used to define functions to calculate conditional probabilities of event tree branches, timings of the accident progression and amounts of releases. A CETL function is defined for each branch of a dynamic containment event tree, and a CET also contains an initial conditions section, where the plant damage state, source term computation routine, and some probability and process variable values are defined. In addition, the model contains a global "common section", where some global variables and functions can be defined. CETL programming is very flexible. At any branch, a new value can be set or calculated for any global variable, and that way accident progression can be modelled dynamically. Binning rules can also be defined to divide the end points of the CET into release categories.

To account for uncertainties related to variable values, it is possible to specify probability distributions for parameters and perform Monte Carlo simulations. At each simulation cycle, a value is sampled from each specified distribution, and based on that, numerical conditional probabilities are calculated for all branches, and values are calculated for all variables at each end point of the CET. After the simulations, statistical analyses are performed to calculate frequency and variable value distributions for each end point and release category among other statistical results and correlation analyses. It is also possible to just calculate point values of the CET based on the mean values of distributions.

3. Modelling techniques and uncertainty analysis

The level 2 modelling in the previous BWR model [2] has been performed using 'probabilities first' approach, which means that the occurrence of each branch in a CET on a given simulation cycle is determined based on a probability parameter (or multiple probability parameters). The benefit of this approach is that it enables proper uncertainty analysis resulting in nice uncertainty curves that are easy to interpret. In the model, values of physical parameters used in source term calculations are determined based on the accident sequence. One could however argue that this modelling approach does not take very well into account the dynamic nature of severe accidents: timings of events and other process parameters do not have an impact on accident sequence probabilities, except in the case where different timings are divided into separate branches in the event tree. Furthermore, it does not fully utilise the capabilities of the dynamic CETs of FinPSA, i.e. computation of probabilities is static, not dynamic.

An alternative modelling approach is 'physical parameters first' approach in which values for physical parameters are determined first (e.g. from uncertainty distribution) and the CET branch probabilities are determined based on the physical parameters, like in [7]. A drawback of that approach is that it is difficult calculate proper uncertainty distributions for release frequencies, i.e. the resulting distributions can be difficult to interpret or they might not be sensible at all [8]. On the other hand, the 'physical parameters first' approach gives better possibilities to model how accident scenarios vary depending on physical parameter values and to model dynamic dependencies related to severe accident phenomena. For better use of the 'physical parameters first' approach, it might be necessary to develop the FinPSA dynamic containment event tree modelling tool to take into account that there are two types of uncertainties.

Uncertainties can be divided into two categories: aleatoric and epistemic [9-14]. Aleatoric uncertainty represents uncertainty resulting from inherent randomness, e.g. it is known that the toss of a coin can result in heads or tails based on chance. Characteristic of aleatoric uncertainty is that it can usually be reliably quantified, and in this sense, the amount of uncertainty is known: for example, the probability of a perfect coin arriving at tails after a toss is 0.5. In a level 2 model, branches and accident sequences of a CET represent possible realisations of aleatoric uncertainties, i.e. it is known that one sequence occurs given the PDS, but it is a matter of chance which one it is. The realisation of a specific value of a physical parameter, such as core meltdown fraction, is also subject to aleatoric uncertainty. Epistemic uncertainty is the uncertainty related to our lack of knowledge about a system or phenomenon. For example, the probability of successful depressurisation is not known exactly; there is epistemic uncertainty about it. Other epistemic uncertainties appearing in level 2 are related to the probability distributions of physical parameters, such as core meltdown fraction; the mean values, levels of deviation and shapes of distributions are not known exactly, there can be significant uncertainties about them.

Another way to characterize the difference between aleatoric and epistemic uncertainty is as follows [11]. Consider a class of objects which we wish to assess; for example, the class might be the core meltdown process, and its objects are the individual meltdowns that might happen. Some variables related to the class are uncertain, but whatever their values, they affect all the members of the class in the same way; for example, the probability that a valve in the emergency core cooling system works affects each core meltdown in the same way. Such variables possess epistemic uncertainty. On the other hand, there are variables whose values vary by each object independently of the other objects; for example, the reactivity of the molten fuel as a function of time varies in each meltdown, depending e.g. on the geometry of the corium. Such variables possess aleatoric uncertainty.

When aleatoric and epistemic uncertainties are handled uniformly, the resulting uncertainty distributions are often difficult to interpret. Separation of epistemic and aleatoric uncertainties

has been found necessary in many probabilistic analyses [9, 12-18], including dynamic event tree analyses [10, 19, 20] and level 2 PRA [21, 22]. The separation is particularly important when calculating the frequency of an accident sequence. The frequency itself should represent the aleatoric uncertainty related to the occurrence of the accident sequence, and the uncertainty distribution of the frequency should represent the epistemic uncertainty. This means that the frequency should not be conditional to the realisations of aleatoric uncertainties. Instead, the whole range of possible realisations of aleatoric uncertainties should be evaluated in the computation of each point in the uncertainty distribution of the frequency.

If epistemic and aleatoric uncertainties are not separated, uncertainty may be significantly overestimated because in this case also aleatoric uncertainties affect it. Aleatoric uncertainty is sometimes also called variability, and it can be claimed that it is not real uncertainty, since it is related to known behaviour of the system. Aleatoric uncertainty cannot be reduced, but epistemic uncertainty can. Therefore, it is desirable to measure the epistemic uncertainty related to risk, rather than total uncertainty.

One solution to improve the handling of uncertainties is to perform the uncertainty analysis in two phases [9, 10], as outlined in Figure 1. In this method, there are N simulation cycle blocks containing M simulation cycles. For the simulation results of one simulation cycle block, statistical analysis is performed to calculate average frequency and average release fractions for each accident sequence (along with some other results). Then, statistical analysis is performed over the simulation cycle blocks based on their average results to produce uncertainty distributions for release frequencies, source variables and other collected variables. These distributions show the effects of epistemic uncertainties only. Statistical analysis can also be performed over both simulation loops to calculate uncertainty distributions that show the combined effects of both epistemic and aleatoric uncertainties. However, these distributions should not be calculated for frequencies.
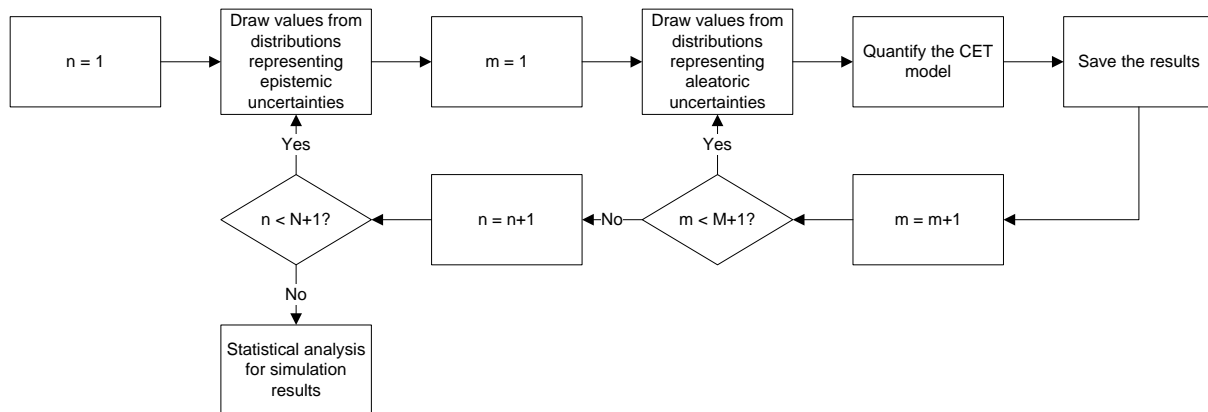

Figure 1: An outline for the progression of two-phase uncertainty analysis.

The two-phase uncertainty analysis results in uncertainty distributions that reflect only epistemic uncertainties related to the input parameters. Aleatoric uncertainties are completely evaluated inside simulation cycle blocks and the results of one simulation block are based on full range of possible occurrences of events and physical parameter values given specific values from distributions representing epistemic uncertainties.

The two-phase uncertainty analysis is computationally more demanding than normal one-phase uncertainty analysis. The analysis contains NM simulation cycles in total. The number of simulation cycles inside one block (M) needs to be sufficiently large so that results can be produced for each accident sequence. Suitable number of simulations depends significantly on the model.

If ordinary Monte Carlo simulation methods were used and the model would contain some rare event sequences that would occur e.g. once in 1000 simulation cycles, then the number of

simulations inside one block should be tens of thousands to obtain statistically reliable simulation results. The needed number of simulations can be affected by modelling decisions. Reasonable handling of rare event sequences is crucial to keep the number of needed simulations moderate. If very little or not at all data is produced about some event sequence, the model needs to be modified if the event sequence is considered relevant. It can, for example, mean addition of a new branch in the event tree. In principle, handling of rare event sequences should not be a problem in event trees.

The number of simulation cycle blocks needs to also be sufficiently large so that proper uncertainty distributions can be produced (at least hundreds). Some approximate methods have been developed to reduce the required number of simulation cycles [10, 12, 20]. Their applicability to FinPSA level 2 could be studied. Use of intelligent sampling and simulation techniques could also be studied in this context to reduce the number of required simulations [23-26].

In previous models, such as the BWR model [2], no division to epistemic and aleatoric uncertainties has been made. For example, there is only one uncertainty distribution for emergency core cooling system recovery time in a specific scenario. This uncertainty distribution covers both epistemic and aleatoric uncertainties. To make the analysis more correct, there should be separate uncertainty distributions for the mean recovery time and deviation parameter that would represent epistemic uncertainty on the core cooling recovery. The separation of the uncertainties makes the modelling more complicated and challenging. In some cases, simplifications may be sufficient, such as treating all the uncertainty of a variable as epistemic. On the other hand, in some cases the portion of aleatoric uncertainty is significant and it should not be treated as epistemic; such is the case of the emergency core cooling system recovery time.

4. Modelling emergency core cooling system recovery time

This section studies different ways to model emergency core cooling system (ECCS) recovery time and its effects. Different modelling techniques are evaluated with regard to uncertainty analysis.

4.1 The previous BWR models

In the previous BWR models [2, 7], the ECCS recovery is modelled with two branches: successful recovery and no recovery. In the original model [7], the recovery time was drawn from a distribution, and time available for recovery was drawn from a distribution as well. If the recovery time was larger than the available time, the 'no recovery' branch had probability 1. Respectively, if the recovery time was smaller than the available time, the 'successful recovery' branch had probability 1. This way of modelling is valid, if the aim is only to determine the mean frequencies of accident sequences. Proper uncertainty analysis cannot be performed this way due to the reasons discussed in Section 3 concerning the physical parameters first approach. It is also inefficient to evaluate only one value from each distribution in one simulation cycle.

In the latest model [2], the ECCS recovery is modelled with the same two branches, but the recovery probability is drawn from a distribution instead of using the recovery time. This way proper uncertainty analysis can be performed. If the recovery is successful, the recovery time is drawn from a distribution, but it is only used to determine the end time for core melting, which further affects other accident timings and source term calculation.

From the results of [2], it can be noticed that the recovery time does not affect core meltdown fraction and ex-vessel accident phenomena in the previous models, except that the core meltdown fraction is set to 1 if the recovery is not successful. If the recovery is successful, the core meltdown fraction is drawn from a distribution. However, in reality, the core meltdown

fraction is highly dependent on the ECCS recovery time as the ECCS recovery is typically able to stop the meltdown. Therefore, the model could be improved by modelling this dependence. The previous modelling decision has been inherited from an old BWR model developed by Okkonen [27]. The old model is significantly more complicated than the example model in [2]. It models thermohydraulic conditions in the reactor core and containment explicitly by physical equations. However, the core meltdown fraction has been modelled in a very simple way due to lack of knowledge of the melting phenomenon.

4.2   One branch covering all timings

To model the dependence between ECCS recovery time and core meltdown fraction, a simple event tree model has been developed. The event tree is presented in Figure 2, and the CETL scripts after the figure. First, the mean and error factor of ECCS recovery time distribution are drawn from uncertainty distributions. The recovery time distribution is a rough lognormal approximation of the distribution used in [7] for high pressure case. It should be noticed that the high pressure core cooling system is called ECCS here, but in Section 5, only the low pressure core cooling system is called ECCS.
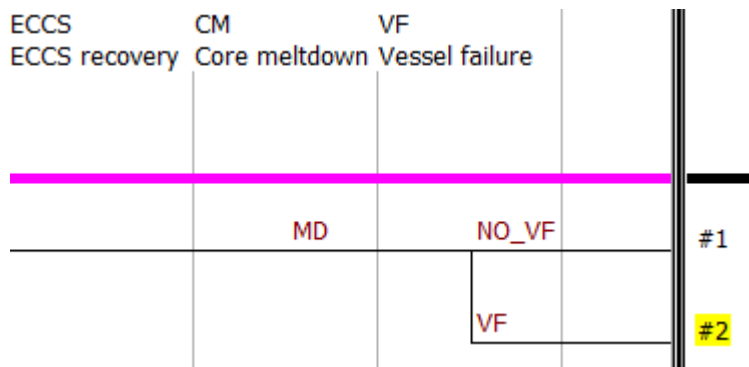

Figure 2: Emergency core cooling system recovery event tree.

Initial section

```
real M, EF, ECCSRecT, CoreMDF, MelStT, FuMelT

source ECCSRecT, MelStT, CoreMDF, FuMelT

routine init
  M = raneven(1000, 3000)
  EF = raneven(5, 30)
  ECCSRecT = ranlogn(M,EF)
return

routine finish

return

CUTFREQ = 0
```

CM

```
real x1, x2, x3, MM, S, D

routine init
```

```
  MM = raneven(3000,4000)
  S = raneven(150,250)
  x1 = rannorm (MM,S)
  x2 = raneven(-3000,3000)
  x3 = raneven(9000,14000)
  D = raneven(0.5,1.5)
return

function nil MD
  MelStT = x1
  FuMelT = x1+x3+x2
  CoreMDF = (ECCSRecT-MelStT)/(FuMelT-MelStT)
  if CoreMDF > 1 then CoreMDF = 1
  if CoreMDF < 0 then CoreMDF = 0
  CoreMDF = pow(CoreMDF,D)
return nil
```

VF

```
real p

normal RCSdebF = (0.3,0.1)

routine init

return

$-----------------------------------------------------

function real NO_VF

$ No vessel melt-through if not enough melt
p = 1-cumul(RCSdebF, CoreMDF)
if CoreMDF <= 0 then p = 1

return p

$-----------------------------------------------------

function nil VF

return nil
```

In the CM section, the core meltdown fraction is calculated based on the ECCS recovery time. Hypothetical melting start time and end time (assuming that the ECCS recovery is not successful) are drawn from distributions. Core meltdown fraction is calculated using the following formula:

$$CoreMDF = \left(\frac{\text{ECCSRecT} - \text{MelStT}}{\text{FuMelT} - \text{MelStT}}\right)^{D},$$

where FuMelT is the hypothetical melting end time, MelStT is hypothetical melting start time, and D is a factor that is assumed evenly distributed between 0.5 and 1.5. The formula is used

only if the ECCS recovery occurs during the melting. If the recovery occurs before the melting, the core meltdown fraction is assumed to be 0. This is a rough model that assumes that core melting is approximately linear as a function of time, and that the ECCS recovery stops the melting immediately. This formula is used purely for the demonstration of modelling techniques and is not based on any real data or physical considerations beyond the approximate linearity assumption. In reality, core meltdown is an extremely complicated phenomenon that is very challenging to model accurately [28]. NKS-395 [22] presents a core meltdown fraction curve (Figure 3.55 in [22]) that is close to linear, but evidently that is not always the case. A more realistic model could be developed by varying the ECCS recovery time in a set of deterministic analyses similar to those performed in [7], but the accuracy of the model is not relevant for the evaluation of modelling techniques.

In the VF section, the vessel failure probability is modelled as depending only on the core meltdown fraction. The amount of core melt needed for the vessel failure is approximated as a normal distribution in the same way as in [7]. CETL function CUMUL is used to determine the probability that the core meltdown fraction exceeds the limit value (RCSdepF), and this probability is used as the vessel failure probability.

The model was simulated 10000 times. The mean probability of vessel failure was 0.062. Proper uncertainty curve was not produced for the probability because aleatoric and epistemic uncertainties were mixed in the analysis. Uncertainty analysis requires the two-phase procedure presented in Section 3.

The model was also implemented in Excel where it was possible to perform the two-phase analysis. Variables representing aleatoric uncertainties were simulated 200 times in each simulation block (M in Figure 1), and variables representing epistemic uncertainties where simulated 100 times (N in Figure 1). Variables representing epistemic uncertainties were M, EF, MM, S, x3 and D, and variables representing aleatoric uncertainties were ECCSRecT, x1 and x2. The mean vessel failure probability was calculated for each of 100 simulation blocks, and an uncertainty distribution was drawn for the vessel failure probability based on those 100 points. The cumulative uncertainty distribution is presented in Figure 3. The mean failure probability was 0.060, approximately same as calculated in FinPSA. From the uncertainty curve, it can also be seen that e.g. 95th percentile value is around 0.11. Figure 4 illustrates how the vessel failure probability depends on the mean ECCS recovery time (variable M, the data set is different from Figure 3).
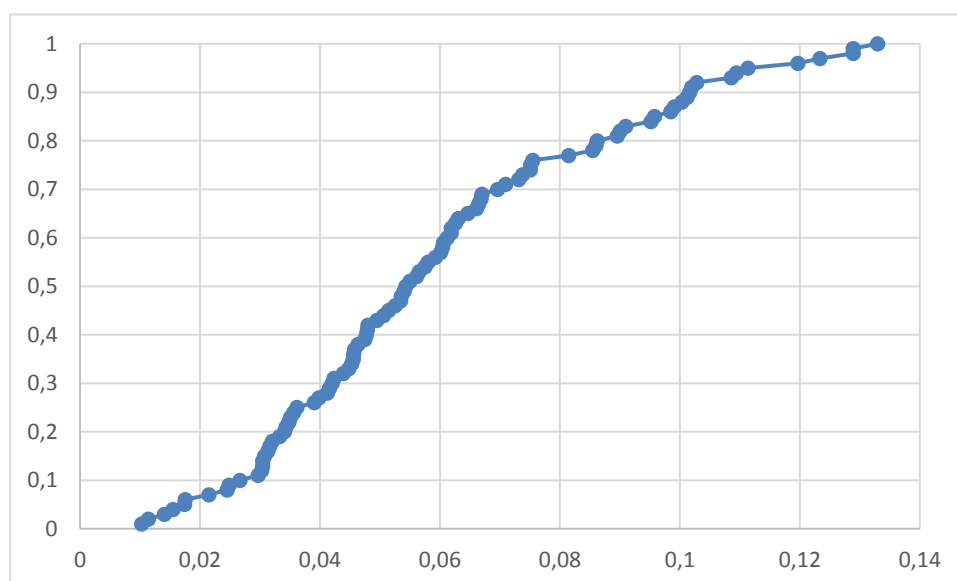

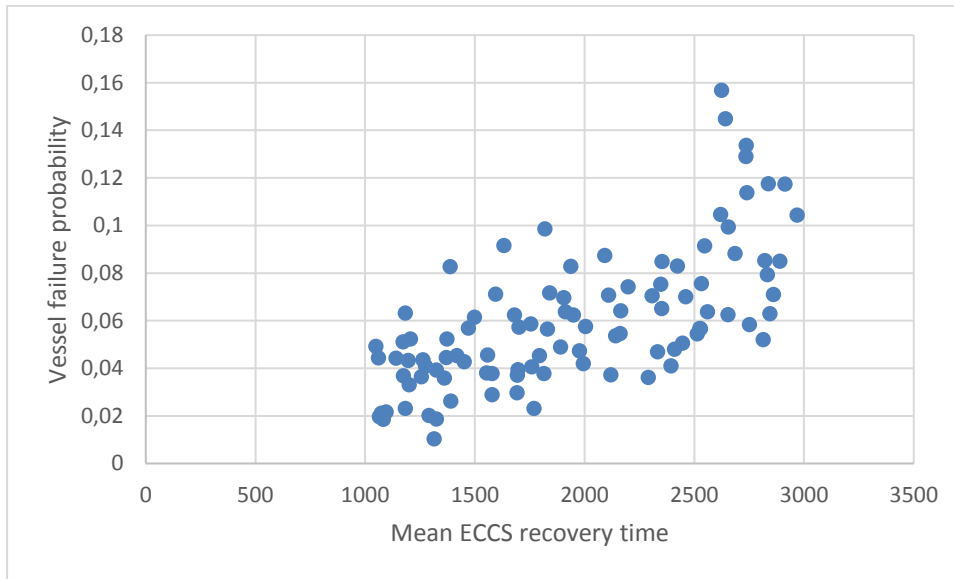*Figure 3: Cumulative distribution of the vessel failure probability.*

Figure 4: Scatter plot between the mean ECCS recovery time and the vessel failure probability.

4.3 Division to early and late recovery

With the previous example model, FinPSA calculated the vessel failure probability to be 0 approximately in 88% of the simulation cycles, even though those scenarios with late ECCS recovery are the most interesting cases. To focus more on the scenarios with late recovery, the event tree model is developed so that scenarios with early recovery and late recovery are analysed in separate accident sequences. The new event tree is presented in Figure 5. In this model, recovery is assumed to be late if it occurs after 2000 s. The limit value was selected because the earliest possible melting starting time is close to 2000 s. It can be noticed that late recovery defined this way does not automatically lead to vessel failure, but early recovery means that vessel failure is avoided. The new CETL scripts are presented after the figure. The CM and VF sections are the same as in the previous section.
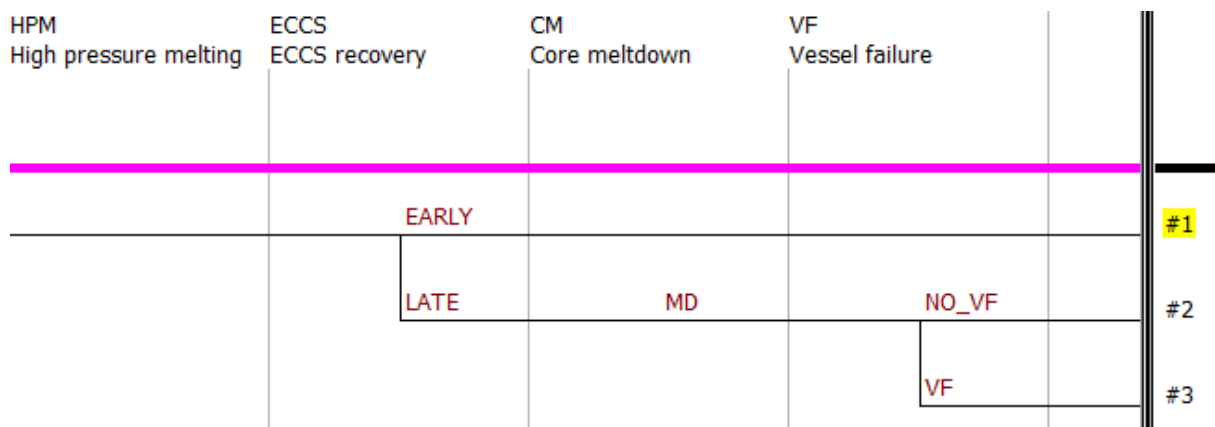

Figure 5: Event tree with division to early and late ECCS recovery.

Initial section

```
real ECCSRecT, CoreMDF, MelStT, FuMelT

source ECCSRecT, MelStT, CoreMDF, FuMelT

routine init
```

```
return

routine finish

return

CUTFREQ = 0
```

ECCS

```
real M, EF, xe, RT, rn

LOGNOR RTD = (2000,17.5)

routine init
  M = raneven(1000, 3000)
  EF = raneven(5, 30)
  RTD = LOGNOR(M,EF)
  xe = 1-cumul(RTD,2000)
  rn = 1-random()*xe
  RT = icumul(RTD,rn)
return

function nil EARLY
  ECCSRecT = 1000
return nil

function real LATE
  ECCSRecT = RT
return xe
```

The probability of late recovery is now calculated using the CUMUL function, which returns here the probability that the recovery time is smaller than 2000 s. The time of late recovery time is drawn only from the part of the recovery time distribution (RTD) where 2000 s is exceeded, i.e. a random number between 1-xe and 1 is drawn and the corresponding recovery time is calculated using the ICUMUL function. In the case of early recovery, the actual time is not interesting, so the recovery time is just set to 1000 s.

It can be noticed that instead of limit value 2000 s the real melting start time could be used if it was drawn already in the ECCS section, but it would not change the vessel failure probability. It would only change the probabilities of sequences 1 and 2.

The model was again simulated 10000 times. The mean probability of vessel failure was 0.060, approximately the same as before. The division to early and late recovery did not change the problem with uncertainty analysis. The probability of late recovery was correctly simulated only based on realizations of epistemic uncertainties (the mean recovery time and the error factor), but the vessel failure probability calculation still involved aleatoric uncertainties.

The model was again also implemented in Excel, and a two-phase uncertainty analysis was performed. Results similar to those presented in the previous section were produced. The main difference was that now there was more data with late recovery times, making the results more accurate. A smaller number of simulations related to aleatoric uncertainties (M in Figure 1) would have produced results with the same accuracy as in the previous section.

4.4 Early recovery, late recovery or recovery during core melting

Another model was implemented where the late ECCS recovery was divided into two branches: recovery during the core melting and recovery after the core melting. The new event tree is presented in Figure 6. In this model, the recovery is late if it occurs after 21000, which is approximately the latest possible end time for core melting. The recovery is assumed to occur during core melting if it occurs between 2000 s and 21000 s (these limit values only determine which recovery times are evaluated in the middle branch and do not affect the total vessel failure probability). Late recovery automatically leads to vessel failure. The CETL scripts of the ECCS section are presented after the figure. The scripts of other sections are the same as in the previous model version (see section 4.2 for CM and VF, and section 4.3 for initial section).
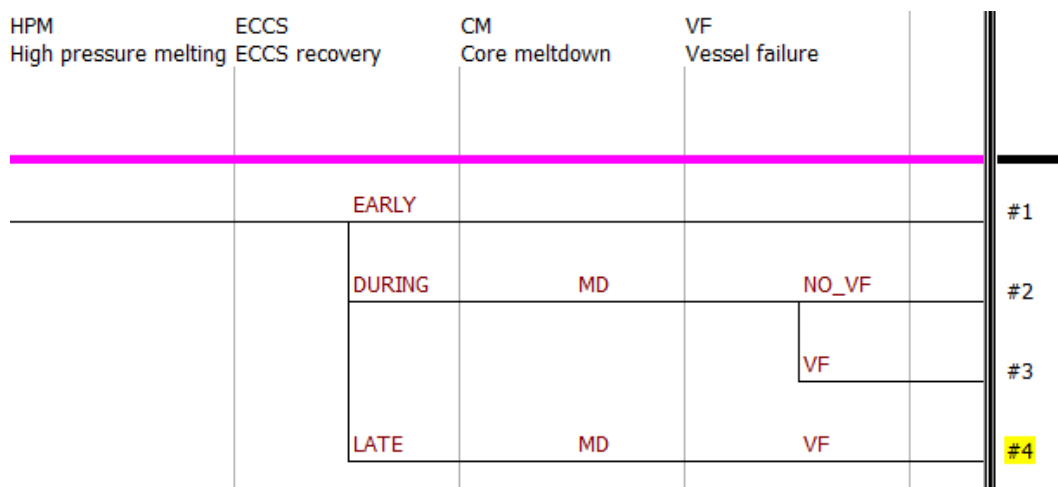

Figure 6: Event tree with three branches for the ECCS recovery.

ECCS

```
real M, EF, xe1, RT, rn, xe2

LOGNOR RTD = (2000,17.5)

routine init
  M = raneven(1000,3000)
  EF = raneven(5, 30)
  RTD = LOGNOR(M,EF)

  xe1 = 1-cumul(RTD,2000)
  xe2 = 1-cumul(RTD,21000)
  xe1 = xe1-xe2

  rn = 1-xe2-random()*xe1
  RT = icumul(RTD,rn)
return

function nil EARLY
  ECCSRecT = 1000
return nil

function real LATE
  ECCSRecT = 1E5
```

```
return xe2

function real DURING
  ECCSRecT = RT
return xe1
```

Variables xe1 and xe2 are the probabilities of recovery during core melting and late recovery. They are calculated from the recovery time distribution (RTD) using the CUMUL function. The recovery time for branch DURING is calculated by drawing a random number between 1-xe1-xe2 and 1-xe2 and calculating the corresponding recovery time from the distribution using the ICUMUL function. In the case of late recovery, the actual time is not interesting so the recovery time is just set to 100000 s.

The model was again simulated 10000 times. The mean probability of sequence 3 was 0.048 and the mean probability of sequence 4 was 0.012, which means that the mean probability of vessel failure was again 0.060. An improvement compared with the previous models was that the uncertainty analysis was performed correctly for sequence 4, because aleatoric uncertainties did not play any role in the computation of its probability. The uncertainty distribution is presented in Figure 7. However, for sequence 3, the uncertainty analysis still involved aleatoric uncertainty.
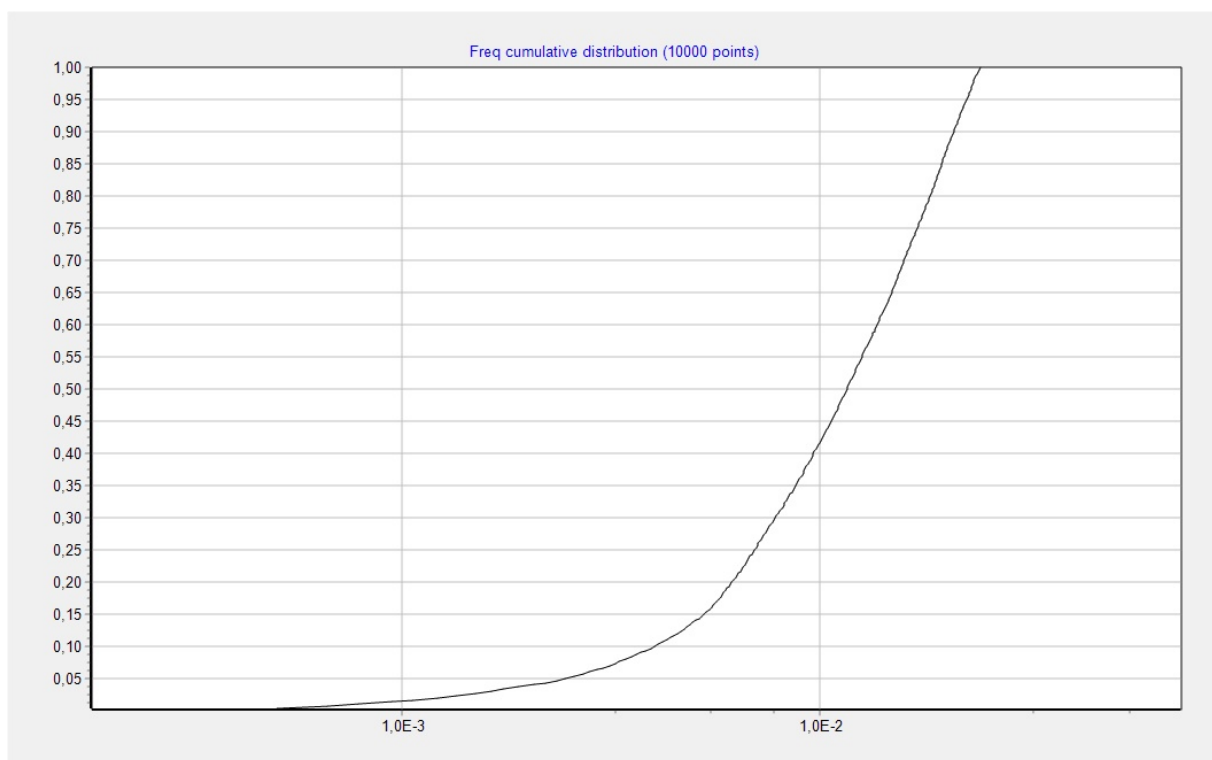

Figure 7: Cumulative distribution of the probability of sequence 4.

The model was again also implemented in Excel, and a two-phase uncertainty analysis was performed. Results similar to those presented in the previous section were produced. The results were more accurate than in the previous section, because the probability of late recovery was calculated accurately for each of 100 simulation cycles concerning epistemic uncertainties, and there were slightly more simulation data where the recovery occurred during the core melting. It would be possible to increase the accuracy even more by separating the recovery during core melting into multiple branches. However, concerning a full scope level 2 PRA model, the number of branches has to be considered carefully to keep the size of the model reasonable. Likely, a better idea would be to increase the number of simulation cycles for aleatoric uncertainties (M in Figure 1).

4.5 Uncertainty distribution of conditional vessel failure probability

The two-phase uncertainty analysis can be avoided if a distribution is directly assigned to the conditional vessel failure probability in the case that the ECCS recovery occurs during core melting, because the probability calculated in one simulation cycle is then not conditional on realisations of aleatoric uncertainties. The dependence to the mean ECCS recovery time can still be modelled, because the uncertainty of the mean value is epistemic. The distribution can be estimated based on the previous results. The mean conditional vessel failure probability in sequence 3 varies approximately between 0.2 and 0.34 depending on the mean ECCS recovery time. A lognormal distribution with error factor 1.5 is used in the VF section:

```
real p, MP

routine init
  MP = 0.2+0.14*(M-1000)/2000
  p = 1-ranlogn(MP, 1.5)
  if p < 0 then p = 0
return


$----------------------------------------------------


function real NO_VF
  VFail = false
return p


$----------------------------------------------------


function nil VF
  VFail = true
return nil
```

A binner specifying a release category covering sequences 3 and 4 was also added to the model.

With these modifications, normal one-phase uncertainty analysis was sufficient to produce a distribution for the vessel failure probability. The distribution is presented in Figure 8.
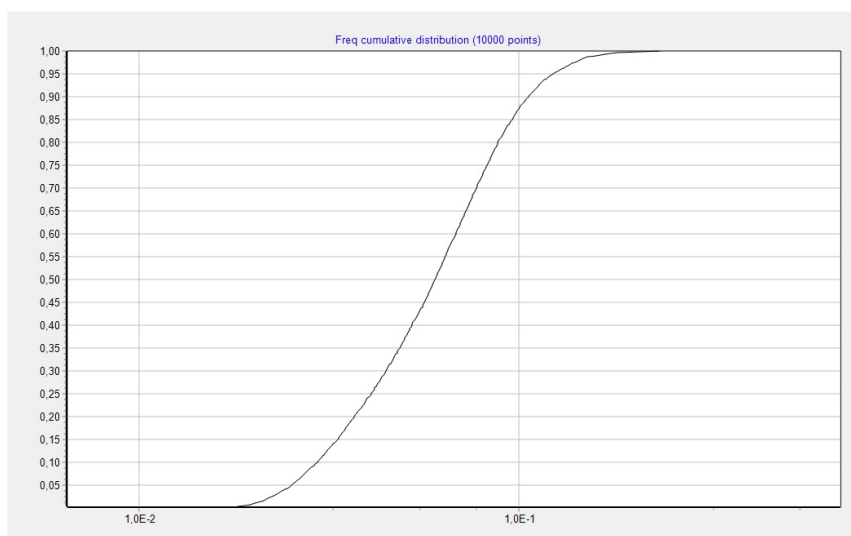

Figure 8: Cumulative distribution of the vessel failure probability produced by FinPSA.

This new version of the model does not include all the dependencies that the model in the previous section did. The vessel failure probability also depended on meltdown timing parameters, deviation parameters and the D parameter in the core meltdown fraction model, but these dependencies are now neglected. If it is not practical to use more accurate way of modelling like in the previous section, this type of simplification should be acceptable, especially if it is made in conservative manner.

4.6 Problems with one-phase uncertainty analysis

A problem with one-phase uncertainty analysis not separating epistemic and aleatoric uncertainties is that modelling decisions can affect results significantly. Aleatoric uncertainties can be modelled in several different ways resulting with different uncertainty distributions. Vessel failure probability distributions of models from sections 4.2-4.4 calculated by one-phase Monte Carlo simulation are presented in Figures 9-11. The probability distribution of the model of section 4.4 was calculated by adding a binner that sums the probabilities of sequences 3 and 4 in each simulation cycle. The distributions are totally different even though the same problem was modelled in each case, and the only difference was the division of ECCS recovery scenarios into event tree branches.
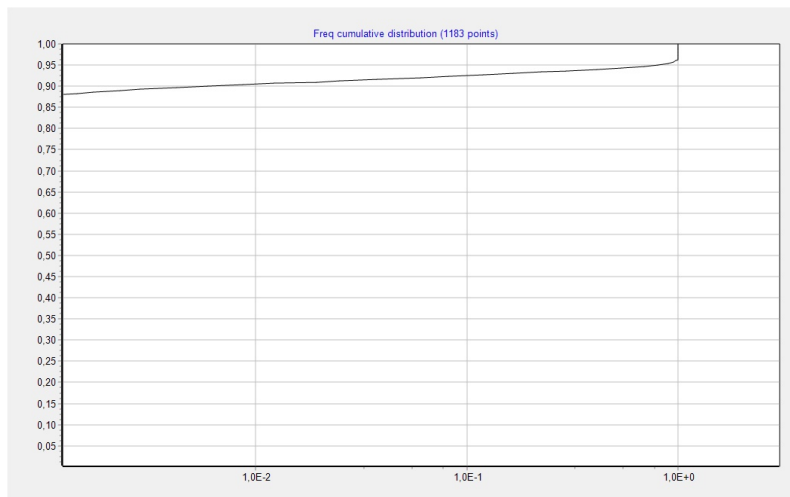

Figure 9: Total uncertainty distribution of vessel failure probability from the model of section 4.2.
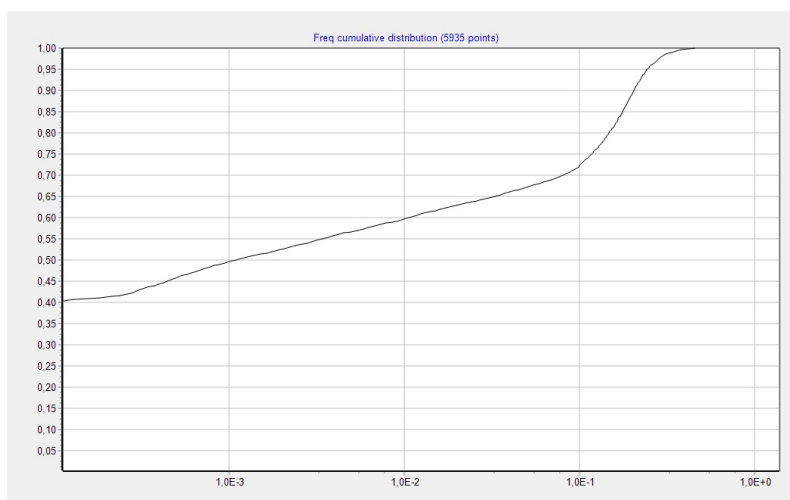

Figure 10: Total uncertainty distribution of vessel failure probability from the model of section 4.3.
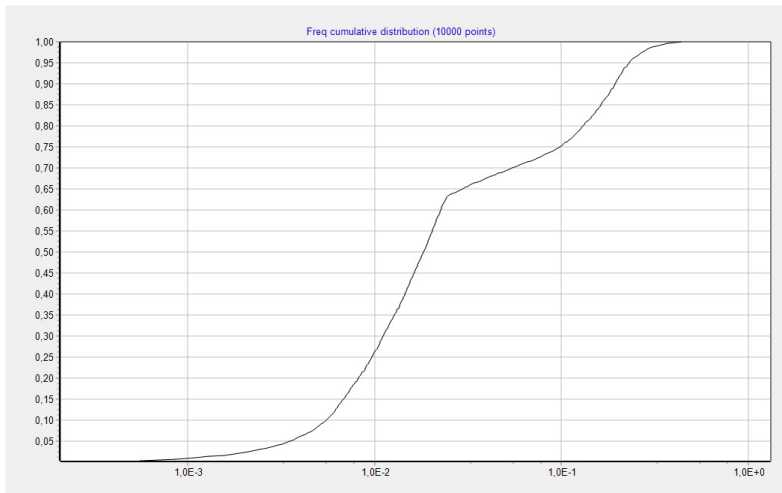
Figure 11: Total uncertainty distribution of vessel failure probability from the model of section 4.4.

There is also another way to calculate the uncertainty distributions of the models of sections 4.2 and 4.3. It is to remove those simulation cycles where the probability is 0, and scale the probabilities of other simulation cycles with the portion of the simulation cycles with non-zero probability. FinPSA calculates release category frequencies/probabilities this way. Therefore, binners were also added to the models of sections 4.2 and 4.3, even though they include only one sequence for vessel failure. The alternative uncertainty distributions are presented in Figures 12 and 13. These distributions are closer to each other and the distribution presented in Figure 11, though not exactly similar. Still, the interpretation of these distributions is problematic. In Figure 12, the right tail is clearly incorrect and gives an underestimation of highest possible vessel failure probabilities (see Figure 3 for comparison). In some other case, this type of underestimation could be more significant. The scaling procedure does not treat epistemic uncertainties correctly. Firstly, in some cases, the probability could really be 0 (not in this example). Secondly, the scaling procedure scales all non-zero values with the same portion, and does not take into account that the occurrence of 0 probability in a simulation cycle is more likely with specific realisations of epistemic uncertainties, and higher probabilities are more likely with other realisations of epistemic uncertainties. For example, it could be that specific realisations of epistemic uncertainties would not return probability 0 in any case, which means that the scaling of the related output probabilities would clearly be wrong.
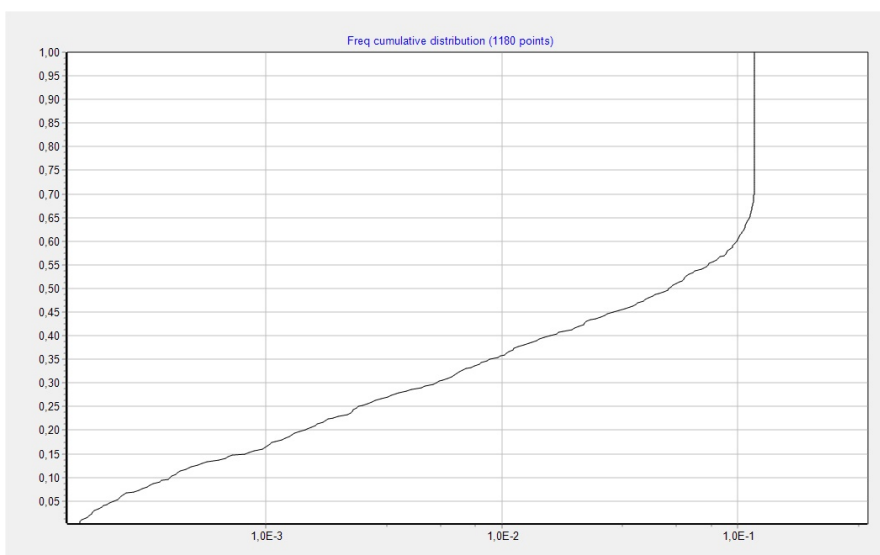

Figure 12: Alternative total uncertainty distribution of vessel failure probability from the model of section 4.2.
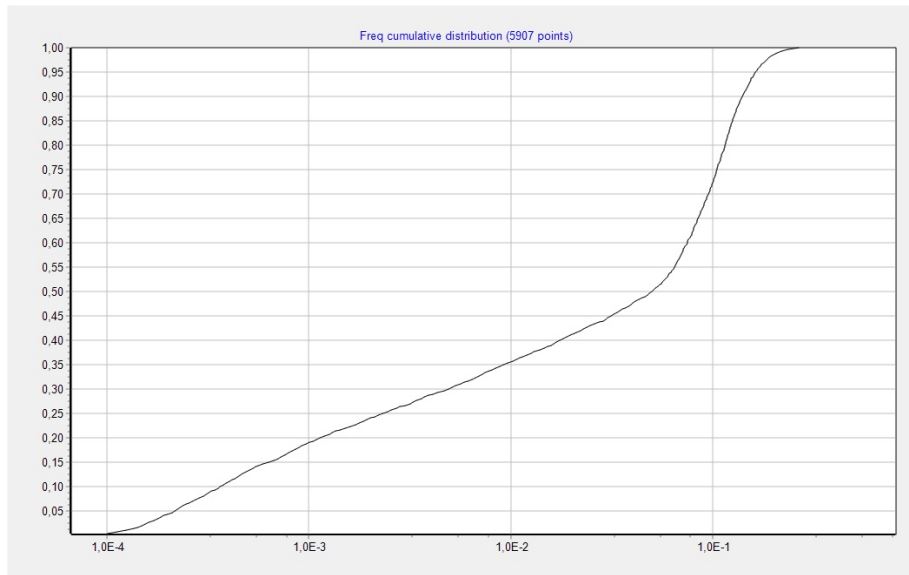
Figure 13: Alternative total uncertainty distribution of vessel failure probability from the model of section 4.3.

When aleatoric uncertainties are not treated separately, the resulting uncertainty distributions can be very sensitive to the modelling choices, whereas the two-phase uncertainty analysis produces approximately same distribution regardless of how aleatoric uncertainties are modelled. This does not mean that one-phase uncertainty analysis is totally useless. By improving the modelling of aleatoric uncertainties, e.g. by adding more event tree branches, the resulting uncertainty distribution can be made to reflect the aleatoric uncertainties less. By adding enough event tree branches for each aleatoric variable, the resulting uncertainty distribution could be made to represent almost exclusively epistemic uncertainties. In summary, it is a matter of modelling choices how aleatoric uncertainties are seen in the results. To conduct the uncertainty analysis in a consistent manner, either aleatoric uncertainties need to be handled carefully, or two-phase uncertainty analysis needs to be used.

4.7 Conclusions on the example models

The previous examples illustrated the role of a timing of an event in probabilistic CET analysis. The ECCS recovery was used as the example case, but the general principles and conclusions drawn are quite generally applicable to different timing modelling cases. Timings of events, such as depressurisation, ECCS recovery and lower drywell flooding, can significantly affect accident progression. The analysis can be made most accurate and dynamic if the timing information is included explicitly in the computation of sequence frequencies. However, to perform proper uncertainty analysis, the separation of epistemic and aleatoric uncertainties with a two-phase procedure is needed.

A drawback of the two-phase uncertainty analysis is that it requires a significantly larger number of simulation cycles than normal one-phase uncertainty analysis. With a large and complex model, it can mean that a very limited number of simulations can be performed resulting in low accuracy, or alternatively calculations last for days. It might be practical to make some simplifications so that one-phase uncertainty analysis can be performed and produces sufficiently accurate results. Section 4.5 presented an example on how to make such simplification. However, the results of a two-phase uncertainty analysis were the basis for the simplification. Hence, even if a full scope level 2 model would be implemented so that one-phase uncertainty analysis would be sufficient, it could be beneficial to perform some supporting analyses using two-phase uncertainty analysis to provide input data for the full scope analysis.

It could also have been possible to perform the probability calculations entirely using distribution functions. In that approach, a probability distribution would have been calculated for the core meltdown fraction on each simulation cycle based on the distributions of the ECCS recovery time, meltdown start time and hypothetical meltdown end time. Then, the vessel failure probability would have been calculated by comparing the core meltdown fraction distribution to the RCSdebF (reactor coolant system failure limit value) distribution. However, script compilation problems prevented trying that. There seems to be a bug in the assignment of a distribution to a DISTR variable. Distribution based probability computation would enable accurate uncertainty analysis with one phase only without simplifications like in section 5.5, but on the other hand, it is quite complicated and distribution functions are limited to basic operations (e.g. there is no power function). The number of operations allowed for distribution functions could be extended by utilizing transform formulae for functions of random variables (see, e.g., [29], Chapter 6). Also different probability distributions could be implemented, for example utilizing the information in [30].

5. High pressure melting analysis

A new version of the high pressure melting CET of the BWR model [2] has been prepared utilising dynamic modelling of timings of depressurisation, emergency feedwater system (EFWS) recovery, ECCS recovery and lower drywell (LDW) flooding. To perform uncertainty analysis for this new version, a two-phase procedure is needed. Since FinPSA does not currently include two-phase uncertainty analysis procedure, and the model is too large to be implemented in Excel or other tool with available resources, only one-phase uncertainty analysis is performed for the full CET to calculate the mean frequencies of accident sequences. In addition, a limited two-phase uncertainty analysis is performed for a small part of the CET in Excel.

The upper part of the CET is presented in Figure 14. Compared with [2], a new section for the EFWS recovery has been added (branches not shown in the figure because the high pressure part of the tree has been cut off). Some parts of the CET structure have also changed and some new CET functions have been introduced as presented in the following subsections. The most significant changes are in the CETL scripts. The source term model is the same as in the original model [7]. Table 1 presents the release categories and containment failure modes of the model. The plant damage state frequency is calculated by a level 1 model and an interface tree as in [2].

Table 1: Containment failure categories and the corresponding failure modes used in the CET model.

| Release category	Containment failure/vent mode
No containment failure of filtered venting (OK)	-
Isolation failure (ISOL)	1. Containment not leak-tight (ISOL)
Very early containment failure (VEF)	1. Containment over-pressurization (COP) 2. Hydrogen deflagration/detonation (H2) 3. Alpha-mode failure (ALPHA)
Early containment failure (EF)	1. Ex-vessel steam explosion (STEAM) 2. Failure of containment penetrations (PENE)
Late containment failure (LF)	1. Non-coolable ex-vessel debris causes basemat melt-through (BASE)
Filtered venting (FV)	1. Very early venting (VEFV) 2. Early venting (EFV) 3. Late venting (LFV)
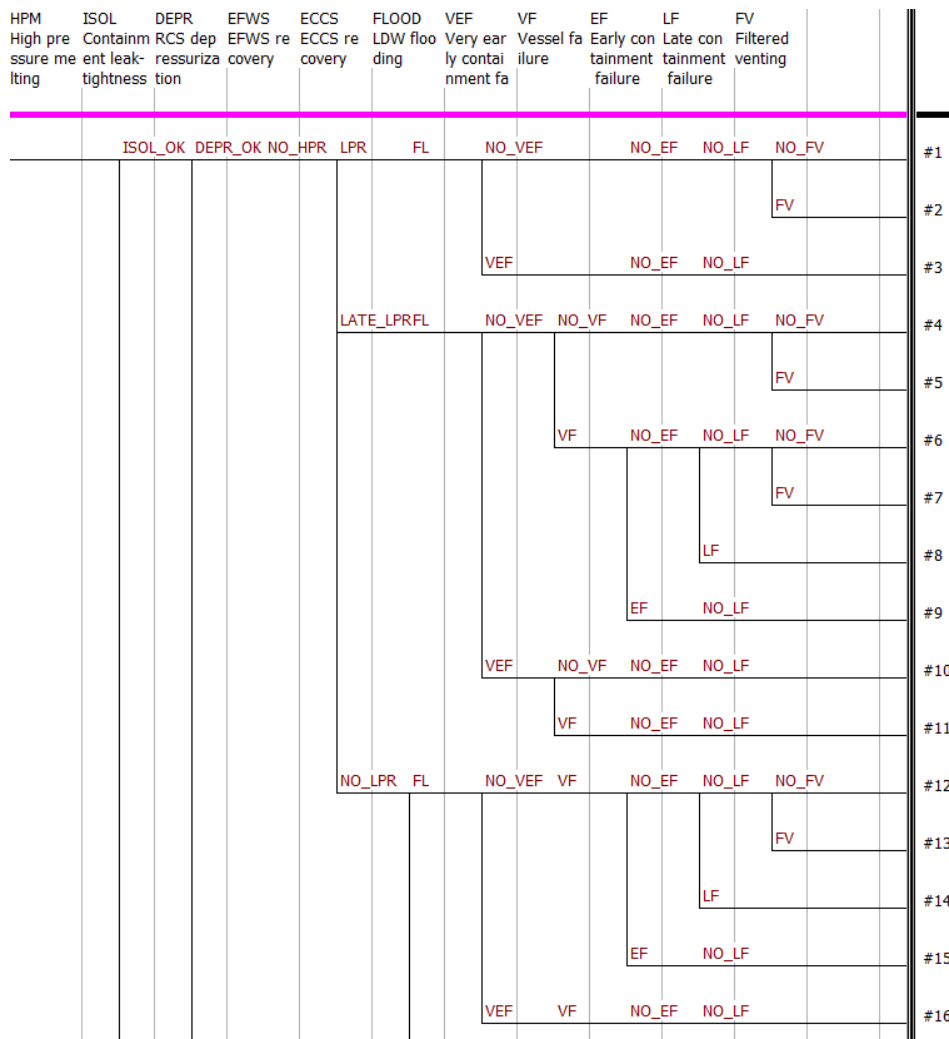
Figure 14: The upper part of the high pressure melting containment event tree.

5.1 Depressurisation

Three branches are used to model different depressurisation scenarios:

- DEPR_OK: depressurisation before meltdown

- DEPR_DM: depressurisation during meltdown

- NO_DEPR: no depressurisation during accident

The modelling is performed in the same way as for the ECCS recovery in Section 4.4. A lognormal distribution is used for the depressurisation time (depressurisation is assumed to occur instantaneously at this single time point with no delays). The mean value and error factor are drawn from distributions, and the probabilities of the branches are calculated from the lognormal distribution. On each simulation cycle, depressurisation time before meltdown and depressurisation time during meltdown are drawn from the distribution.

5.2 Emergency feedwater system recovery

The emergency feedwater system, which is used in the case of high pressure, is modelled in a section separate from the ECCS, whereas in the previous model [2], the cooling systems were modelled in the same section. The EFWS is modelled using two branches corresponding to the success and failure of recovery.

As in the previous model [2], level 1 results are utilised to determine what kind of failure caused the EFWS to fail in the first place. Different failure types that are considered are cooling system component failures (e.g. pumps and valves), power supply failures, heating ventilating and air conditioning (HVAC) system failures, demineralised water tank failure and reactor protection system failure. For each failure type, the conditional probability is calculated using Fussell-Vesely in the same way as in [2]. A lognormal recovery time distribution is also specified for each failure type, and the probability of successful recovery is calculated based on the distribution in each case. If depressurisation occurs during the meltdown, the success probability is the probability that the EFWS is recovered before the depressurisation, and therefore the depressurisation time is used in the calculation of the probability. The probability of successful recovery is a weighted sum of the success probabilities of the failure types weighted by the conditional probabilities of the failure types.

On each simulation cycle, for the success branch, a recovery time is drawn from the distributions. First, one failure type is drawn based on the conditional probabilities of the failure types given that the recovery is successful. Then, the recovery time is drawn from the recovery time distribution of that failure type.

5.3   Emergency core cooling system recovery

The low pressure ECCS recovery is modelled using three branches:

-   LPR: recovery immediately after depressurisation

-   LATE_LPR: recovery during meltdown, but not immediately after depressurisation

-   NO_LPR: no recovery during accident

The probability of failure of immediate recovery is drawn from a lognormal distribution with mean value 0.02. In the case of immediate recovery, the recovery is set to 10 seconds after the depressurisation time. If immediate recovery fails, a lognormal distribution is used for the recovery time. The distribution is the same as the one used for the EFWS recovery in the case of power supply failure. However, the depressurisation time is added to the time obtained from the distribution. The probability that the recovery occurs during the meltdown is calculated based on the distribution, and a recovery time is drawn from the distribution on each simulation cycle.

5.4   Lower drywell flooding

The modelling of the LDW flooding is similar to [2], except that a different flooding time distribution is used. Flooding is assumed always successful if the EFWS or ECCS is recovered. In the previous studies [2, 7], a very narrow flooding time distribution was used so that the flooding was always performed before the vessel failure if it was successful. Now, a lognormal distribution is used to cover the case of a late manual flooding.

5.5   Core meltdown

As in the previous studies [2, 7], the VEF section calls a function called MeltDown, which determines the melting start and end time, and core meltdown fraction. The core melting model used is similar to the one described in Section 4. However, the possibility of depressurisation during core melting and the two cooling systems complicate the computation. Table 2 presents core melting start time, end time and core meltdown fraction in different scenarios. Time is measured in seconds from initiating event. Some of the time estimates are roughly based on deterministic analyses performed in [7] and some are heuristic: physical (deterministic) modelling would be needed to obtain more accurate time estimates. In the table,

-   S_{LP} is the meltdown start time in low pressure without cooling,

- R_{LP} is the ECCS recovery time,

- L_{LP} is the time it takes for the core to melt fully in low pressure without cooling,

- D is an uncertain parameter in the core meltdown model,

- T_D is the depressurisation time,

- S_{HP} is the meltdown start time in high pressure without cooling,

- R_{HP} is the EFWS recovery time,

- L_{HP} is the time it takes for the core to melt fully in high pressure without cooling.

Table 2: Core meltdown scenarios.

Depressurisation	EFWS recovery	ECCS recovery	Start time	End time	Core meltdown fraction
Early	-	Early	-	-	0
Early	-	During melting	S_{LP}	R_{LP}	$\left(\dfrac{R_{LP} - S_{LP}}{L_{LP}}\right)^D$
Early	-	-	S_{LP}	$S_{LP} + L_{LP}$	1
Between early and late melting start time	-	During melting	T_D	R_{LP}	$\left(\dfrac{R_{LP} - T_D}{L_{LP}}\right)^D$
Between early and late melting start time	-	-	T_D	$T_D + L_{LP}$	1
During melting	Early	During melting	T_D	R_{LP}	$\left(\dfrac{R_{LP} - T_D}{L_{LP}}\right)^D$
During melting	Early	-	T_D	$T_D + L_{LP}$	1
During melting	During melting	During melting	S_{HP}	R_{LP}	$\left(\dfrac{R_{HP} - S_{HP}}{L_{HP}} + \dfrac{R_{LP} - T_D}{L_{LP}}\right)^D$
During melting	During melting	-	S_{HP}	$T_D + L_{LP}\left(1 - \dfrac{R_{HP} - S_{HP}}{L_{HP}}\right)$	1
During melting	-	During melting	S_{HP}	R_{LP}	$\left(\dfrac{T_D - S_{HP}}{L_{HP}} + \dfrac{R_{LP} - T_D}{L_{LP}}\right)^D$
During melting	-	-	S_{HP}	$T_D + L_{LP}\left(1 - \dfrac{T_D - S_{HP}}{L_{HP}}\right)$	1
-	Early	-	-	-	0
-	During melting	-	S_{HP}	R_{HP}	$\left(\dfrac{R_{HP} - S_{HP}}{L_{HP}}\right)^D$
-	-	-	S_{HP}	$S_{HP} + L_{HP}$	1

Uncertainties related to high pressure melting timings are modelled in the same way as in Section 4. Normal distributions are used for the low pressure melting start time and duration.

5.6 Very early containment failure

The modelling of very early containment failure is similar to the previous model [2]. Modelling of recriticality however differs. The reactor is assumed to become recritical if core cooling is recovered within a critical time window. The starting time of the time window is evenly distributed between 50 s and 150 s after the start of meltdown. The duration of the critical time window is evenly distributed between 500 s and 1000 s.

In the previous model [2], very early containment failure was conservatively assumed possible even if the core cooling was recovered in time. In the new model, very early containment failure is possible only due to hydrogen explosion if the core cooling is recovered early.

5.7 Vessel failure

The vessel failure probability is calculated based on the core meltdown fraction in the same way as in Section 4.2. The vessel failure time is calculated based on the melting end time and a delay parameter, which is around 5000 s. In the case of a cooling system recovery during melting, a hypothetical melting end time assuming no cooling is used in the computation instead, which means that the delay after the end of core melting is longer.

A LDW flooding fraction (the proportion of the LDW that is filled with water compared to the maximum water level) is also calculated in the way that it was calculated in the original model [7]. It is assumed that the LDW is filled linearly so that the flooding fraction is

$$\frac{T_{VF} - T_{FS}}{T_{FE} - T_{FS}},$$

where T_{VF} is the vessel failure time, T_{FS} is the start time of LDW flooding, and T_{FE} is the end time of the flooding. If the flooding is over before the vessel failure, the fraction is 1, and if it has not been started, the fraction is 0.

Probabilities for melt flow modes concerning the injection of core melt to the LDW are drawn in the VF section. They are highly dependent on the core meltdown fraction as presented in Table 3. In the table, F_{CM} is the core meltdown fraction, P_{LF} is the probability of large flow, and P_{MF} is the probability of medium flow. The probabilities are completely made up, but they are based on the idea that the larger the core meltdown fraction the larger the probability of large flow. Compared with NKS-395 [22], which is the reference for the selection of the melt flow modes, the large flow is emphasised more. In NKS-395, all melt flow modes were assumed to be equally probable in the case of no core cooling (core meltdown fraction = 1) due to lack of data.

In the case of an alpha-mode steam explosion, the vessel is assumed to fail with certainty along with the containment, and no further considerations of ex-vessel phenomena are made.

5.8 Early containment failure

Possible causes of early containment failure are an ex-vessel steam explosion and a failure of containment penetrations. Both failure modes are modelled as dependent on the LDW flooding fraction. In addition, the probability of a steam explosion depends on the melt flow mode.

Containment failure probabilities due to a steam explosion are taken from NKS-395 [22] and they are presented in Table 4. Here, a single containment failure probability combines the probability that a steam explosion occurs and the probability of containment failure given that a steam explosion occurs. Lognormal uncertainty distributions are assigned to the probabilities, except for dripping flow. LDW pool is considered deep when the flooding

fraction is at least 0.7, and shallow when the flooding fraction is between 0.2 and 0.7. Same probabilities are used for high and low pressure cases.

Table 3: Probabilities of melt flow modes.

Core meltdown fraction	Large flow	Medium flow	Dripping flow
0.8 - 1.0	Uniform distribution between 0.8 and 1.0	$1 - P_{LF}$	0
0.3 - 0.8	Uniform distribution between $$0.3 + 0.3\frac{F_{CM} - 0.3}{0.5}$$ and $$0.7 + 0.3\frac{F_{CM} - 0.3}{0.5}$$	$1 - P_{LF}$	0
0.1 - 0.3	Uniform distribution between $$0.3\frac{F_{CM} - 0.1}{0.2}$$ and $$0.2 + 0.3\frac{F_{CM} - 0.1}{0.2}$$	Uniform distribution between $$0.3 + 0.2\frac{F_{CM} - 0.1}{0.2}$$ and $$0.5 + 0.2\frac{F_{CM} - 0.1}{0.2}$$	$1 - P_{LF} - P_{MF}$
0.0 - 0.1	0	Uniform distribution between $3F_{CM}$ and $0.2 + 3F_{CM}$	$1 - P_{MF}$

Table 4: Mean containment failure probabilities due to a steam explosion.

LDW flooding	Dripping flow	Medium flow	Large flow
Deep pool	0	0.0155	0.636
Shallow pool	0	3.60E-4	0.378

In high pressure, the probability of failure of containment penetrations is assumed to be around 0.2 when the LDW flooding fraction is smaller than 0.5. If the flooding fraction is larger, the probability is around 0.1. Without flooding at all, the probability is around 0.5. In low pressure, the probability is 0, if the flooding is even partially successful.

5.9   Late containment failure

The only failure mode for late containment failure is basemat melt-through. The mean basemat melt-through probabilities are also taken from NKS-395 [22] and lognormal distributions are applied. If the LDW flooding fraction is larger than 0.5, the mean melt-through probability is 0.852 in the case of large melt flow, 0.283 in the case of medium flow, and 0.0361 in the case of dripping flow. Otherwise, the melt-through probability is 1.

5.10 Results

The model was simulated 1000 cycles, which takes a bit less than half an hour. Calculated release category frequencies are presented in Table 5. Release frequencies are smaller than in the previous study [2], because the conservative assumption of core melting in the case of successful ECCS recovery was removed. On the other hand, ex-vessel steam explosion and basemat melt-through probabilities were increased, which compensated the direction of the core melting modelling. Hydrogen explosion causing very early containment failure dominates the risk, because it is the only way for the containment to fail if core cooling is recovered early in addition to isolation failure. Hydrogen explosion modelling is also likely very conservative.

Table 5: Release category frequencies.

Release category	OK	ISOL	VEF	EF	LF	FV
Frequency	2.82E-7	9.29E-9	1.35E-7	1.66E-8	1.24E-8	4.66E-7
Frequency computed with old model [2]	2.60E-7	1.20E-8	2.29E-7	3.08E-8	2.51E-8	7.01E-7

Table 6 presents release category frequency increase factors of CET functions. A release category frequency increase factor is the relative increase of the release category frequency given that the analysed CET function has probability 1, basically the equivalent to the risk increase factor in level 1. Values below 1 mean that the frequency is decreased by the CET function. Release category frequency increase factors appear currently only in a developer version of FinPSA.

Table 6: Release category frequency increase factors of CET functions.

CET function	Section	VEF	EF	LF
DEPR_OK	DEPR	0.989	0.116	0.0789
DEPR_DM	DEPR	1.00	1.10	1.13
NO_DEPR	DEPR	0.991	9.79	3.20
NO_HPR	EFWS	1.03	4.46	4.33
HPR	EFWS	0.989	0.331	0.229
LPR	ECCS	1.00	0.827	0.879
LATE_LPR	ECCS	1.02	7.87	5.97
NO_LPR	ECCS	0.988	34.4	20.1
FL	FLOOD	1.00	1.00	0.999
NO_FL	FLOOD	1.00	0.992	1.01

Release category frequency increase factors indicate that the ECCS system is the most important safety system to mitigate severe accidents. The depressurisation and EFWS also have significant impact on the risk, while the LDW flooding has very small impact. The risk of very early containment failure was not changed much by any of the CET functions. The reason for this is that the risk of hydrogen explosion dominates the very early containment failure risk, and the main safety function against it is inerting of the containment, which is not represented by a CET function. The analysed safety functions have larger impacts on the early containment failure risk and late containment failure risk.

The reason for the small impact of the LDW flooding is that the risks of early and late containment failure are dominated by sequences where core cooling is recovered, because successful recovery is so likely. In those accident sequences, the LDW flooding is successful with certainty, and the frequencies of those sequences are kept in their nominal values also in the analysis of NO_FL, because NO_FL is not an option in those sequences. An alternative way to calculate the increase factors for NO_FL would be to set also the core cooling recovery failure probabilities to 1, because the failure of flooding requires the failure of core cooling. Then, the frequencies of early containment failure and late containment failure would be increased by factors of 36 and 48. On the other hand, the factors would then not measure only the impact of the LDW flooding failure. This underlines that the numbers cannot be read blindly. Instead, some effort is needed for their interpretation.

5.11 Uncertainty analysis

The part of the CET covering early depressurisation and ECCS recovery during core melting (sequences 4-11 in Figure 14) was analysed with two-phase uncertainty analysis in Excel. The analysis focused on

- the vessel failure probability

- the probability of ECCS recovery in the critical time window

- the probabilities of the melt flow modes

- the LDW flooding.

It was studied how the vessel failure probability correlates with different variables representing epistemic uncertainties. The highest correlations were with the ECCS recovery time mean value and the error factor. A regression model was developed to calculate approximate vessel failure probability based on the mean and error factor. Figure 15 shows how the fit of the regression model correlates with the real vessel failure probability. The regression model is used in an alternative version of the high pressure melting CET to calculate the vessel failure probability.
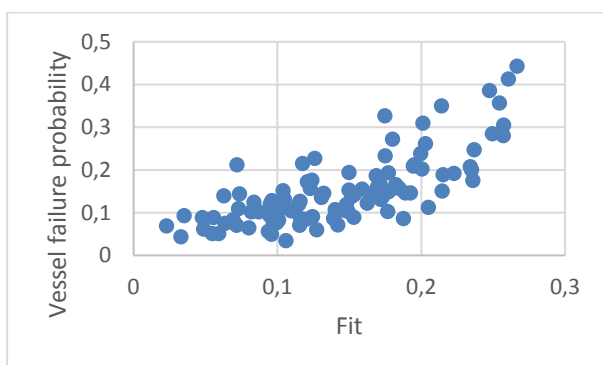

Figure 15: Scatter plot between the real vessel failure probability and the fit of the regression model.

Similarly, it was studied how the probability of ECCS recovery in the critical time window correlates with different variables. Again, the highest correlations were with the ECCS recovery time mean value and the error factor. The correlation with the error factor was higher, and it was used as the only explanatory variable in a regression model, which was implemented in the new model version.

When analysing the probability of large melt flow from the pressure vessel, it has to be noticed that the probability has to be analysed as conditional to the vessel failure. Raw simulation data cannot therefore be applied directly. Instead, the conditional probability has to be calculated on each simulation cycle of the outer loop of the two-stage procedure:

$$P_n(LF|VF) = \frac{\sum_{m=1}^{M} P_{n,m}(LF) \cdot P_{n,m}(VF)}{\sum_{m=1}^{M} P_{n,m}(VF)},$$

where $P_n(LF|VF)$ of the conditional probability of large melt flow in n:th simulation cycle of the outer loop, M is the number of simulation cycles in the inner loop, $P_{n,m}(LF)$ is the probability of large melt flow in n:th simulation cycle of the outer loop and m:the simulation cycle of the inner loop, and $P_{n,m}(VF)$ is the probability of vessel failure in n:th simulation cycle of the outer loop and m:the simulation cycle of the inner loop. Based on $P_n(LF|VF)$ values, the cumulative distribution of the conditional probability of large melt flow was created. It is presented in Figure 16. The conditional probability does not correlate much with other parameters. Therefore, the conditional probability of large melt flow was simply approximated with even distribution between 0.5 and 0.9 in the new model version.
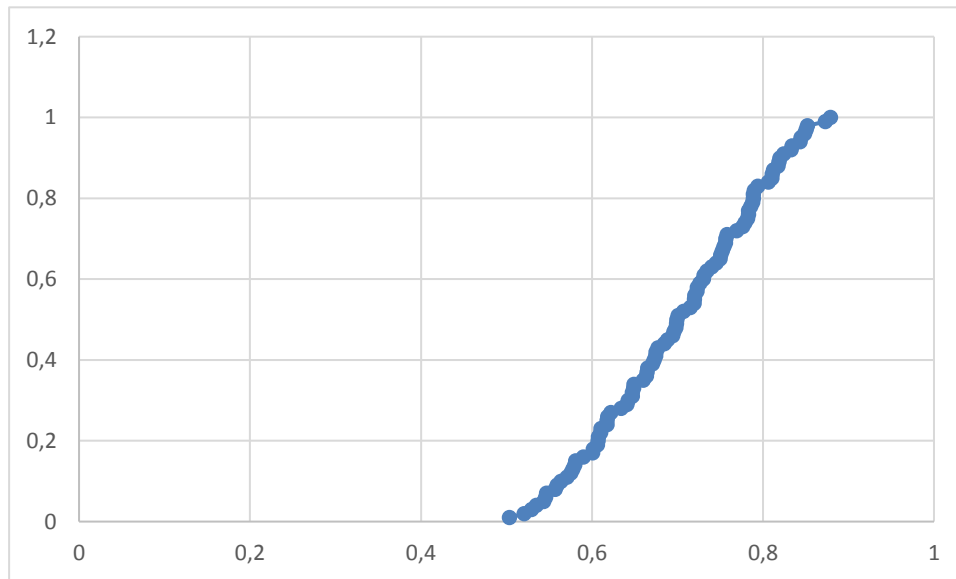

Figure 16: Cumulative distribution of the conditional probability of large melt flow.

It was found out that the probability of dripping melt flow is quite small (the mean value smaller than 0.02, maximum smaller than 0.04). Therefore, to simplify analysis, it was conservatively assumed that the probability of medium melt flow is the complement of the probability of large melt flow, and the probability of dripping flow is 0 in the alternative model.

With regard to the LDW flooding, the model was simplified a bit. The results indicated that the probability of a shallow pool in the LDW (flooding between 20% and 70%) is very small (less than 0.01), because the flooding rarely occurs so close to the vessel failure time. Therefore, the flooding was divided only to the two cases used in the basemat melt-through modelling: flooding fraction larger than 0.5 and smaller than 0.5. A regression model for the probability of small flooding fraction was developed using the mean value and the error factor of the flooding start time distribution as explanatory variables. In the ex-vessel steam explosion computation,

the pool was now conservatively assumed deep if the flooding fraction was over 0.5 (previously 0.7) and shallow if the flooding fraction was smaller than 0.5. As earlier, it was assumed that late containment failure occurs with certainty if the flooding fraction is smaller than 0.5. Therefore, it was considered better to estimate the probability of small flooding fraction slightly conservatively.

With the updates described above, it was possible to perform one-phase uncertainty analysis for the analysed part of the CET using FinPSA. The results are presented in Table 7. The mean frequencies are generally relatively close to the original values, which gives confidence that the model simplifications were successful. It can be noticed that the 2000 simulation cycles performed are not enough for the frequencies to converge to the "accurate" values, which means that the results naturally vary a bit between simulation runs. New frequencies are systematically a bit larger because of such variation, but the model simplifications have also increased the frequencies of some sequences.

Table 7: Uncertainty analysis results for sequences 4-11.

Sequence	Release category	Original frequency	New mean frequency	5th percentile	Median	95th percentile
4	OK	7.40E-10	7.60E-10	3.38E-12	1.31E-10	3.34E-9
5	FV	1.26E-9	1.35E-9	7.80E-12	2.43E-10	5.80E-9
6	OK	1.92E-11	2.78E-11	7.61E-14	4.00E-12	9.75E-11
7	FV	3.10E-11	4.92E-11	1.63E-13	7.79E-12	1.83E-10
8	LF	1.09E-10	1.73E-10	7.10E-13	2.85E-11	6.53E-10
9	EF	1.13E-10	1.93E-10	6.31E-13	3.20E-11	8.26E-10
10	VEF	3.93E-10	4.29E-10	1.78E-12	6.75E-11	1.81E-9
11	VEF	4.29E-11	9.23E-11	3.17E-13	1.31E-11	3.58E-10

5.12   Discussion

Even though the new high pressure melting model is mostly based on fictitious data, it is an attempt for more realistic modelling by explicit consideration of timings of events and their impacts. The main purpose has been to study and demonstrate dynamic modelling rather than to make conclusions about the safety of a real nuclear power plant. Because of that, liberties have been taken to make some strong assumptions in the model not backed up by real data, physical equations or deterministic analyses.

The model could be developed further by performing deterministic analyses varying different timings, such as depressurisation time, core cooling recovery time and LDW flooding time. Particularly, it would be interesting to develop the core meltdown model utilising deterministic analyses, because that part has been overly simplified in the previous models, and the current model is just a sketch based on the assumption that the melting behaves nearly linearly until the recovery of core cooling.

In the model, epistemic and aleatoric uncertainties were separated. Epistemic uncertainties were mainly represented as uncertainties related to parameters of probability distributions, which in turn represented aleatoric uncertainties. The separation was made very roughly

without any in-depth analysis. It is one area that could be studied in the future. Uncertainties related to distribution types were not modelled. The lognormal distribution that was used in many cases might not be the best option to model e.g. timings of events, but for this study it was considered sufficient. The DPD distribution type of FinPSA (a user-given discretized distribution specified by 13 percentile values) [31] is used often in practical modelling, but the modelling of epistemic uncertainties would be even more challenging, because the DPD distribution contains so many parameters. It could be worthwhile to implement some other distributions, such as Weibull distribution, for timing modelling in FinPSA level 2.

A limited two-phase uncertainty analysis was performed in Excel, and an alternative version of the model was created to enable the use of one-phase uncertainty analysis for some accident sequences. This type of procedure could be practical if a full two-phase uncertainty analysis is considered too heavy:

1. Create a dynamic and more realistic model with explicit modelling of timings (scope can be limited rather than cover all aspects of severe accidents).

2. Perform two-phase uncertainty analysis.

3. Create a simplified full scope model to enable one-phase uncertainty analysis.

4. Perform full analyses with the simplified model.

In the creation of the simplified model, correlation and regression analyses are useful. They would likely require collecting several variable values that would normally not be collected, such as different probability parameters, parameters of ECCS recovery time distribution and parameters of flooding start time distribution in this study.

6. Conclusions

This report has studied dynamic containment event tree modelling particularly focusing on the modelling of timings of events and uncertainty analysis. Dynamic CETs provide a good opportunity to analyze the effects of different timings and timing combinations. PRA modelling is more realistic when timings are explicitly included in the model and affect accident sequences in the model.

A drawback of the explicit modelling of the effects of timings is that normal one-phase uncertainty analysis cannot be used to produce proper uncertainty distributions for release frequencies, because the timings involve aleatoric uncertainties. A two-phase uncertainty analysis procedure has been proposed and demonstrated in a limited case study to treat epistemic and aleatoric uncertainties separately. The two-phase uncertainty analysis would improve level 2 analysis, but on the other hand, it is computationally very demanding. It might not be practical to apply it to full scope level 2 PRA. Instead, it could be used to perform some supporting analyses to produce inputs for full scope model. It has been suggested that first limited model version could be made by applying dynamic modelling, and a simplified full scope model could be developed based on the results of two-phase uncertainty analysis. It is recognized that the possibility to perform two-phase uncertainty analysis would be an asset for FinPSA level 2. Note that normal one-phase uncertainty analysis is a special case of the two-phase uncertainty analysis in which only one simulation cycle is performed in the inner loop.

An example BWR model has been developed further by improving the modelling of timings of events and core meltdown modelling, along with some other changes. The study was limited only to the high pressure melting case. Similar updates could also be made to other CETs. The low pressure cases would be simpler because depressurization and the high pressure cooling system do not need to be considered. Even more importantly, a set of deterministic analyses could be carried out to provide input data to make the model more realistic. Core

meltdown fraction would particularly be an interesting variable to study in different scenarios, because its modelling has been very simplified in previous level 2 models. Another direction that could be taken in the modelling would be to implement more physical modelling, e.g. thermo-hydraulic equations, in the CETL scripts as was done in [27].

References

[1]	International Atomic Energy Agency, IAEA. Development and application of level 2 probabilistic safety assessment for nuclear power plants: Specific safety guide No: SSG-4. Vienna, 2010.

[2]	Tyrväinen, T, Karanta, I. Level 2 studies – Steam explosions and integration of PRA levels 1 and 2. VTT Technical Research Centre of Finland Ltd, Espoo, 2018. VTT-R-00191-18.

[3]	Tyrväinen, T, Karanta, I. Level 2 studies – Source term characteristics and hydrogen explosions. VTT Technical Research Centre of Finland Ltd, Espoo, 2017. VTT-R-00354-17.

[4]	Authén, S, Holmberg, J-E, Tyrväinen, T, Zamani, L. Guidelines for reliability analysis of digital systems in PSA context – Final Report, NKS-330. Nordic nuclear safety research (NKS), Roskilde, 2015.

[5]	Tyrväinen, T, Silvonen, T, Mätäsniemi, T. Computing source terms with dynamic containment event trees. 13th International conference on probabilistic safety assessment and management (PSAM13), Seoul, Korea, 2-7 October, 2016.

[6]	VTT Technical Research Centre of Finland Ltd. FinPSA – Tool for promoting safety and reliability. 2018. https://www.simulationstore.com/finpsa (link accessed 8.1.2018)

[7]	Silvonen, T. Steam explosion case study using IDPSA methodology. VTT Technical Research Centre of Finland, Espoo, 2013. VTT-R-05974-13.

[8]	Tyrväinen, T, Silvonen, T. Summary on integrated deterministic and probabilistic safety assessment development and case studies. VTT Technical Research Centre of Finland, Espoo, 2015. VTT-R-04473-15.

[9]	Jyrkama, MI, Pandey, MD. On the separation of aleatory and epistemic uncertainties in probabilistic assessments. Nuclear Engineering and Design, 303, 68-74, 2016.

[10]	Karanki, DR, Rahman, S, Dang, VN, Zerkak, O. Epistemic and aleatory uncertainties in integrated deterministic and probabilistic safety assessment: Tradeoff between accuracy and accident simulations. Reliability Engineering and System Safety, 162, 91-102, 2017.

[11]	Kurowicka, D, Cooke, R. Uncertainty analysis - with high dimensional dependence modelling. Wiley, 2006.

[12]	Hofer, E, Kloos, M, Krzykacz-Hausmann, B, Peschke, J, Woltereck, M. An approximate epistemic uncertainty analysis approach in the presence of epistemic and aleatory uncertainties. Reliability Engineering and System Safety, 77, 229-238, 2002.

[13]   Apostolakis, G. The distinction between aleatory and epistemic uncertainties is important: an example from the inclusion of aging effects in PSA. PSA 99', Washington, DC, 22-25 August, 1999.

[14]   Der Kiereghian, A, Ditlevsen, O. Aleatory or epistemic? Does it matter? Structural Safety, 31, 105-112, 2009.

[15]   Pedroni, N, Zio, E, Ferrario, E, Pasanisi, A, Couplet, M. Hierarchical propagation of probabilistic and non-probabilistic uncertainty in the parameters of a risk model. Computers and Structures, 126, 199-213, 2013.

[16]   Vose, D. Risk analysis, A quantitative guide, third edition. John Wiley & Sons, Ltd, West Sussex, England, 2008.

[17]   Durga Rao, K, Kushwaha, HS, Verma, AK, Srividya, A. Quantification of epistemic and aleatory uncertainties in level-1 probabilistic safety assessment studies. Reliability Engineering and System Safety, 92, 947-956, 7, 2007.

[18]   Chen, X, Yao, W, Zhao, Y, Ouyang, Q. An extended probabilistic method for reliability analysis under mixed aleatory and epistemic uncertainties with flexible intervals. Structural and Multidisciplinary Optimization, 54, 1641-1652, 2016.

[19]   Karanki, DR, Dang, VN, MacMillan, MT, Podofillini. A comparison of dynamic event tree methods - Case study on a chemical batch reactor. Reliability Engineering and System Safety, 169, 542-553, 2018.

[20]   Rahman, S, Karanki, DR, Epiney, A, Wicaksono, D, Zerkak, O, Dang, VN. Deterministic sampling for propagating epistemic and aleatory uncertainty in dynamic event tree analysis. Reliability Engineering and System Safety, 175, 62-78, 2018.

[21]   Ahn, K-I, Yang, J-E, Ha, J. Formal handling of the level 2 uncertainty sources and their combination with level 1 PSA uncertainties. OECD/NEA/CSNI workshop on evaluation of uncertainties in relation to severe accidents and level 2 probabilistic safety analysis, Cadarache, France, 7-9 November, 2005.

[22]   Kudinov, P, Galushin, S, Grishchenko, D, Yakush, S, Adolfsson, Y, Ranlöf, L, Bäckström, O, Enerholm, A. Scenarios and phenomena affecting risk of containment failure and release characteristics. Nordic nuclear safety research, Roskilde, 2017. NKS-395.

[23]   Bucklew, JA. Introduction to rare event simulation. Springer, 2004.

[24]   Blanchet, J, Lam, H. State-dependent importance sampling for rare-event simulation: An overview and recent adbances. Surveys in Operations Research and Management Science, 17, 38-59, 2012.

[25]   Juneja, S, Shahabuddin, P. Rare event simulation techniques: an introduction and recent advances. In Simualtion, Handbooks in Operations Research and Management Science Vol. 13, 291-350. Elsevier, 2006.

[26]   L'Ecuyer, P, Demers, V, Tuffin, B. Splitting for rare-event simulation. Proceedings of the 2006 Winter Simulation Conference, Perrone et al eds., IEEE, 2006.

[27]   Okkonen, T. Development of a parametric containment event tree model for a
         severe BWR accident. Finnish centre for radiation and nuclear safety, Helsinki,
         1995. STUK-YTO-TR81.

[28]   Galushin, S, Kudinov, P. Analysis of core degradation and relocation
         phenomena and scenarios in a Nordic-type BWR. Nuclear Engineering and
         Design, 310, 125-141, 2016.

[29]   Spanos, A. Statistical foundations of econometric modelling. Cambridge
         University Press, 1986.

[30]   Law, AM. Simulation modeling and analysis, 5th edition. McGraw-Hill, 2015.

[31]   Tyrväinen, T, Mätäsniemi, T, Björkman K. FinPSA manual, Release 1. VTT
         Technical Research Centre of Finland Ltd, Espoo, 2017.

Appendix B
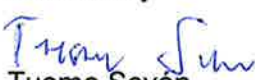
Comparison of simulations for debris bed behaviour in postdryout conditions
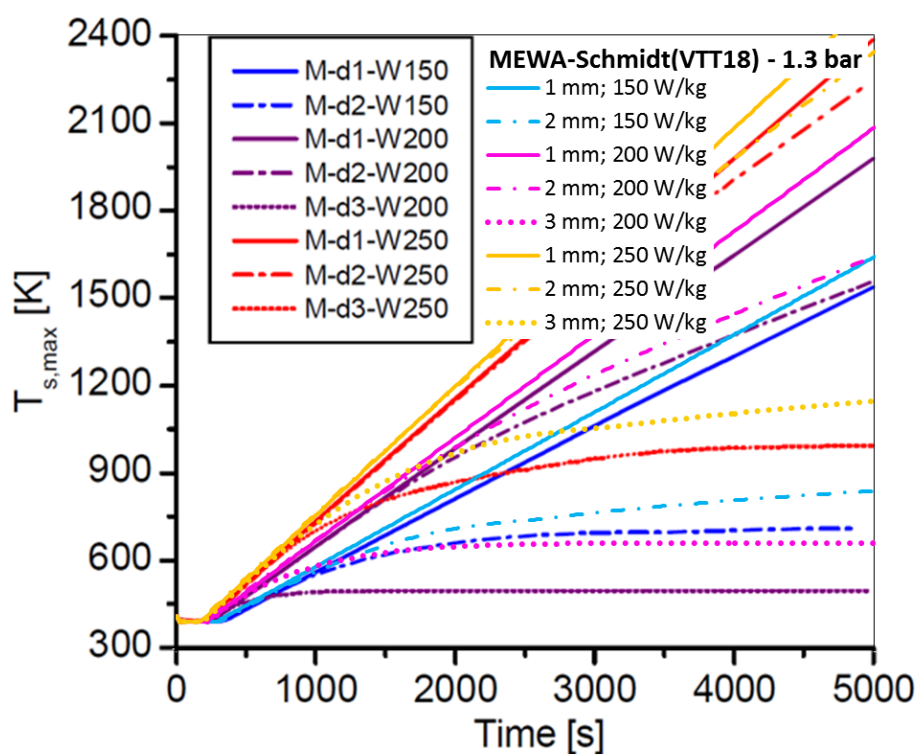
Comparison of simulations for debris bed behaviour in post-dryout conditions

Author: Veikko Taivassalo

Confidentiality: Public

Report's title		
Comparison of simulations for debris bed behaviour in post-dryout conditions		
Customer, contact person, address		**Order reference**
SAFIR2018 Research Programme on Nuclear Power Plant Safety 2015 – 2018		**SAFIR 9/2018**
Project name		**Project number/Short name**
Comprehensive Analysis of Severe Accidents		**117298/CASA**
Author(s)		**Pages**
Veikko Taivassalo		47/
Keywords		**Report identification code**
debris bed, coolability, post-dryout conditions		VTT-R-00223-19

Summary

Achieving long-term coolability of molten corium is the main objective in the unlikely event of a severe nuclear reactor accident. The Nordic boiling water reactors (BWRs) rely on cooling the corium in the flooded drywell. During corium discharge to the flooded drywell, the molten material fragments into droplets and subsequently solidifies into particles, which settle on the floor of the containment, forming a porous debris bed. The coolability of these debris beds has been studied extensively experimentally and computationally.

The coolability limit based on the minimum dryout heat flux might be overly conservative, since the temperature may remain on an acceptable level even in the dry zone. It has been proposed that the coolability limit should be based on an increase in the particle temperature. Previously post-dryout conditions were analysed by performing MEWA and Fluent simulations for the conical debris beds studied by Yakush & Kudinov (2014). The MEWA results differed considerably from the DECOSIM results of Yakush & Kudinov. As the friction model can influence significantly the bed behaviour and as MEWA does not feature the friction model used in DECOSIM, it was added into the Fluent implementation of the debris bed models. The same friction model improved the agreement with the DECOSIM results.

In this work the friction model applied in DECOSIM was implemented in the MEWA code and MEWA simulations were performed for the same conical and truncated-cone-shaped particle beds as Yakush & Kudinov studied. The MEWA results are consistent with the Fluent results. However, the comparison of the MEWA and DECOSIM results reveals some significant differences. Especially the lowest particle temperatures and saturation temperatures reported by Yakush & Kudinov (2014) are not consistent with the MEWA results. Since the change of the top surface pressure from 3 bar to 1.3 bar removes these obvious discrepancies, speculative simulations were performed with MEWA for the reduced pressure. With the modified boundary conditions, the MEWA results agree satisfactory with the DECOSIM results for both the conical and truncated-cone-shaped beds.

Confidentiality	Public

Espoo 13.2.2019

Written by	Reviewed by	Accepted by
Veikko Taivassalo	Tuomo Sevón	Anitta Hämäläinen
Principal Scientist	Senior Scientist	Principal Scientist

VTT's contact address
PO Box 1000, 02044-VTT, Finland

Distribution (customer and VTT)
SAFIR2018 Reference Group 2

Preface

This report is prepared in the project Comprehensive Analysis of Severe Accidents (CASA). The project is a part of the national nuclear energy program SAFIR2018. This study was carried out at the Technical Research Centre of Finland (VTT) in 2018 and 2019. The work was funded by the State Nuclear Waste Management Fund (VYR) and VTT.

Espoo 13.2.2019

Author

Contents

1. Introduction

Achieving long-term coolability of molten corium is the main objective in the unlikely event of a severe nuclear reactor accident. The Nordic boiling water reactors (BWRs) rely on cooling the corium in the flooded lower drywell of the containment as a cornerstone of the severe accident management strategy. During the discharge of the corium in the deep (~10 m) water pool, the molten material fragments into droplets and subsequently solidifies into particles, which settle on the floor of the containment forming a porous debris bed. The coolability of these debris beds has been studied extensively experimentally and computationally.

The coolability of heap-shaped (conical) and flat-shaped, top-flooded (cylindrical) particle beds was studied in the COOLOCE experiments, in which the dryout power and heat flux were measured (Takasuo 2016). In the impressive amount of research on the dryout heat flux and debris bed coolability conducted in recent decades, studies on heat transfer after dryout has occurred are rare. In the post-dryout conditions, the heating power required for dryout and for a local loss of water has been reached and possibly exceeded.

For debris beds of realistic shapes (heaps and cones), the post-dryout conditions are of interest since the particle temperature may stabilize even though a local dry zone has been formed (Atkhen & Berthoud, 2006). The coolability limit based on the minimum dryout heat flux might be overly conservative, since the temperature may remain on an acceptable level even in the dry zone. It has been proposed that instead of the dryout heat flux, the coolability / non-coolability limit should be based on the increase of the particle temperature (Takasuo 2016, Yakush & Kudinov 2014). It should be noted that in the case of a top-flooded bed, local dryout usually leads to a temperature increase above the corium melting temperature and thus the post-dryout coolability is mainly of interest with the heap-shaped debris beds.

Previously (Taivassalo & Takasuo 2017), the behaviour of two types of hypothetical conical debris beds was studied by performing MEWA (Bürger et al. 2006, Rahman 2013) simulations. Coolability and especially conditions after dryout were analysed for a reference reactor debris bed and for conical debris beds studied at KTH by Yakush & Kudinov (2014). The influences of the bed particle size, heating power and porosity were examined. For each particle size, 1, 2, and 3 mm, several specific heating powers were used with the objective to cover conditions from no-dryout to the corium remelting temperature. The MEWA results showed that the temperature-based coolability criterion increases the coolability limit compared to the void-based criterion (the dryout heat flux). In the dryout conditions, after the bed temperature stabilization, i.e., after achieving a steady-state, the bed temperature might locally be considerably higher than the saturation temperature.

The simulation results of the MEWA code were, however, not in a full agreement with the DECOSIM results reported by Yakush & Kudinov (2014) (introduced in Section 2) (Taivassalo & Takasuo 2017). In the 1 mm particle cases without temperature stabilization, the codes agree satisfactorily. On the other hand, these cases are not interesting because the maximum particle temperature eventually exceeds the temperatures where zirconium oxidation or even corium remelting begins. In the other conical bed cases studied by Yakush & Kudinov (2014), both the codes predict that the beds are coolable but MEWA and DECOSIM predict different transient behaviours and final steady-state conditions. Therefore, before trying to quantify the temperature-based coolability criterion, it was considered essential to identify the origin of the significant differences between the MEWA and DECOSIM results.

Taivassalo & Takasuo (2017) examined different heat transfer models available in MEWA. Alternative models available in MEWA for the solid-to-gas heat transfer coefficient and for the effective dry-zone thermal conductivity were tested. Their influence on the post-dryout behaviour of the particle beds could not explain the differences between the DECOSIM and MEWA results.

It was thus concluded necessary to study importance of the friction model (Taivassalo 2018). The MEWA results show that the friction model can influence significantly the computed bed behaviour for the conical beds. As MEWA does not feature the same friction model used in DECOSIM, the DECOSIM model was added into the Fluent implementation (Takasuo et al. 2015) of the debris bed coolability models and simulations for the conical beds of Yakush & Kudinov were performed with Fluent. The usage of the same friction model improved the agreement with the DECOSIM results. However, the convection and viscous term in the full multiphase flow equations solved by Fluent modify the flow field especially close to the tip of the conical beds hampering quantitative comparisons with the MEWA and DECOSIM results.

There are also some other differences between the MEWA and DECOSIM simulations but the influence of the friction model is most likely dominating. MEWA simulations with the same friction model used in DECOSIM were thus considered necessary (Taivassalo 2018).

In this work the friction model applied in the DECOSIM simulations of Yakush & Kudinov (2014) was implemented in the MEWA code. The implementation will be discussed in Section 4 after summarising the features and especially the friction models and heat transfer models of the MEWA code in Section 3. All the conical and truncated-cone-shaped beds studied by Yakush & Kudinov (2014) were computed with the MEWA code using the implemented friction model. The DECOSIM results are summarised in the next section. The MEWA computations for all the particle beds studied by Yakush & Kudinov (2014) will be discussed in Section 5 with comparisons of the MEWA results to the results of the DECOSIM and Fluent codes. Since even with the same friction model some obvious discrepancies remain between the MEWA and DECOSIM results, speculative MEWA simulations were performed for a reduced pressure (Section 5.4).

2. Conical particle beds of Yakush & Kudinov

2.1   Case specifications

Yakush & Kudinov (2014) studied computationally conical and truncated-cone-shaped (mound-shaped) particle beds. The studied beds are idealised representations of actual debris beds. In addition to the bed shape, the other properties of real debris beds were also idealised assuming a homogenous porous medium formed by homogenous spherical particles of one size with constant physical properties and heat production.

This work considers the debris beds of Yakush & Kudinov (2014). The studied beds are characterised in Table 1. The conical beds are 3 m in height and the truncated-cone-shaped ones 2.5 m. Otherwise the bed geometry is the same in all cases. The diameter of the spherical particles is 1, 2 or 3 mm. The other properties are same in all cases. The heating power varies and the powers used with the different particle sizes are given in Table 2 and Table 3.

2.2   DECOSIM simulations of Yakush & Kudinov

2.2.1   Computational domains and spatial discretizations

The computational domains and spatial discretizations used in the DECOSIM simulations of Yakush & Kudinov (2014) are shown in Figure 1. The domains and meshes are axisymmetric respect to the vertical axis of the bed on the left. The mesh consists of 30 x 51 cells. The white lines in Figure 1 represent the ideal, conical or truncated-cone-shaped surfaces of the

beds. It is however unclear which cells around the white lines are considered to be inside the bed area.

The main features of the DECOSIM code are introduced by Yakush & Kudinov (2014). In large, it is similar to the MEWA code discussed in Section 3.2.

Table 1. Characteristics of the idealised debris beds studied at KTH (Yakush & Kudinov 2014).

	Conical	Truncated-cone
Height of the debris bed (m)	3	2.5
Diameter of the debris bed (m)	6	6
Diameter of the water pool (m)	9	9
Height of the water pool (m)	6	6
Pressure at the top boundary (bar)	3	3
Porosity of the debris bed (-)	0.4	0.4
Diameter of the bed particles (mm)	1, 2, or 3	1, 2, or 3
Density of corium (kg/m^3)	8285	8285
Specific heat capacity of corium (J/kgK)	566	566
Thermal conductivity of corium (W/Km)	1.9	1.9

Table 2. Conical debris bed cases studied at KTH (Yakush & Kudinov,2014). The computed cases are indicated by the maximum solid particle temperature.

Specific power (W/kg)	Maximum particle temperature (K)		
	Particle diameter (mm)		
	1	2	3
150	1587*	1008	
200	1699*,**	1837*,***	729
250			1250

*   No dryout. Values given for the time of 5000 s.
**   Probably given for the time of 4000 s (cf., Figure 4). The correct value is about 2050 K (cf., Figure 2).
*** Probably a typing error in the table of Yakush & Kudinov (2014). The correct value is about 1650 K, cf., Figure 2).

Table 3. Truncated-cone-shaped debris bed cases studied at KTH (Yakush & Kudinov 2014). The computed cases are indicated by the maximum solid particle temperature.

Specific power (W/kg)	Maximum particle temperature (K)		
	Particle diameter (mm)		
	1	2	3
150	1537*	710	
200	1978*	1557*	496
250	2387*	2250*	1005

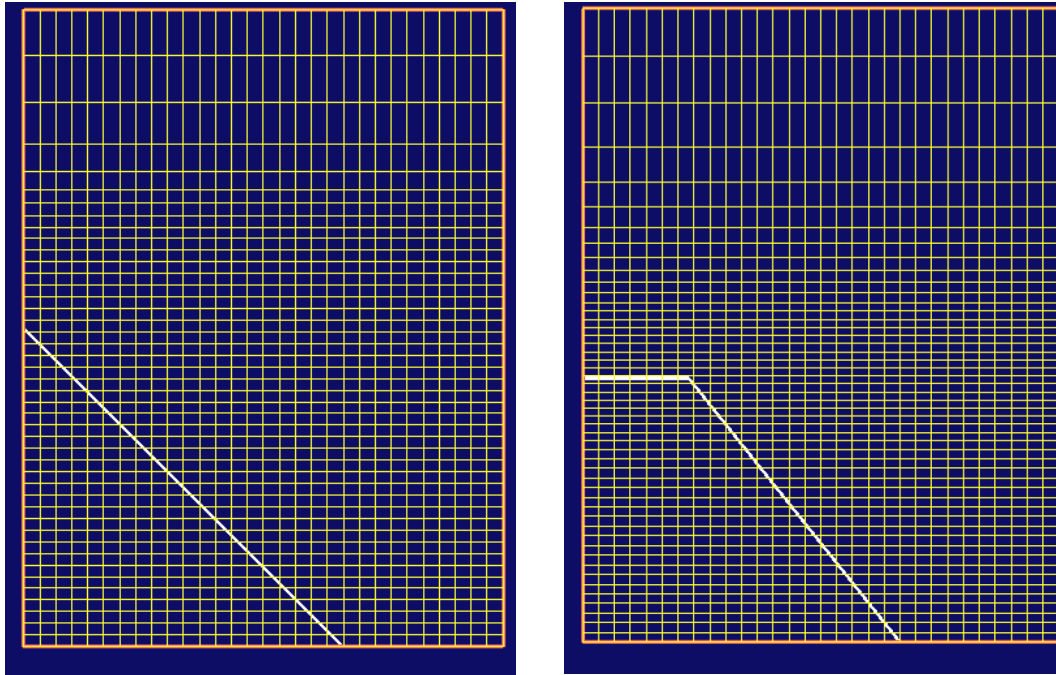*   No dryout. Values given for the time of 5000 s.

Figure 1. Computational domains, meshes and bed shapes (the white lines) for the conical (left) and truncated-cone-shaped (right) debris beds in the study of Yakush & Kudinov (2014).

2.2.2 DECOSIM results of Yakush & Kudinov

Yakush & Kudinov (2014) report the results of the DECOSIM simulations for the conical and truncated-cone-shaped debris beds. Some of the results needed in the comparison studies are introduced in following.

Figure 2, Figure 3, Figure 4, Figure 5, Table 1 and Table 2 summarize the main results of the DECOSIM simulations (Yakush & Kudinov 2014). The maximum particle temperature as a function of time is presented in Figure 2 and Figure 3. In the 1 mm particle cases, the maximum particle temperature increases without stabilization as a function of time with an almost constant, power-specific rate. In the cases of the 3 mm particles, the maximum particle temperature stabilizes or almost stabilizes to heating-power dependent values at least in 5000 s. In the beds of the 2 mm particles, the evolution of the maximum temperature depends on the heating power. In all 2 mm cases, the maximum particle temperature increases first almost with the same rate as in the 1 mm particle cases with the same heating power but later on the temperature increase rate decreases and in the lowest-power cases the steady-state conditions would likely be reached if the simulations had continued further.

Figure 4 shows distributions of the void fraction and temperature of the solid bed particles at the time of 4000 s in the cases of the specific power equal to 200 W/kg. In the 1 and 2 mm particle cases, the steady-state conditions have not been reached (c.f., Figure 2). The results for the 3 mm particles in Figure 4 are for a steady-state but the dry area is very small in this case.

The void fraction and temperature of the solid bed particles in truncated-cone-shaped beds are depicted in Figure 5 at the time of 4000 s in three cases: 1 mm particles with the specific power of 200 W/kg and 3 mm particles with the specific power equal to 200 and 250 W/kg. The 1 mm particle plots are not steady-state results (cf., Figure 3). In the 3 mm case with the lower heating power, the dry area is very small.
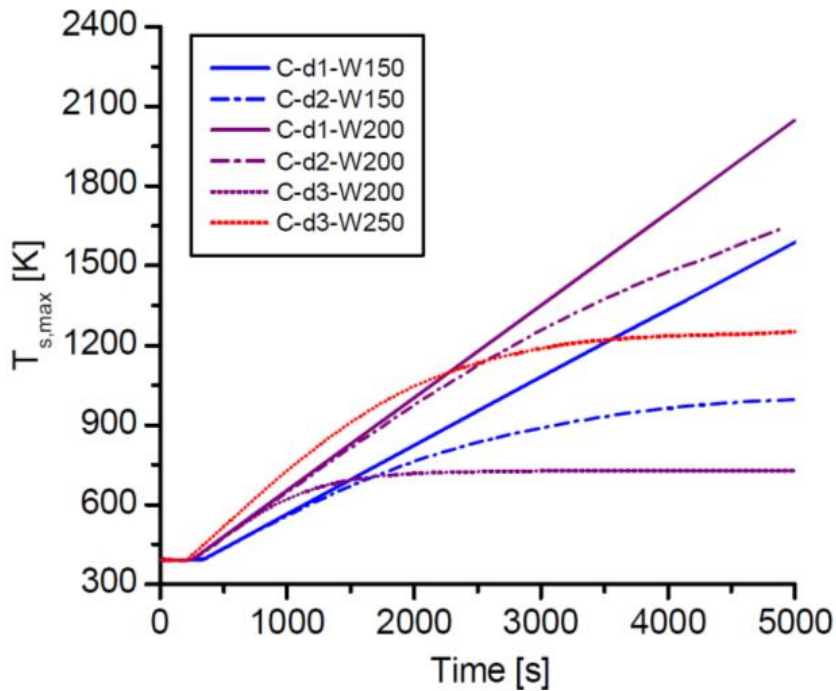
Figure 2. Maximum solid particle temperature as a function of time in the DECOSIM simulations for conical beds (Yakush & Kudinov 2014). In the legend, the particle diameter in mm is given by the number after "d" and the specific heating power in W/kg by the number after "W".
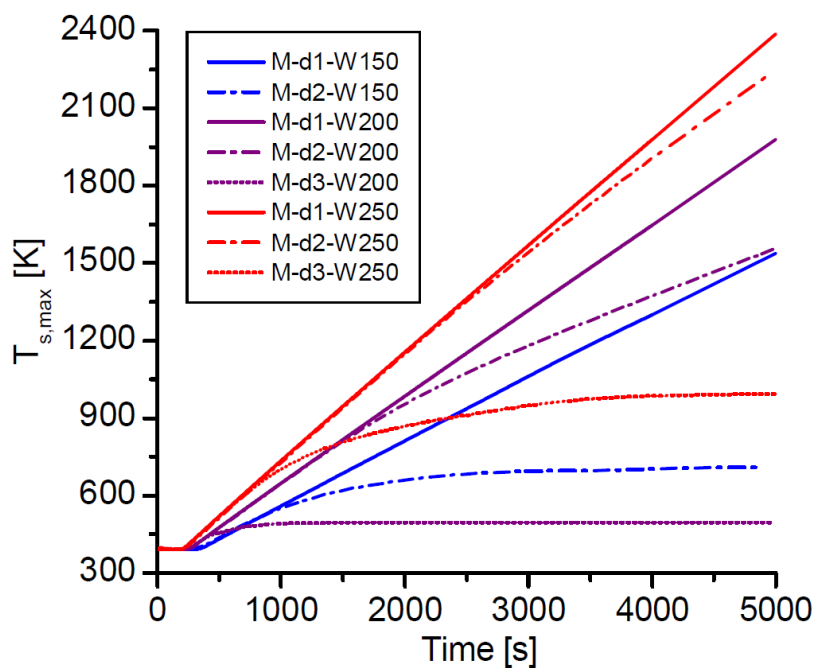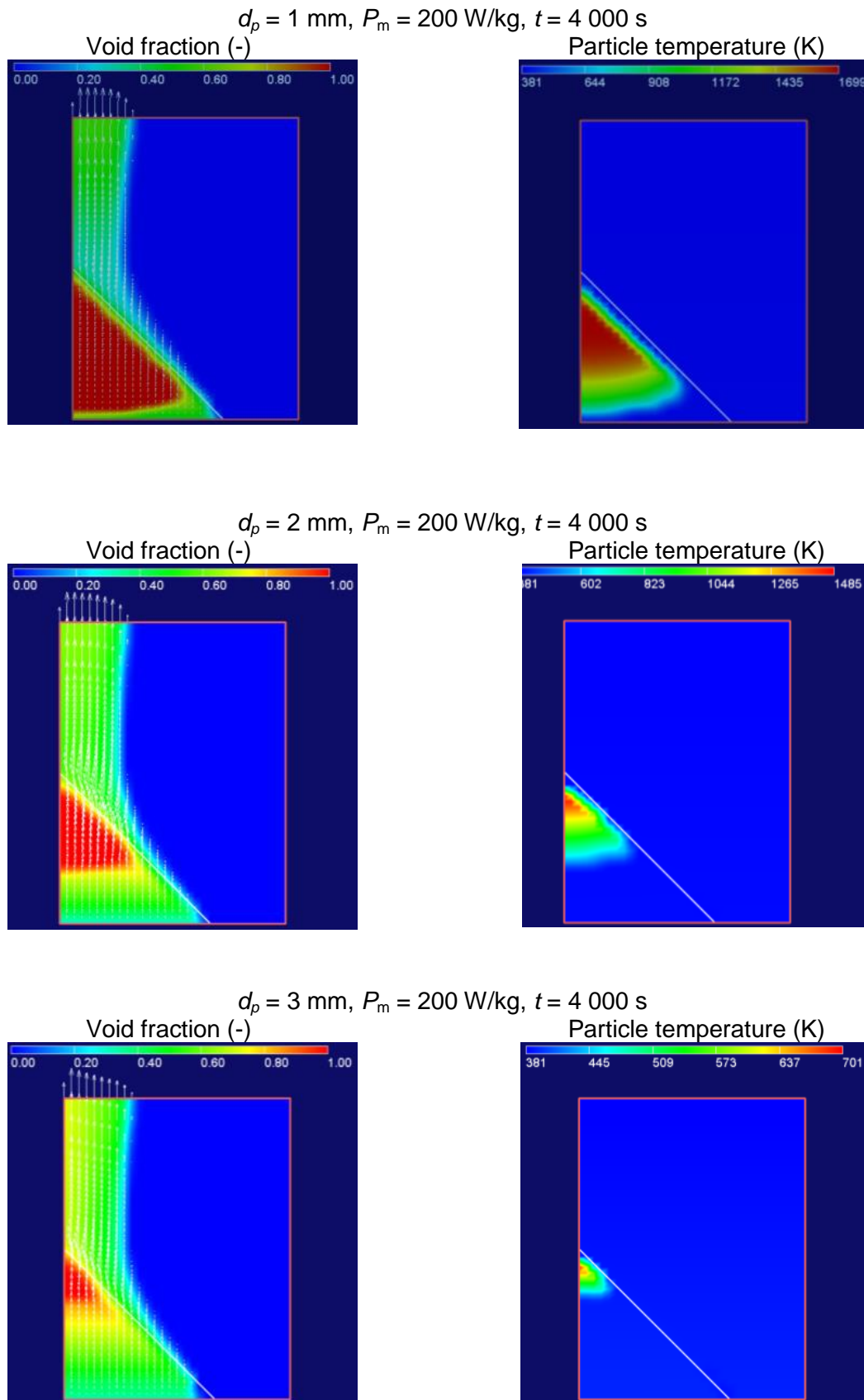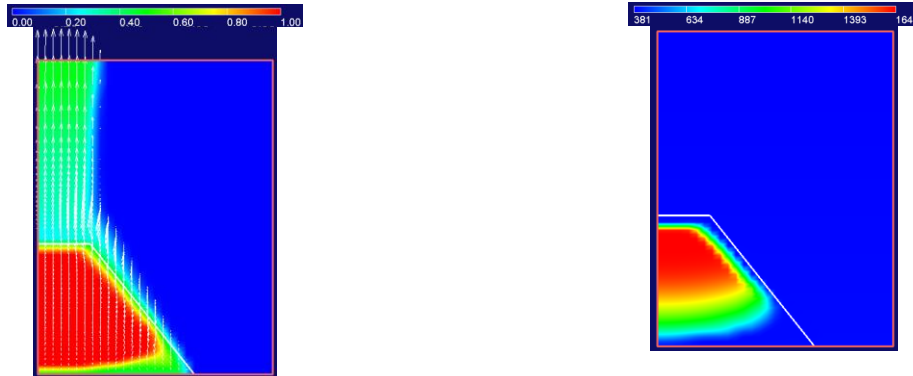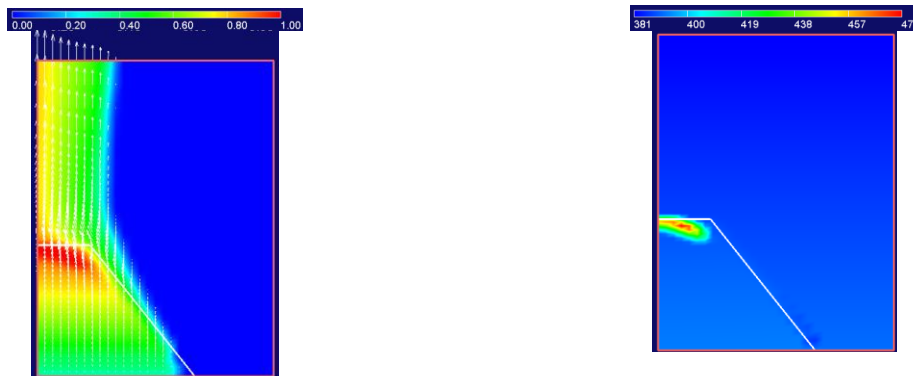

Figure 3. Maximum solid particle temperature as a function of time in the DECOSIM simulations for truncated-cone-shaped beds (Yakush & Kudinov 2014). In the legend, the particle diameter in mm is given by the number after "d" and the specific heating power in W/kg by the number after "W".
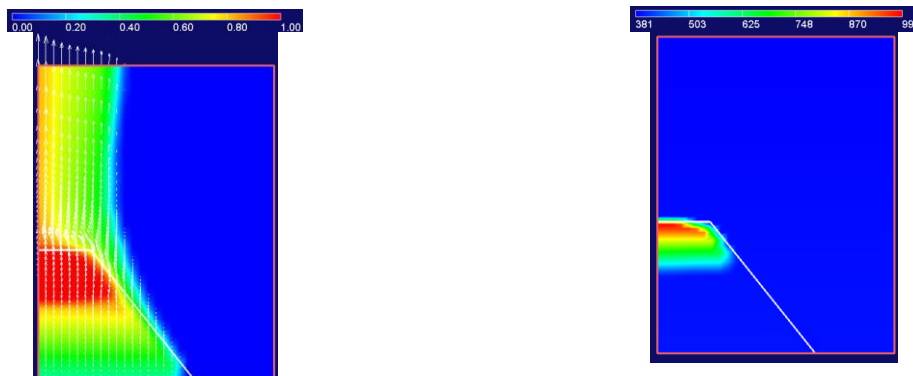
Figure 4. Void fraction (left) and solid particle temperature (right) in the DECOSIM simulations at the time of 4000 s for the conical beds of 1, 2 and 3 mm particles with the specific power equal to 200 W/kg (Yakush & Kudinov 2014).

d_p = 1 mm, P_m = 200 W/kg, t = 4 000 s

Void fraction (-)	Particle temperature (K)
0 – 1	381 – 1646

d_p = 3 mm, P_m = 200 W/kg, t = 4 000 s

Void fraction (-)	Particle temperature (K)
0 – 1	381 – 476

d_p = 3 mm, P_m = 250 W/kg, t = 4 000 s

Void fraction (-)	Particle temperature (K)
0 – 1	381 – 992

Figure 5. Void fraction (left) and solid particle temperature (right) in the DECOSIM simulations at the time of 4000 s for the truncated-cone-shaped beds of 1 mm particles with the specific power equal to 200 W/kg as well as of 3 mm particles with the specific power equal to 200 and 250 W/kg (Yakush & Kudinov 2014).

3. On the MEWA code

3.1 General

A detailed description of the updated models in the MEWA code is given by Rahman (2013). This report concentrates on the models considered of primary importance in modelling post-dryout conditions in a heated, idealised particle bed. The MEWA version dated 6.3.2014 was used in this study and is identified as MEWA2014.

The MEWA code was recently validated by Huang and Ma (2018). Interestingly, the results for the Reed friction model were found to be in a good agreement with the experimental results. Unfortunately, it is not documented which version of the MEWA code was used in the validation study.

3.2 Conservation equations

A drying debris bed is hydrodynamically a three-phase problem. In most numerical simulations, the solid phase of particles is taken into account applying the porous medium approach considering the liquid and gas phases as continuous fluids. In MEWA, two-dimensional Cartesian cylindrical coordinate systems are used in numerical formulations.

The mass conservation equations solved in MEWA are (Rahman 2013)

$$\varepsilon \frac{\partial}{\partial t}(\alpha_i \rho_i) + \nabla \cdot (\varepsilon \alpha_i \rho_i \vec{v}_i) = (-1)^{(1+\delta_{ig})} \Gamma \tag{1}$$

where ε is the porosity (-), α_i is the volume fraction of the phase i (for the gas phase: $i=g$, for the liquid phase: $i=l$), ρ_i is the phase (material) density (kg/m^3), $\vec{v}_i$ is phase (pore) velocity (m/s), δ_{ig} is the Kronecker delta (-) and Γ is the mass source term due to evaporation (kg/m^3/s).

Simplified forms of the momentum equations are solved in MEWA. The convective and viscous stress terms are ignored and the momentum equations are written as follows (Rahman 2013):

$$0 = -\nabla p_i + \rho_i \vec{g} - \vec{F}_{s,i} - (-1)^{(1+\delta_{ig})} \frac{\vec{F}_i}{\alpha_i} \tag{2}$$

where p_i is the pressure of the phase (Pa), g is the gravitational acceleration (m/s^2), $\vec{F}_{s,i}$ if the drag force between the solid particles and a fluid phase i (kg/m^{2}s^2) and $\vec{F}_i$ is the interfacial drag force between the fluid phases (kg/m^{2}s^2). (The inertial term is missing in Eq. (2) consistent with the MEWA documentation (Bürger et al. 2006, Rahman 2013). In the MEWA code, the time-dependent term is included.)

The energy conservation equation for the fluid phases is (Rahman, 2013):

$$\varepsilon \frac{\partial}{\partial t}(\alpha_i \rho_i e_i) + \nabla \cdot (\varepsilon \alpha_i \rho_i \vec{v}_i h_i) = \nabla \cdot (\lambda_{i,eff} \nabla T_i) + Q_{s,i} + (-1)^{(1+\delta_{ig})} \Gamma h_{i,sat} \tag{3}$$

where e_i is the specific internal energy of the phase i (J/kg), h_i is the specific internal enthalpy of the phase i (J/kg), $h_{i,sat}$ is the specific enthalpy of the phase i at saturation (J/kg), $\lambda_{i,\text{eff}}$ is the effective thermal conductivity of the phase i (W/m·K), T_i is the phase temperature

(K) and $Q_{s,i}$ is the heat flux from the solid phase to the fluid phase i (W/m^3). The effective thermal conductivity $\lambda_{i,eff}$ (W/m/K) is calculated from the phase thermal conductivity, $\lambda_{i,eff} = \lambda_i \varepsilon \alpha_i$.

In MEWA, the temperature of the bed particles is computed by solving the energy balance equation for the solid phase (Rahman, 2013):

$$\frac{\partial}{\partial t}[(1-\varepsilon)\rho_s e_s] = \nabla \cdot (\lambda_{s,eff} \nabla T_s) + Q_{decay} - Q_{s,sat} - Q_{s,g} - Q_{s,l} \tag{4}$$

where ρ_s is the density of solid particles (kg/m^3), e_s is the specific internal energy of solid particles (J/kg), $\lambda_{s,eff}$ is the effective thermal conductivity of the solid particles (W/m·K) and T_s is the temperature of the solid particles (K). Q_{decay} (W/m^3) represents the internal (decay) heat generation in the solid particles. $Q_{s,sat}$, $Q_{s,g}$ and $Q_{s,l}$ (W/m^3) are the sources of heat due to the boiling at the particle surfaces (*sat*) as well as of the heat transfer rate from the particles to the gas (*g*) and liquid (*l*) phases, respectively. Since the focus of this study is on the post-dryout behaviour, in the conditions of the main interest the solid particles are in contact with the gas phase. Accordingly, boiling and heat transfer from the solid particles directly to the liquid phase are less important.

3.3 Closure models

3.3.1 Friction force models

A detailed discussion on the friction models of MEWA can be found in Rahman (2013).

In the MEWA code, the drag force between the solid particles and a fluid phase is calculated from the following formulation

$$\vec{F}_{s,i} = \frac{\varepsilon \alpha_i \mu_i}{K K_{r,i}} \vec{v_i} + \frac{\varepsilon^2 \alpha_i^2 \rho_i}{\eta \eta_{r,i}} |\vec{v_i}| \vec{v_i} \tag{5}$$

where the permeability K and passability η describe the capability of a porous medium to transmit fluid. They are expressed according to Ergun (1952) as follows

$$K = \frac{\varepsilon^3 {d_p}^2}{150(1-\varepsilon)^2} \tag{6}$$

$$\eta = \frac{\varepsilon^3 d_p}{1.75(1-\varepsilon)}. \tag{7}$$

where d_p is the bed particle diameter.

The presence of the other fluid phase in the two-phase flow is taken into account in the relative permeability $K_{r,i}$ (-) and relative passability $\eta_{r,i}$ (-) which are functions of the phase volume fraction

$$K_{r,i} = \alpha_i^n \tag{8}$$

$$\eta_{r,i} = \alpha_i^m. \tag{9}$$

3.3.1.1 Classical friction models

There are several models for the relative permeability and passability. The powers *n* and *m* vary and depend on the respective experiments. For the relative permeability, *n = 3* is typically used. For the relative passability, Lipinski (1982) suggested originally *m = 3*. Reed (1982) proposed *m = 5* which yields a somewhat increased friction and was later on used also by Lipinski (1984). In the model of Hu and Theofanous (1991), *m* was increased to 6. These three classical models differ from each other only in the relative passability with no explicit consideration of the gas-liquid drag (i.e., $\vec{F}_i = 0$ in Eq. (2)). As the empirical models aim to describe the total pressure loss, the gas-liquid drag is thus implicitly included in the models.

3.3.1.2 Friction model of Tung and Dhir

To take explicitly into account the interfacial drag term $\vec{F}_i$, Tung and Dhir (1988) developed a detailed model in which the drag coefficients are calculated according to the flow regimes. The flow regimes are given in Table *4* and in Figure 6. The upper boundary of the bubble flow regime looks odd and originates from the fact that Tung & Dhir (1988) considered only large particle cases, in which "pore size is much larger than the bubble diameter".

The bubble diameter is calculated as follows (Rahman, 2013)

$$d_b = 1.35 \sqrt{\frac{\sigma}{g(\rho_l - \rho_g)}}, \tag{10}$$

where σ is the surface tension of water. The diameter of droplets is calculated from the same formula.

The relative permeability and passability for the liquid phase are

$$K_{r,l} = \alpha_l^3, \eta_{r,l} = \alpha_l^3, \tag{11}$$

Table 4. Flow regimes in the friction model of Tung and Dhir in the MEWA code (Rahman 2013).

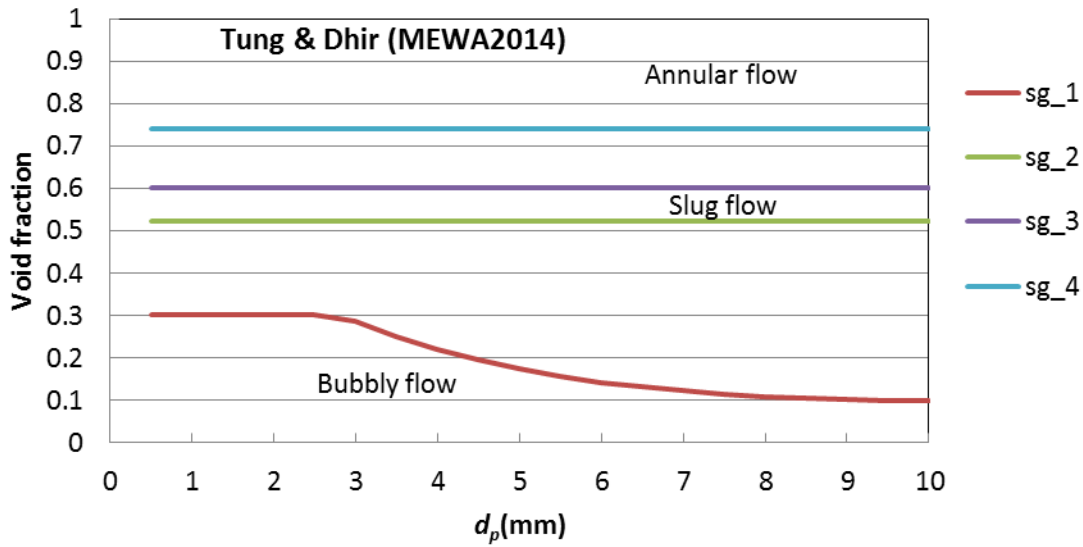|	Flow regime	Void fraction range
Liquid continuous	Low void bubbly	$\alpha_g \le \alpha_{g,0};\quad \alpha_{g,0} = MAX\left[0., \frac{\pi(1-\varepsilon)}{3\varepsilon}\gamma(1+\gamma)\big(6\beta - 5(1+\gamma)\big)\right]$ $\gamma = \frac{d_b}{d_p};\quad \beta = \left[\frac{\sqrt{2}\,\pi}{6(1-\varepsilon)}\right]^{1/3}$
	High void bubbly	$\alpha_{g,0} < \alpha_g \le \alpha_{g,1}; \alpha_{g,1} = MIN[0.3, 0.6(1-\gamma)^2]$
	Transition	$\alpha_{g,1} < \alpha_g \le \frac{\pi}{6}$
	Slug flow	$\frac{\pi}{6} < \alpha_g \le 0.6$
Transition	Transition	$0.6 < \alpha_g \le \frac{\sqrt{2}\,\pi}{6}$
Gas continuous	Annular flow	$\alpha_g > \frac{\sqrt{2}\,\pi}{6}$

Figure 6. Flow regimes for the Tung and Dhir (Rahman 2013). (For the conditions at the top of the particle bed.)

In case of the gas phase, the relative permeability and passability are formulated differently for flow regimes of continuous gas and continuous liquid flows. In bubbly and slug flows ($\alpha_g < 0.6$), the relative permeability and passability for the gas phase are as follows

$$K_{r,g} = \alpha_g^3 \left(\frac{1-\varepsilon}{1-\alpha_g\varepsilon}\right)^{\frac{4}{3}}, \qquad \eta_{r,g} = \alpha_g^3 \left(\frac{1-\varepsilon}{1-\alpha_g\varepsilon}\right)^{\frac{2}{3}}. \tag{12}$$

In annular flows ($\alpha_g > \frac{\sqrt{2}\,\pi}{6} \approx 0.74$), the following expressions are applied:

$$K_{r,g} = \alpha_g^2 \left(\frac{1-\varepsilon}{1-\alpha_g\varepsilon}\right)^{\frac{4}{3}}, \qquad \eta_{r,g} = \alpha_g^2 \left(\frac{1-\varepsilon}{1-\alpha_g\varepsilon}\right)^{\frac{2}{3}}. \tag{13}$$

In the transition region ($0.6 < \alpha_g < \frac{\sqrt{2}\,\pi}{6}$), the friction coefficient for the gas phase is interpolated.

The interfacial drag force between the gas and liquid phase are determined differently for each flow regime. The interfacial drag force is calculated from the friction coefficients $K_{g,l}$ given in Table 5 by multiplying with the velocity difference

$$\vec{F}_i = K_{g,l}(\vec{v}_g - \vec{v}_l). \tag{14}$$

3.3.1.3 Modified Tung and Dhir friction model

The Tung and Dhir friction model is not working satisfactorily in pure top-flooding cases. This is not unexpected in case of small particles, since the Tung and Dhir model was not developed for those conditions. Therefore, some modifications have been proposed. A modification was made by Schmidt (2007) but it is not available in the standard MEWA code. It was however used in the DECOSIM simulations discussed in Section 2. The Schmidt version of the modified Tung and Dhir friction model is introduced in Section 4.

Table 5. Drag force between the gas and liquid phases in the model of Tung and Dhir in the MEWA code *(Rahman 2013).*

	Flow regime	Void fraction range
Liquid continuous	Low void bubbly	$K_{g,l} = 18 \dfrac{1+\gamma}{2} ln\left(1+\dfrac{2}{\gamma}\right)\dfrac{\alpha_g\alpha_l\mu_l}{d_b^2}$ $+ 0.34\left[\dfrac{1+\gamma}{2}ln\left(1+\dfrac{2}{\gamma}\right)\right]^2 \alpha_g\alpha_l^5 \dfrac{\alpha_g\rho_g+\alpha_l\rho_l}{d_b}\, \big\lvert\vec{v}_g$ $- \vec{v}_l\big\rvert$
	High void bubbly	$K_{g,l} = 18\left[\alpha_{g,0}\dfrac{1+\gamma}{2}ln\left(1+\dfrac{2}{\gamma}\right)+\alpha_g-\alpha_{g,0}\right]\dfrac{\alpha_l\mu_l}{d_b^2}$ $+ 0.34\left\{\alpha_{g,0}\left[\dfrac{1+\gamma}{2}ln\left(1+\dfrac{2}{\gamma}\right)\right]^2 + \alpha_g\right.$ $\left.- \alpha_{g,0}\right\}\alpha_l^5 \dfrac{\alpha_g\rho_g+\alpha_l\rho_l}{d_b}\,\lvert\vec{v}_g-\vec{v}_l\rvert$
	Transition	Interpolated
	Slug flow	$K_{g,l} = 5.21\dfrac{\alpha_l\alpha_g\mu_l}{d_b^2} + 0.92\alpha_g\alpha_l^5\dfrac{\alpha_g\rho_g+\alpha_l\rho_l}{d_b}\,\lvert\vec{v}_g-\vec{v}_l\rvert$
Transition	Transition	Interpolated
Gas continuous	Annular flow	$K_{g,l} = \dfrac{\varepsilon\alpha_l\mu_g}{K\alpha_g^2}\left(\dfrac{1-\varepsilon}{1-\alpha_g\varepsilon}\right)^{-\frac{4}{3}} + \dfrac{\varepsilon^2\alpha_l\rho_g}{\eta\alpha_g}\left(\dfrac{1-\varepsilon}{1-\alpha_g\varepsilon}\right)^{-\frac{2}{3}}\lvert\vec{v}_g-\vec{v}_l\rvert$

Currently MEWA (the 2014 version) applies a different modification of the friction model of Tung and Dhir. The flow regimes in the recent MEWA version of the modified Tung and Dhir model are depicted in Figure 7 and Table 6. In the modified Tung and Dhir model of MEWA, the relative permeability and passability for the friction between the gas phase and solid particles are formulated as follows: In the liquid-continuous regime ($\alpha_g < 0.6$),

$$K_{r,g} = \alpha_g^3, \qquad \eta_{r,g} = \alpha_g^3 \tag{15}$$

and in the gas continuous regime ($\alpha_g > \frac{\sqrt{2}\,\pi}{6} \approx 0.74$),

$$K_{r,g} = \alpha_g^2, \qquad \eta_{r,g} = \alpha_g^2. \tag{16}$$

In the transition region ($0.6 < \alpha_g < \frac{\sqrt{2}\,\pi}{6}$), the friction coefficient for the gas phase is interpolated.

The relative permeability and passability for the liquid phase are

$$K_{r,l} = \alpha_l^2, \qquad \eta_{r,l} = \alpha_l^5. \tag{17}$$

The friction coefficient in Eq. (14) for the drag force between the gas and liquid phases is formulated as follows

$$K_{g,l} = K_{g,l,TD} \text{MIN} \left[1, \frac{d}{0.012\text{m}} \right] \tag{18}$$

for the bubbly and slug flows and as

$$K_{g,l} = 0.25 K_{g,l,TD} \text{MIN} \left[1, \left(\frac{d}{0.003\text{m}} \right)^3 \right] \tag{19}$$

for the annular flow regime. Here $K_{g,l,TD}$ is the interfacial drag according to the original Tung and Dhir model for the flow regime in question. (In the MEWA code used, the constant of 0.25 in Eq. (19) is 0.2 and if the porosity is at least 0.8, the interfacial drag force is ignored).

Table 6. Flow regimes in the modified Tung and Dhir model of MEWA (Rahman 2013).

|	Flow regime	Void fraction range
Liquid continuous	Low void bubbly	$\alpha_g \leq \alpha_{g,0}; \quad \alpha_{g,0} = MAX \left[0., \frac{\pi(1-\varepsilon)}{3\varepsilon} \gamma(1+\gamma)\left(6\beta - 5(1+\gamma)\right) \right]$ $\gamma = \frac{d_b}{d_p}; \quad \beta = \left[\frac{\sqrt{2}\,\pi}{6(1-\varepsilon)} \right]^{1/3}$
	High void bubbly	$\alpha_{g,0} < \alpha_g \leq \alpha_{g,1}; \quad \alpha_{g,1TD} = MIN[0.3, 0.6(1-\gamma)^2]$ $\alpha_{g,1} = MIN\left[\alpha_{g,1TD}, 400000(d_p - d_{p,0})^3 + \alpha_{g,1TD}\right]; \; d_{p,0} = 12 \text{ mm}$
	Transition	$\alpha_{g,1} < \alpha_g \leq MIN \left[\frac{\pi}{6}, 400000(d_p - d_{p,0})^3 + \frac{\pi}{6} \right]$
	Slug flow	$MIN \left[\frac{\pi}{6}, 400000(d_p - d_{p,0})^3 + \frac{\pi}{6} \right] < \alpha_g$ $\leq MIN\left[0.6, 400000(d_p - d_{p,0})^3 + 0.6 \right]$
Transition	Transition	$MIN\left[0.6, 400000(d_p - d_{p,0})^3 + 0.6 \right] < \alpha_g$ $\leq MIN \left[\frac{\sqrt{2}\,\pi}{6}, 400000(d_p - d_{p,0})^3 + \frac{\sqrt{2}\,\pi}{6} \right]$
Gas continuous	Annular flow	$\alpha_g > MIN \left[\frac{\sqrt{2}\,\pi}{6}, 400000(d_p - d_{p,0})^3 + \frac{\sqrt{2}\,\pi}{6} \right]$
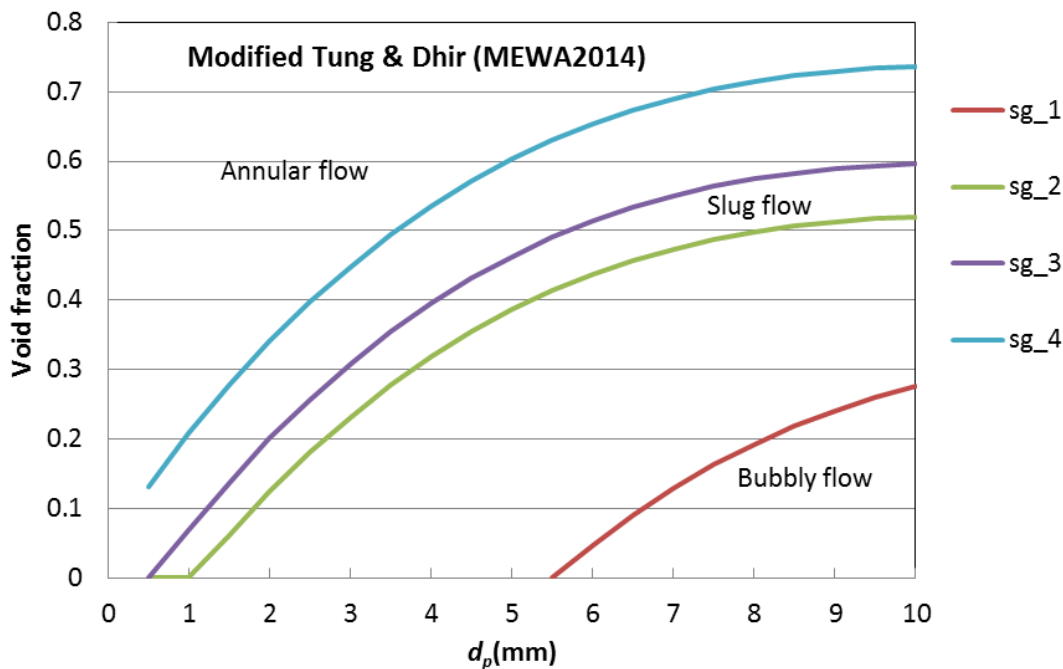
Figure 7. Flow regimes for the modified Tung and Dhir in MEWA (Rahman 2013). (For the conditions at the top of the particle bed.)

3.3.2 Heat transfer models

3.3.2.1 Effective thermal conductivity in a dry bed

The effective thermal conductivity of the solid particles $\lambda_{s,\text{eff}}$ in the energy balance equation (Equation (4)) is a bulk property, which describes macroscopically the ability of a system of two fluids and particles to conduct heat. It accounts for the combined effects of conduction through the contact points of the solid particles and through the fluids, and possibly radiation across the fluid space as well as convection and mixing in pores.

In MEWA, there are two alternative basic approaches for calculating the effective thermal conductivity for a dry bed (Taivassalo & Takasuo 2017):

(i)   The first approach is the conductivity model of Imura (Imura & Takegoshi 1974) combined with a radiation model. For the radiation model, there are three options: the Yagi (Yagi & Kunii 1957), Vortmeyer (1978) and Luikov (Luikov et al. 1968) models.

(ii)   The second approach is the Maxwell model for predicting the properties of a heterogeneous medium (Maxwell 1873, p. 365).

The Maxwell model does not include radiative heat transfer, and it is best suited for particles dispersed in a continuous medium (very large porosity). Therefore, the other conduction-radiation combinations can be considered as the primary models for calculating the effective thermal conductivity in packed low-porosity beds. In MEWA, the default model for the effective dry-bed thermal conductivity $\lambda_{s,\text{eff}}$ is the Imura conductivity model with the radiation model of Yagi. In the previous study (Taivassalo & Takasuo 2017), the influence of the thermal conductivity model was studied. In this study, the default model was applied.

3.3.2.2   Heat transfer between particles and gas

In the pre-dryout conditions, the solid particles, liquid and gas are considered to be close to a thermal equilibrium at the saturation temperature. Heat released in the solid particles is mainly used in evaporation. The heat transfer rate from the solid particles to the steam fluid becomes important close to dryout and especially after dryout, when the temperature of the solid particle increases.

In MEWA the heat transfer rate from the particles to the gas phase is given by

$$Q_{s,g} = a_{s,g} \kappa_{s,g} (T_s - T_g) \tag{20}$$

where the interfacial area density $a_{s,g}$ is given by

$$a_{s,g} = \frac{6(1-\varepsilon)}{d_p} \frac{(\alpha_g - 0.7)}{0.3} \tag{21}$$

if $\alpha_g \geq 0.7$ (continuous gas phase) otherwise $a_{s,g} = 0$. The heat transfer coefficient $\kappa_{s,g}$ (W/m²K) in Eq. (20) is calculated on the basis of the Nusselt number $Nu_{s,g}$ as follows

$$\kappa_{s,g} = \frac{Nu_{s,g} \lambda_g}{D_p} \tag{22}$$

Here λ_g is the thermal conductivity of the gas phase (W/m·K).

There are the following three alternatives in MEWA to define the heat transfer coefficient $\kappa_{s,g}$ for heat transfer from the solid particles to the gas phase. In practice, a user selects a method to determine the Nusselt number $Nu_{s,g}$.

(i)   In the default model, the Nusselt number is calculated from a simple formula

$$Nu_{s,g} = 2 + 0.6 \sqrt{\mathrm{Re}_g} \tag{23}$$

In Eq. (23), Re_g is the Reynolds number

$$\mathrm{Re}_g = \frac{|\vec{v}_g \rho_g D_p|}{\eta_g} \tag{24}$$

where $\vec{v}_g$ is the gas velocity (m/s) and η_g is the gas viscosity (Pa·s).

(ii)   The second option is the model of Gnielinski (Stephan et. al. 2010, p. 743), in which both the laminar and turbulent Nusselt numbers are

$$Nu_{s,g}^{lam} = 0.644 \sqrt{\mathrm{Re}_g} \sqrt[3]{\mathrm{Pr}_g} \tag{25}$$

$$Nu_{s,g}^{turb} = 0.037 \frac{\mathrm{Re}_g^{0.8} \mathrm{Pr}_g}{1 + 2.443 \mathrm{Re}_g^{-0.1} (\mathrm{Pr}_g^{\frac{2}{3}} - 1)} \tag{26}$$

Here Pr_g is the Prandtl number

$$\mathrm{Pr}_g = \frac{\eta_g c_{p,g}}{\lambda_g} \tag{27}$$

where $c_{p,g}$ is the specific heat capacity of the gas phase (J/kgK). The heat transfer coefficient is calculated from Eq. (22) using the Nusselt number obtained from the following formula

$$Nu_{s,g} = \left[2 + \sqrt{\left(Nu_{s,g}^{lam} \right)^2 + \left(Nu_{s,g}^{turb} \right)^2} \right] \left[1 + \frac{2}{3}(1 - \varepsilon) \right] \tag{28}$$

(iii) A user defined constant value is the third alternative to determine the Nusselt number.

This default option (i) was used in this study.

3.3.2.3 Boiling heat transfer

The local boiling rate is obtained by dividing the heat flux rate from the solid particles with the latent heat of evaporation:

$$\Gamma = \frac{Q_{s,sat}}{\Delta H_{evap}} \tag{29}$$

To calculate the boiling heat transfer coefficient, the Rohsenow correlation (Rohsenow 1952) is applied for nucleate pool boiling regime and the Lienhard correlation (Lienhard 1987) for the film boiling regime (with transition zone calculated by an interpolation function).

4. Implementation of the Schmidt version of the modified Tung and Dhir model

The Schmidt (2007) version of the modified Tung and Dhir friction model, shortly the Schmidt (friction) model, was used in the DECOSIM simulations discussed in Section 2. Previously the Schmidt model was implemented in the Fluent implementation of the debris coolability models (Taivassalo 2018). Since the Fluent results with the Schmidt model were in the best agreement with the DECOSIM simulations, it was decided to implement the Schmidt friction model also in the MEWA code.

The flow regime map for the Schmidt model is shown in Figure 8. In the range of 1 – 3 mm particles, the flow is mostly either annular or in the transition from slug flow to annular flow. There are thus significant differences compared to the Tung and Dhir friction model and the modified Tung and Dhir friction model in MEWA (Figure 6 and Figure 7). For the relative permeability and relative passability, the formulas of the Tung and Dhir model are used as such for the bubbly and slug flows as well as for the annular flows (Eqs. (12) and (13)). However, Schmidt (2007) does not consider the transition region between the slug flow and annular flow regimes. The same interpolation formula which is used with other friction models in MEWA is applied also with the Schmidt model.

Schmidt (2007) modified also the interfacial drag term $\vec{F}_i$ to increase the capability of the model to predict dryout heat flux in both the top and bottom flooding conditions. In the annular flow regime, the interfacial drag force $\vec{F}_i$ is calculated from the following formula

$$\vec{F}_i = \left[\frac{\varepsilon \alpha_l \mu_g}{KK_{rg}} \vec{v_r} + \frac{\varepsilon^2 \alpha_l \alpha_g \rho_g}{\eta \eta_{rg}} |\vec{v_l}| \vec{v_l} \right] \alpha_l^2 \cdot \text{MIN} \left[1, \left(\frac{d_p}{0.006\text{m}} \right)^2 \right] \tag{30}$$

In the other flow regimes, the formulations of the Tung and Dhir friction model in Table 5 are applied.

The bubble diameter is calculated as follows (Schmidt 2007)

$$d_b = MIN\left(1.35\sqrt{\frac{\sigma}{g(\rho_l - \rho_g)}}, 0.41d_p\right),$$

(31)

where σ is the surface tension of water. The diameter of droplets is assumed to be the same as indicated by Schmidt (2007).
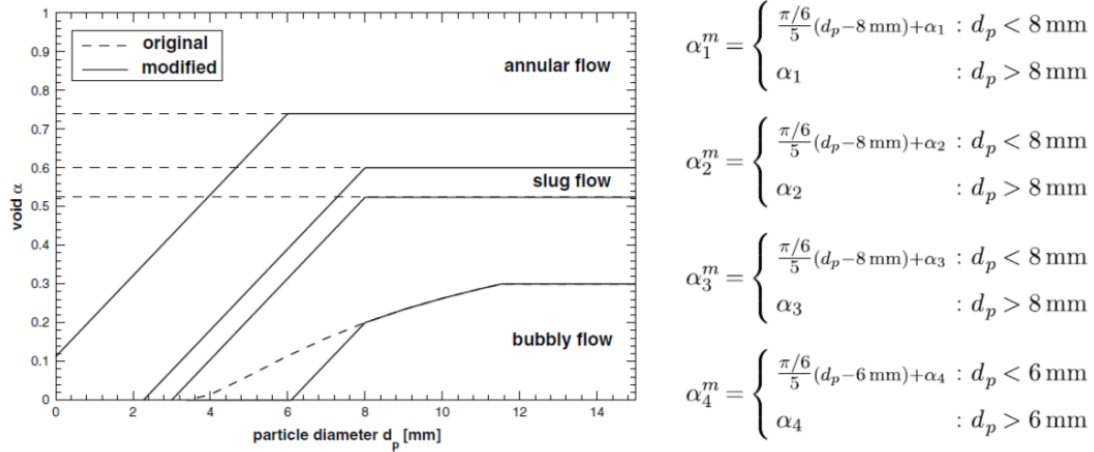

$$\alpha_1^m = \begin{cases} \frac{\pi/6}{5}(d_p - 8\,\text{mm}) + \alpha_1 & : d_p < 8\,\text{mm} \\ \alpha_1 & : d_p > 8\,\text{mm} \end{cases}$$

$$\alpha_2^m = \begin{cases} \frac{\pi/6}{5}(d_p - 8\,\text{mm}) + \alpha_2 & : d_p < 8\,\text{mm} \\ \alpha_2 & : d_p > 8\,\text{mm} \end{cases}$$

$$\alpha_3^m = \begin{cases} \frac{\pi/6}{5}(d_p - 8\,\text{mm}) + \alpha_3 & : d_p < 8\,\text{mm} \\ \alpha_3 & : d_p > 8\,\text{mm} \end{cases}$$

$$\alpha_4^m = \begin{cases} \frac{\pi/6}{5}(d_p - 6\,\text{mm}) + \alpha_4 & : d_p < 6\,\text{mm} \\ \alpha_4 & : d_p > 6\,\text{mm} \end{cases}$$

Figure 8. Flow regime map in the Schmidt version of the modified Tung and Dhir friction model (Schmidt 2007).

5. MEWA simulations

5.1 Computational cases

The computational domains and spatial discretizations with the (ideal) shapes of the analysed beds are shown in Figure 9 and Figure 10. The dimensions are given in Table 1. The domains and meshes are axisymmetric with respect to the vertical symmetry axis of the beds (on the left). The DECOSIM meshes are also presented in Figure 9 and Figure 10 for comparison. The MEWA meshes are very similar to the meshes applied in the DECOSIM simulations. In the radial direction, the mesh features 30 columns of 15 cm cells. Vertically there are 51 cell layers with a varying thickness.

The orange areas in the MEWA mesh representations in Figure 9 and Figure 10 show the domains defined as particle beds. In the MEWA computations, the cells with centres located in the orange areas are considered to represent the particle beds. The actual shapes of the heated particle beds used in numerical simulations are shown in Figure 11. In the simulations, the bed shapes follow approximatively, within the used spatial discretisation, the shapes of ideal beds.

In Figure 11 the cells are coloured according to the porosity. In the MEWA simulations, the porosity must always be less than 0.95. In this work, the porosity was assumed to be 0.9 in the cells representing the water pool outside the particle beds. In order to reduce the artificial friction forces, the particle diameter in the pool area was set to a large value of 10 mm.

MEWA simulations were performed for the same combinations of the particle size and heating power as the DECOSIM simulations and given in Table 2 and Table 3. The initial and boundary conditions and physical properties were set in the MEWA simulations consistent with the DECOSIM simulations discussed in Section 2. Especially the initial temperatures were set to slightly smaller values than the saturation temperature in the top part of the particle bed. The top surface temperature was set to the saturation temperature at the top surface pressure.

The 2014 version of the MEWA code (marked as MEWA2014) was used in the simulations. The default models were used for the effective thermal conductivity in a dry bed and for the heat transfer between the particles and the gas. The implemented (Section 4) Schmidt version of the modified Tung and Dhir model was applied for the friction forces.

Simulations were continued 5000 s of the physical time.

5.2   Conical beds

5.2.1   MEWA results

The maximum particle temperature from MEWA simulations is plotted in Figure 12 as a function of the simulation time for all the conical beds studied by Yakush & Kudinov (2014). In the 3 mm cases and in the 2 mm case with the specific power of 150 W/kg, steady states are reached in less than 2000 s and the maximum solid particle temperature stabilises to case-specific values. The 2 mm case with the higher heating power of 200 W/kg needs somewhat more than 5000 s seconds to reach a steady state. The 1 mm particle beds behave as in all previous simulations with all friction models and codes (cf., Taivassalo 2018) and the maximum particle temperature increases almost as without any cooling.

Figure 13, Figure 14 and Figure 15 show distributions of the void fraction and particle temperature at the time of about 4000 s for all conical beds. At least small dry zones are obtained in all cases. For the 1 mm particles the dry zones are still increasing. In the cases of 2 and 3 mm particles, the dry zones are larger than a few cells only for the higher specific heating powers of 200 and 250 W/kg.
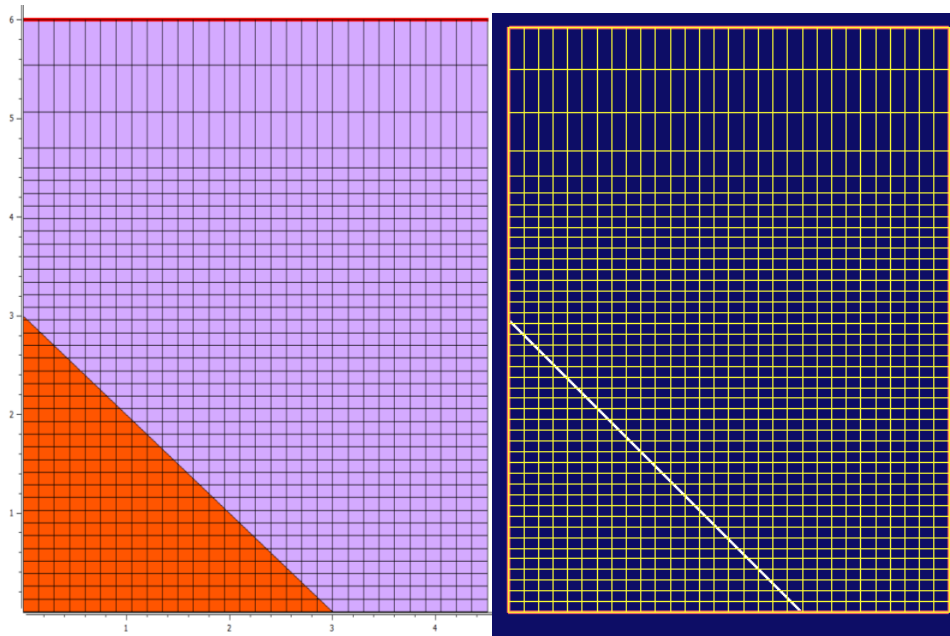
Figure 9. Computational domains, meshes and bed shapes for the conical debris beds studied computationally with MEWA in this study (left) and in the DECOSIM simulations of Yakush & Kudinov (2014) (right). The orange area represents the shape of an ideal conical particle bed.
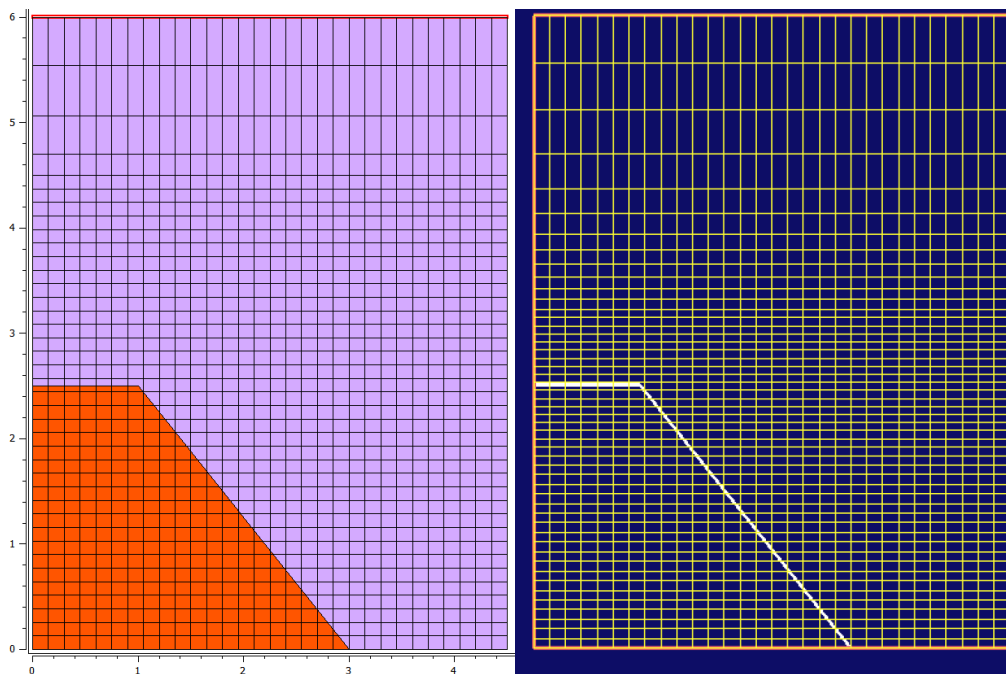
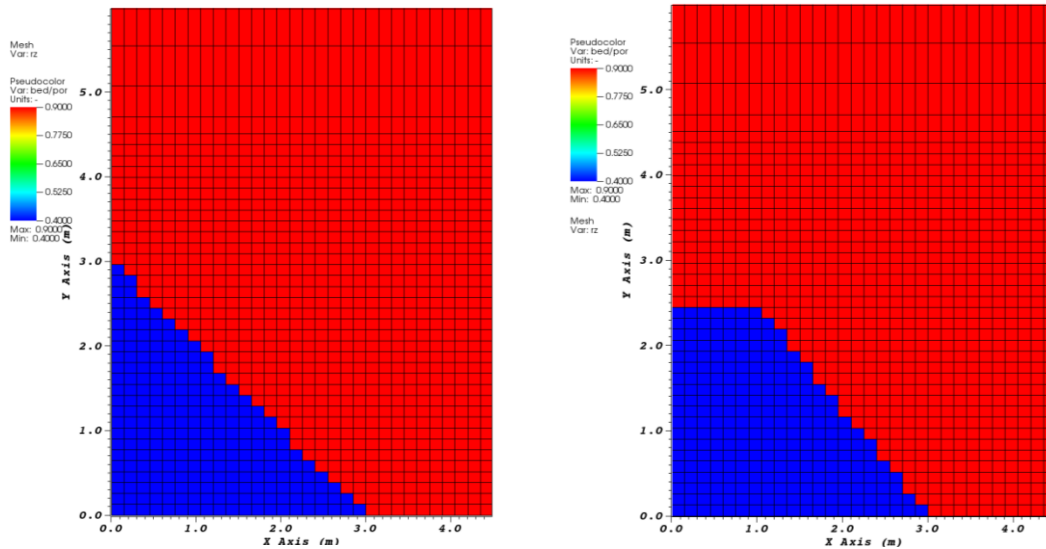Figure 10. Computational domains, meshes and bed shapes for the truncated-cone-shaped debris beds studied computationally with MEWA in this study (left) and in the DECOSIM simulations of Yakush & Kudinov (2014) (right). The orange area represents the shape of an ideal truncated-cone-shaped particle bed.

Figure 11. Actual computational shapes of the heated particle beds (the blue areas) in the MEWA simulation for the conical and truncated-cone-shaped debris beds studied at KTH (Yakush & Kudinov 2014). The cells are coloured by the porosity.

5.2.2 Comparison of the MEWA and Fluent results

The results of the MEWA simulations are compared in Figure 12, Figure 13, Figure 14 and Figure 15 to the Fluent results computed also with the Schmidt version of the modified Tung and Dhir model. The agreement is good in most cases but there are also discrepancies. Fluent solves full multiphase transport equations with the convection terms and the viscous forces and predicts an increased pressure due to the tapering flow above the bed. In fact, water penetrates into the bed not only horizontally but also downward in the tip part of the conical bed. The difference is largest for the 2 mm and the heating power of 200 W/kg (Figure 12 and Figure 14). An exception is the case of the 3 mm particles with the specific power equal to 250 W/kg; in this case the topmost cell dries in the MEWA simulation leading to a thicker dry zone and to a higher maximum particle temperature. For the 3 mm particles with the heating power of 200 W/kg, the dry zone is especially in the MEWA simulation small (Figure 15). The tapering of flow is important when the dry zone is very small and those cases should not be emphasised.

5.2.3 Comparison of the MEWA and DECOSIM results

The Schmidt (2007) version of the modified Tung and Dhir friction model was thus applied also in the MEWA simulations as it had been applied by Yakush & Kudinov (2014) in the DECOSIM simulations. The MEWA and DECOSIM results for the time evolution of the maximum particle temperature are compared in Figure 16. Distributions of the void fraction and solid particle temperature at the time of about 4000 s are shown in Figure 17 for those conical bed cases for which contour plots are given in Yakush & Kudinov (2014). An obvious difference is that in MEWA results the flow does not taper in the water pool.

For the 1 mm particles, the agreement is good. A small difference in the maximum particle temperature curves (Figure 16) originates mainly from the differences in the initial temperature for the first 200 s where the maximum particle temperature is in the MEWA calculations somewhat lower. For larger particles, there are significant differences. Steady states are achieved in the MEWA simulations in all 2 and 3 mm particle cases and the maximum particle temperature stabilises to reasonably low values. In the DECOSIM results for 2 and 3 mm particles, the maximum particle temperature increases to significantly higher

values and a steady state is actually achieved only for 3 mm particles with the specific heating power equal to 200 W/kg.

The dry zones in Figure 17 are smaller in the MEWA results than in the DECOSIM results. Furthermore, the lowest values of the temperature ranges in the DECOSIM results (381 K) are smaller than the lowest temperatures in the MEWA simulations (407 K). (This could be just because of a preselected lower limit of the temperature range in the visualization of the DECOSIM results. In that case, in Figure 5 in the plot for 3 mm particles and 200 W/kg power, the colouring would be different if the lowest temperature were close to the lowest temperature in the MEWA simulations.)

In comparing the results of the MEWA and DECOSIM codes, the uncertainties in the implementation of the Schmidt (2007) version of the modified Tung and Dhir friction model (Section 4) should be recalled. The implementation in DECOSIM might differ from the MEWA implementation done in this study. There are also differences in boiling models and numerics.
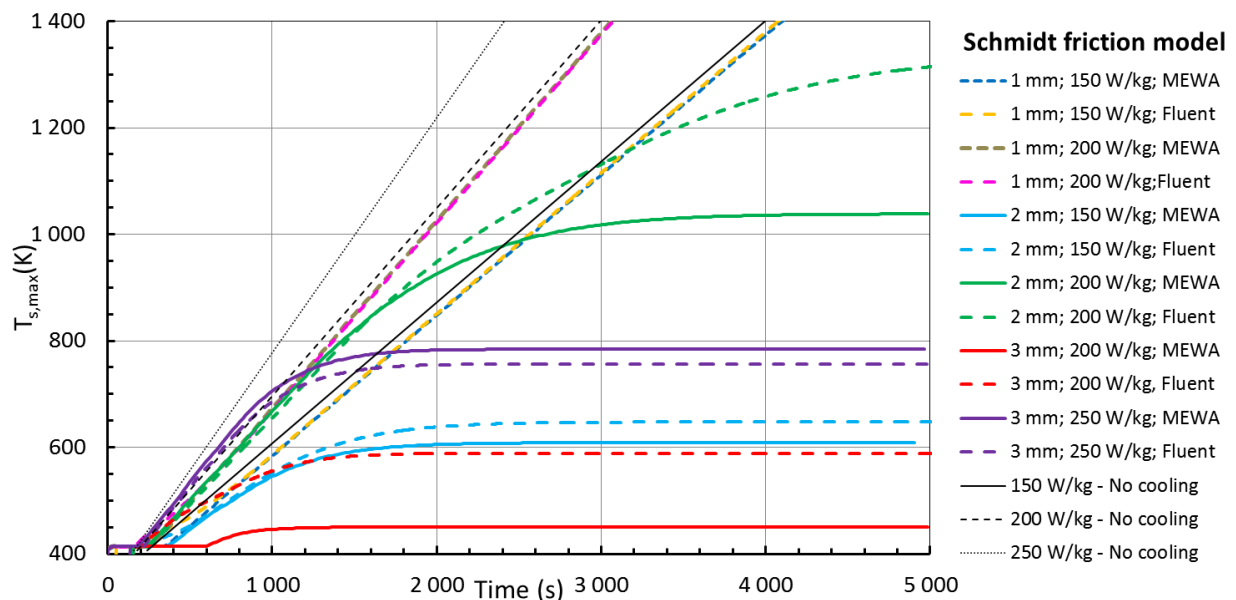
Figure 12. Comparison of the time evolution of the maximum solid particle temperature in the MEWA2014 and Fluent simulations for the conical bed cases studied by Yakush & Kudinov (2014). The Schmidt (2007) version of the modified Tung and Dhir friction model (Section 4) was used with the both codes. The "No cooling" curves show the particle temperature without any cooling phenomena. The top surface pressure is 3 bar.

p_{top} = 3 bar, d_p = 1 mm, P_m = 150 W/kg, t = 4 000 s
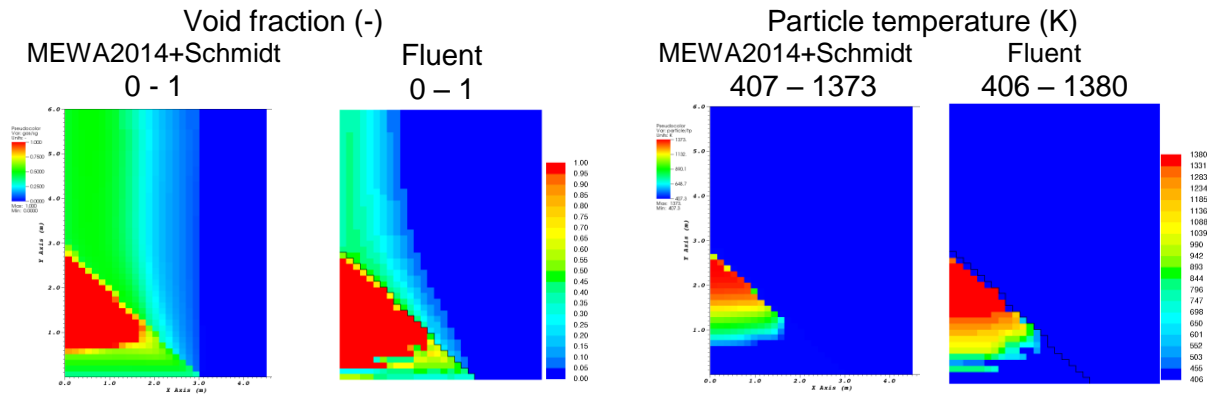
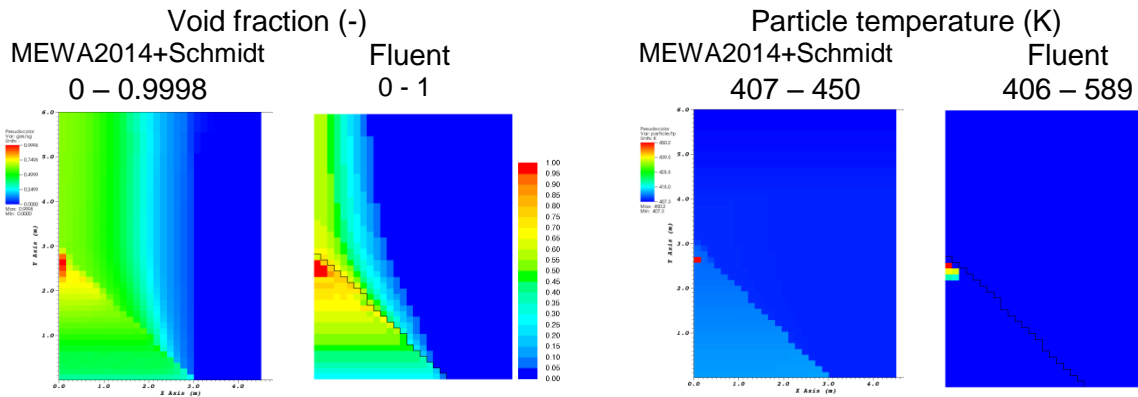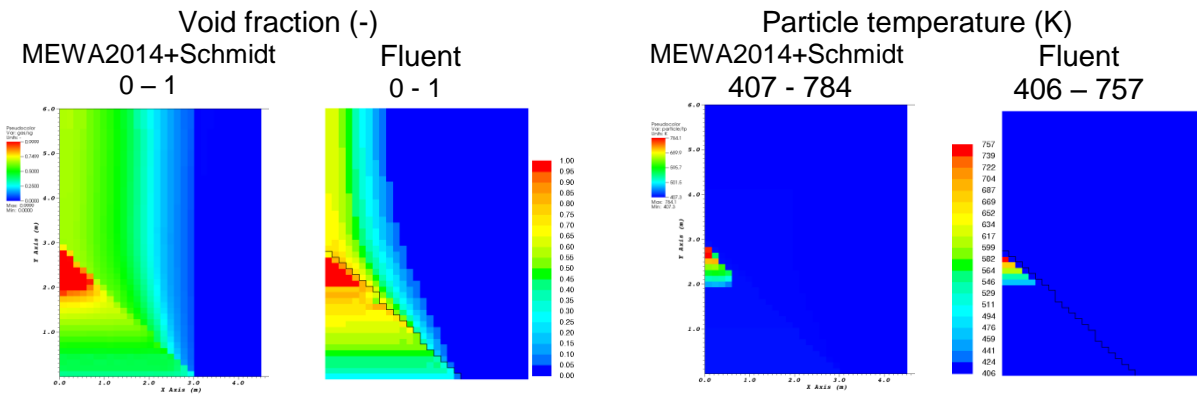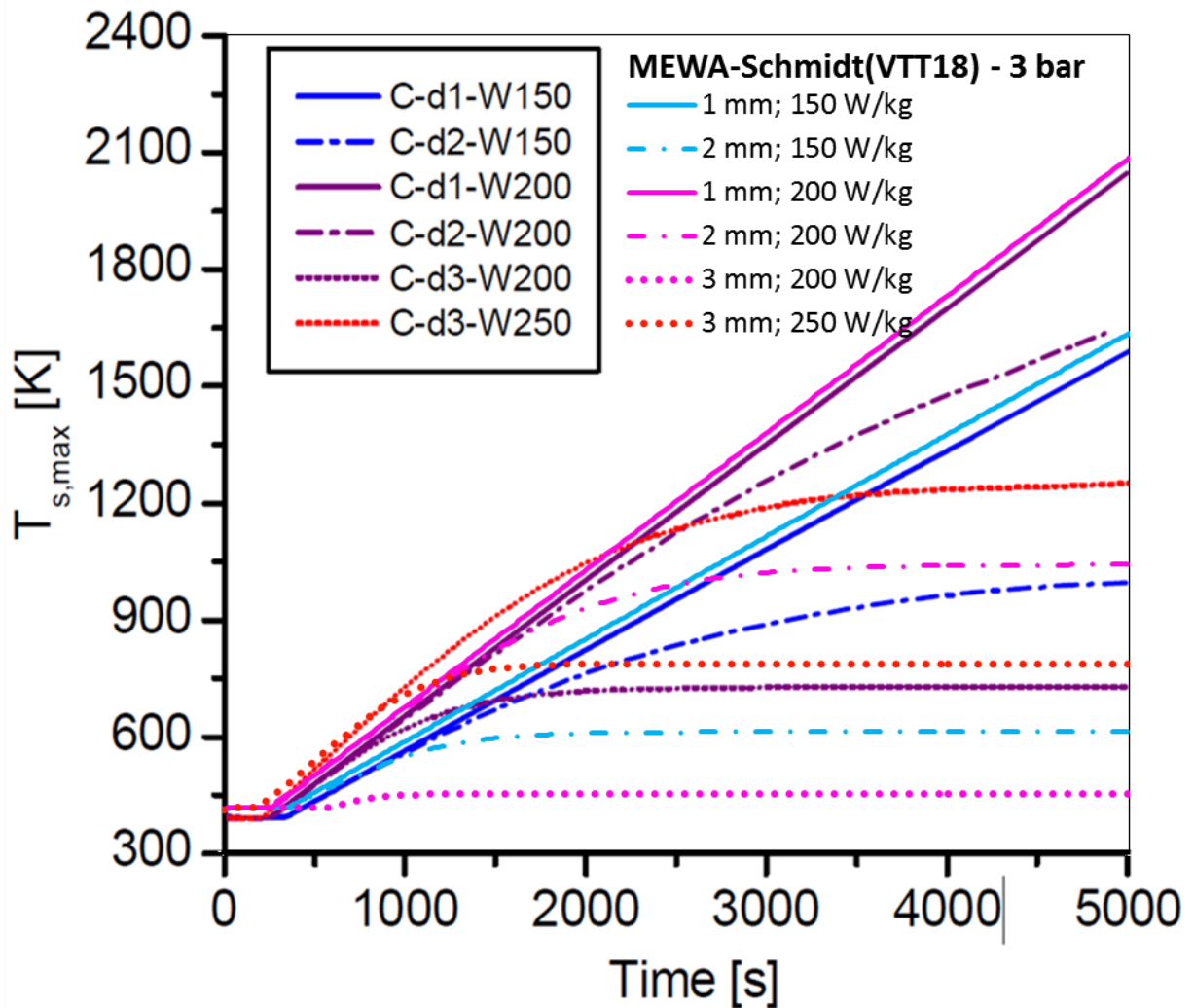p_{top} = 3 bar, d_p = 1 mm, P_m = 200 W/kg, t = 4 000 s
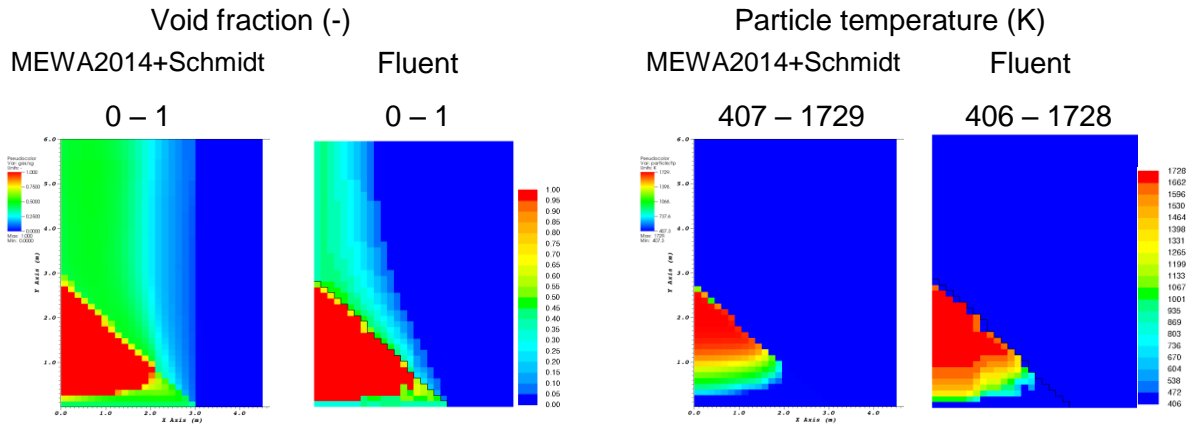
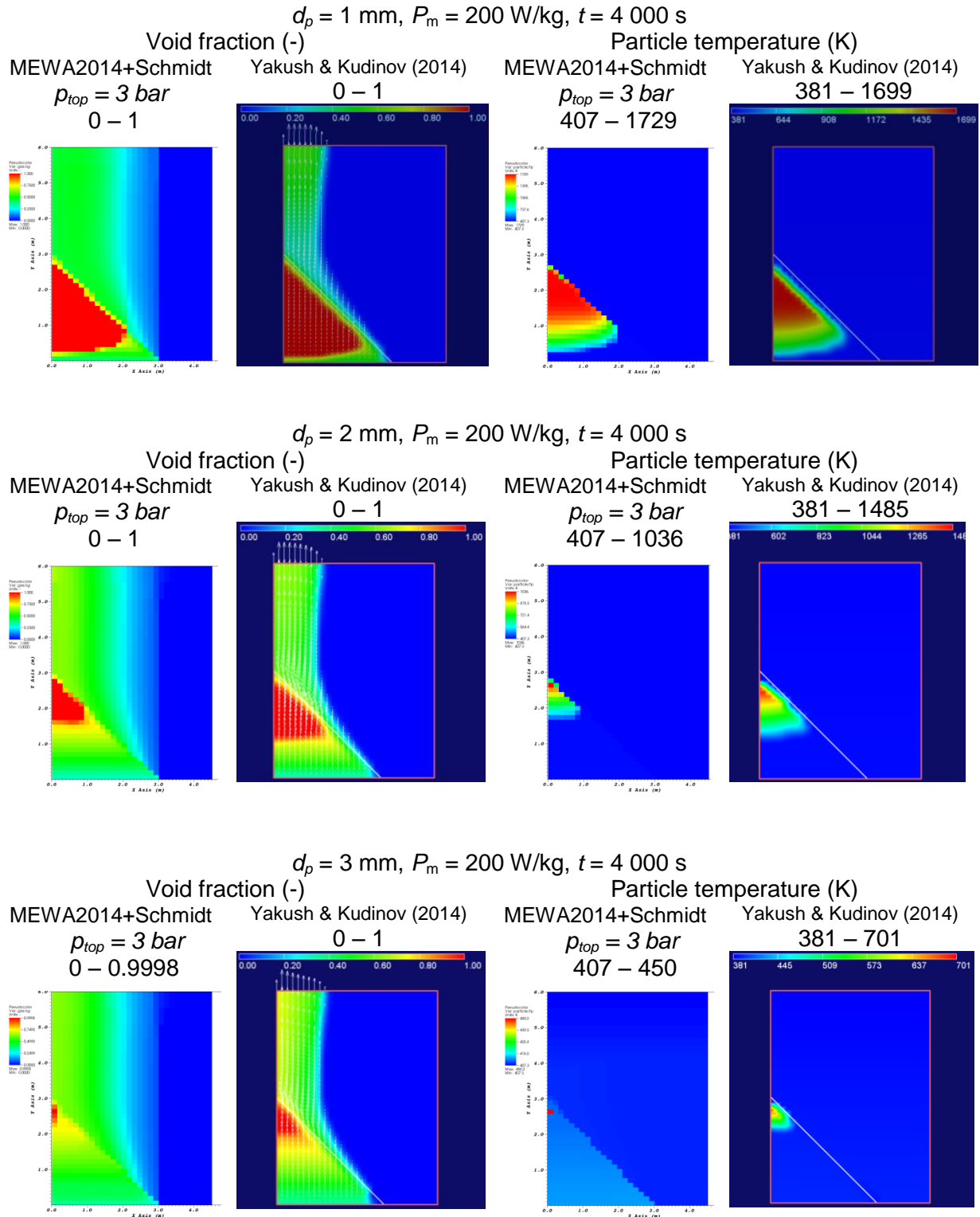*Figure 13. Void fraction (two left columns) and solid particle temperature (two right columns) at the time of 4000 s in the MEWA2014 and Fluent simulations for the conical bed of the 1 mm particles and the specific power equal to 150 and 200 W/kg studied by Yakush & Kudinov (2014). The Schmidt (2007) version of the Tung and Dhir friction model was applied. The top surface pressure is 3 bar.*

p_{top} = 3 bar, d_p = 2 mm, P_m = 150 W/kg, t = 4 000 s
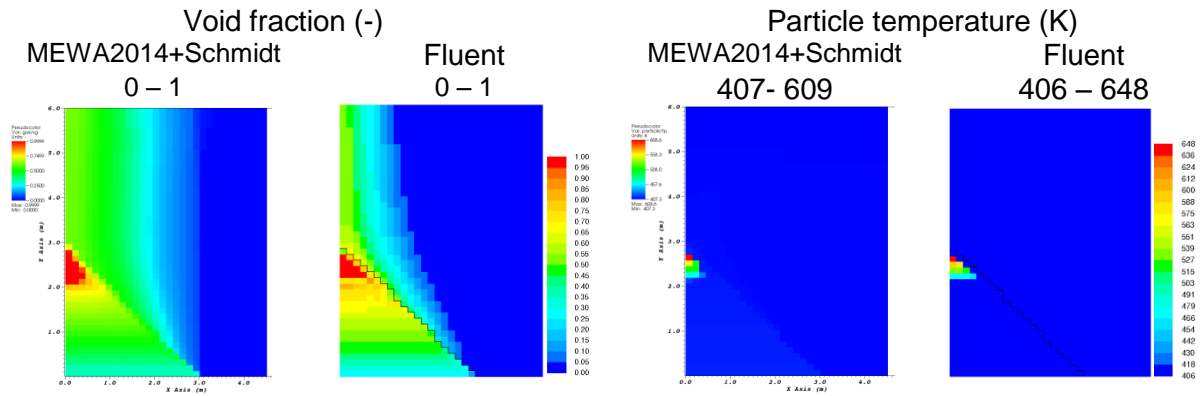
p_{top} = 3 bar, d_p = 2 mm, P_m = 200 W/kg, t = 4 000 s
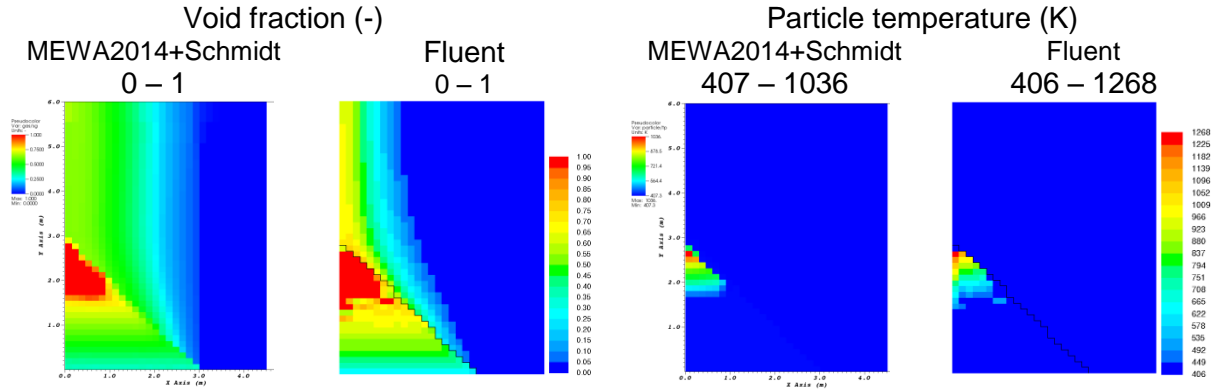
Figure 14. Void fraction (two left columns) and solid particle temperature (two right columns) at the time of 4000 s in the MEWA2014 and Fluent simulations for the conical beds of the 2 mm particles and specific power equal to 150 and 200 W/kg studied by Yakush & Kudinov (2014). The Schmidt (2007) version of the Tung and Dhir friction model was applied. The top surface pressure is 3 bar.

p_{top} = 3 bar, d_p = 3 mm, P_m = 200 W/kg, t = 4 000 s

p_{top} = 3 bar, d_p = 3 mm, P_m = 250 W/kg, t = 4 000 s

Figure 15. Void fraction (two left columns) and solid particle temperature (two right columns) at the time of 4000 s in the MEWA2014 and Fluent simulations for the conical beds of the 3 mm particles and specific power equal to 200 and 250 W/kg studied by Yakush & Kudinov (2014). The Schmidt (2007) version of the Tung and Dhir friction model was applied. The top surface pressure is 3 bar.

Figure 16. Comparison of the time evolution of the maximum solid particle temperature in the MEWA2014 simulations of this study and in the DECOSIM simulations of Yakush & Kudinov (2014) (C-d1/2/3-W150/200/250 curves) for the same conical bed cases. The Schmidt (2007) version of the modified Tung and Dhir model is used. The top surface pressure is 3 bar.

Figure 17. Void fraction (two left columns) and solid particle temperature (two right columns) in conical beds at the time of 4000 s in the MEWA2014 simulations of this study and in the DECOSIM simulations according to Yakush & Kudinov (2014). The Schmidt (2007) version of the modified Tung and Dhir friction model was applied in the MEWA simulations and by Yakush & Kudinov (2014). The top surface pressure is 3 bar.

5.3 Truncated-cone-shaped beds

5.3.1 MEWA results

The maximum particle temperature is plotted in Figure 18 as a function of the simulation time for all the truncated-cone-shaped beds studied by Yakush & Kudinov (2014). Figure 19, Figure 20 and Figure 21 show distributions of the void fraction and particle temperature at the time of about 4000 s.

Qualitatively the results are similar as for the conical beds in Figure 12, Figure 13, Figure 14 and Figure 15. In the 2 and 3 mm particle cases with lowest heating powers (150 and 200 W/kg, respectively) no dryout occurs in the MEWA results. In addition, the dry zone is thin for the 3 mm particles also with the higher heating power.

MEWA predicts steady-states with dry zones only for the 2 mm particles with the power 200 W/kg and for the 3 mm particles with the power 250 W/kg. The 2 mm particle bed with the highest heating power (250 W/kg) does not fully stabilise in 5000 s and the maximum particle temperature is still increasing slowly. The truncated-cone-shaped beds with the 1 mm particles behave as conical beds and the maximum particle temperature increases to high values almost as without any cooling.

5.3.2 Comparison of the MEWA and DECOSIM results

The time evolutions of the maximum particle temperature computed for the truncated-cone-shaped beds in the MEWA simulations are compared in Figure 18 to the corresponding results from the DECOSIM simulations (Yakush & Kudinov, 2014). The void fraction and particle temperature fields are compared in Figure 19 in those cases for which contour plots were given by Yakush & Kudinov (2014).

In the 1 mm cases, the influence of cooling is small and the agreement is again good at least for the first 5000 s. In the MEWA simulations, the maximum particle temperature is somewhat larger. In the other cases, the maximum particle temperature is however lower in the MEWA simulations. In some cases the difference is hundreds of degrees.

The dry zones are smaller in the MEWA results. For 3 mm particles with the lower heating power (200 W/kg), no dryout is obtained in the MEWA simulations and DECOSIM ends up to a small dry zone (Figure 19). As with the conical beds in Figure 16, the lower limit of the temperature ranges are different.

The void fraction distributions outside the particle bed are largely similar (Figure 19). Steam flows slower outside the bed and flow is not tapering as much as in the DECOSIM results. These differences arise from the differences in the modelling of the pool zone discussed in Section 5.1.
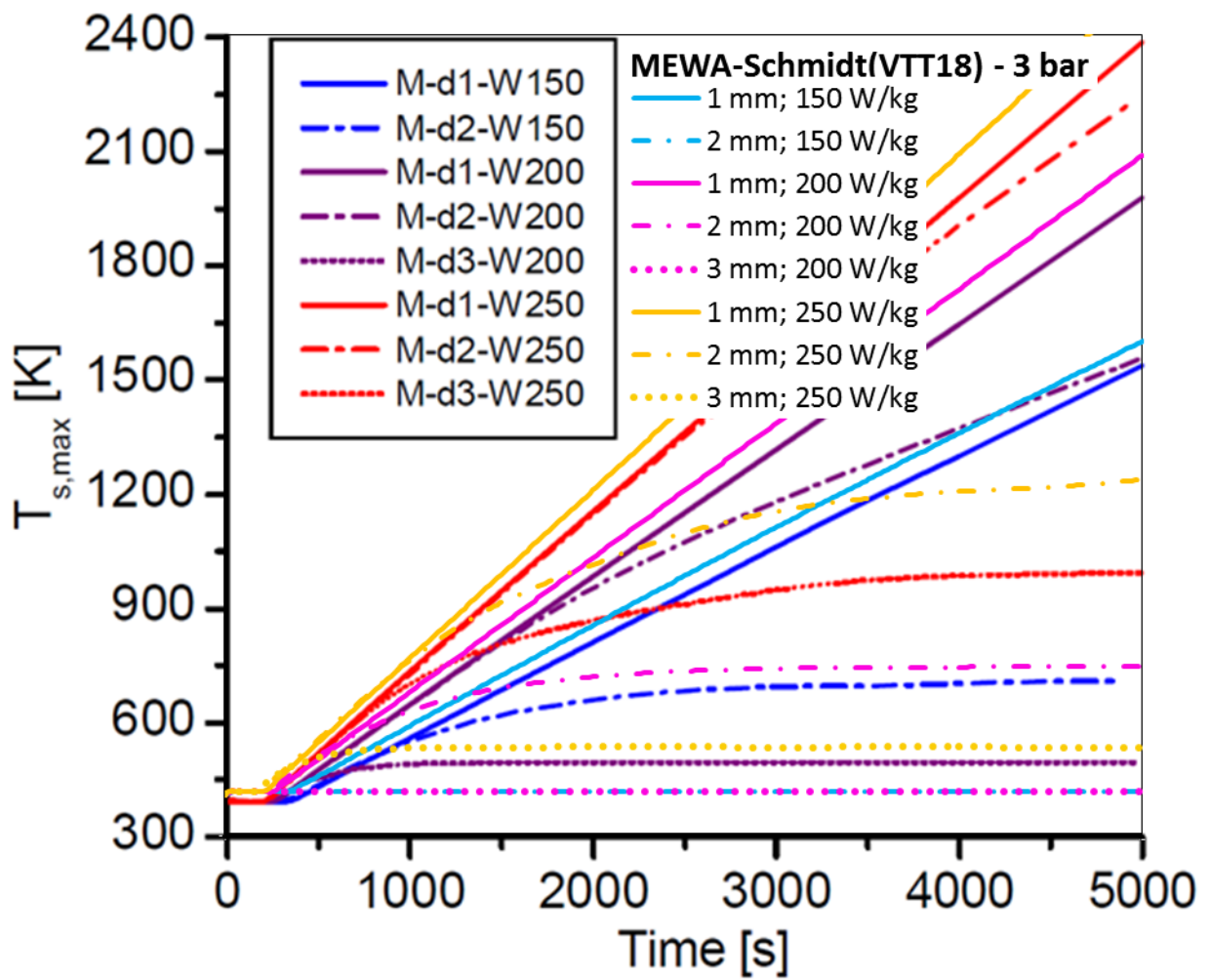
Figure 18. Comparison of the time evolution of the maximum solid particle temperature in the MEWA2014 simulations of this study and in the DECOSIM simulations of Yakush & Kudinov (2014) (M-d1/2/3-W150/200/250 curves) for the same truncated-cone-shaped bed cases. The Schmidt (2007) version of the modified Tung and Dhir friction model is used. The top surface pressure is 3 bar.
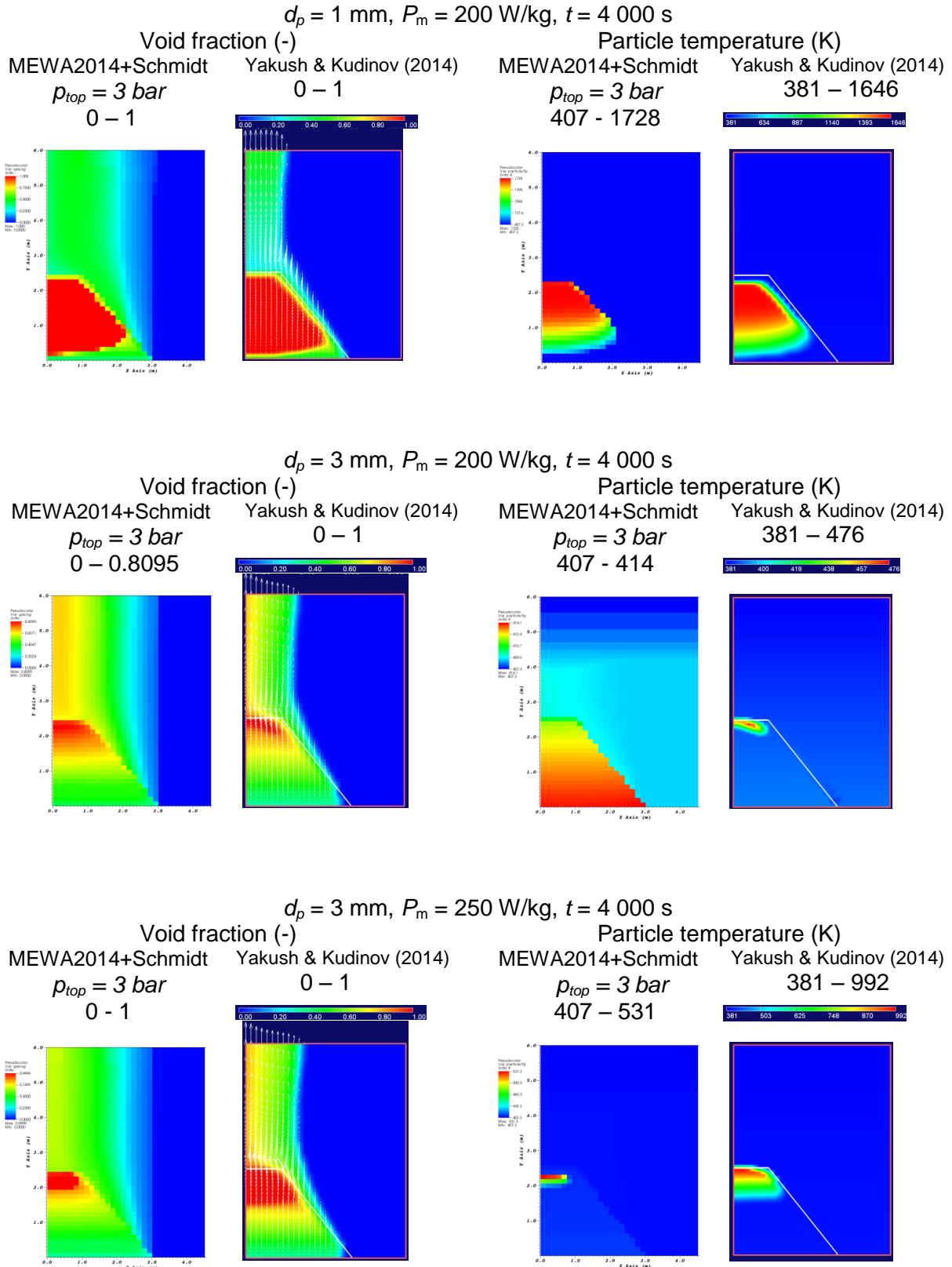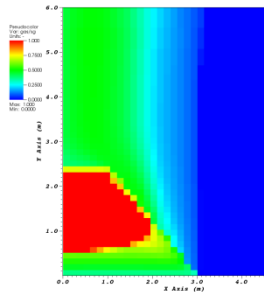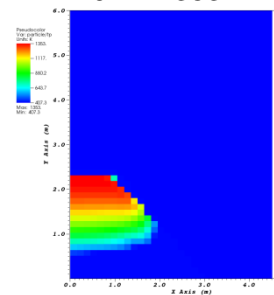
d_p = 1 mm, P_m = 200 W/kg, t = 4 000 s

Void fraction (-)		Particle temperature (K)	
MEWA2014+Schmidt	Yakush & Kudinov (2014)	MEWA2014+Schmidt	Yakush & Kudinov (2014)
p_{top} = 3 bar	0 – 1	p_{top} = 3 bar	381 – 1646
0 – 1		407 - 1728	

d_p = 3 mm, P_m = 200 W/kg, t = 4 000 s

Void fraction (-)		Particle temperature (K)	
MEWA2014+Schmidt	Yakush & Kudinov (2014)	MEWA2014+Schmidt	Yakush & Kudinov (2014)
p_{top} = 3 bar	0 – 1	p_{top} = 3 bar	381 – 476
0 – 0.8095		407 - 414	

d_p = 3 mm, P_m = 250 W/kg, t = 4 000 s

Void fraction (-)		Particle temperature (K)	
MEWA2014+Schmidt	Yakush & Kudinov (2014)	MEWA2014+Schmidt	Yakush & Kudinov (2014)
p_{top} = 3 bar	0 – 1	p_{top} = 3 bar	381 – 992
0 - 1		407 – 531	

Figure 19. Void fraction (two left columns) and solid particle temperature (two right columns) at the time of 4000 s in the MEWA2014 simulations of this study and in the DECOSIM simulations according to Yakush & Kudinov (2014) for the same truncated-cone-shaped bed cases. The Schmidt (2007) version of the modified Tung and Dhir friction model was applied in the MEWA simulations and by Yakush & Kudinov (2014). The top surface pressure is 3 bar.

p_{top} = 3 bar, d_p = 1 mm, P_m = 150 W/kg, t = 4 000 s

Void fraction (-)
0 – 1

Particle temperature (K)
407 – 1353

p_{top} = 3 bar, d_p = 1 mm, P_m = 250 W/kg, t = 4 000 s
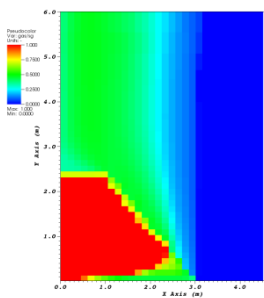
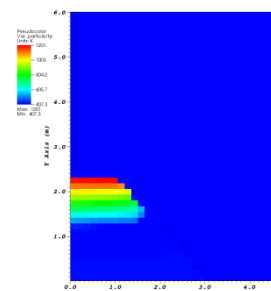Void fraction (-)
0 – 1

Particle temperature (K)
407 - 2081
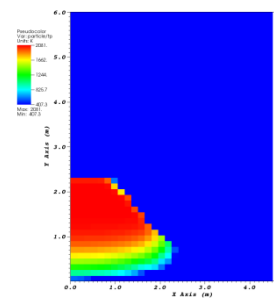
Figure 20. Void fraction (left) and solid particle temperature (right) in truncated-cone-shaped bed at the time of 4000 s in the MEWA2014 simulations for the 1 mm particles with the heating powers of 150 (top) and 250 (bottom) W/kg. The Schmidt (2007) version of the modified Tung and Dhir friction model was used. The top surface pressure is 3 bar.

p_{top} = 3 bar, d_p = 2 mm, P_m = 150 W/kg, t = 4 000 s

Void fraction (-)
0 – 0.8883
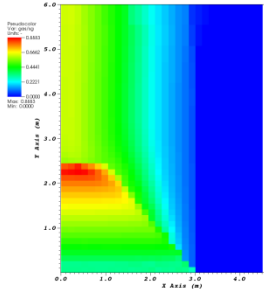
Particle temperature (K)
407 - 414
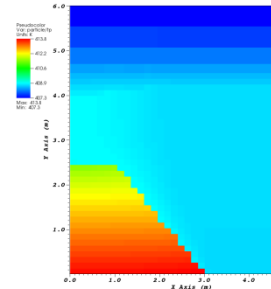
p_{top} = 3 bar, d_p = 2 mm, P_m = 200 W/kg, t = 4 000 s
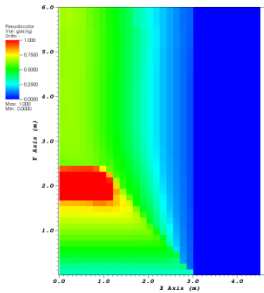
Void fraction (-)
0 – 1

Particle temperature (K)
407 - 741
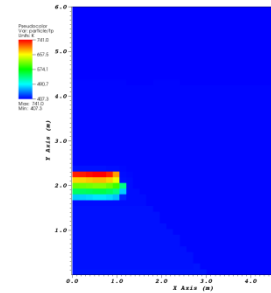
p_{top} = 3 bar, d_p = 2 mm, P_m = 250 W/kg, t = 4 000 s
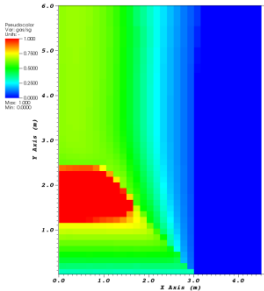
Void fraction (-)
0 – 1

Particle temperature (K)
407 - 1201

Figure 21. Void fraction (left) and solid particle temperature (right) in the truncated-cone-shaped bed at the time of 4000 s in the MEWA2014 simulations for the 2 mm particles and heating powers of 150 (top), 200 (middle) and 250 (bottom) W/kg. The Schmidt (2007) version of the modified Tung and Dhir friction model is used. The top surface pressure is 3 bar.

5.4 Speculative simulations for 1.3 bar

5.4.1 Motivation for the speculative simulations

There are some obvious inconsistencies between the MEWA results discussed above and the DECOSIM results of Yakush & Kudinov (2014). The range of the particle temperature distribution in the DECOSIM results is from 381 K (as discussed, this does not mean that the temperature in the coldest bed cells is 381 K but Figure 5 indicates that this is the case). In the MEWA simulations the initial bed and domain top temperatures are set close to the saturation temperature at the cone tip, 407 K, and a lower temperature is not obtained.

Furthermore, the saturation temperature seems to be different in the MEWA and DECOSIM simulations. In the DECOSIM results, the saturation temperature is reported to be 386 - 388 K (Yakush & Kudinov 2014, Table 1). The saturation temperatures in the DECOSIM simulations are plotted in Figure 22 as a function of the height. The height is the typical level of the location of the maximum particle temperature and it was estimated from Figure 6 and Figure 7. For the conical beds, the height of the maximum particle temperature was taken to be 2.7 m and for the truncated-cone-shaped beds 2.3 m. In all the truncated-cone-shaped bed cases, the saturation temperature is reported to be 386 K. In the conical cases, the saturation temperature varies from 386 to 388 K (note that the available values are in full degrees). Presumably and as indicated by the plots in Figure 4 and Figure 5, also in DECOSIM simulations, the vertical level of the maximum temperature varies and likely the higher saturation temperatures are obtained in lower levels.

The saturation temperature in the MEWA simulations discussed above in Sections 5.2 and 5.3 is also plotted in Figure 22 (p_top = 3 bar curve) as a function of the height. In these MEWA simulations, the pressure on the top surface is 3 bar consistent with the case definitions of Yakush & Kudinov (2014). Clearly, the saturation temperature in the MEWA simulations is significantly higher.

Figure 22 shows also the saturation temperature in a MEWA simulation in which the pressure on the top surface is 1.3 bar (p_top = 1.3 bar curve). This curve meets the points for the saturation temperature in the DECOSIM simulations. The 1.3 bar curve is in agreement with the values of the NIST Chemistry WebBook (Linstrom & Mallard 2019). The values for the topmost cells (381 K) are also the same as the lower limits of the temperature ranges in the plots for the DECOSIM results in Figure 4 and Figure 5. It was therefore decided to repeat the MEWA simulations for the top surface pressure of 1.3 bar.

The Schmidt (2007) version of the modified Tung and Dhir friction model was used in all speculative simulations for the top surface pressure of 1.3 bar. In the MEWA simulations the pressure in the dry zones is about 1.65 bar instead of the 3.35 bar in case of 3 bar surface pressure.

5.4.2 Results of the MEWA simulations and influence of the pressure reduction

The computed void fraction and particle temperature at the time of about 4000 s are presented as contour plots in Figure 23 and Figure 24 for the conical beds with the top surface pressure of 1.3 bar. The corresponding results for the truncated-cone-shaped beds are shown in Figure 25, Figure 26 and Figure 27.

In order to facilitate comparison with the DECOSIM results, the contour plots in Figure 23 and Figure 25 for the MEWA results are based on the nodal values as most likely the DECOSIM plots are. The nodal values are obtained applying an interpolation routine on the actually calculated cell values. The nodal values based results look physically more realistic but are influenced by an unknown interpolation routine. In the MEWA results, the maximum

of the nodal values is no more than a few degrees lower than the maximum cell value if a steady state is not achieved and the maximum particle temperature is still increasing. This is the case especially with the 1 mm particles. However, if the maximum particle temperature has stabilized, the difference can be even several tens of degrees.
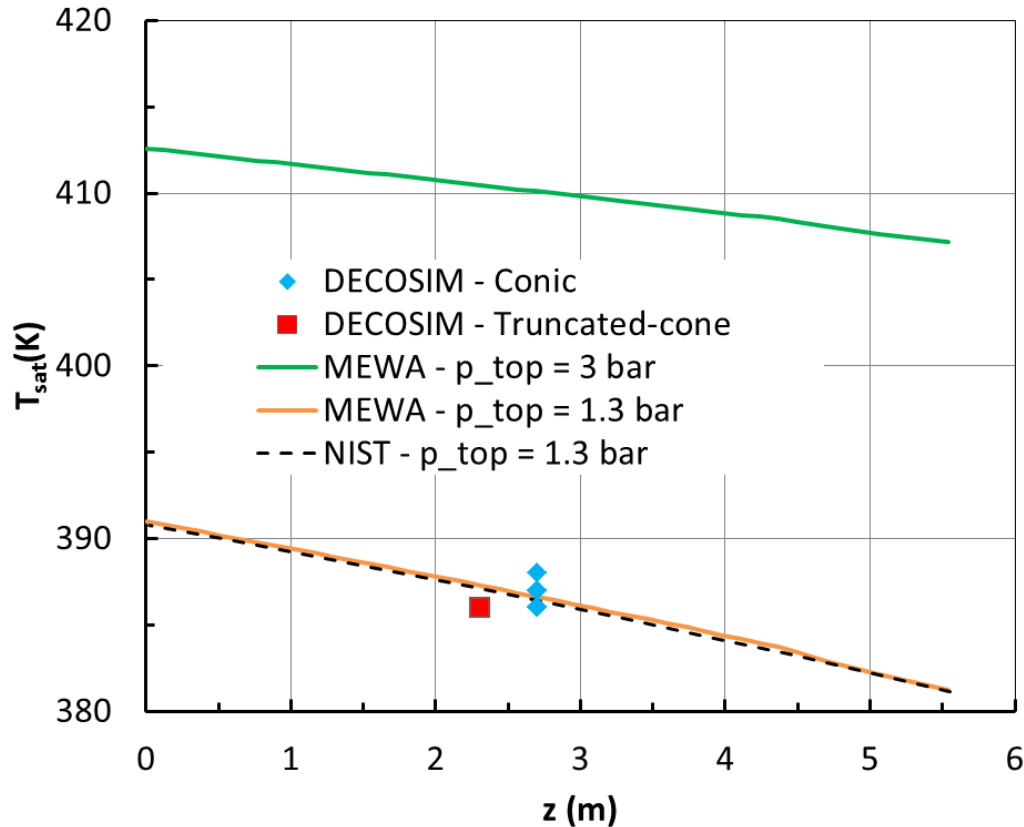

Figure 22. Saturation temperature as a function of the height in the DECOSIM simulations of Yakush & Kudinov (2014) and in the MEWA2014 simulations for the cases of the top surface pressure equal to 3 and 1.3 bar. For DECOSIM, the height is the vertical distance from the bottom for the location of the maximum particle temperature estimated from Figure 4 and Figure 5. The "NIST - p_{top} = 1.3bar" values are from Linstrom & Mallard (2019).

Compared to the 3 bar MEWA results in Figure 13, Figure 14 and Figure 15 for conical beds and Figure 19, Figure 20 and Figure 21 for truncated-shaped-cone beds, with the reduced pressure dryout occurs now in all cases and the dry zones are larger. The results for 1 mm particle beds do not change significantly. In the 2 and 3 mm particle cases, the temperature of the solid bed particles is higher.

The time evolution of the maximum particle temperature in the MEWA simulations for the top surface pressure of 1.3 bar is presented in Figure 28 and Figure 29 for the conical and truncated-cone-shaped beds, respectively. The MEWA results in Figure 28 and Figure 29 are for cell values being in a disagreement with the contour plots for the MEWA results in Figure 23 and Figure 25. No straightforward way was found to plot the maximum of the nodal temperatures as a function of time. Probably it would have required an implementation of another interpolation routine. In the paper of Yakush & Kudinov (2014), the time evolutions for the maximum particle temperature are likely for the nodal values.

Compared to the MEWA results for 3 bar in Figure 16 and Figure 18, the maximum particle temperature rises in all 1.3 bar cases from the original saturation temperature value consistent with the dryout occurrences. In cases of the 2 and 3 mm particle, the maximum

particle temperature for the reduced pressure rises to higher values. Steady states are achieved in 5000 s only for the 3 mm particles with the 250 W/kg heating power, and the maximum particle temperature stabilises to higher values than with the 3 bar boundary condition. After 4000 s, the maximum particle temperature can be even several hundreds of degrees higher. The reduction of the pressure does not influence on the results for 1 mm particles.

5.4.3 Comparison to the DECOSIM results for 3 bar

The contour plots for the void fraction and particle temperature are compared in Figure 23 and Figure 25 for the cases for which the DECOSIM results are reported by Yakush & Kudinov (2014). The DECOSIM results are thus for the 3 bar surface temperature. In these figures, the MEWA results are also presented as nodal values to facilitate comparison. Compared to the 3 bar MEWA results in Figure 13 and Figure 19, the agreement with the DECOSIM results is improved significantly. The dry zones and the particle temperatures are mostly similar as in the DECOSIM results. The lowest particle temperature is now 381 K as in the MEWA simulations.

The time evolution of the maximum particle temperature in the MEWA simulations for the top surface pressure of 1.3 bar is presented in Figure 28 and Figure 29 for the conical and truncated-cone-shaped beds, respectively, together with the DECOSIM results of Yakush & Kudinov (2014) for the top surface pressure of 3 bar. The shapes of the time evolution curves are also similar and the steady-state conditions are obtained in the same case and not in any other case. The agreement is better for the truncated-cone-shaped beds.

There are still significant differences in the maximum particle temperature of the solid particles. In all cases, the maximum particle temperature is higher in the MEWA simulations. The plotted MEWA results are for cell values and the nodal values would be at least in cases of steady state conditions several tens of degrees lower. Clearly in the MEWA simulations (cf., Figure 23), the flow is tapering more forcing more steam to flow through the dry zones enhancing cooling especially close to the bed surface and reducing the thickness of the dry zone as well as the maximum particle temperature. The weak tapering in the MEWA simulations results from poor representation of the open pool above the bed (cf., Section 5.1).

In the case of the 3 mm particle truncated-cone-shaped bed with the heating power equal to 200 W/kg, MEWA obtains for the (nodal) maximum particle temperature 630 K whereas the DECOSIM result is 476 K (Figure 25). The maximum particle temperatures are small but there is a relatively large difference if we compare the difference to the increases of the maximum particle temperatures. As Figure 25 shows, the flow is tapering more in the DECOSIM simulation and modifies the dry zone. However, in both the MEWA and DECOSIM simulations the dry zones so thin that the computed maximum particle temperature involves large uncertainties because of the sparse discretization. Therefore, in evaluating the agreement of the results of the two codes, the differences in results for the cases of small dry zones should not be emphasised.

When comparing the result of the DECOSIM results and the MEWA results computed with the Schmidt (2007) version of the modified Tung and Dhir friction model, possible differences in the model implementations should also be recalled. For instance, Schmidt (2007) does not give formulas for the transition zones. There can also be other implementation differences and differences in numerics. In addition, there are still some differences in the boiling models between MEWA and DECOSIM.

d_p = 1 mm, P_m = 200 W/kg, t = 4 000 s
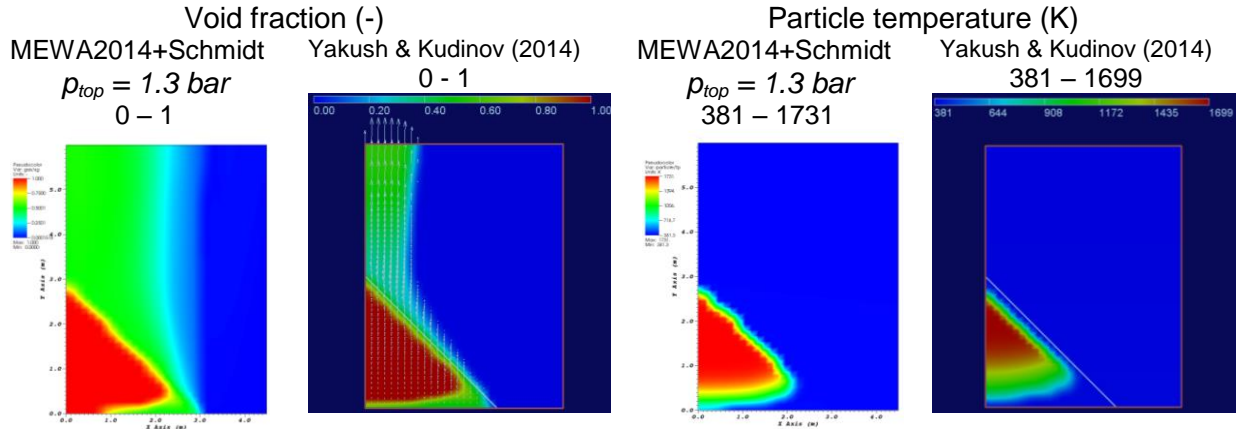
d_p = 2 mm, P_m = 200 W/kg, t = 4 000 s
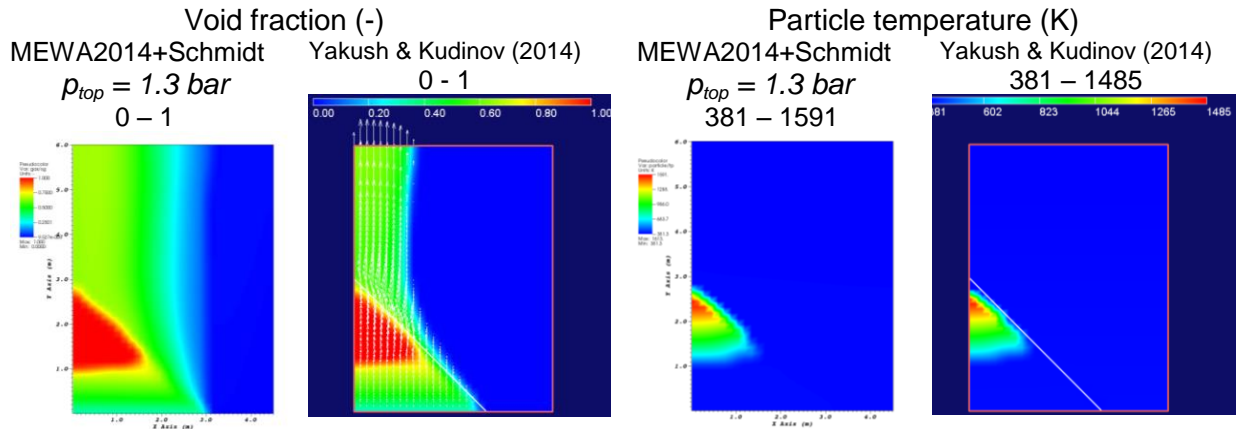
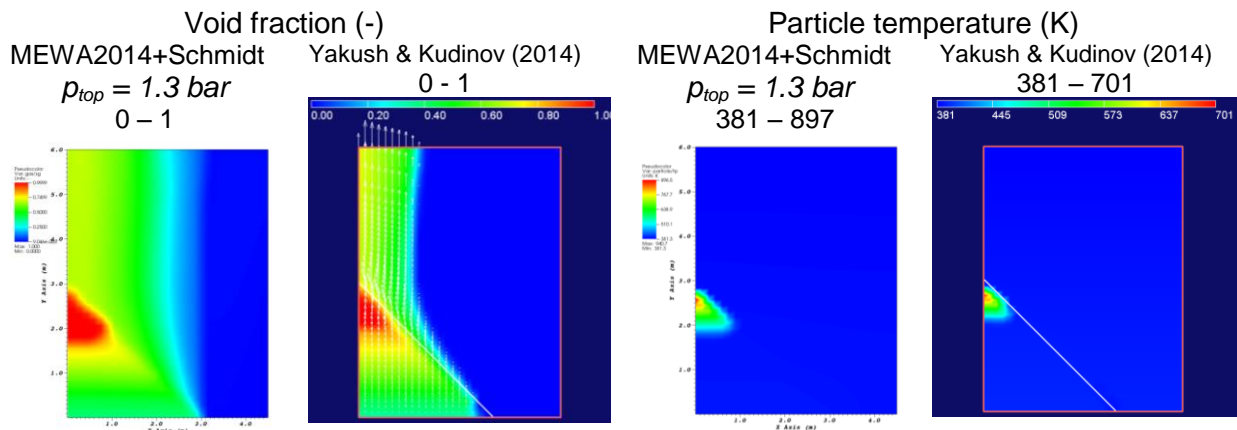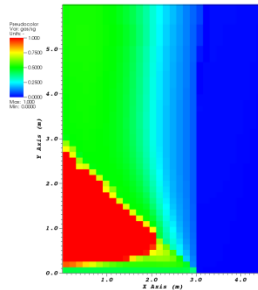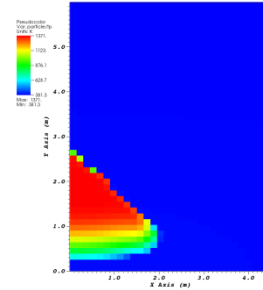d_p = 3 mm, P_m = 200 W/kg, t = 4 000 s

*Figure 23. Void fraction (two left columns) and solid particle temperature (two right columns) in three conical beds at the time of 4000 s in the MEWA2014 simulations of this study (nodal values) and in the DECOSIM simulations according to Yakush & Kudinov (2014). The Schmidt (2007) version of the modified Tung and Dhir friction model was applied in the MEWA simulations and was used by Yakush & Kudinov (2014). **In the MEWA simulations, the top surface pressure is 1.3 bar.***

p_{top} = 1.3 bar, d_p = 1 mm, P_m = 150 W/kg, t = 4 000 s

Void fraction (-)
0 – 1

Particle temperature (K)
381 – 1371

p_{top} = 1.3 bar, d_p = 2 mm, P_m = 150 W/kg, t = 4 000 s
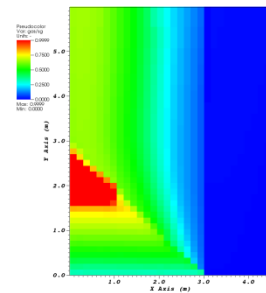
Void fraction (-)
0 – 1

Particle temperature (K)
381-1043
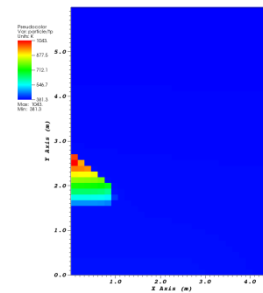
p_{top} = 1.3 bar, d_p = 3 mm, P_m = 250 W/kg, t = 4 000 s
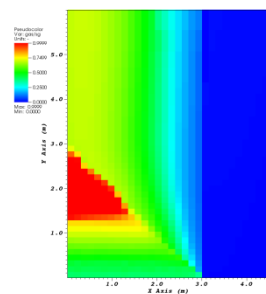
Void fraction (-)
0 – 1
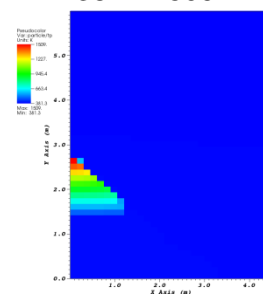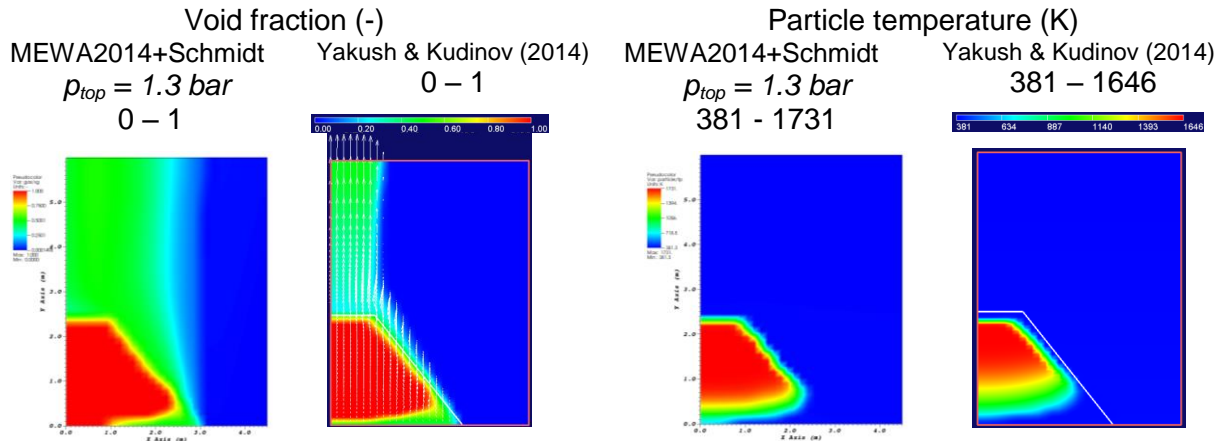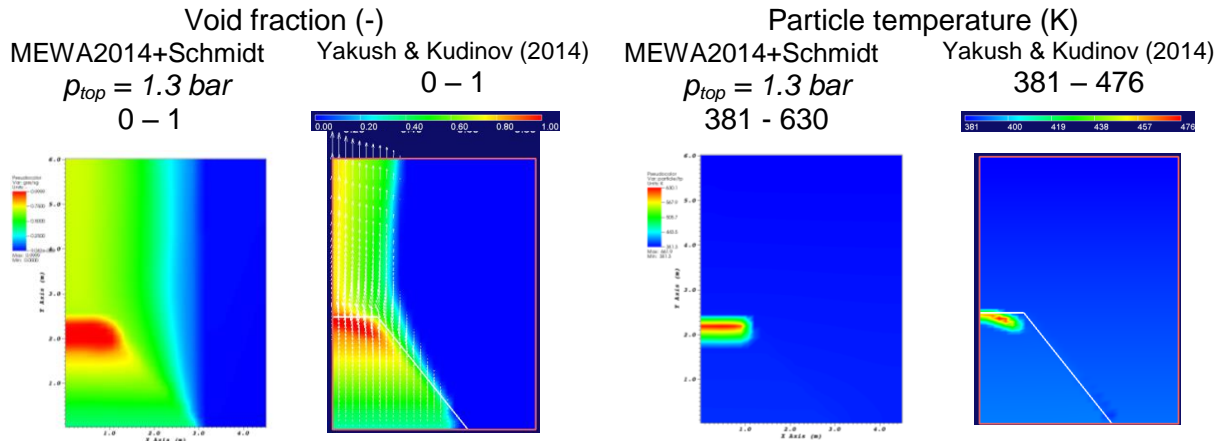
Particle temperature (K)
381 - 1509

*Figure 24. Void fraction (left) and solid particle temperature (right) at the time of 4000 s in the MEWA2014 simulations in three conical beds. The Schmidt (2007) version of the modified Tung and Dhir friction model is used. **The top surface pressure is 1.3 bar.***

d_p = 1 mm, P_m = 200 W/kg, t = 4 000 s

d_p = 3 mm, P_m = 200 W/kg, t = 4 000 s

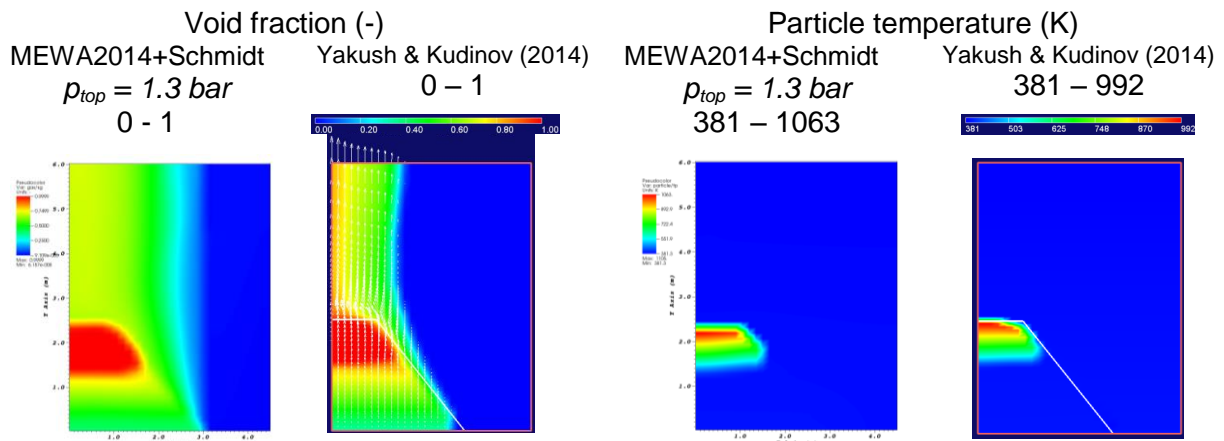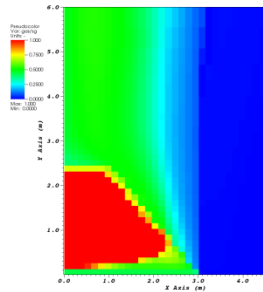d_p = 3 mm, P_m = 250 W/kg, t = 4 000 s

*Figure 25. Void fraction (two left columns) and solid particle temperature (two right columns) in three truncated-cone-shaped beds at the time of 4000 s in the MEWA2014 simulations of this study (nodal values) and in the DECOSIM simulations according to Yakush & Kudinov (2014). The Schmidt (2007) version of the modified Tung and Dhir friction model was applied in the MEWA simulations and by Yakush & Kudinov (2014)***. In the MEWA simulations, the top surface pressure is 1.3 bar.***

p_{top} = 1.3 bar, d_p = 1 mm, P_m = 150 W/kg, t = 4 000 s

p_{top} = 1.3 bar, d_p = 1 mm, P_m = 250 W/kg, t = 4 000 s
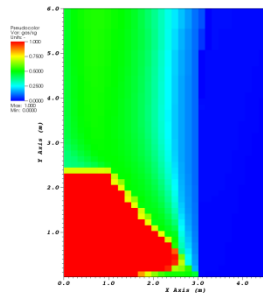
Figure 26. Void fraction (left) and solid particle temperature (right) at the time of 4000 s in the MEWA2014 simulations for the 1 mm particle truncated-cone-shaped beds and for th heating powers of 150 (top) and 250 (bottom) W/kg. The Schmidt (2007) version of the modified Tung and Dhir friction model is used. **The top surface pressure is 1.3 bar***.*

p_{top} = 1.3 bar, d_p = 2 mm, P_m = 150 W/kg, t = 4 000 s

Void fraction (-)
0 – 1

Particle temperature (K)
381 - 807

p_{top} = 1.3 bar, d_p = 2 mm, P_m = 200 W/kg, t = 4 000 s
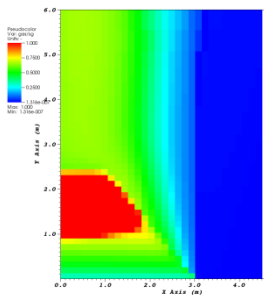
Void fraction (-)
0 – 1

Particle temperature (K)
381 - 1443
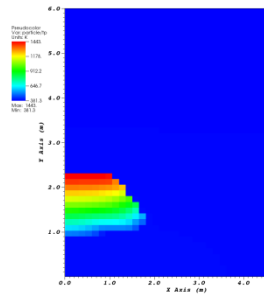
p_{top} = 1.3 bar, d_p = 2 mm, P_m = 250 W/kg, t = 4 000 s
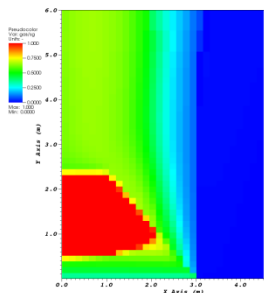
Void fraction (-)
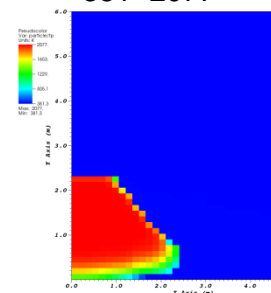0 – 1

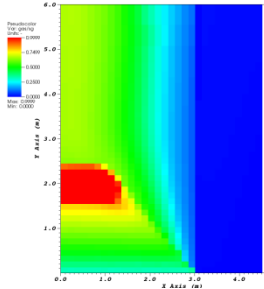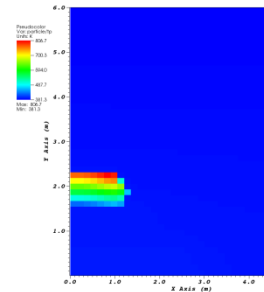Particle temperature (K)
381 - 1974
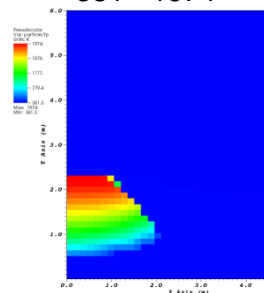
*Figure 27. Void fraction (left) and solid particle temperature (right) at the time of 4000 s in the MEWA2014 simulations for the 2 mm particle truncated-cone-shaped beds and for the heating powers of 150 (top), 200 (middle) and 250 (bottom) W/kg. The Schmidt (2007) version of the modified Tung and Dhir friction model is used. **The top surface pressure is 1.3 bar.***
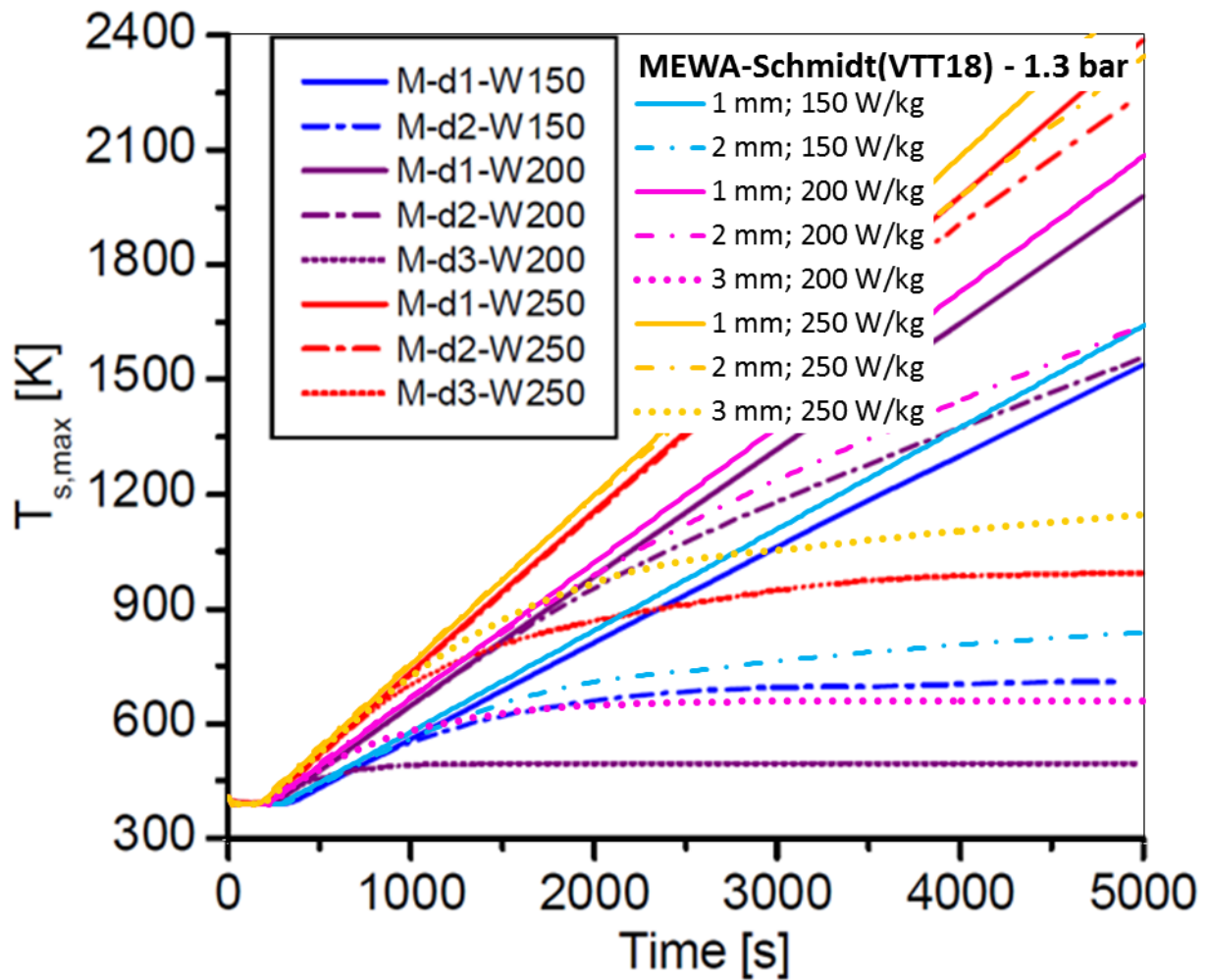
*Figure 28. Comparison of the time evolution of the maximum solid particle temperature in the MEWA2014 simulations of this study (cell values) and in the DECOSIM simulations according to Yakush & Kudinov (2014) (C-d1/2/3-W150/200/250 curves) for the conical bed cases (Figure 9). The Schmidt (2007) version of the modified Tung and Dhir friction model was applied in the MEWA simulations and was used by Yakush & Kudinov (2014). **In the MEWA simulations, the top surface pressure is 1.3 bar.**
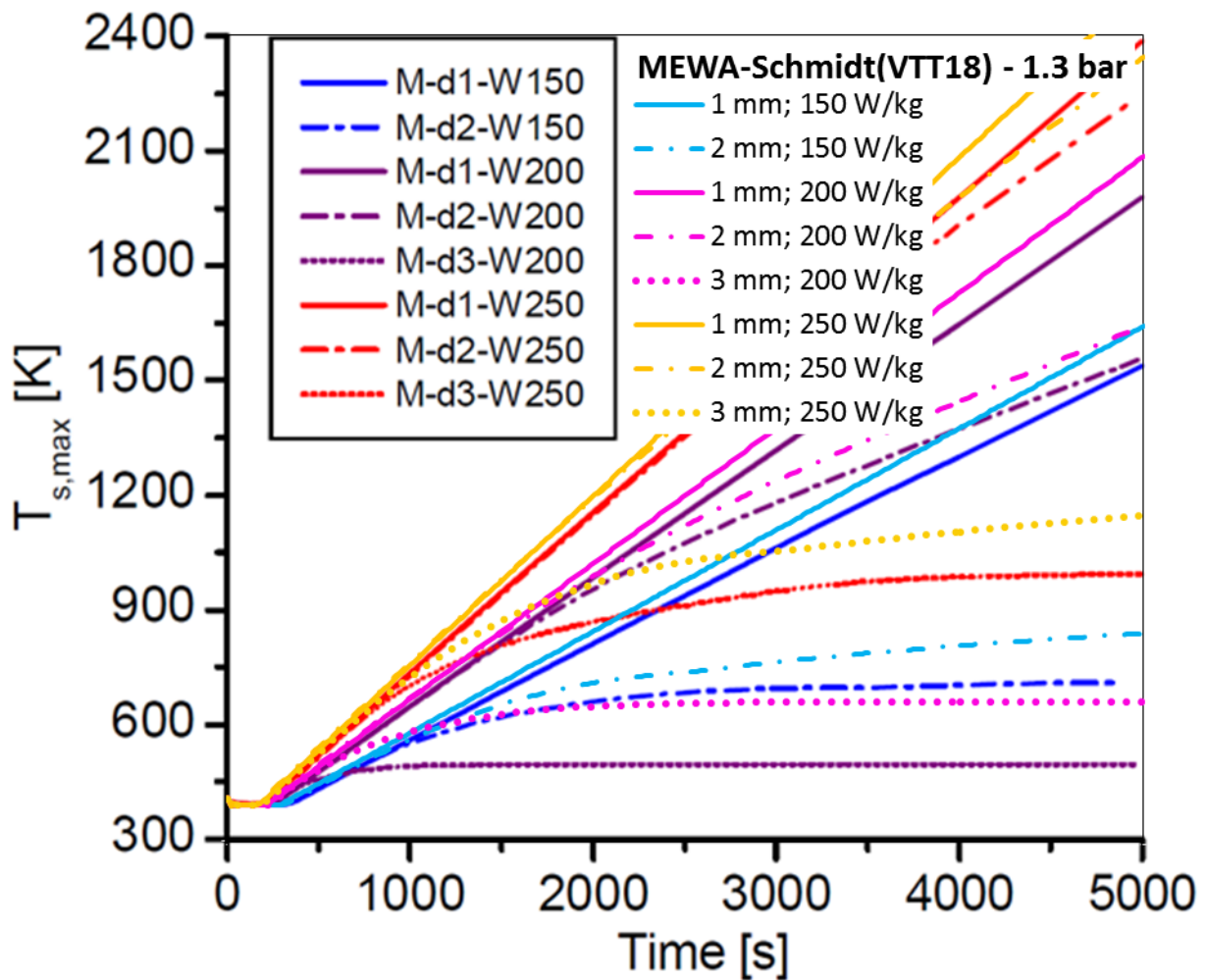
Figure 29. Comparison of the time evolution of the maximum solid particle temperature in the MEWA2014 simulations of this study (cell values) and in the DECOSIM simulations according to Yakush & Kudinov (2014) (M-d1/2/3-W150/200/250 curves) for the truncated-cone-shaped beds (Figure 10). The Schmidt (2007) version of the modified Tung and Dhir friction model was applied in the MEWA simulations and was used by Yakush & Kudinov (2014). **In the MEWA simulations, the top surface pressure is 1.3 bar.**

6. Conclusions

Coolability of corium debris beds was studied by performing numerical simulations with the MEWA code (Bürger et al. 2006, Rahman 2013). Especially post-dryout conditions were analysed computationally for the hypothetical idealized particle beds studied at KTH by Yakush & Kudinov (2014). The beds are conical and truncated-cone-shaped in geometry. Yakush & Kudinov (2014) apply the DECOSIM code in their computations. The results from MEWA and DECOSIM were compared and potential reasons for the differences were discussed and tested.

In the previous studies (Taivassalo & Takasuo 2017, Taivassalo 2018) the DECOSIM results of Yakush & Kudinov (2014) could not be reproduced. However, previous work showed that in case of 2 and 3 mm particles, the friction model affects strongly the area of the dry zone and thus the maximum particle temperature. Since MEWA does not feature the Schmidt version of the modified Tung and Dhir friction model used in the DECOSIM simulations of Yakush & Kudinov (2014), it was implemented in the MEWA code.

The modified MEWA was verified in the conical beds against the Fluent impelementation of the debris bed coolability models (Takasuo et al., 2015). The new MEWA results are mainly in a good agreement with the Fluent results for the same friction model in the previous study (Taivassalo 2018), but the outcome is not conclusive. The challenges in comparing two representations of a multiphase flow were discussed previously (Taivassalo 2018). In the Fluent results, the strongly tapering flow in the water pool increases the pressure above the bed surface and reduces the flow inside the tip of the cone. In addition, the horizontal penetration of water into the bed is larger due to the coarseness of the mesh. The coarse-mesh representation of an ideal conical bed does not influence significantly the MEWA results and presumably neither the DECOSIM results. However, when the complete multiphase momentum equations with the convective and viscous terms are solved applying the same coarse spatial discretization, the flow field is characterized by significant water fluxes penetrating horizontally relatively deep into the bed. On the other hand, if the complex flow fields obtained in the CFD simulations for the cone-tip area are realistic, the simplified momentum equations do not predict the bed behaviour correctly and especially not conservatively.

The comparison of the MEWA results of this study and the DECOSIM results of Yakush & Kudinov (2014) for the same boundary conditions reveals some significant differences. The maximum temperature of the solid particles in the bed is generally lower in the MEWA results. There are also some obvious inconsistencies between the MEWA and DECOSIM results. The lower limit of the range of the particle temperature in the contour plots for the DECOSIM results (Figure 4 and Figure 5) and the saturation temperature reported by Yakush & Kudinov (2014) (Figure 22) are not consistent with the MEWA results. The saturation temperature is in the MEWA simulations about 23 degrees higher than reported to be in DECOSIM computations.

The saturation temperature in the MEWA simulations is close to the values reported to have been obtained in the DECOSIM simulation, if the top surface pressure is changed from 3 bar to 1.3 bar (Figure 22). In the reduced pressure, the saturation temperature calculated in MEWA is consistent with the values provided by the NIST Chemistry WebBook (Linstrom & Mallard 2019). Speculative simulations were thus performed with MEWA for the reduced pressure. With the 1.3 bar top pressure, the MEWA results agree reasonably well with the DECOSIM results for both the conical and truncated-cone-shaped beds. The remaining differences could be because of the differences in the modelling of the water pool hydrodynamics and boiling phenomena as well as potential differences in model implementations and numerics.

In summarising the previous computational studies on the coolability of debris beds (Taivassalo & Takasuo 2017, Taivassalo 2018) and findings of this work, we can conclude that in many cases the time evolution of the maximum particle temperature varies with the friction model. The post-dryout behaviour is also strongly influenced by the particle size and a small particle bed is considered more representative for realistic beds of random irregular particles (Chikhi et al. 2014). However, for the 1 mm particles, the cooling influence of steam is very small after dryout and the maximum particle temperature does not stabilize but increases with a heating-power specific rate to intolerably high values almost as without any cooling. If we assume that the true hydrodynamical behaviour of particle beds is within the predictions of the applied friction models and three-dimensional effects are unimportant, the 3 mm (and larger) particle beds stabilise to acceptable conditions at least, if the specific heating power is less than 250 W/kg. The maximum particle temperature stabilises to values which depend on the particle size, heating power and friction model. For the particles between 1 and 3 mm, the computational predictions of the post-dryout behaviour includes significant uncertainties. The results are strongly influenced by the particle size, heating power and friction model. In addition, the pressure, porosity and three-dimensional hydrodynamical phenomena can easily be of some importance. To reduce numerical uncertainties, denser meshes should be applied. Therefore, before trying to quantify a

temperature-based coolability criterion, it would be essential to be able first to select a friction model which is most valid or at least conservative in post-dryout conditions.

References

Atkhen, K. & Berthoud, G. 2006. SILFIDE experiment: Coolability in a volumetrically heated debris bed. Nuclear Engineering and Design, 236, pp.2126–2134.

Bürger, M. et al. 2006. Validation and application of the WABE code: Investigations of constitutive laws and 2D effects on debris coolability. Nuclear Engineering and Design, 236, pp.2164–2188.

Chikhi, N., Coindreau, O., Li, L.X. , Ma, W.M., Taivassalo, V., Takasuo, E., Leininger, S., Kulenovic, R., Laurien, E. 2014. Evaluation of an effective diameter to study quenching and dry-out of complex debris bed. Annals of Nuclear Energy, 74, pp.24–41.

Ergun, S. 1952. Fluid flow through packed columns. Chem. Eng. Prog. 48 (1952).

Hu, K., Theofanous, T.G. 1991. On the measurement and mechanism of dryout in volumetrically heated coarse particle beds. International Journal of Multiphase Flow, 17 (No. 4).

Huang, Z., & Ma, W. 2018. Validation and application of the MEWA code to analysis of debris bed coolability. Nuclear Engineering and Design, 327, pp.22–37.

Imura, S. & Takegoshi, E. 1974. Effect of Gas Pressure on the Effective Thermal Conductivity of Pack Beds. Heat Transfer Japanese Research, 3(4).

Lienhard, J.H. 2012. A Heat Transfer Textbook, 4th edition. Phlogiston Press, Cambridge, Massachusetts, USA.

Linstrom, P.J. and Mallard, W.G. Eds. 2019. NIST Chemistry WebBook, NIST Standard Reference Database Number 69, National Institute of Standards and Technology, Gaithersburg MD, 20899, https://doi.org/10.18434/T4D303, (retrieved February 8, 2019).

Lipinski, R.J. 1982. A Model for Boiling and Dryout in Particle Beds. US Nuclear Regulatory Committee, NUREG/CR-2646, SAND82-0765

Lipinski, R.J. 1984. A coolability model for postaccident nuclear reactor debris. Nuclear Technology, 65, pp. 53-66

Luikov, a. V. et al. 1968. Thermal conductivity of porous systems. International Journal of Heat and Mass Transfer, 11(2), pp.117–140.

Maxwell, J.C. 1873. A treatise on electricity and magnetism. Vol. 1. Clarendon press, Oxford.

Rahman, S. 2013. Coolability of Corium Debris under Severe Accident Conditions in Light Water Reactors. Insitut für Kernenergetik und Energiesysteme, University of Stuttgart.

Reed, A.W. 1982. The effect of channeling on the dryout of heated particulate beds immersed in a liquid pool. Doctoral Thesis, Department of Mechanical Engineering, Massachusetts Institute of Technology, 1982.

Rohsenow, W. 1952. A method of correlating heat transfer data for surface boiling of liquids. Trans. ASME, 74, pp. 969–976.

Schmidt, W. 2007. Interfacial Drag of Two-phase Flow in Porous Media. Int. J. Multiphase Flow, Vol. 33, pp. 638–657.

Stephan, P., Martin, H., Kabelac, S., Mewes, D., Kind, M., & Schaber, K. ed. 2010. VDI Heat Atlas.

Taivassalo, V. 2018. Comparison of friction models for debris beds in post-dryout conditions. Research report VTT-R-01003-18. VTT, Espoo.

Taivassalo, V., & Takasuo, E. 2017. Predicting debris bed behaviour in post-dryout conditions. Research report VTT-R-00762-17. VTT, Espoo.

Takasuo, E., Taivassalo, V., Kinnunen, T., Lehtikuusi, T. 2015. Coolability analyses of heap-shaped debris bed. Research report VTT-R-00367-15. VTT, Espoo.

Takasuo, E. 2015. Coolability of porous core debris beds: Effects of bed geometry and multi-dimensional flooding. VTT Technical Research Centre of Finland Ltd. D.Sc. thesis. Available at: http://www.vtt.fi/inf/pdf/science/2015/S108.pdf.

Takasuo, E. 2016. An Experimental Study of the Coolability of Debris Beds with Geometry Variations. Annals of Nuclear Energy, 92, pp.251–261. Available at: http://www.sciencedirect.com/science/article/pii/S0306454916300408.

Tung, V.X., Dhir, V.K. 1988. A hydrodynamic model for two-phase flow through porous media. International Journal of Multiphase Flow Vol. 14, pp. 47-65.

Vortmeyer, D. 1978. Radiation in Packed Solids. In 6th International Heat Transfer Conference, Toronto, Canada.

Yagi, S. & Kunii, D. 1957. Studies on effective thermal conductivities in packed beds. AIChE Journal, 3(3), pp.373–381. Available at: http://onlinelibrary.wiley.com/doi/10.1002/aic.690030317/full.

Yakush, S. & Kudinov, P. 2014. A model for prediction of maximum post-dryout temperature in decay-heated debris bed. In 22nd International Conference on Nuclear Engineering. July 7-11, 2014, Prague, Czech Republic.

Appendix C

Developing uncertainty analysis for PSA from ROAAM+

Lloyd's Register

Developing uncertainty analysis for PSA from ROAAM+

SPARC 2018 WP2

Report for:
NKS

Report no: PRJ11084933_R001   Rev: 1.1

Date: September 06, 2019

Summary

Developing uncertainty analysis for PSA from ROAAM+

SPARC 2018 WP2

Security classification of this report: Distribute only after client's acceptance

Report no:	**Revision:**	**Report date:**
PRJ11084933_R001	1.1	September 06, 2019

Prepared by:	**Reviewed by:**	**Approved by:**
Sergey E. Galushin	Ola Bäckström	Anders Olsson
Senior consultant	Principal consultant	VP Nuclear operations Sweden
Anders Riber Marklund	Anders Riber Marklund	
Principal consultant	Principal consultant	
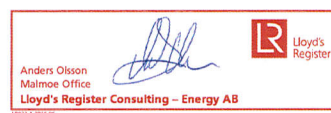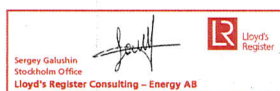
Entity name and address:

Lloyd's Register Consulting - Energy AB
P.O. Box 1288
SE-172 25 SUNDBYBERG
Sweden

Client name and address:

NKS
NKS Secretariat
P.O. Box 49
DK-4000 Roskilde
Denmark

Our contact:

Anders Riber Marklund

T: +46 70 230 41 14

E: anders.ribermarklund@lr.org

Client contact :

Christian Linde

T: +46 (0)70 146 77 44

E: christian-linde@ssm.se

Document history

Revision	Date	Description/changes	Changes made by
1.0	2019-06-30	First version	Sergey Galushin
1.1	2019-09-06	Added list of authors contributed to the report.	Sergey Galushin

Authors

Sergey Galushin, Anders Riber Marklund, Ola Bäckström, Pavel Kudinov, Dmitry Grishchenko, Sergey Yakush, Mikhail Davydov.

Glossary/abbreviations

ANN	Artificial Neural Network
BWR	Boiling Water Reactor
CDF	Core Damage Frequency
CDF	Cumulative Distribution Function
CCDF	Complimentary Cumulative Distribution Function
CCFP	Conditional Containment Failure Probability
CET	Containment Event Tree
CRD	Control Rod Drive
CRGT	Control Rod Guide Tube
EOPs	Emergency Operation Procedures
ET	Event Tree
IGT	Instrumentation Guide Tube
FCI	Fuel-Coolant Interaction
FM	Full Model
FT	Fault Tree
FTA	Fault Tree Analysis
LERF	Large Early Release Frequency

MCSs	Minimal Cut sets
MCCI	Molten Core-Concrete Interaction
PSA/PRA	Probabilistic Safety Assessment/Probabilistic Risk Assessment
PCV	Primary Containment Vessel
PDF	Probability Density Function
PDS	Plant Damage State
SM	Surrogate Model
SAM	Severe Accident Management
SA	Severe Accident
RC	Release Category
URF	Unacceptable Release Frequency

Table of contents

1 Introduction

This report summarizes the experience and results achieved within the NKS-SPARC WP2 project during 2018-2019. Which is a continuation of the NKS-SPARC activities performed in [66]. The project is motivated by high sensitivity of effectiveness of severe accident management (SAM) strategy to the uncertainties in physical phenomena (deterministic) and accident scenarios (stochastic). Furthermore, scenarios, including timing of events, and physical phenomena are also important sources of uncertainty for estimation of the consequences of containment failure, i.e. characteristics of the fission product release. Adequate approaches are necessary in order to address both deterministic (epistemic) and stochastic (aleatory) sources of uncertainty for a consistent assessment of the effectiveness of the accident mitigation strategy and environmental impact.

The project aims at integrating probabilistic and deterministic methods to improve scope and quality of risk analyses. Ideally, a risk analysis would at all point consider all challenges that can occur at that particular point in time. The process could be thought of like a dynamic event tree covering all possible failures (aleatory) and uncertainties associated with the lack of knowledge about system response (epistemic uncertainty). As much this is an appealing approach, the state space that would need to be analyzed to cover all possible scenarios and epistemic uncertainties is enormous and it will not be feasible to perform this analysis.

To make it possible to analyze the problem in a PSA-like framework, the problem can be viewed upon from two angles: deterministic and probabilistic viewpoints. From a deterministic analysis point of view a few simultaneous failures are considered during a sequence and the failures may be represented by "super components". This would allow for a simplified process like the dynamic event tree. The merit would be that the approach would consider all possible effects, known and unknown, of the represented failures. To further limit the state space, consideration needs to be taken to the probability of failures, in such a way that negligible failure combinations are omitted. This approach would hence give a complete picture of the scenarios studied, and not only a few defined scenarios as in the current deterministic calculations.

From a probabilistic point of view all possible failure combinations should be covered by the PSA model. The simplifications therefore need to be regarding grouping of sequences (failure combinations that have similar effect) and simplified treatment of timing of failure combinations. The dynamic approach would give enhanced input about which scenarios that should be studied separately (where epistemic uncertainty can be quantified and eventually reduced), and information about timing of events of importance. This information is expected especially relevant regarding PSA-L2. The enhanced information requires improvements in the PSA quantification methods to include the information in the PSA model.

The static PSA is built on choosing the correct scenario parameters to describe the accident progression and typically uses a pre-set choice of physical parameters in the underlying deterministic analysis. It is however difficult to handle both deterministic modelling & intangible parameters and physical parameters influencing more than one sequence of events. Such parameters may for example influence more than one phenomenon. The benefit of the dynamic approach, such as ROAAM+ framework, is the possibility to address all these sources of uncertainty in a transparent way.

The enhanced information from a dynamic approach can be used in the PSA in several ways. It can be used to improve sequence definitions, when phenomena can be relevant (improved PDS definitions and sequences in the containment event tree). This corresponds to improvement in the definition of scenario parameters based on deterministic modelling. Estimation of probabilities for phenomena, including the effect of accident scenarios (aleatory) and phenomenological (epistemic) sources of uncertainty. This follows from the improved definition of scenario parameters which also results in improved understanding of how the accident scenario parameters and epistemic uncertainty affect phenomena, and it should be reflected in PSA modelling. Information about the timing of the events. Insights form dynamic behavior of especially timing in sequences may also be relevant for increased realism when a PSA is developed to reach "safe state" – as the transient time studied will be long and hence would call for better treatment of repair.

The project employs the two above mentioned concepts in order to provide consistent treatment of the uncertainties. The main benefits of the project are:

- Better understanding of the modelling pre-requisites in current PSA (level 1 input to level 2 and level 2 design).
- New methods for combined deterministic-probabilistic analysis and
- Practical experience in using them in combination with existing PSA models.

The project outcome will allow the end users to enhance understanding, completeness and consistency of safety analysis dealing with risk analysis in:

- management of severe accident issues;
- improved reliability analysis modelling methods for level 2 PSA (what is relevant to consider in the modelling);
- presentation of results in level 2 PSA, and related risk criteria;
- handling of epistemic uncertainties and use of this results in PSA.

Not being the main focus of the proposed project, but the methodology could also be used for (for example): identify safety vulnerabilities (scenarios of safety importance which can threaten safety barriers) in active and passive safety systems. Additionally, the proposed approaches can provide insights on the effect of possible design modification on PSA results, taking into account different sources of uncertainties.

Experiences from performed studies are summarized in the report as well as suggestions of areas which need further investigations.

2 Background

2.1 Severe Accident Management Strategy in Nordic BWR.

Severe accident management (SAM) strategy in Nordic boiling water reactors (BWRs) employs ex-vessel debris coolability. Molten core materials are released from the vessel into a deep pool of water under the reactor (see Figure 1) and expected to fragment, quench, and form a debris bed that is coolable by natural circulation of water. An energetic steam explosion and formation of non-coolable debris bed pose credible threats to containment integrity.
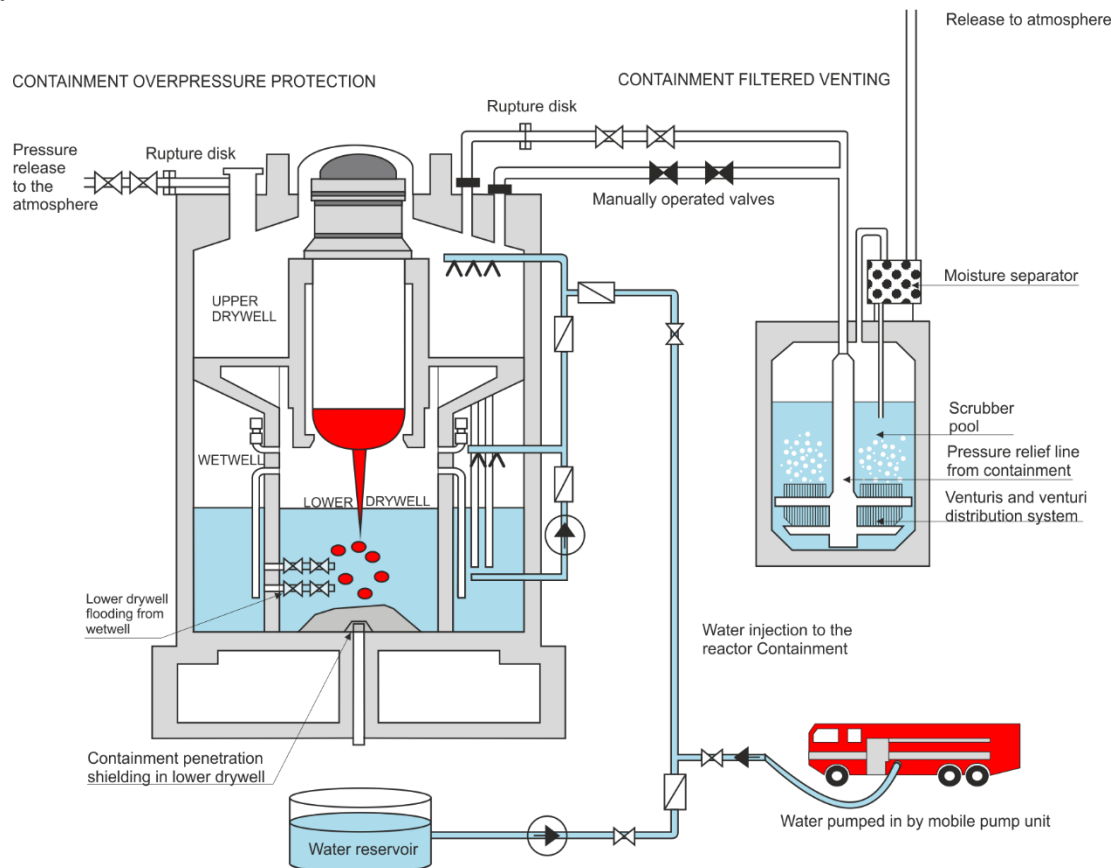
Figure 1: Severe Accident Management in Nordic BWR [3].

Conditions of melt release from the vessel determine (i) debris bed properties and thus coolability, and (ii) steam explosion energetics. The strategy involves complex phenomena (see Figure 2) affected by the transient accident scenarios.
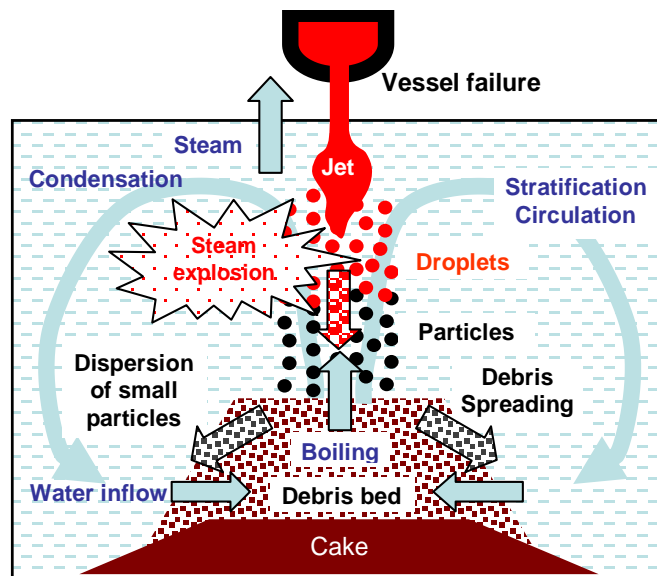
Figure 2: Severe Accident Phenomena in Nordic BWR [1].

The progress that has been achieved during the last few decades in understanding and predicting physical phenomena, was not sufficient to make a solid conclusion on the robustness and effectiveness of the existing SAM strategy for Nordic BWR. It became apparent that the issue is intractable [4], [1] for separate probabilistic or deterministic analysis due to the uncertainty that comes from the interactions between multistage accident progression scenarios (see Figure 3) and deterministic phenomena (see Figure 2).
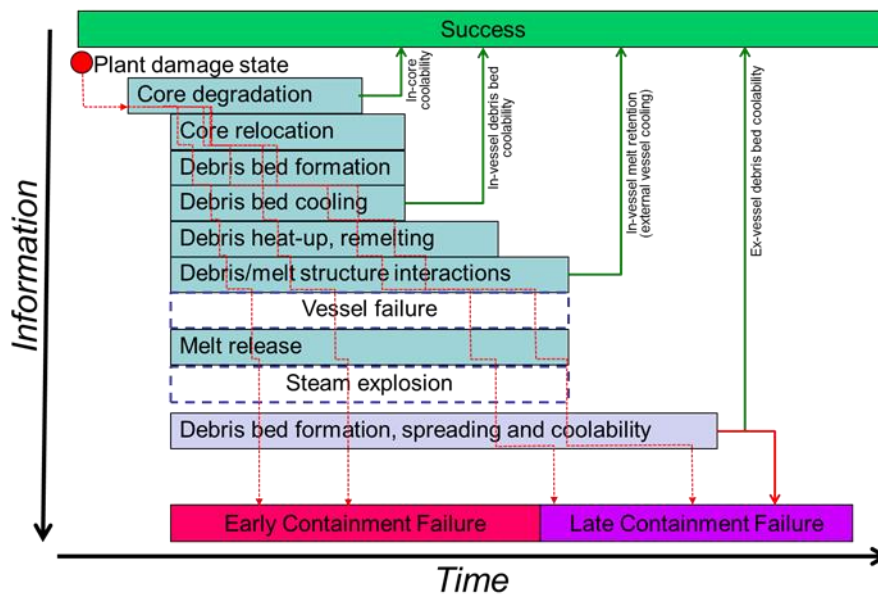
Figure 3: Severe Accident Progression in Nordic BWR [1].

2.2 Risk Oriented Accident Analysis Methodology

The Risk Oriented Accident Analysis Methodology (ROAAM) that marries probabilistic and deterministic approaches was proposed to address problems where both stochastic phenomena (aleatory) and phenomenological (epistemic) uncertainties are significant. The ROAAM was developed and successfully applied by Professor Theofanous and co-workers for assessment and management of severe accident risks [5], [6]. After Fukushima accident, the Risk Management Task Force provided recommendation that NRC should implement a consistent process that includes both deterministic and probabilistic methods in risk assessments that can inform decisions about appropriate defense-in-depth measures [7].

The ROAAM integrates risk assessment (analysis) and risk management (modifications in the design, procedures, etc.) for effective management of rare, high-consequence hazards. ROAAM requires the simultaneous and consistent consideration of (i) safety goal, (ii) assessment methodology, and (iii) application specifics. Important premise of ROAAM is that safety goals can be defined only qualitatively when epistemic uncertainty is significant.

For severe accident the safety goal is usually defined as: "containment failure is a physically unreasonable event for any accident sequence that is not remote and speculative" [5]. ROAAM provides guidelines for bounding of epistemic (modelling) and aleatory (scenario) uncertainties in a transparent and verifiable manner that enables convergence of experts' opinions on the outcomes of the analysis. When the whole community of experts in a given problem area is convinced that issue resolution is regarded as successful, the problem may be considered solved in a robust and final way [5].

In order to achieve the transparency and clarity, ROAAM employs its principal ingredients: (i) identification, separate treatment, and maintenance of separation (to the end results) of aleatory and epistemic uncertainties; (ii) identification and bounding/conservative treatment of uncertainties (in parameters and scenarios, respectively) that are beyond the reach of any reasonably verifiable quantification; and (iii) the use of external experts in a review, rather than in a primary quantification capacity.

3 ROAAM+ Framework for Nordic BWR

This chapter provides a brief overview of ROAAM+ Framework for Nordic BWR[1], including an overview of (i) probabilistic framework and its implementation (based on [3][16][75]), as well as (ii) an overview of full and surrogate models used in the analysis (based on [75]).

While ROAAM has been successful in resolving several severe accident issues (e.g. [8][9][10][11]), when applied to the Nordic BWR plants, the tight coupling between severe accident threats and high sensitivity of the SAM effectiveness to timing of events (e.g., vessel failure) and characteristics (e.g., melt release conditions) present new challenges in decomposition, analysis and integration (see Figure 3). Furthermore, in classical ROAAM approach applications (e.g. [8][9][10][11]) the safety margins are (or were made by design modifications) sufficiently large, thus making possible conservative treatment of uncertainties in risk assessment. In case of SAM of Nordic BWR it is not possible to demonstrate effectiveness of the SAM with conservative assumptions. On the other hand, there is a question if assumptions in the analysis are too conservative and the SAM can achieve its goal while state-of-the-art knowledge is insufficient to demonstrate that.

To overcome these issues a further extension of ROAAM (called ROAAM+) was developed [16]. Development and application of the ROAAM+ framework is based on an iterative process of knowledge refinement followed by risk analysis. The process is a guiding tool for identification and addressing of the major sources of uncertainty. The goal of ROAAM+ is to support decision making regarding the effectiveness of SAM strategy in Nordic BWR. In order to achieve that aim ROAAM+ framework provides an extended treatment of safety goals in support for both possible decisions:

(i)   current SAM strategy is sufficiently reliable ("possibility" of the containment failure is low);

(ii)   SAM strategy is not sufficiently reliable ("necessity" of the containment failure is high) and thus changes in the SAM design are necessary.

3.1 ROAAM+ Probabilistic Framework

3.1.1 Theoretical background

It was emphasized by Kaplan and Garrick [12] that "the purpose of risk analysis and risk quantification is always to provide input to an underlying decision problem, which involves not just risks but also other forms of costs and benefits. Risk must thus be considered always within a decision theory context" [12].The analysis of complex systems usually involves answering to the three following questions [12]: (i) what can happen? (ii) how likely? (iii) if it happens, what are the consequences? Which leads to the "risk triplet idea" presented in Kaplan and Garrick's paper "On the quantitative definition of risk" (see [12]), which has become a cornerstone of modern risk analysis. The risk R_i associated with a specific scenario s_i can be characterized by its frequency f_i and consequences c_i. Consequences are obtained from assessments which are subject to uncertainty due to incomplete knowledge (epistemic uncertainty, degree of confidence), which can be quantified as probability P_i (likelihood) of c_i [12].

$$R_i = \{s_i, f_i, P_i(c_i)\} \qquad (1)$$

To quantify the confidence in the assessment of the frequency and consequences, equation (1) can be written in more general form:

$$R_i = \{s_i, pdf(f_i, P_i(c_i))\} \qquad (2)$$

Consequences c_i of scenario s_i can be presented as joint probability density function $\mathrm{pdf}_{C_i L_i}(L_i, C_i)$ of loads (L_i) on the system and its capacity (C_i) to withstand such loads. Thus, failure probability P_{Fi} for scenario s_i can be evaluated as

$$P_{Fi} = P(L_i \geq C_i) = \iint_{L_i \geq C_i} \mathrm{pdf}_{C_i L_i}(c, l) dcdl \qquad (3)$$

Residual risk is judged in ROAAM with screening frequency for aleatory, and with screening probability for epistemic. I.e. plant damage states (D_j) selected for the analysis include those that have frequency higher than

selected screening frequency f_s and lower than target frequency f_t achieved as the prevention goal, that is, $f_s < f_j(D_j) < f_t$ (severe accident mitigation window [13]. Demonstration of reaching the safety goal is successful if P_{Fi} is below respective screening probability level P_s. An arbitrary scale for probability is introduced in ROAAM to define the process likelihood [5]:

- 1/10 - Behavior is within known trends but obtainable only at the edge-of-spectrum parameters;
- 1/100 - Behavior cannot be positively excluded, but it is outside the spectrum of reason;
- 1/1000 - Behavior is physically unreasonable and violates well-known reality. Its occurrence can be argued against positively.

3.1.1.1 Decision Making

Screening frequency for aleatory, and the physically unreasonable concept for epistemic uncertainties are introduced for clarity and consistency of the ROAAM analysis results.

The aim of the ROAAM+ framework is to provide an assessment in support of the decision whether the risk associated with current SAM strategy is acceptable.

Scenario frequencies are the inputs to ROAAM+ framework provided from PSA L1 analysis results, i.e. frequencies of correspondent plant damage states (PDSs). Conditional containment failure probability (or probability distribution of conditional containment failure probability) for each scenario is a main outcome of ROAAM+ framework analysis. It is instructive to note that different modes of failure can potentially lead to quite different consequences in terms of fission products release. At this point we consider any failure mode as unacceptable for the sake of conservatism.
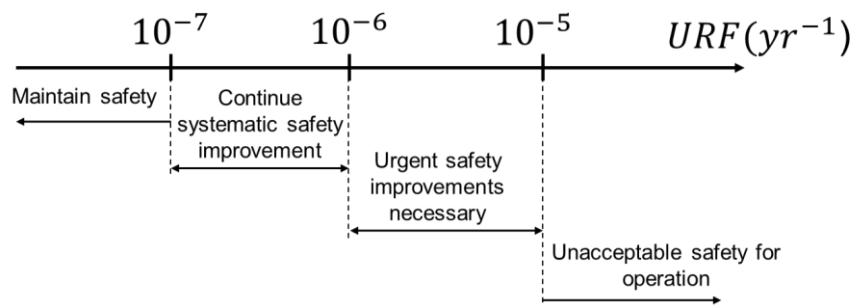
Figure 4. Unacceptable Release Frequency (URF(yr^{-1})) [60].

Figure 4 presents the decision alternatives with respect to URF, which is an outcome of PSA Level 2 analysis. Furthermore, the results of PSA L2 analysis can be evaluated according the relative safety significance, using eq.(4), by normalizing with respect to the goal value for unacceptable release frequency - $f_{Nominal}^U = 10^{-7}(yr^{-1})$ [60].

$$S^U = f^U/f_{Nominal}^U \qquad (4)$$

Then, the results can be interpreted according to the Table 1.

Table 1. Probabilistic Safety Significance Decision Matrix [60].

Relative Safety Significance		Description
$S \geq 100$	Unacceptable	Unacceptable Safety for Operation - Risk-reducing measures must be taken immediately. If immediate risk reduction cannot be achieved the operation should be suspended until temporary or permanent risk mitigating measures have been taken.
$100 > S \geq 10$	Operation Limiting	Urgent safety improvements necessary – Temporary measures generally are necessary. Operation can continue for a limited period, depending on the medium-term risk-increase. Cost-effective compensatory measures should be developed for permanent implementation.
$10 > S \geq 1$	Tolerable	Continue systematic safety improvement – Continue normal operation, no additional measures are necessary. Compensating measures should be considered and planned to the extent that this is considered reasonable.

Relative Safety Significance		Description
1 > S	Negligible	Maintain safety – Continue normal operation, no additional measures are necessary.

Figure 5a presents decision criterion as a function of accident scenario frequency (CDF – Core Damage Frequency) and Conditional Containment Failure Probability (CCFP) or Conditional Probability of Unacceptable Release (CPUR) which is used in classical ROAAM. If there is no uncertainty in CCFP, then the decision can be made directly using the correspondent values of CDF and CCFP as it demonstrated in the Figure 5a. In case of CCFP values being uncertain and represented by $pdf(P_{Fi})$ – as in Figure 5b where ROAAM+ results - $pdf(P_{Fi})$ are presented as box and whiskers plots for scenarios s_i, with respective frequencies f_i; the abovementioned approach can be used to support decision making.
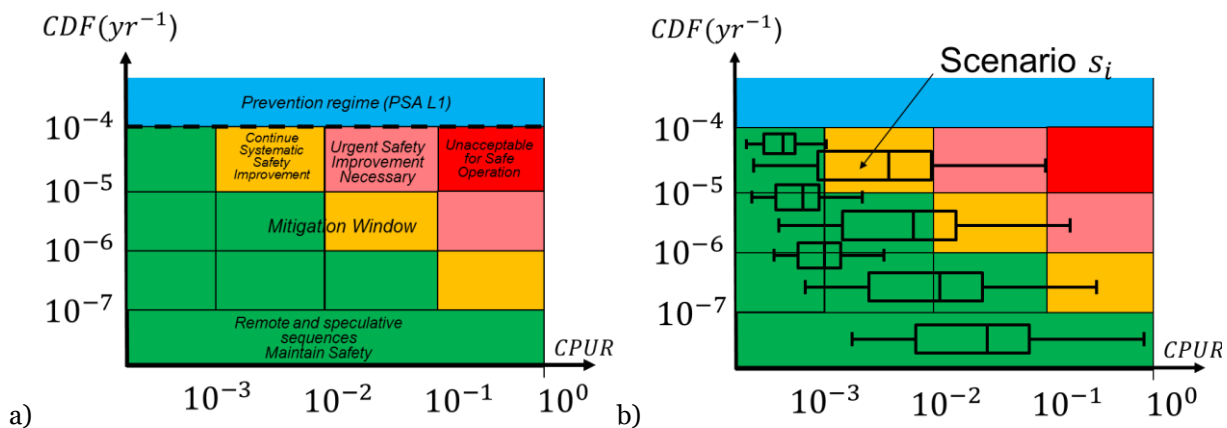
Figure 5. Conditional Probability of Unacceptable Release, (a) Decision Support in Classical ROAAM; (b) Decision support in ROAAM+.

3.1.2 ROAAM+ Framework for Nordic BWR

One of the key ingredients of ROAAM methodology is decomposition of severe accident processes into key physical phenomena that can be described by well-posed mathematical problems that can be solved independently from each other.
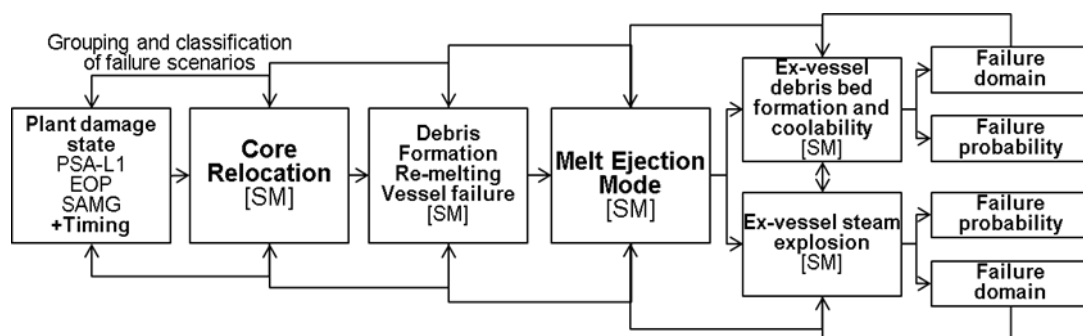
Figure 6. ROAAM+ framework for Nordic BWR[1].

Figure 6 illustrates the top layer of the ROAAM+ framework for Nordic BWR which decomposes severe accident progression into a set of causal relationships (CR) represented by respective surrogate models (SM) connected through initial and boundary conditions such that the uncertainty can be propagated from the initial plant damage state $\{D_i\}$ to the ex-vessel containment phenomena.

Computational efficiency of the top layer of the framework is achieved through application of surrogate models (SMs), and is a must for extensive sensitivity and uncertainty analysis in the forward and reverse analyses:

- Forward analysis defines conditional containment failure probability for each scenario $\{s_i\}$.
- Reverse analysis identifies failure domains in the space of scenarios $\{s_i\}$, and model input parameters $\{p_i\}$.

For each plant damage state $\{D_j\}$ defined in PSA Level 1 there is a set of respective scenarios $\{s_{ji}\}$ ($\{s_i\}$ – for brevity) characterized by their frequencies $\{f_i\}$. Scenarios introduce specific combinations of initial and boundary conditions for the models used in the framework and the structure of the probabilistic framework.

We distinguish four different kinds of parameters in the framework. For example, a causal relation - CR_k have:

(i)   scenario $\{s_i\}$ parameters (determined by initial plant damage states, possible operator actions and random success/failures of activation of different systems),

      a. These parameters usually represent initial boundary conditions in the set of coupled casual relationships (CRs), it can be timings of safety systems activation (e.g. depressurization, water injection, operation of containment sprays, etc.)

      b. Note that other plant response parameters can be considered as scenario parameters, e.g. water pool depth in the LDW, temperatures, pressures, etc.

(ii)   model input/output parameters $\{p_{ki}\}$ (predicted/used by the models at earlier/later stages of the framework respectively).

      a. In general, these parameters are predicted by causal relationship in the framework, e.g. response of in-vessel phase of severe accident progression to operator actions, mass of relocated debris, vessel failure mode, temperature and rate of ejected materials from the vessel.

The epistemic (modeling) parameters are treated differently depending on the degree of knowledge [6], [14].

(iii)   deterministic $\{d_{ki}\}$ modeling parameters (internal model parameters) have complete probabilistic knowledge (i.e. probability distribution).

      a. Set of deterministic modeling parameters is problem specific, e.g. debris porosity and particle size due to melt jet fragmentation (obtained from experiments) in the model for debris agglomeration and coolability (see section 3.2.3).

(iv)   intangible $\{i_{ki}\}$ modeling parameters (internal model parameters). have incomplete or no probabilistic knowledge, i.e. one can only argue regarding possible ranges of such parameters.

      a. Set of intangible parameters is problem specific, e.g. in MELCOR code the parameters that control radial and axial relocation (SC1020-1, SC1020-2, VFALL), the switch for the mode of debris ejection from the vessel (IDEJ), the fraction of ejected instrumentation guide tubes (EIGT) (see section 3.2.1).

Grouping and classification of failure scenarios corresponding to the specific initial plant damage states helps to identify plant vulnerabilities and provides insights into possible efficient mitigation actions by operator. Failure domain in the space of deterministic and intangible modeling parameters $\{d_{ki}, i_{ki}\}$ identifies the need for improvement of knowledge, modeling and data.

3.1.3   Surrogate models and Full Models

In ROAAM+, the necessary computational efficiency is achieved through extensive application of Surrogate Models (SMs).

The process of development and validation of the individual surrogate models is the most important for completeness, consistency, and transparency of the results. General ideas of the process are illustrated in Figure 7.
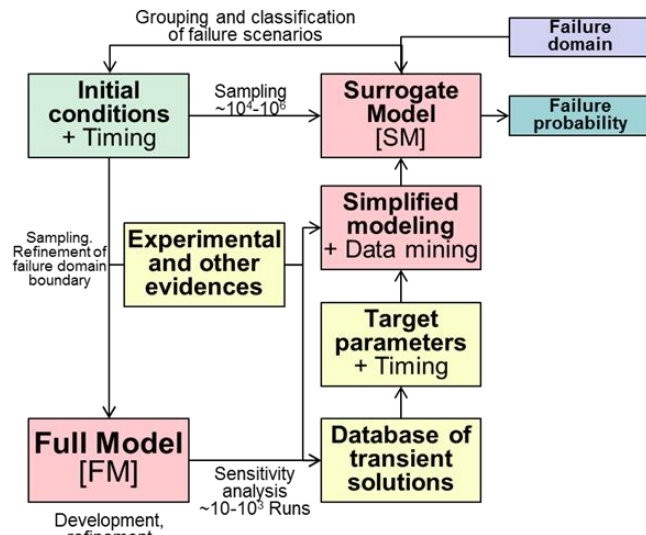
Figure 7. Full and Surrogate model development, integration with evidences, refinement, prediction of failure probability and failure domain identification [1].

ROAAM+ framework employs a two-level coarse-fine analysis and iterative process of framework refinement in the development of the SMs:

- Initial conditions for FM and SM development and analysis come from the respective stages of the analysis at the previous stages of the framework (Figure 6).
- Experimental and other evidences provide a knowledge base for validation of the FMs and calibration of SMs.
- Full Model (FM) is implemented as detailed fine resolution (computationally expensive) simulation approach. FMs are used assuming wider possible ranges of the input parameters:
  - To provide better understanding in the key phenomena and interdependencies.
  - To identify transitions between qualitatively different regimes and failure modes.
  - To generate a database of the FM transient solutions.
- Surrogate model (SM) is developed as an approximation of the FM model prediction of the target parameters which employ simplified (coarse resolution) physical modeling, calibratable closures, or approximations of the response surface of FM (e.g. using machine learning, such as artificial neural networks (ANNs) [15]).

This process is iterative in nature and is guided by failure domain analysis, which is used to identify the needs for further refinement of Full and Surrogate models and overall structure of the framework.

3.1.4 Probability of Failure and Failure Domain

Probability of failure and failure domain are the two main outcomes of forward and reverse analysis in ROAAM+ Framework [4],[1].

Probability of Failure

Probability of failure is determined by forward propagation of uncertainties through the framework as illustrated in Figure 8.
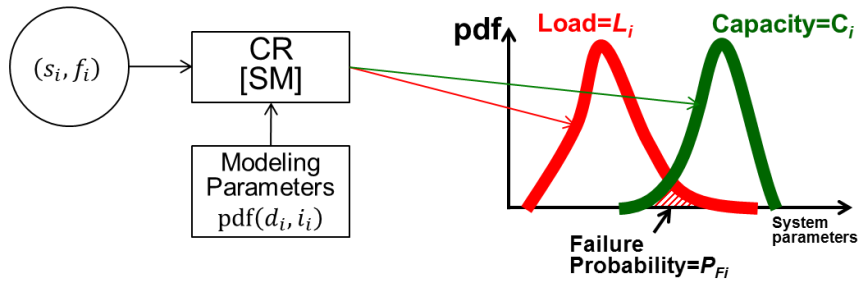
Figure 8. Failure Probability in Single Stage Process.

In Figure 8 the epistemic uncertainty in prediction of the load $\{L_i\}$ and capacity $\{C_i\}$ is due to the uncertainty in intangible $\{i_i\}$ and deterministic $\{d_i\}$ modelling parameters characterized by a multidimensional probability density function $\{\mathrm{pdf}(d_i, i_i)\}$. The joint distribution of the load and capacity define respective probability of the consequences $\{P_i(c_i)\}$ or, more specifically, the probability of containment failure $\{P_{Fi}\}$ in scenario $\{s_i\}$.

$$P_{Fi} = P(L_i \geq C_i) = \iint_{L_i \geq C_i} \mathrm{pdf}_{C_i L_i}(c, l) dc dl \tag{5}$$
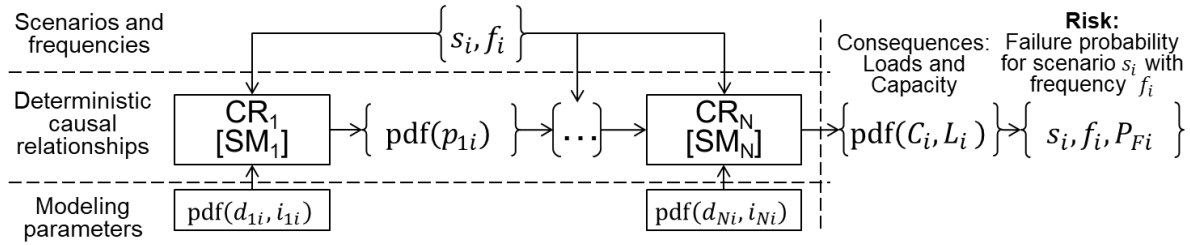
Figure 9. Failure probability in a multistage framework.

Similarly to Figure 8, the probability of failure $\{P_{Fi}\}$ can be calculated in a multistage process, where the set of initial conditions $\{p_{ki}\}$ for every consequent model is predicted by an "upstream" model, as illustrated in the Figure 9. Then, the probability of failure for every step in the multi-stage process can be calculated using equation (6).

$$P_F(s_i, p_{N-1i}) = \iint_{L>C} \mathrm{pdf}(p_{Ni}(s_i, p_{N-1i})) dp_{Ni} \tag{6}$$

Failure Domain

The failure domain analysis aims to identify the conditions and explain the reasons for failure. Identification of the failure domain is a product of the "reverse" analysis which propagates information about failure "backwards" from the last stage of the accident progression to the spaces of scenario and model input parameters at the previous stages of the framework. By identifying and grouping scenarios and conditions that lead to failure, we can determine and explain the reasons for failure (in terms of key physics and scenarios) using compact representation of information, amenable to scrutiny.

In general form, the "Failure Domain" (FD) in the space of scenario and model input parameters $\{s_i, p_{ki}\}$ is defined as a subdomain where the probability of failure $\{P_{Fi}\}$ is larger than a "screening" probability level (P_S) i.e. ($P_{Fi} \geq P_S$).

$$\{s_i, p_{ki} | \mathrm{pdf}(d_i, i_i)\}: P_F(s_i, p_{ki}) \geq P_S \tag{7}$$

More general definition of failure domains used in ROAAM+ is given in section 3.1.6, in order to account for the treatment of model intangible parameters in the framework, which is discussed in section 3.1.5.

Screening Probability

ROAAM+ framework employs an extended treatment of safety goals and support for both possible decisions, either to maintain current SAM strategy as sufficiently reliable ("possibility" of the containment failure is low) or SAM strategy is not sufficiently reliable ("necessity" of the containment failure is high) and thus changes are necessary.

This is achieved through application of two definitions of screening probability levels P_S for

- "Possibility" of failure: P_s=1.e-3.
  - According to [5] P_s=1.e-3 defines the process likelihood as *physically unreasonable* and violates well-known reality. Its occurrence can be argued against positively.
- "Necessity" of failure: P_s=0.999.
  - Is equivalent to statement that possibility that containment doesn't fail is low (P_s=1.e-3), i.e. the likelihood of success can be considered as *physically unreasonable* which would violate well-known reality, thus non-failure can be argued against positively.

3.1.5 Treatment of Model Intangible Parameters

In classical ROAAM uncertainty in the intangibles can only be qualitatively approached, but it can always be bounded [5]. Such bounding approach is, in fact, similar to the interval analysis [17]. In case of large inherent safety margins, the bounding approach will not affect conclusions from the risk analysis. However, if failure probability P_f is sensitive not only to the ranges but also to the distributions, then the uncertainty in prediction of P_f with "conservative" or "optimistic" bounding assumptions might be too large (e.g. probability of failure can range from 0 to 1 in both cases), and results would not be suitable for decision making.
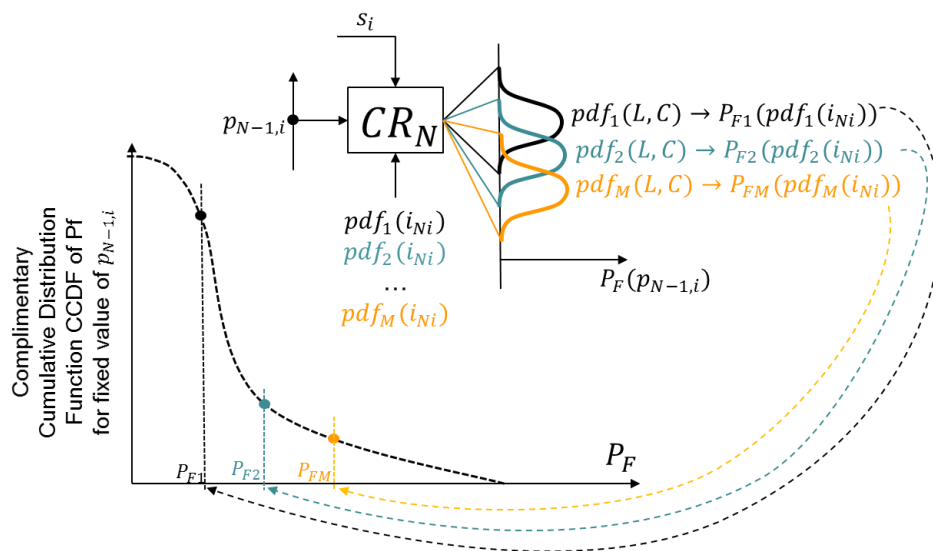
Figure 10: Treatment of model intangible parameters in ROAAM+ framework for Nordic BWR[16].

While ranges of the intangible parameters can be always (conservatively) bounded, the knowledge about distributions within the ranges is missing (i.e. no probabilistic knowledge [14]). In order to assess the importance of the missing information about the distributions we consider distributions as uncertain (i.e. parameters that characterize probability distributions are considered as uncertain parameters).

We randomly select a set of distributions of model intangible parameters $pdf_k(i_{N,i})$ and calculate the value of P_{Fk} for selected combination of model input ($p_{N-1,i}$) and scenario parameters (s_i). Repeating this process for every possible set of distributions of $i_{N,i}$ would yield a probability distribution of P_F, which can be expressed as complimentary cumulative distribution (tail distribution) of probability of failure – $CCDF\left(P_F(s_i, p_{N-1,i})\right)$ (Figure 10).

Repeating the same process for each stage of the framework in the reverse analysis provides distributions of the failure probability for all possible combination of model input p_{ki} and scenario parameters s_i.

3.1.6 Failure Domain

Failure domain is defined as the domain of model input and scenario parameters where the values of P_f exceed respective screening probability level P_S. In the analysis we obtain not a single value of failure probability but a distribution of possible values of P_F. Figure 11 shows an example of possible CCDFs of P_F that can be obtained in ROAAM+ failure domain analysis. These resultant CCDFs can be color-coded as follows:

- o **Green**: at most in 5% of the cases $P_f > P_s$, i.e. with 95% confidence the probability of failure P_F will not exceed selected screening probability P_s. If selected P_s is sufficiently small, then green domain indicates a combination of parameters where "failure is physically unreasonable" regardless of the modeling uncertainties.
- o **Red**: at least in 95% of the cases $P_f > P_s$, i.e. with 95% confidence the probability of failure P_F will exceed selected screening probability P_s. If selected P_s is sufficiently large, then red domain indicates a combination of parameters where "failure is imminent" regardless of the modeling uncertainties.
- o **Blue**: P_F exceeds P_s in 5-50% of the cases.
- o **Purple**: P_F exceeds P_s in 50-95% of the cases.

In the blue and purple domains, we can neither positively exclude failure nor conclude that the failure is imminent, due to the uncertainties in the model deterministic and intangible parameters and their distributions. The two colors were introduced in order to indicate the domains with relatively higher or lower likelihood of failure.
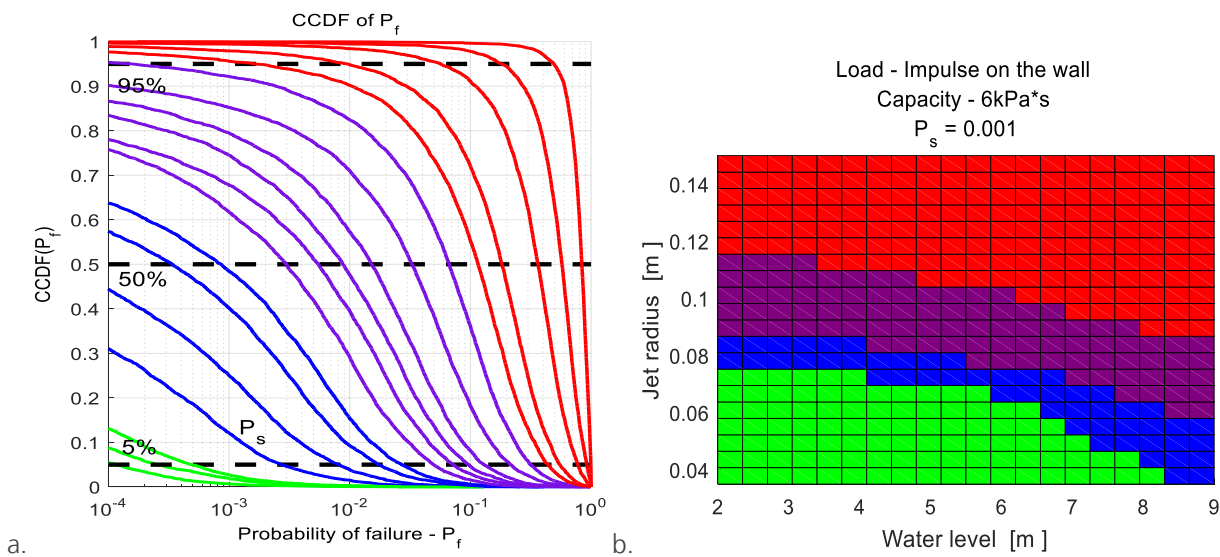
Figure 11. Complimentary cumulative distribution function of probability of failure $CCDF(P_F)$ (a) and an example of the failure domain map (b). [16]

3.1.7 Probabilistic Framework Implementation

This chapter presents a brief overview of implementation of the probabilistic framework in ROAAM+ [16].

The top layer of the ROAAM+ framework is implemented as a set of modules (ROAAM Driver, FoRevAn and SMS), implemented in MATLAB, with respective methods and properties to perform forward and reverse analysis for the whole sequence of casual relationship represented by respective surrogate models (SM). The schematic diagram of probabilistic framework implementation is illustrated in Figure 12.

The main functions of ROAAM+ Driver are:

- User input processing (list of SMs, framework settings for sampling, type of analysis, etc.).
- Generation of the jobs for sensitivity analysis and uncertainty quantification in FoRevAn (Forward and Reverse Analysis) based on the user input (e.g. SM execution order and structure, etc.).

FoRevAn module is responsible for carrying out forward (calculation of failure probability - P_f) and reverse (failure domain) analyses. The main functions of FoRevAn are:

- Execution of the jobs received from the ROAAM+ Driver.
  - Coupling between SMs and generation of the general input/output structure for the whole set of SMs to be used in the analysis.
- Generation of the sampling set in the space of model input - p_{ki} and scenario s_i parameters with static/adaptive grid.

- Random generation of the set of the parameters characterizing probability density functions of model intangible parameters $\{pdf(i_{ki})\}$.
- Generation of the set of multidimensional $pdf(d_{ki}, i_{ki})$, given the information provided by the user.
- Calculation of the probability of failure P_F.
- Failure Domain Analysis.
- Model (SM) sensitivity analysis for individual and coupled SMs.
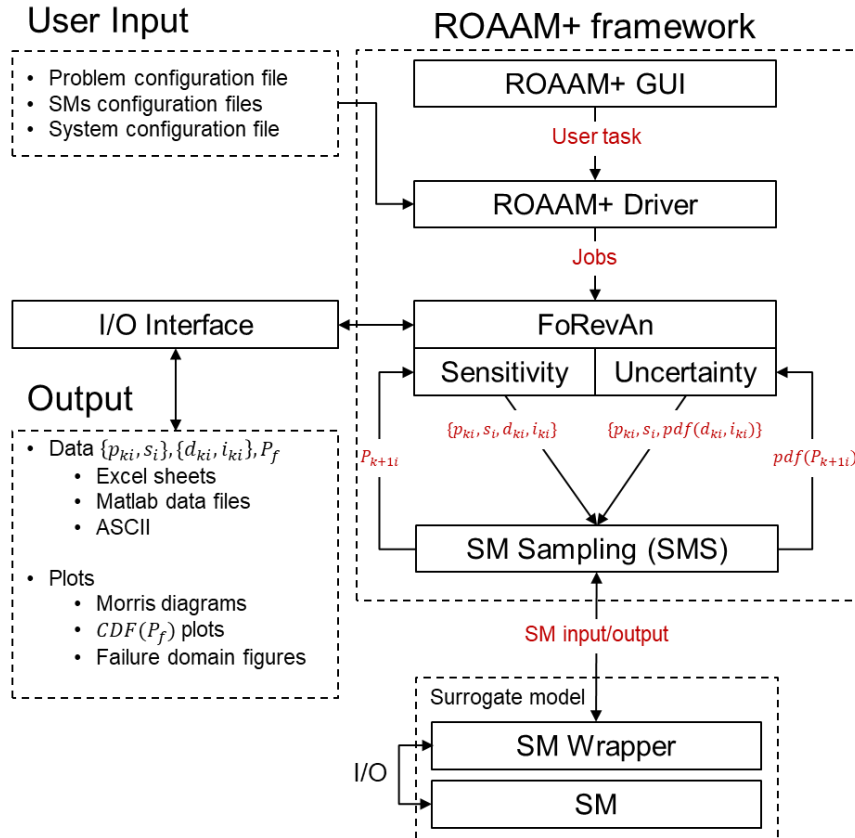
Figure 12. Schematic Diagram of Probabilistic Framework [16].

The execution of individual surrogate models is performed in SMS (Surrogate Model Sampling) Module, where the main functions are:

- Iterative generation of the sampling sets in the domains of model deterministic and intangible parameters according to $pdf(d_{ki}, i_{ki})$ specified by FoRevAn module.
- Execution of the Surrogate model (generating SM input, running the SM, and collecting SM output, checking output ranges).
- Preliminary analysis of the results for each iteration to check statistical convergence of the SM output.
- Reporting of the SM outputs to FoRevAn module.

3.1.8 Sampling

Within the probabilistic framework we perform the sampling in the space of model input and scenario parameters $\{p_{ki}, s_i\}$, deterministic modelling and intangible parameters $\{d_{ki}, i_{ki}\}$ and the space of parameters characterizing probability density functions of model intangible parameters $\{i_{ki}\}$.

For model input and scenario parameters $\{p_{ki}, s_i\}$, the grid-based sampling is used in order to provide coverage of the uncertainty space and knowledge about failure domain location. Note that grid-based approach is most adequate when the size of the failure domain is relatively large (as in the specific application to Nordic BWR case). If size of the failure domain is small and its location is a-priori unknown, adaptive sampling (e.g. based on global optimum search) would be more adequate. In this work we use sampling in the space of model input and scenario parameters $\{p_{ki}, s_i\}$ on the regular (static) grid, with optional Adaptive Mesh Refinement of the boundary of the

failure domain [18],[19]. Application of the grid-based sampling techniques, in general, is computationally expensive, thus, in order to make failure domain analysis more efficient, it is necessary to identify a few most influential parameters. This is done by performing model sensitivity analysis (e.g. using Morris method [20]) with respect to a) individual models; b) coupled models. Model sensitivity analysis allows to improve our understanding of the impact of each step in multi-stage analysis process on the final outcome and on the probability of failure (e.g. Jet diameter – is the most influential parameter for steam explosion, on the other hand Jet diameter is predicted by Melt-Ejection SM [21] and defined by the properties of relocated debris in LP, which in turn depends on the accident scenario and recovery time of safety systems [25].

It is important to note that we use combined space of $\{p_{ki}, s_i\}$ only for the first model in the multistage analysis involving several SMs, if only one SM is used, then both parameter types $\{p_i, s_i\}$ are treated in the same manner.

In probabilistic framework the probability space of model intangible parameters is represented by the joined probability density function that characterize the uncertain parameters. Currently, two distribution families are implemented in the framework: (i) Truncated normal distribution[23]; (ii) Scaled beta distribution [24]. Parameters that characterize probability distributions of model intangible parameters are considered uniformly distributed:

- Truncated normal distribution.
  - Mean values – μ are uniformly distributed on the whole range of respective parameters.
  - Standard deviation – σ is sampled uniformly on the interval (0.1-0.25)(b-a).
- Beta distribution.
  - Beta distribution shape factors - α, β are uniformly distributed on the range [0.1,10].

This selection was motivated by the wide variety of different shapes that these distributions can take. Moreover, if evidence is provided that some values of the distribution are more likely than the others, these distributions can be easily updated to non-uniform, based on the new knowledge, and risk analysis results will be updated (note that consideration of non-uniform distributions of the parameters that characterize pdf's of model intangible parameters is beyond the scope of this work, and subject of the future research).

a.   b.
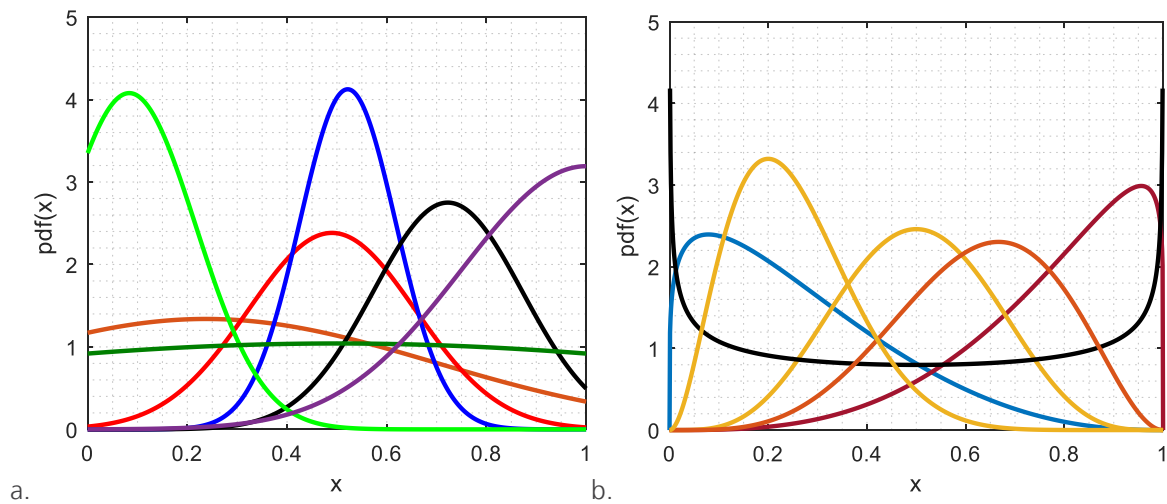
Figure 13. Example of randomly generated PDFs with different shape factors or parameters using (a) Truncated Normal Distribution Family; (b) Beta Distribution Family.

Sampling in the space of model deterministic and intangible parameters $\{d_i, i_i\}$ is performed using Halton [25][27][28] sequence based on respective probability distributions. The number of samples in space of $\{d_i, i_i\}$ parameters depends on the convergence of the SM output.

Currently there are two approaches for sampling in the space of model deterministic and intangible parameters $\{d_i, i_i\}$ implemented in the framework. These approaches are schematically represented in Figure 14 and briefly discussed below:

- Monte Carlo sampling.

- In case of Monte Carlo sampling, the sampling in the space of $\{d_i, i_i\}$ is performed based on the joint PDF, which include randomly generated PDFs for model intangible parameters. The sampling is performed for every set of randomly generated PDFs until either convergence of the resultant distribution is achieved or maximum number of samplings is reached, defined for both – amount of randomly generated PDFs and SM samplings.
- The probability of failure is approximated as the fraction of samples resulted in failure (load exceeding capacity) for every set of randomly generated PDFs.
- Importance Sampling.
  - In case of Importance sampling, the sampling in the space of $\{d_i, i_i\}$ is performed using uniform distribution. The sampling is performed until convergence of the resultant SM output distribution is reached or the max. amount of SM samplings is reached.
  - The probability of failure is approximated as the fraction of samples resulted in failure (load exceeding capacity), where every sample is weighted by the importance weights derived from the target PDF and sampling PDF (uniform) [29][30]. The sampling of target PDFs is performed until either convergence of the distribution of probability of failure or the max. number of samples is reached.
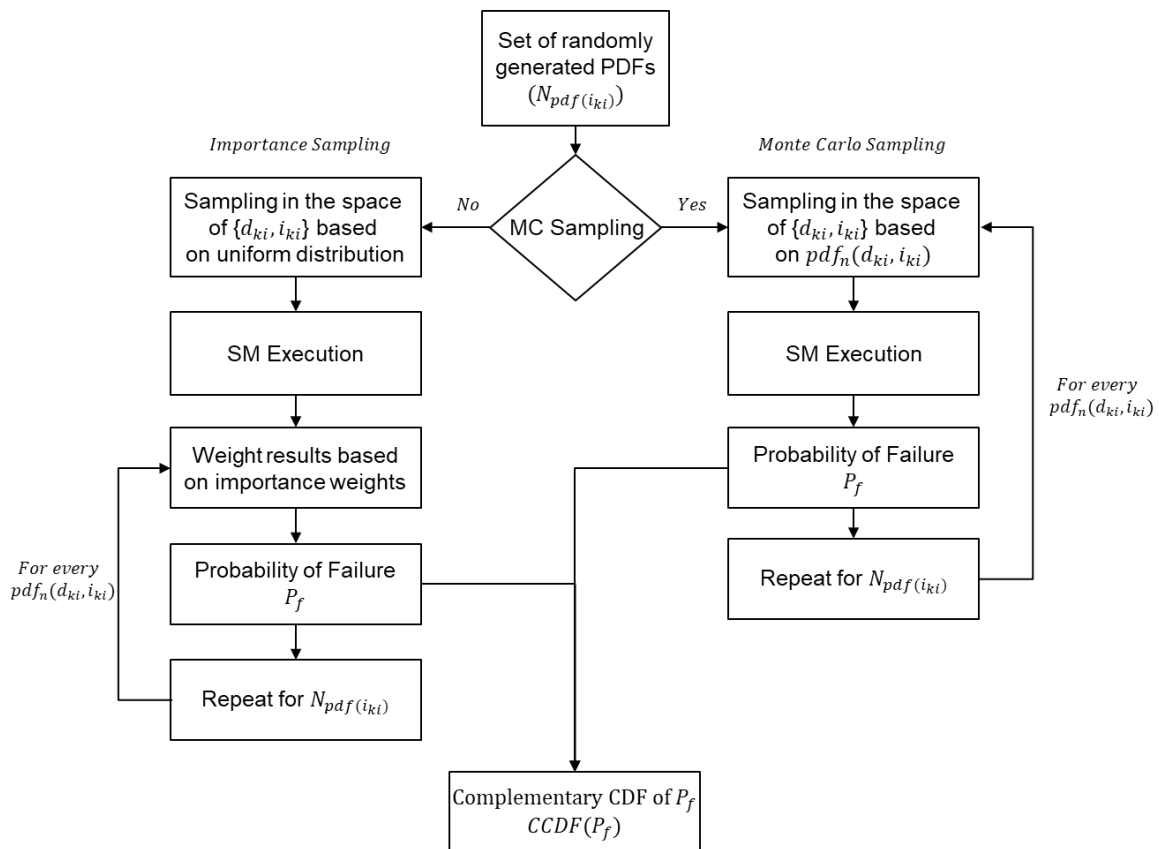
Figure 14. Schematic representation of approach for quantification of the uncertainty in P_f [16].

3.1.9 ROAAM+ GUI

The graphical user interphase has been developed based on the main modules of the ROAAM+ probabilistic framework, described in the previous sections. The software implementation is designed to facilitate the usage of the main features of the probabilistic framework, such as model (SM) sensitivity analysis, forward and reverse analysis, post-processing of the results and results visualization. Furthermore, it provides a quick access to the major part of the framework execution settings, problem configuration and surrogate model input files.

Within this software tool the user can perform:

- Model sensitivity analysis (using Morris method).
  - For individual and coupled surrogate models.
- Probabilistic framework execution, which include:
  - Forward analysis (for coupled and individual surrogate models).
  - Reverse analysis (for coupled and individual surrogate models).
- Generation and visualization of failure domains
  - Visualization of failure domains can be performed for failure domains that include up to 3 scenario/input parameters (0D,1D,2D and 3D).
- Data and analysis results export (probability of failure and all relevant data) to Excel
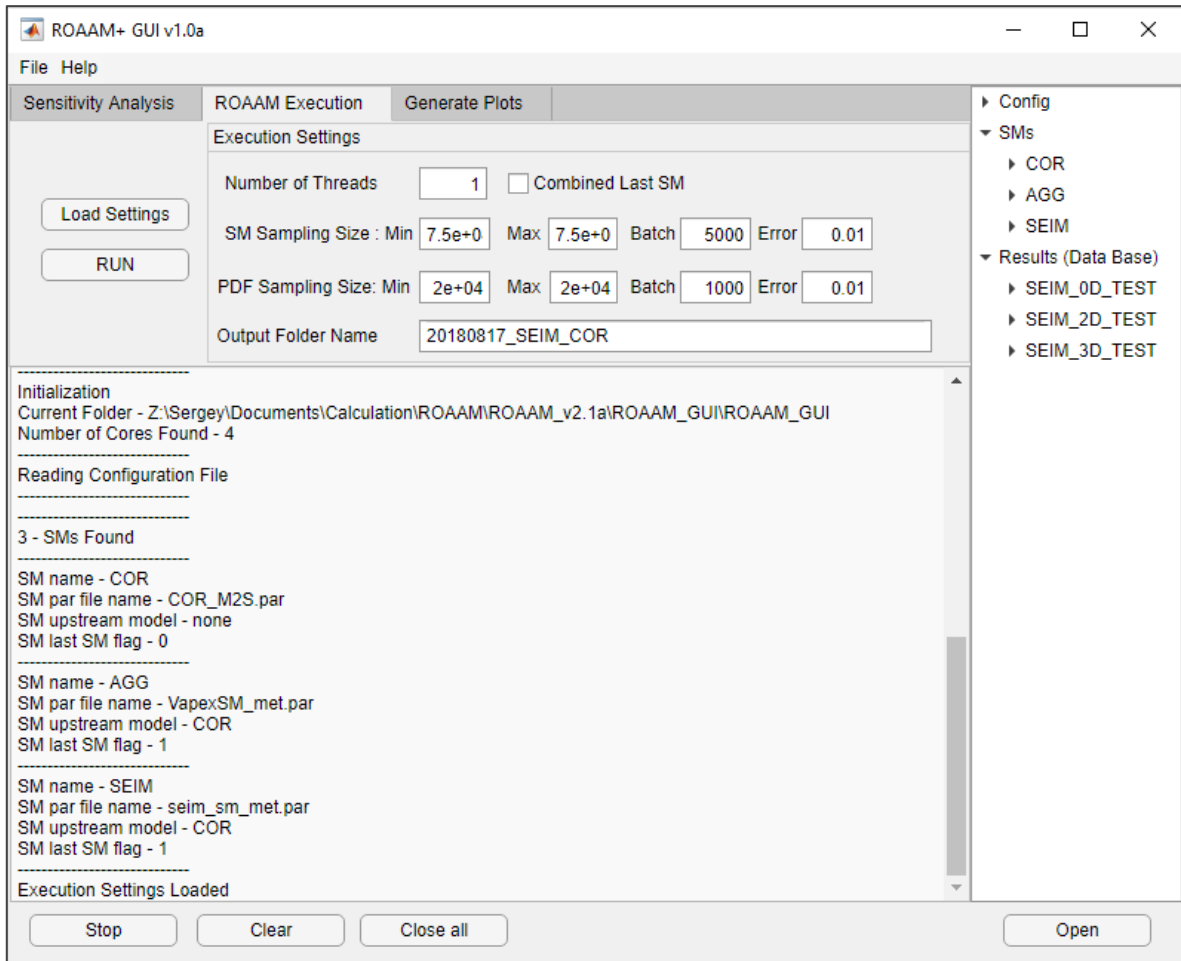
Figure 15. ROAAM+ GUI Interface.

An extension to ROAAM+ GUI has been developed to export analysis results into specific format that can be used directly in the RiskSpectrum PSA, in form of "user defined simulation values". In RiskSpectrum PSA these values can be used as probabilities, failure rates, frequencies, etc., for uncertainty analysis in PSA models [67].

In current implementation ROAAM+ results are exported into RS PSA user defined simulation parameters as probabilities ("ParamType<Number>=1"), that can be used as basic events probabilities (e.g. probability of failure due to ex-vessel steam explosion, ex-vessel debris coolability). This functionality is accessible through the following menu in ROAAM+ GUI (File->Export->Export results to RS PSA), and schematically illustrated in Figure 16. Furthermore, basic information regarding each case can be found in the file "!_CaseData.txt" generated automatically during ROAAM+ results export.

This information includes:

- Names of scenario parameters, (record I.Names followed by parameter names (e.g. [XPW], [SLPA] – the same names are used in SM\FM parameter definitions presented in the tables 2, 4, 6 and 8).

- ROAAM data base scenario number.

- Respective output file number (CASEID_NNN) with the values of probability of failure.

- Failure mode number (FM-N) and the record O.Names followed by output parameter names (e.g. [TEMPMAX]>[TEMPMAXLIMIT2] – the same names are used in SM\FM output parameter definitions presented in the tables 3, 5, 7 and 9)).

- Descriptive statistics, such as:
  - o 0.05,0.25,0.5,0.75,0.95 quantiles of distributions.
  - o Expected value and standard deviation.
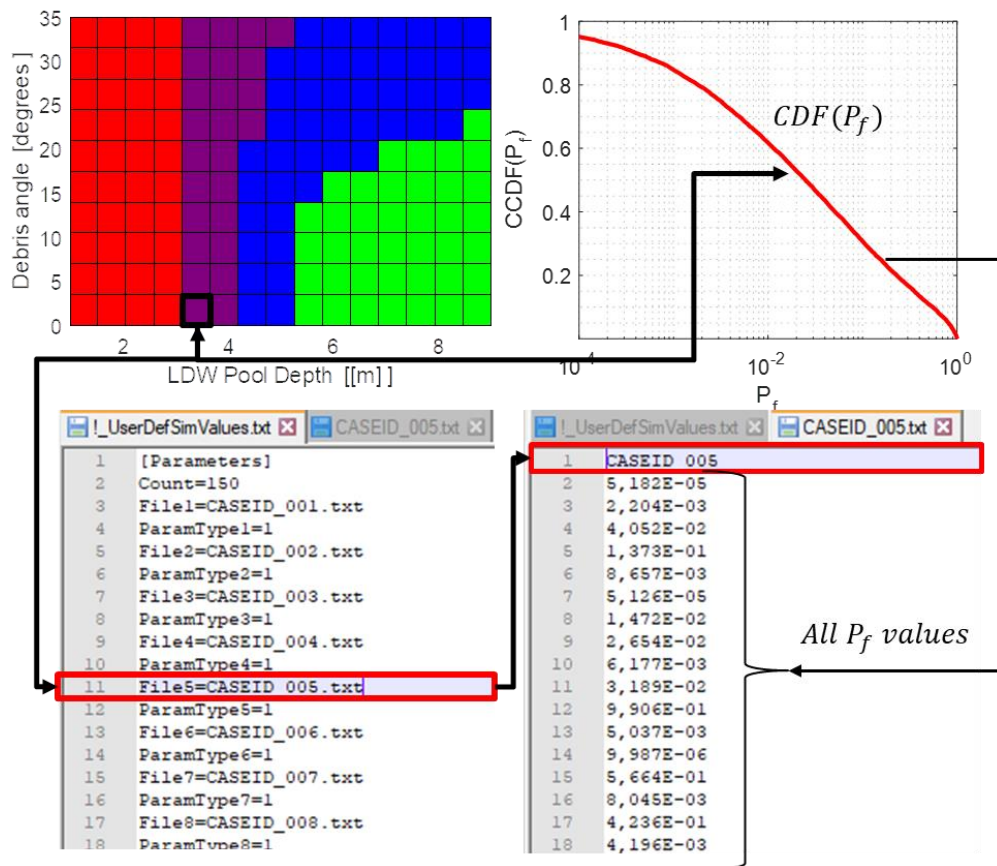
Figure 16. ROAAM+ Results Export to RiskSpectrum PSA.

3.2 ROAAM+ Deterministic Models

This chapter provides a brief overview of full and surrogate models used in the ROAAM+ framework for Nordic BWR, that connect plant damage states with respective threats to containment integrity. This models include (i) Melt ejection surrogate model (MEM SM), based on MELCOR code; (ii) Steam explosion surrogate model (SEIM SM), based on TEXAS V code; (ii) Ex-vessel debris agglomeration (AGG SM) – based on VAPEX SD code; (iv) ex-vessel debris coolability (DECO SM), based on DECOSIM code.

3.2.1 Melt Ejection Surrogate Model

The goal of Melt Ejection Framework (MEM) in ROAAM+ for Nordic BWR is to develop deterministic and surrogate models to establish connection between plant damage states and respective characteristics of (i) core relocation; (ii) vessel failure (timing and mode); and (iii) melt ejection (vessel breach size, melt superheat, composition, flow

rate and total amount of ejected melt). Figure 17 show the general approach for development of Core relocation and Vessel Failure frameworks and respective surrogate model (MEM SM) in ROAAM+ for Nordic BWR.
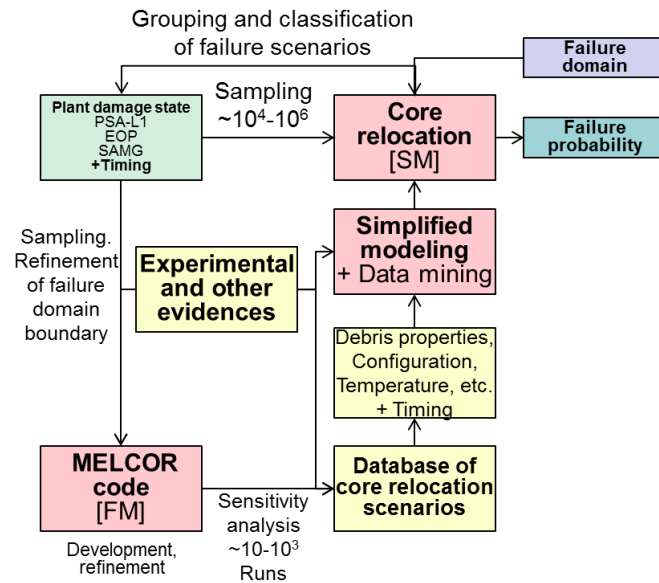
Figure 17. Core relocation and Vessel Failure Framework in ROAAM+ for Nordic BWR [1].

In ROAAM+ Framework for Nordic BWR Melt Ejection Surrogate Model (MEM SM) is used to predict melt release conditions from the vessel. Melt ejection mode surrogate model (MEM SM)[21] is based on the uncertainty analysis results of vessel failure mode and melt release conditions in Nordic BWR[32] predicted by MELCOR code[34][35].
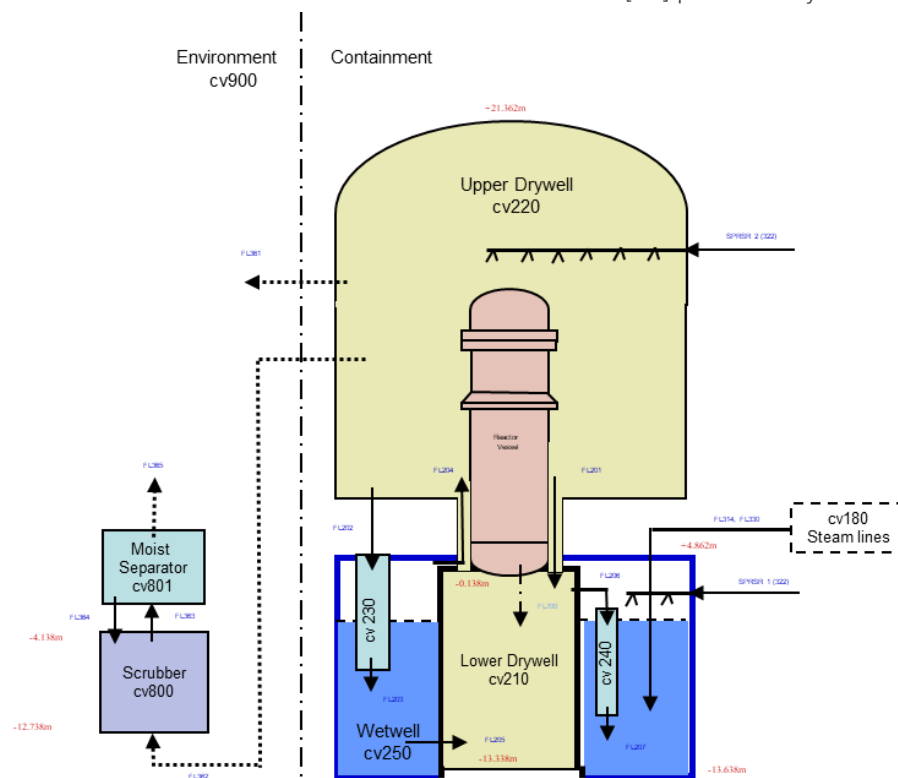
Figure 18. Nordic BWR Containment MELCOR Nodalization.

The MEM SM is built for the unmitigated station blackout (SBO) scenario with depressurization, denoted as (SBO LP). In considered scenario (Figure 19), the accident is initiated by the station blackout that results in complete loss of safety systems that require AC power. That is, the systems such as Emergency Core Cooling System (ECCS, both high and low pressure), Residual Heat Removal System (RHR) are considered unavailable during the whole

transient. Reactor shutdown, safety relief valves and automatic depressurization systems are activated according to the control logic. Flooding of the lower dry well (LDW) from the wet well for ex-vessel debris coolability is initiated according to the standard control logic, i.e. (water level below TAF for 10min.). Containment venting system (CVS) includes filtered (through CVS MVVS – multi-venturi scrubbing system) and non-filtered containment venting, which are activated when correspondent pressure set-points are reached (5.5Bar and 6.5Bar in the upper drywell).
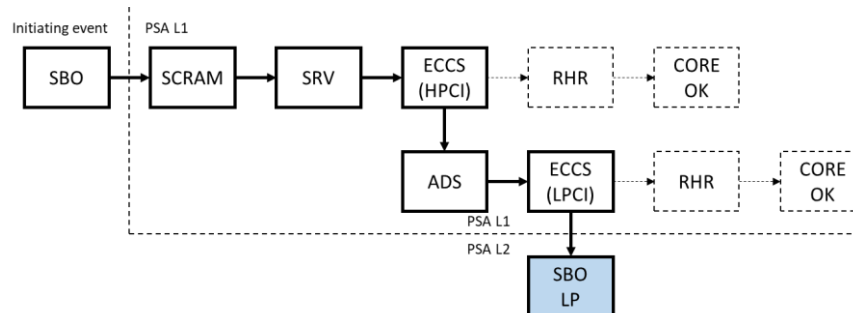
Figure 19. Block diagram for SBO LP Scenario.

The mode of vessel failure and melt release conditions depend on in-vessel phase of accident progression and respective phenomena, such as thermal hydraulic behavior in the reactor pressure vessel, degradation and relocation of the fuel and respective structures in the core, debris bed formation in the lower plenum, debris interaction with lower plenum structures and eventual vessel lower head failure, either due to ejection of one\several of IGTs or CRGTs or vessel lower head wall failure due to creep-rupture. In MELCOR code these phenomena are represented by MELCOR models and respective modelling parameters that can affect MELCOR predictions of these phenomena. In MELCOR analysis performed to study these phenomena[32][33], and generate necessary data for surrogate model development, we considered 11 MELCOR modelling parameters, presented in Table 2. Detailed discussion on parameters selection and sensitivity of the MELCOR code response to the variability of these parameters can be found in [33] and MELCOR code manuals [34][35].

Additionally to the parameters defined in Table 2, we considered the effect of the solid debris ejection mode in MELCOR code (denoted as *IDEJ0* vs *IDE1*) and the fraction of failed penetration once penetration failure criterion is reached (denoted as *EIGT25* and *EIGT100*), which is discussed further in this section.

Note that in the MELCOR code the vessel lower head can fail due to penetration failure and\or vessel lower head wall failure, and these mechanisms are not mutually exclusive, i.e. failure of a penetration(s) in one (several) radial rings does not exclude eventual vessel LH wall failure. The vessel lower head wall can fail either due to creep-rupture which can occur as a result of mechanical loading under conditions of material weakening at elevated temperatures, or when the temperature of the bottom lower head node exceeds the penetration failure temperature TPFAIL defined by the user. In case of gross failure of vessel wall (e.g. due to creep-rupture), it is assumed that all debris in the bottom axial level of the corresponding ring, regardless its state, is discharged linearly over 1s time step without taking into account failure opening diameter. In case of penetration(s) failure there are two options for the mode of debris ejection from the vessel provided by so called solid debris ejection switch (Figure 20). In the default option (ON, IDEJ = 0), the masses of each material available for ejection are the total debris and molten pool material masses, regardless of whether or how much they are molten. In the second option (OFF, IDEJ = 1), the masses of steel, Zircaloy, and UO_2 available for ejection are simply the masses of these materials that are molten; the masses of steel oxide and control poison materials available for ejection are the masses of each of these materials multiplied by the steel melt fraction, based on an assumption of proportional mixing; the mass of ZrO_2 available for ejection is the ZrO_2 mass multiplied by the Zircaloy melt fraction. Additionally, the mass of solid UO_2 available for ejection is the Zircaloy melt fraction times the mass of UO_2 that could be relocated with the Zircaloy as calculated in the candling model using the secondary material transport model [34][35].
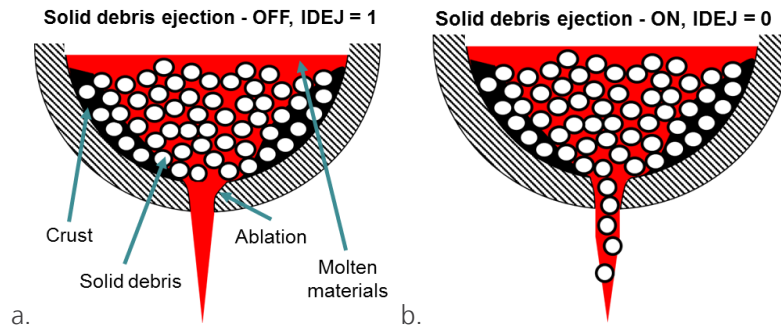
Figure 20. MELCOR modelling of debris ejection in case of penetration failure: (i) IDEJ1 – Solid debris ejection – OFF; (ii) IDEJ0 – Solid debris ejection – ON.

The effect of the number of failed penetrations is considered in the MEM SM to account for inherit randomness of the process, through total breach area (denoted as *EIGT100, EIGT25* – where we consider that either 100% of 25% of IGTs in respective radial rings would fail once the correspondent failure criterion is reached). The scenario with ejection of CRGTs is not considered in the analysis, since CRD housing support located under the vessel should limit the downward displacement of the tube.

More details on MELCOR analysis of vessel failure mode and melt release conditions can be found in [32][33].

Current state of the art knowledge in the field of vessel failure mode and multi-component debris ejection from the vessel is quite limited. In reality it is difficult to assess the fraction of failed (ejected) penetrations. The process of vessel failure and debris ejection involve several interacting phenomena, which include formation and accumulation of liquid melt, gravity driven drainage of molten materials through the porous debris bed, melt resolidification and crusts formation in colder regions of the debris bed, that prevent further material drainage, which can result either in slow dripping of the melt from the vessel or in accumulation of significant amounts of superheated metallic melt above the crust, which will be released upon crust remelting/failure. The crust formation can result in interaction of significant amounts of debris at high temperature with vessel lower head wall, and significant mechanical load on the structure which can lead to creep-rupture failure of the vessel lower head and massive ejection of debris from the vessel.

Fraction of failed penetrations and debris ejection mode (solid debris ejection switch) are treated as splinters [5] in ROAAM+ considering the (i) high sensitivity of MELCOR results to the selection of these parameters and (ii) lack of knowledge about them.

Splinter scenario in ROAAM [5] is defined as a scenario where relevant epistemic uncertainties are *beyond the reach of any reasonably verifiable quantification*.

Thus, the total of 4 different splinter scenarios, represented by the combinations of the fraction of failed penetrations (*EIGT*) and the mode of debris ejection from the vessel (*IDEJ*), with respective surrogate models are considered in the analysis:

- Solid debris ejection – on (*IDEJ0*) with 100% of IGTs ejected at penetration failure in respective radial ring (*EIGT100 IDEJ0 LP*)
- Solid debris ejection – off (*IDEJ1*) with 100% of IGTs ejected at penetration failure in respective radial ring (*EIGT100 IDEJ1 LP*).
- Solid debris ejection – on (*IDEJ0*) with 25% of IGTs ejected at penetration failure in respective radial ring (*EIGT25 IDEJ0 LP*).
- Solid debris ejection – off (IDEJ1) with 25% of IGTs ejected at penetration failure in respective radial ring (*EIGT25 IDEJ1 LP*).

Furthermore, it is important to emphasize that the mode of debris ejection from the vessel (IDEJ) was identified as the major contributor to the uncertainty in the mode and properties (massive release vs. dripping release) of debris ejection from the vessel (Figure 21) [32][33], and conditional containment failure probability due to ex-vessel steam explosion[22].
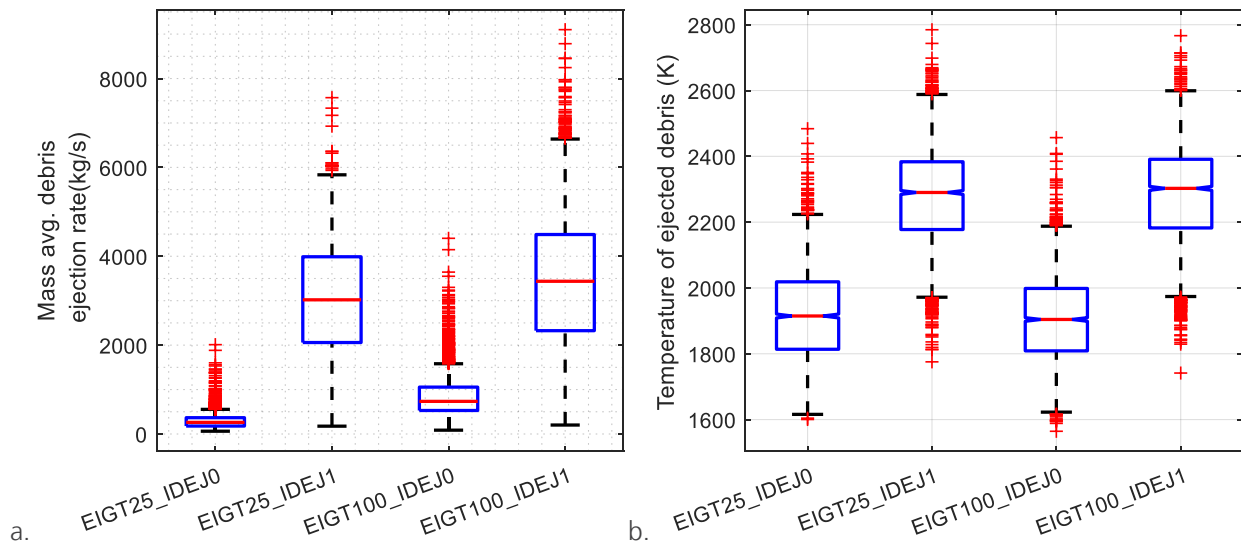
Figure 21. (a) Mass averaged debris ejection rate (kg/s); (b) Mass averaged temperature of ejected debris (K)[32].

For instance, it has been found[32][33] that in case of IDEJ1 – 100% of the MELCOR simulations resulted in eventual vessel lower head wall failure due to creep-rupture after some time delay after initial vessel breach due to failure of IGTs in one of the radial rings, on the other hand in case of IDEJ0 – only ~25% of the cases results in creep-rupture failure of the vessel lower head.

The list of the MEM SM input parameters and their ranges is presented in Table 2.

Table 2. MEM SM epistemic modeling parameters and ranges.

Parameter name	Range	Units
Particulate Debris Porosity (PDPor)	[0.3-0.5]	[-]
LP Particulate debris equivalent diameter (DHYPDLP)	[0.002-0.005]	m
Time Constant for radial (solid) debris relocation (SC10201)	[180-720]	sec
Time Constant for radial (liquid) debris relocation (SC10202)	[30-120]	sec
Velocity of falling debris (VFALL)	[0.01-1.0]	m/s
Molten Zircaloy Melt Break Through Temperature (SC1131-2)	[2100-2540]	K
Molten cladding/pool drainage rate (SC1141-2)	[0.1-2.0]	kg/m-s
Refreezing heat transfer coefficient for Zircaloy (HFRZZR)	[1000-7500]	W/m2-K
Refreezing heat transfer coefficient for stainless steel, control rod poison material (HFRZSS)	[1000-2500]	W/m2-K
Heat transfer coefficient from debris to penetration structures (HDBPN)	[100-1000]	W/m2-K
Penetration Failure Temperature (TPFAIL)	[1273-1600]	K

Post-processing of MELCOR analysis results [32] of vessel failure mode and melt release conditions has been performed, in order to provide initial data base of full model solutions for the development of the MEM SM. This step is necessary, since the MELCOR code does not predict directly such parameters as jet radius and jet speed used as initial conditions in the model for assessment of ex-vessel steam explosion loads on the containment (called SEIM SM) in Nordic BWR. The details of MELCOR code results post-processing can be found in [21]. In the following we list the assumptions and limitations made in the results post-processing, since it can affect risk analysis results.

When performing post-processing of the MELCOR results the following assumptions have been made[21]:

- Uniform distribution of ejected debris flow between all failed IGTs, without taking into account failed IGTs locations (e.g. in the center or periphery).

- Ejected debris density is assumed to be equal to $\rho = 8000 \left(\frac{kg}{m^3}\right)$ (based on SERENA-II BWR benchmark exercise [36][37]).
- Debris ejection rate $\dot{M}_{deb}$ is uniform during MELCOR plotting time step $\Delta T_P(s)$.
- Debris ejection temperature is calculated as the maximum particulate debris temperature in the COR cells adjacent to the vessel lower head.
- No correction is made for the fraction of solid debris during debris ejection from the vessel.
- If gross failure is declared (due to vessel lower head creep-rupture) the ejection is calculated as a single jet with jet radius defined as $R_{MAX} = 300mm$ (max. permitted value of SEIM SM [37]) and respective jet velocity is recalculated based on the jet velocity at water level as follows (see reference [21] for more details):
  1 Jet velocity and radius are recalculated on the water level (U_{WL}, R_{WL}) from (U_{MELC}, R_{ring}) – MELCOR predicted jet velocity and radius (in this case it is assumed to be equal to respective ring cross sectional area, where gross failure has occurred).
  2 Jet velocity (UPIN) is recalculated back assuming jet radius to be equal R_{MAX}.
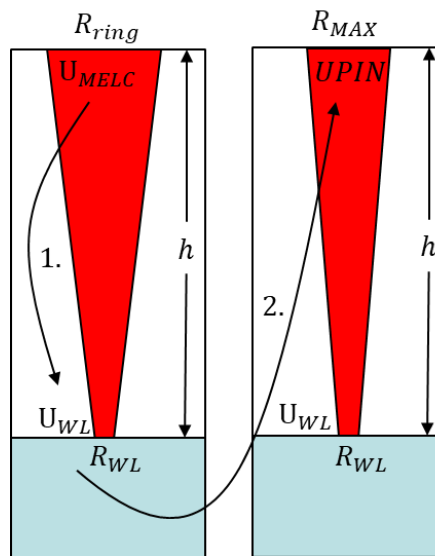
Figure 22. Treatment of Jet Radius and Ejection Velocity in case of vessel lower head wall creep-rupture in MELCOR code and MEM SM.

The last assumption is particularly necessary, since MELCOR code does not consider neither debris state nor breach area when calculating debris ejection in case of gross failure of vessel lower head wall (e.g. due to creep-rupture). Currently, it is assumed in MELCOR code that all debris in the bottom axial level of the corresponding ring, regardless its state, is discharged linearly over 1s time step without taking into account failure opening diameter [34][35].

The list of MEM SM outputs and their ranges is presented in Table 3.

Table 3. MEM SM output parameters and their ranges.

Parameter name	Range	Units
Lower drywell pool depth	[2-9]	M
Lower drywell pressure	[1.e5-5.5e5]	Pa
Lower drywell pool temperature	[293-393]	K
Jet radius	[0.035-0.3]	M
Melt inlet temperature	[1700-3200]	K
Initial jet velocity	[0-8]	m/s
Time after SCRAM	[10000-50000]	sec
Melt release duration	[1000-10000]	sec
Ejected debris mass	[150000-300000]	Kg

3.2.2 Ex-vessel Steam Explosion Surrogate Model

Steam explosion in a deep pool is a credible threat to containment integrity potentially leading to large early release of radioactive products to the environment. The general approach for development of ex-vessel steam explosion impact map (SEIM) and respective surrogate model (SEIM SM) is illustrated in the Figure 23.
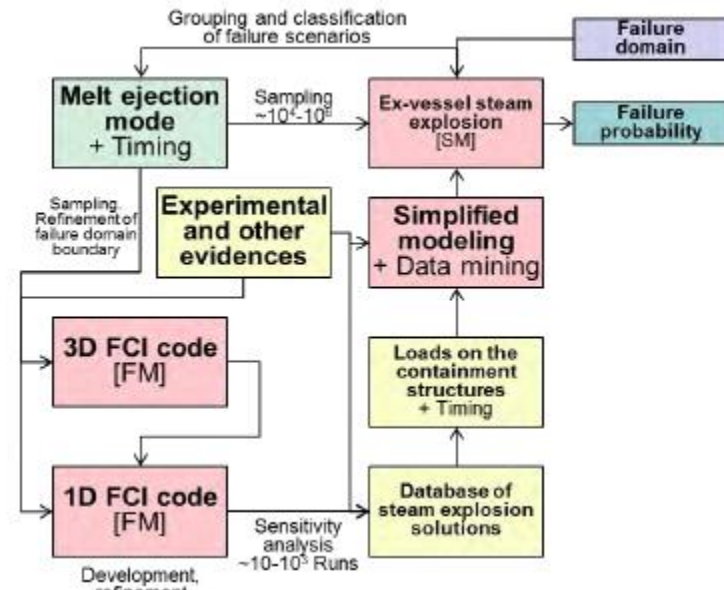
Figure 23. Ex-vessel steam explosion framework in ROAAM+ for Nordic BWR [1].

Steam Explosion Surrogate Model (SEIM SM) is a fast running surrogate model that been developed[37][38] for the assessment of the risk of containment failure due to steam explosion in Nordic BWR [39]. The conceptual problem setting in TEXAS-V for assessment of the effect of melt release conditions in Nordic BWR of the loads on the containment is demonstrated in Figure 24. Development of the SM relies on a database of solutions generated by a 1D FCI code TEXAS-V. Texas-V is a 1D 3-field transient code with Eulerian fields for gas and liquid and a Lagrangian field for fuel particles. It is comprised of two modules for calculation of premixing and steam explosion [41].

The surrogate model is based on TEXAS-V code results and developed using deep (2 hidden layers) Multilayer Perceptron Artificial Neural Network (ANN)[37][38].
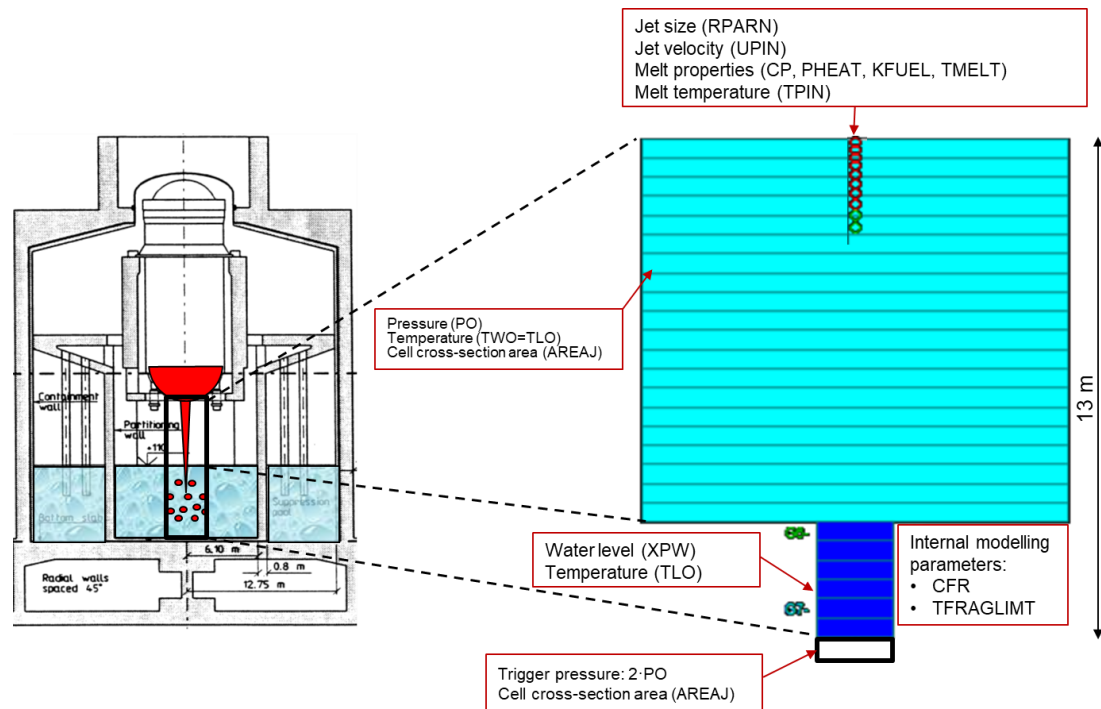
Figure 24. Nordic BWR TEXAS-V model setup [40].

The ANN predicts impulses which correspond to certain percentiles of the impulse distribution for given melt release characteristics (see the list of the parameters in Table 4) and arbitrary triggering time. The motivation for the parameters selection and respective ranges can be found in [37].

Table 4. SEIM SM input and epistemic modelling parameters and ranges.

Parameter name	Range	Units
Water level (XPW)	[2-9]	m
System pressure (PO)	[1.e5-5.5e5]	Pa
Water temperature (TLO)	[288-368]	K
Initial Jet radius (RPARN)	[0.035-0.3]	m
Fuel heat capacity (CP)	[350-650]	J/kg*K
Fuel density (RHOP)	[7500-8000]	kg/m³
Fuel latent heat (PHEAT)	[2.6e5-3.0e5]	J/kg
Fuel melting temperature (TMELT)	1700	K
Fuel inlet temperature (TPIN)	[1710-3200]	K
Melt release velocity (UPIN)	[1-8]	m/s
Fuel thermal conductivity (KFUEL)	[6-32]	W/m*K
Proportionality constant for the rate of fuel fragmentation (CFR)	[2.e-3-2.7e-3]	-
Fragmentation time (TFRAGLIMIT)	[0.5e3-2.5e-3]	s

Table 5. SEIM SM output parameters and ranges.

Parameter name	Range	Units
Explosion impulse on pedestal wall	[0-100]	kPa*s
Explosion impulse of pedestal floor	[0-100]	kPa*s

Note that since MELCOR code in most of the cases predicts melt release temperatures below 2500-2700K [32][33], we assume mostly "metallic release", thus melt properties (such as, CP, RHOP, KFUEL, etc.) were adjusted accordingly.

3.2.3   Ex-vessel Debris Coolability

Non-coolable debris bed in the lower drywell presents a credible threat to containment integrity. Phenomenology of ex-vessel debris formation and coolability includes (i) jet breakup; (ii) melt droplets cooling and solidification; (iii) agglomeration of melt droplets; (iv) particulate debris spreading in the pool; (v) debris self-levelling; (vi) debris coolability; (vii) post-dryout debris behavior (e.g. remelting).

Debris bed is cooled by evaporation water that is pushed inside the debris bed by hydrostatic pressure. Steam generated inside the debris bed is escaping predominantly upwards, generating convection flows in the pool and changing conditions for melt-coolant interactions. This changes particle properties (size distribution and morphology), packing, agglomeration, and bed formation phenomena. The large-scale circulation in the pool can spread effectively the falling corium particles over the basemat floor, distributing the sedimentation flux beyond the projection area of particle source (e.g., size of reactor vessel). Debris is gradually spread under the influence of steam production in the bed, resulting in self-leveling of the settled portion of the debris and changing the shape of debris bed with time.

General approach for development of ex-vessel debris coolability framework in ROAAM+ for Nordic BWR is presented in Figure 25. The whole problem is currently subdivided into 3 subtasks: i) analysis of the effect of melt release conditions on jet breakup, droplets cooling and solidification and agglomeration of melt droplets – treated in Debris Agglomeration analysis (VAPEX SM and Agglomeration mode [42][43]) and Agglomeration SM (AGG SM [44]) ; ii) ex-vessel debris spreading and coolability – threated in DECOSIM code (DECO SM)[45][46].

Figure 25. Ex-vessel debris coolability framework in ROAAM+ for Nordic BWR [1].

The overview of respective full and surrogate models (Figure 25) is presented in sections 3.2.3.1 and 0.

3.2.3.1 Ex-vessel Debris Agglomeration

Hydraulic resistance is a limiting factor that determines maximum decay heat that can be removed from the bed. If decay heat exceeds this maximum value, it will lead to the bed dryout, reheating and remelting of the debris. If melt is not completely solidified prior to settlement on top of the debris bed, agglomeration of the debris and even "cake" formation is possible [47]. Formation of agglomerated debris can significantly increase hydraulic resistance

and reduce maximum decay heat which can be removed without reaching dryout of the debris bed. Thus, agglomeration is important factor which can inhibit effectiveness of ex-vessel debris coolability [47].

Phenomena of agglomeration of the debris and "cake" formation have been observed in fuel-coolant interaction (FCI) experiments with prototypic corium mixtures (e.g. in FARO [49], CWTI and CCM [50] tests) and with corium simulant materials (e.g. in DEFOR-E [51] and DEFOR-S [48] tests), the first systematic experimental data was provided in DEFOR-A [53], [54], [55] tests that was used for development and validation of modeling approaches for prediction of agglomerated debris in various scenarios of melt ejection
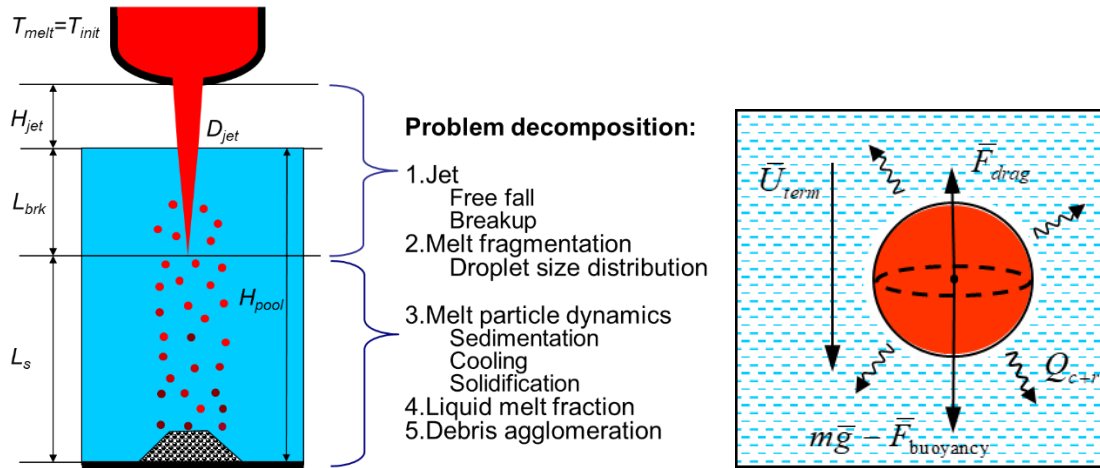
Figure 26. Problem decomposition for development of surrogate model of prediction of debris agglomeration [44].

The data obtained in DEFOR-A tests was used for development and validation of modelling approaches for prediction of agglomerated debris in various scenarios of melt ejection (e.g. [42], [43]). Proposed model for agglomeration is implemented in deterministic code VAPEX [56] that simulates Fuel-Coolant-Interaction (FCI) phenomena including melt jet breakup, formation of liquid droplets, heat transfer between melt and coolant, sedimentation and solidification of the particles.

Based of VEPEX code a physics based surrogate modelling approach was employed where computational efficiency and numerical stability are achieved by (i) considering only most important physical phenomena, and by (ii) decomposing tightly coupled problem into a set of loosely coupled ones with information exchange through initial and boundary conditions. The merits of physics-based SM are (i) reduced number of the full model runs which are necessary for the calibration process; (ii) application of the SM beyond the domain covered with the original model. Physical phenomena and parameters important for assessment of agglomeration fraction are presented in Figure 26. The most important physical phenomena are modelled in the SM explicitly. Mutual feedbacks between such parameters as jet breakup length, coolant void fraction and velocity are considered as closures. Details of model implementation, calibration and verification are provided in [42], [43].

Based on VAPEX code and physics-based agglomeration modelling an ANN based surrogate model (AGG SM) for analysis of the fraction of agglomerated debris has been developed [44]. The AGG SM predicts the fraction of agglomerated debris depending on melt release and pool conditions, provided by MEM SM. The list of input parameters of AGG SM is presented in Table 6. More details on full and surrogate models, experimental data and parameters used for SM development can be found in [42][43] [44] and [47].

Table 6: AGG SM input parameters.

Variable Name	Description	Units	Range
RHOP	Fuel density	kg/m3	[7500 ; 8500]
PHEAT	Fuel latent heat	J/kg	[2.6e5 ; 4.0e5]
CP	Fuel heat capacity	J/kg*K	[350 ; 650]
KFUEL	Fuel thermal conductivity	W/m*K	[2 ; 42]
EM	Emissivity	-	[0.1 ; 1.0]

Variable Name	Description	Units	Range
TMELT	Fuel Melting Temperature	K	[1600 ; 2800]
TSH	Melt superheat	K	[10 ; 1000]
RPARN	Jet radius	m	[0.07 ; 0.6]
UPIN	Melt release velocity(initial)	m/s	[1 ; 8]
TLO	Water pool temperature	K	[288 ; 368]
XPW	Pool depth	m	[5 ; 9]
PO	Containment pressure	Pa	[1e5 ; 4e5]

Table 7. AGG SM output parameters and ranges.

Parameter name	Range	Units
Fraction of agglomerated debris	[0-1]	[-]

3.2.3.2 Ex-vessel Debris Coolability

Ex-vessel debris coolability surrogate model (DECO SM) is based on DECOSIM code. The mathematical models implemented in DECOSIM code are based on multifluid formulation, they include several submodules describing two-phase pool flows, disperse particle sedimentation, as well as flows in heat-releasing porous media related to debris bed coolability in in-vessel and ex-vessel configurations. In this work, we concentrate on validation of the models relevant to modeling natural convection flows in the pool, spreading of particles and their fallout onto the bottom surface of the pool [46]. Air-water flow in the pool is described by the mass and momentum, and energy conservation equations for liquid water and gas; turbulence is taken into account only in continuous liquid and described by the $k-\varepsilon$ model with additional terms for turbulence generation due to relative motion of liquid and gas phases. Validity of $k-\varepsilon$ turbulence model in the context of two-fluid model has been addressed previously [57]. Flow-particle interaction due to drag depends on the diameter of the particle, relative velocity and phase composition of the ambient two-phase mixture. To account for turbulent dispersion of particles, the random walk model is applied. The effects of turbulence on particle dispersion are modelled by adding a fluctuating component to the liquid phase velocity.
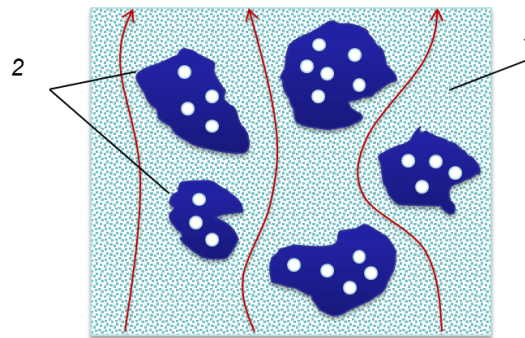

Figure 27. Sketch of porous debris having nominal porosity ε_0 (1) with impermeable agglomerates (2) possessing internal porosity $\varepsilon_{int.d}$. Fluid flow (shown by arrows) is only possible in the part of the volume occupied by the porous material[58].

A set of improvements to full and surrogate models has been performed recently in order to account for low permeability zones in the bulk of debris bed, which can happen due to incomplete fragmentation of corium jet due to e.g. jet penetration depth is larger than pool depth; agglomeration of debris fragments due to incomplete solidification of melt droplets, etc. Furthermore, formation of low permeability zones can be enhanced by effective pool depth decrease with time due to debris bed growth and increase in jet size due ablation of the opening in the vessel.
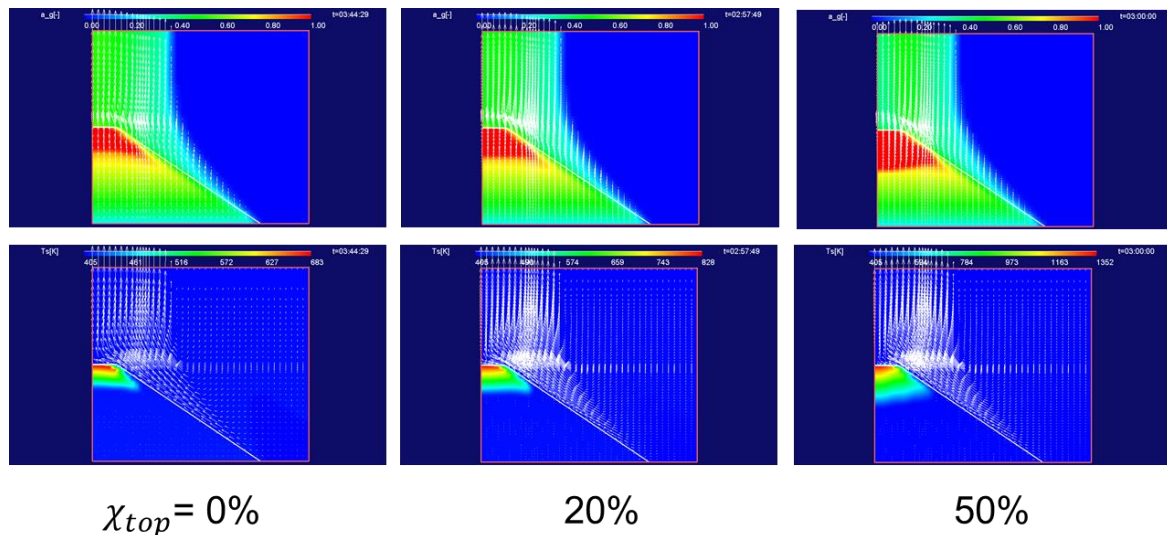
χ_{top}= 0% 20% 50%

Figure 28. Void fraction (top row), particle temperature (bottom row) for particle size (d_p=2mm), decay heat power W=250W/kg [58].

Based on a set of full model simulations it has been shown that agglomerates (χ_{top}) increase drag and promote development of a larger and hotter dry zone on top of the debris bed (Figure 28). Physics based DECO SM has been updated to consider the effect of melt agglomerated on debris bed coolability (Figure 27)[45][58].

Table 8 presents the list of DECO SM input parameters and respective ranges. More details on full and surrogate models for ex-vessel debris coolability can be found in [45][46][47][58].

Table 8: DECO SM input parameters.

Variable Name	Description	Units	Range
RHOP	Fuel density	kg/m3	[7500 ; 8500]
PHEAT	Fuel latent heat	J/kg	[2.6e5 ; 4.0e5]
CP	Fuel heat capacity	J/kg*K	[350 ; 650]
KFUEL	Fuel thermal conductivity	W/m*K	[2 ; 42]
TMELT	Fuel Melting Temperature	K	[1600 ; 2800]
TSH	Melt superheat	K	[10 ; 1000]
TSCRAM	Time after SCRAM	s	[10000-50000]
TREL	Release duration	s	[1000 ; 10000]
MAGG	Mass fraction of agglomerates	[-]	[0 ; 1]
POR	Debris bed porosity	[-]	[0.3 ; 0.45]
SLPA	Slope angle	degrees	[0 ; 30]
DPAR	Effective particle diameter	mm	[1.5 ; 3]
TLO	Water pool temperature	K	[288 ; 368]
XPW	Pool depth	m	[5 ; 9]
PO	Containment pressure	Pa	[1e5 ; 4e5]

Currently, in assessment of the risk of formation of non-coolable debris bed two types of failure criteria were implemented. The first criterion assumes that debris bed is "coolable" if there is "no dryout". However, it might be too conservative. After dryout, particle temperature rises above the saturation temperature, however, a small dry zone can be coolable by steam flow and high temperatures are reached only in case of large dryout zones. Therefore, in updated DECO SM[58] a set of less conservative criteria was introduced - debris bed is non-coolable if debris remelting or oxidation occurs, and it is coolable if debris temperature is stabilized below certain temperature limit. In current implementation we consider three temperature limits: (i) 1200K - for debris oxidation

[59], (ii) 1700K - melting temperature of stainless steel as assumed in MELCOR code MP package [34][35], and 2800K - melting temperature of oxidic debris [34][35].

Table 9. DECO SM output parameters and ranges.

Parameter name	Range	Units
Heat flux	[0-5]	MW/m2
Dryout heat flux	[0-5]	MW/m2
Max. long term temperature of debris	[300-3500]	K

4 Uncertainty Quantification and Risk Analysis Results

This section presents the results of application of the ROAAM+ framework for Nordic BWR for analysis of ex-vessel debris coolability (addressed in the section 4.2) and ex-vessel steam explosion (addressed in section 4.1). Synthesis of the result obtained with ROAAM+ for treatment within enhanced PSA model is presented in section 5.3.1.

4.1 Ex-vessel Steam Explosion

4.1.1 Risk Analysis using SEIM SM

The analysis of the risk of containment failure due to ex-vessel steam explosion has been performed using surrogate model for ex-vessel steam explosion in Nordic BWR [38]. In the analysis two fragility limits for containment hatch door located in the lower drywell of Nordic BWR were considered, where fragility limit for:

  (i)   original design "non-reinforced hatch door" – 6kPa*s; and for
  (ii)   modified design "reinforced hatch door" – 50kPa*s.

The ROAAM+ treatment for Nordic BWR SAM is iterative in nature and aims to reduce the uncertainty to the level where a robust decision can be made (i.e. decision becomes insensitive to the remaining uncertainty). Therefore, as the first step of the analysis we treat all parameters in steam explosion surrogate model (Table 4) as model intangible parameters, i.e. with incomplete probabilistic knowledge.

Using ROAAM+ probabilistic framework the complementary cumulative distribution of probability of failure $CCDF(P_F)$ can be obtained using SEIM SM. Figure 29 illustrate $CCDF(P_F)$ obtained for non-reinforced and reinforced hatch door. The results show that the screening probability P_s =1.e-3 which corresponds to "physically unreasonable" limit (see [5] for details) is exceeded in approximately 99% of the cases with non-reinforced hatch door and in ~70% of the cases with reinforced hatch door. Thus, it is not possible to demonstrate that failure is physically impossible (i.e. "possibility" of containment failure is low) even with reinforced door.

If consider "necessity" of containment failure, i.e. the possibility that containment doesn't fail. For that we set the screening probability to $P_s = 0.999$. The fraction of scenarios where $P_F > P_s = 0.999$, is approximately 0.06 and 0.003 for the original and modified designs respectively. The "necessity" of the containment failure due to ex-vessel steam explosion is not sufficiently high to claim that the failure is unavoidable.
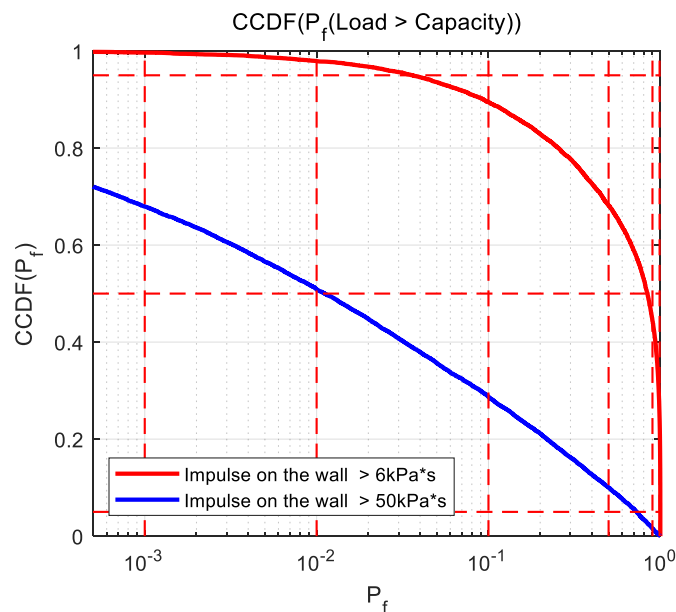

Figure 29. Complimentary CDF of conditional containment failure due to ex-vessel steam explosion: (red) given 6kPa*s fragility limit (non-reinforced hatch door), (blue) given 50kPa*s fragility limit (reinforced hatch door) using SEIM SM[16].

Analysis based on the total failure probability distribution is useful for an overall assessment of system reliability and can be used for decision making in cases when both the possibility and necessity of failure are either low or

high simultaneously. However, in cases such as shown in Figure 29, where possibility of failure can be large but necessity is relatively small, further understanding of the system might be useful in order to make a decision. Note that risk assessments are based on available knowledge. Thus, there can be two possible decisions:

(i) Collect more knowledge, if it is likely that reduced uncertainty and conservatism in the analysis can help to demonstrate effectiveness of the strategy (focus on the improvement of the risk assessment).

(ii) Modify current SAM strategy, if it is unlikely that more knowledge will change conclusion (focus on the risk management).

By considering the failure probability distribution, it might be hard to choose between those decisions. In this example further clarification of the importance of different input parameters for steam explosion analysis will be helpful in order to converge to a decision with respect to (i) effectiveness of SAM, or (ii) need for more information, or (iii) the need to modify the design.

In order to tell which parameters' uncertainty should be addressed first, we perform global sensitivity analysis using Morris method (see [20] for details). In the analysis we considered the effect of SEIM SM input parameters, presented in Table 4 on the magnitude of explosion impulse, predicted by the SEIM SM.
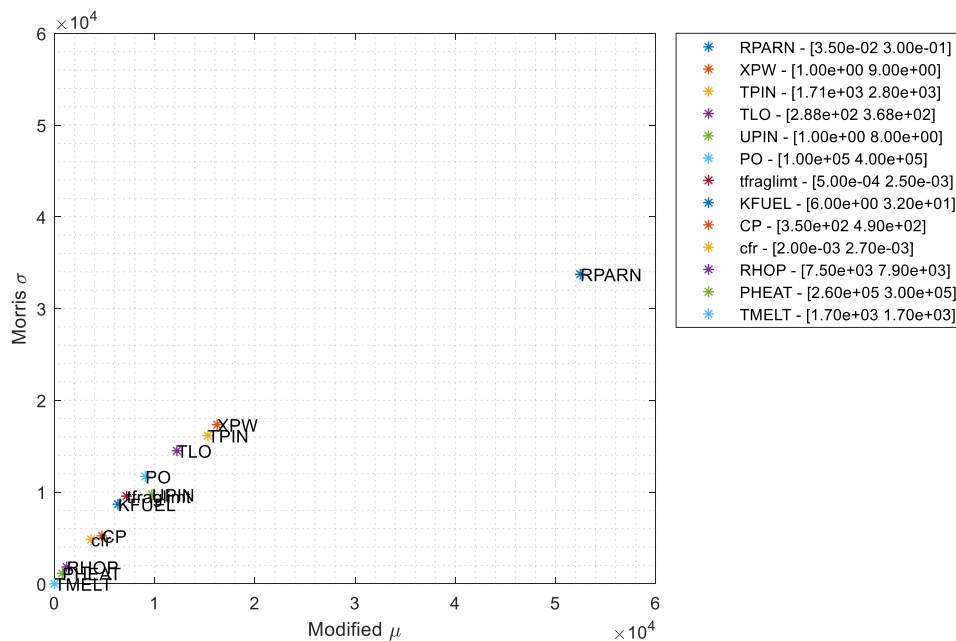
Figure 30. SEIM SM Morris Sensitivity Analysis Results.

The results of sensitivity analysis are presented in Figure 30 in the form of Morris diagram, where the parameters in the legend are ordered according to their influence on the SEIM SM response, characterized by the Morris μ values (see [20] for details).

The results show that the most influential parameters are RPARN (initial jet radius), TPIN (fuel inlet temperature) and XPW (water pool depth).

The next step in ROAAM+ is failure domain analysis, performed to identify combinations of the most influential parameters that lead to failure (or success). Failure domain analysis is performed using probabilistic framework, where respective complementary cumulative distributions of probability of failure $CCDF(P_F)$ are obtained in the space of the influential parameters. In failure domains every $CCDF(P_F)$ is color coded with respect to the exceedance frequency of screening probability level P_s, as shown in Figure 11.

Figure 31 illustrate the failure domain maps for SEIM SM in the space of XPW (water pool depth) and RPARN (jet radius) considering different fragility limits that correspond to non-reinforced (6kPa*s) and reinforced hatch door (50kPa*s).
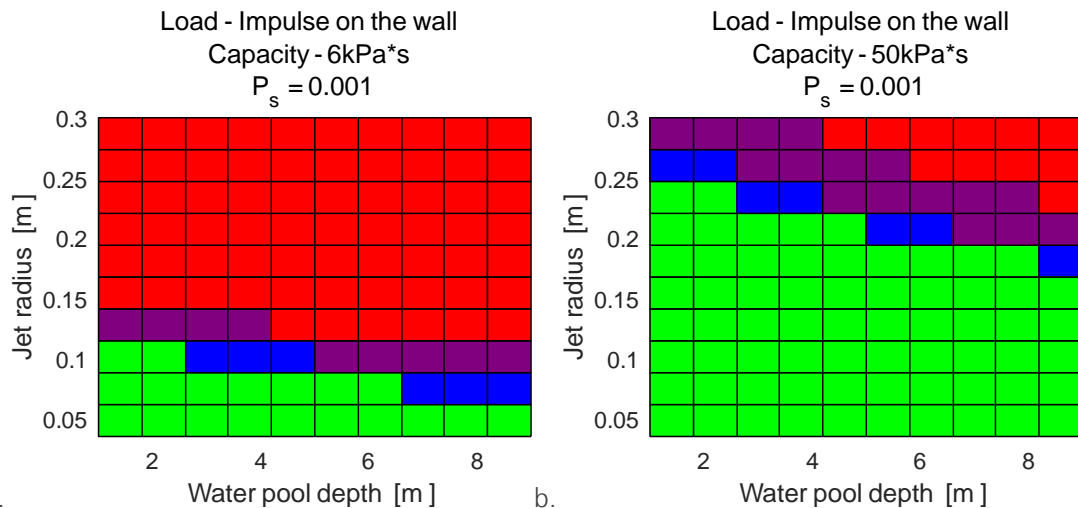
Figure 31. SEIM Failure domains (possibility of failure $P_s = 10^{-3}$) for (a) non-reinforced hatch door; (b) reinforced hatch door.

The results presented in Figure 31 show that failure can be considered as physically unreasonable even with original design (non-reinforced hatch door), regardless of modeling uncertainty if one can demonstrate that the jet radius (RPARN) will be limited to 0.05m (corresponds to vessel lower head opening with only slightly ablated failure of the penetration for instrumentation guide tube (IGT)). If the temperature of ejected debris is below 2400K then the jet radiuses up to 0.09 m (slightly ablated failure of the control rod guide tube (CRGT) penetration) can be considered as safe for ex-vessel steam explosion.

In case of modified design, i.e. reinforced hatch door, containment failure due to ex-vessel stream explosion can be considered as physically unreasonable regardless of the modeling uncertainty if one can demonstrate that the jet radius (RPARN) will be limited to ~0.15 m (corresponds to the vessel LH opening with significantly ablated CRGT penetration failure).

Neither original nor modified design can ensure that containment failure due to steam explosion is physically unreasonable, unless one can demonstrate that the size of the melt jet diameter and initial melt temperature can be limited. Such reduction of uncertainty in the input parameters for steam explosion analysis would require consideration of the effect of phenomena and scenarios at the previous stages of the accident progression. However, analysis of the failure domains suggest that it is quite unlikely that such a demonstration (that jet size is sufficiently small) can be provided for the original design because the maximum "safe" size of the jet is smaller than the size of the CRGT penetrations. On the other hand, reduction of uncertainty in the initial jet diameter and melt temperature might be fruitful for the modified design where "safe" jet size is much larger than the size of CRGT penetration. E.g. one can investigate if the vessel ablation after initial failure of a penetration can be limited, considering prototypic accident scenario conditions.

The lack of clear demonstration of effectiveness of SAM strategy sometimes might be insufficient for rejection of the SAM design by the decision makers. An argument can be that the analysis of the possibility of failure was done too conservative. In order to address the argument, let's consider the question about "what is the possibility that containment doesn't fail". Figure 32 illustrates the results of failure domain analysis with screening probability $P_s = 0.999$. The original design (Figure 32a) has a relatively large domain of input parameters with jet radiuses RPARN > ~0.25 m, where $P_F > P_s = 0.999$ in more than 95% cases (i.e. necessity of containment failure is high). In the modified design with reinforced hatch door (see Figure 32b) the size of the domain with high necessity of failure is significantly reduced ($P_F > P_s = 0.999$ in more than 5% cases when RPARN > ~0.25 m and water pool depth is above 6m (XPW > 6m)).
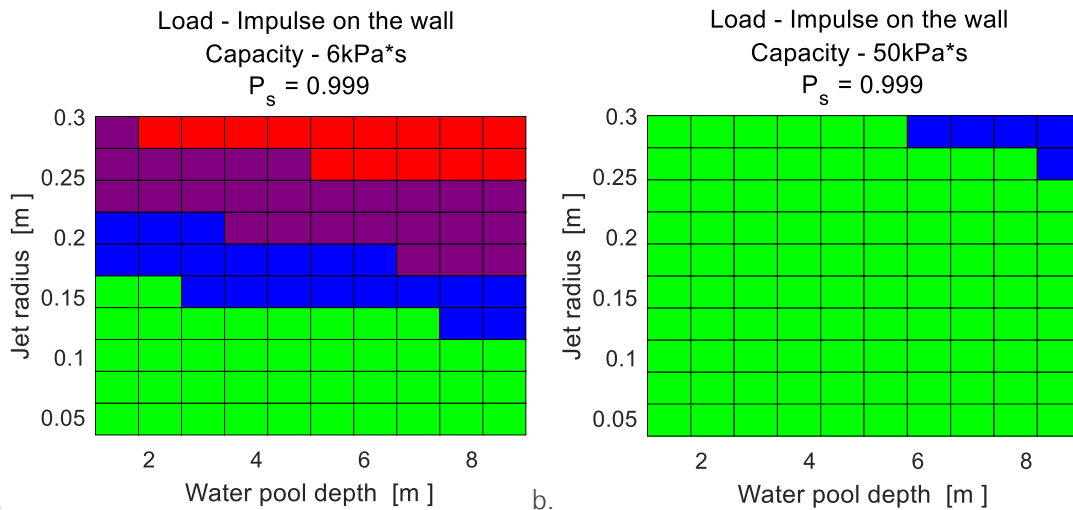
Figure 32. SEIM Failure domains (necessity of failure $P_s = 1 - 10^{-3}$) for (a) non-reinforced hatch door; (b) reinforced hatch door.

The failure domain analysis suggests that it is unlikely that the design with non-reinforced hatch door can be demonstrated as an effective SAM strategy because (i) the maximum "safe" size of the jet is quite small and (ii) the size of the failure domain where necessity of failure is large. Modified design with reinforced door also cannot be proven as an effective strategy, given the current state of knowledge. However, the sizes of the failure domain for both possibility and especially necessity of failure are fairly small. Thus there is much better chance that obtaining more knowledge about vessel failure and melt release phenomena can reduce the uncertainty in the results.

4.1.2 Risk Analysis of Ex-vessel Steam Explosion Using Complete Framework.

The results of sensitivity analysis (see Figure 30) and failure domain analysis (see Figure 31) for ex-vessel steam explosion surrogate model show that the radius of the jet, water pool depth and the temperature of the melt – are the most influential parameters on the magnitude of loads on the containment produced by ex-vessel steam explosion in Nordic BWR. These parameters depend on the in-vessel phase of accident progression, vessel failure mode and melt release conditions predicted by the melt ejection surrogate model in ROAAM+ framework for Nordic BWR.

The ROAAM+ analysis of probability of failure has been performed using complete framework (MEM SM and SEIM SM) for unmitigated SBO scenario with depressurization (see for details). In the analysis using complete framework, SEIM SM predicts steam explosion loads on the containment depending on MEM SM predictions of melt release conditions for 4 splinter scenarios (see Chapter 3.2.1). The results are presented in Figures 33 and 34.

The results show the dominant effect of solid debris ejection mode (IDEJ0 and 1) on melt release conditions from the vessel and resultant loads on the containment due to ex-vessel steam explosion.

In case of IDEJ0 (solid debris ejection – on) – the melt and debris mixture is released in a dripping mode, resulting in relatively small values of jet radius (RPARN), melt release velocity (UPIN) and melt temperature (TPIN) compared to IDEJ1 (solid debris ejection – off) – where the major part of in-vessel debris is ejected in form of massive release (due to vessel lower head wall failure).

Initial breach area due to failed penetrations (EIGT25 vs EIGT100) also has quite significant effect on the results, however it does not change the conclusions in case of a single jet SEIM model. The effects of the number of failed penetrations on melt release conditions and ex-vessel steam explosion are subject to future research and are beyond the scope of the present work.
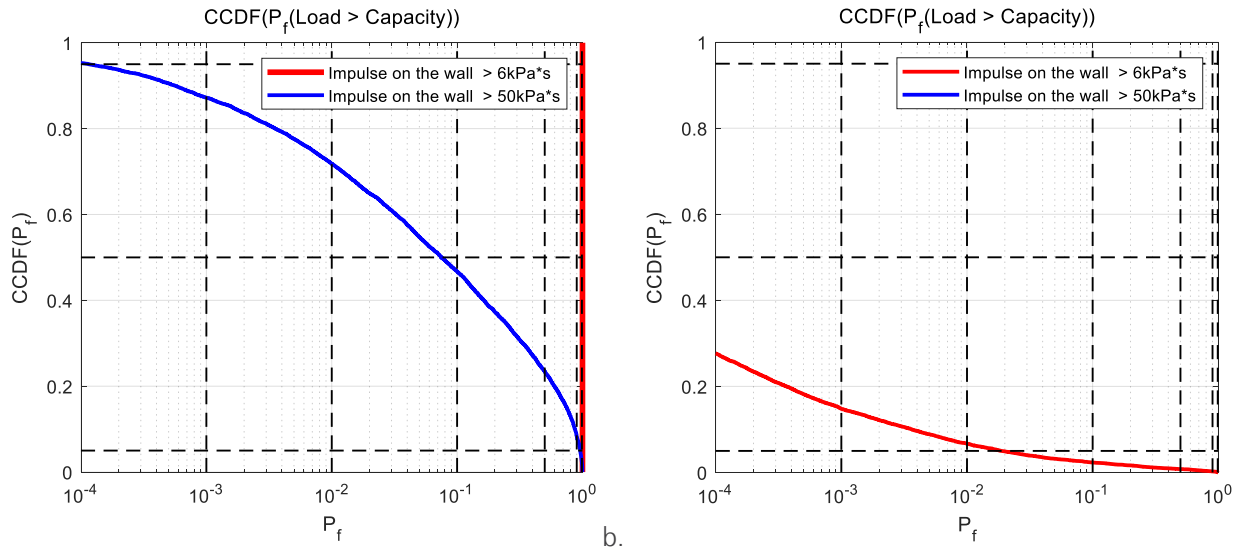
Figure 33. Complimentary CDF of conditional containment failure due to ex-vessel steam explosion: (red) given 6kPa*s fragility limit (non-reinforced hatch door), (blue) given 50kPa*s fragility limit (reinforced hatch door) using complete framework for (a) EIGT100IDEJ, (b) EIGT100IDEJ0 Scenario[22].
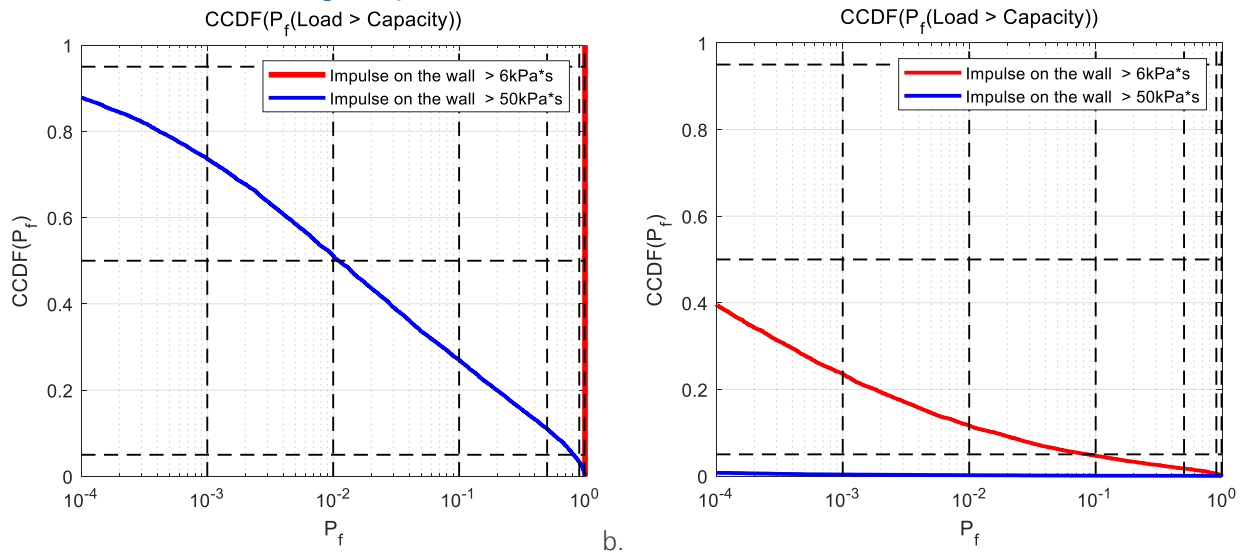

Figure 34. Complimentary CDF of conditional containment failure due to ex-vessel steam explosion: (red) given 6kPa*s fragility limit (non-reinforced hatch door), (blue) given 50kPa*s fragility limit (reinforced hatch door) using complete framework for (a) EIGT25IDEJ1, (b) EIGT25IDEJ0 Scenario[22].

The results show that the probability of containment failure due to ex-vessel steam explosion strongly depends on debris ejection mode from the vessel (solid debris ejection option – IDEJ1 vs IDEJ0). In case of solid debris ejection – off (IDEJ1) containment failure due to ex-vessel steam explosion cannot be considered as physically unreasonable, even in modified design with reinforced hatch door (50kPa*s, see Figures 33a and 34a). Furthermore, in the original design the necessity of failure is high (e.g. all values of $P_f > P_s = 0.999$ [61]).

In case of solid debris ejection –on (IDEJ0) – containment failure due to ex-vessel steam explosion can be considered as physically unreasonable only in case of modified design (with reinforced hatch door); in the original design – physically unreasonable level is exceeded in ~15-25% of the cases, however the necessity of failure is small, therefore further reduction of uncertainty can yield positive results.

Figure 35 and 37 show the results of sensitivity analysis for coupled melt ejection and ex-vessel steam explosion surrogate models (MEM-SEIM SMs) for EIGT100IDEJ1 and EIGT100IDEJ0 splinter scenarios. Note that water pool depth is considered as scenario parameter in these calculations.
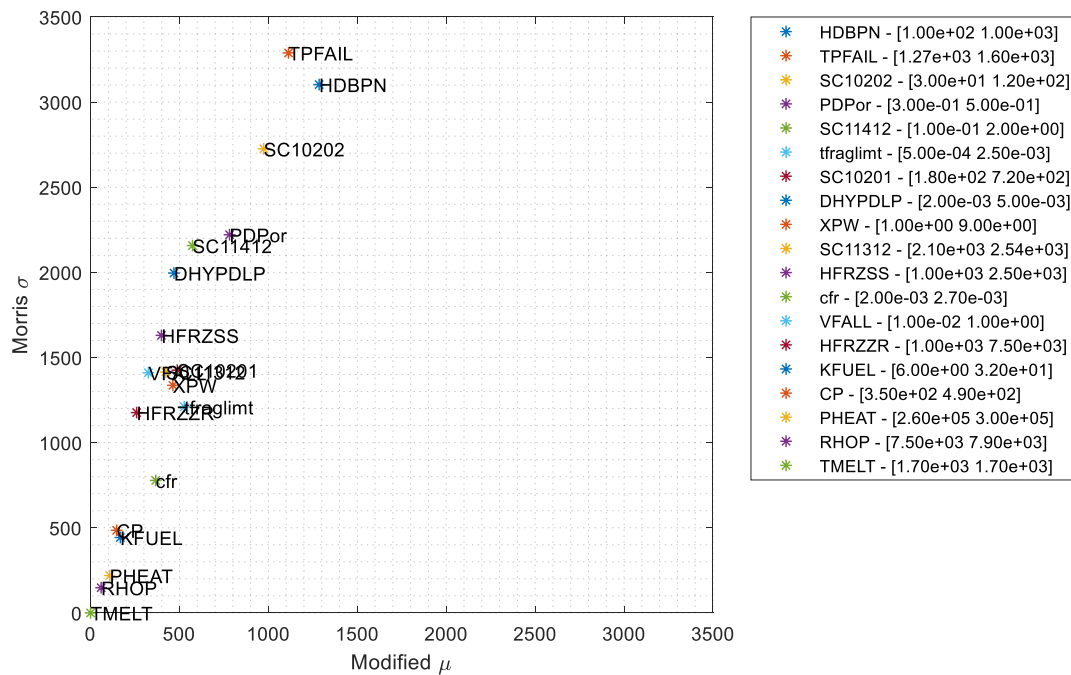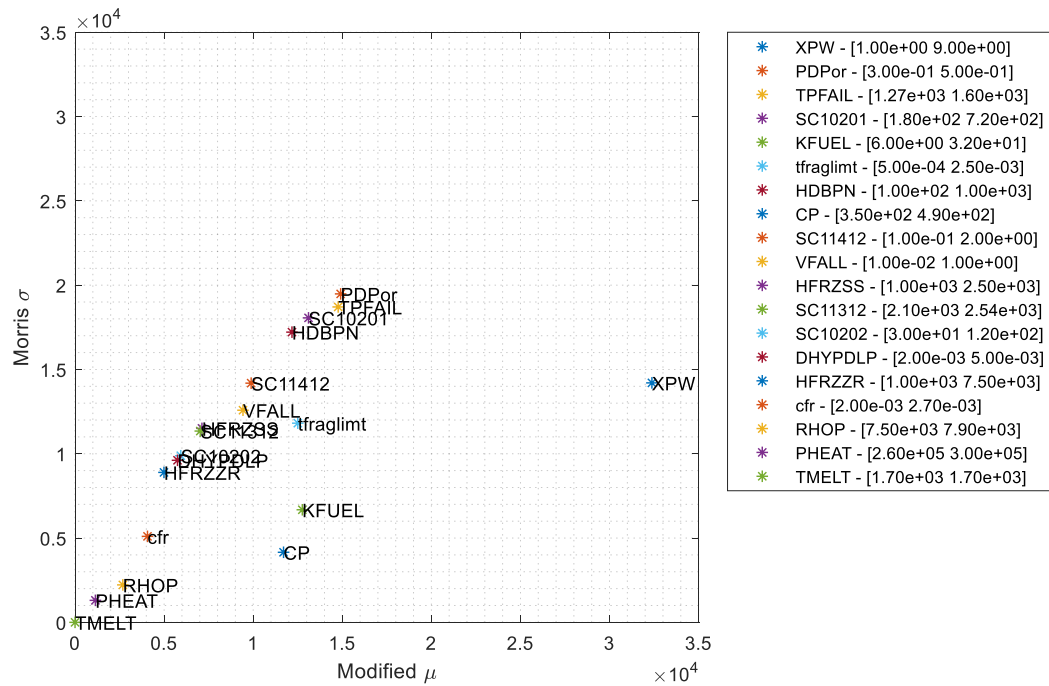
Figure 35. Sensitivity of steam explosion impulse on pedestal wall (kPa*s) in EIGT100IDEJ0 scenario.

The results of sensitivity analysis indicate that the uncertainty in the results in coupled MEM-SEIM analysis in case of IDEJ0 is majorly driven by parameters that control failure of penetrations (HDBPN and TPFAIL – heat transfer coefficient from debris bed to penetrations and penetrations failure temperature respectively) in MELCOR code (see section 3.2.1, and references [21][34][35] for details). It can be explained by overall small values of jet radiuses and ejected debris temperatures predicted by MELCOR code in case of IDEJ0 (see Figure 36a and b), and the uncertainty is mostly dominated by TPFAIL and HDBPN, as demonstrated in [33].
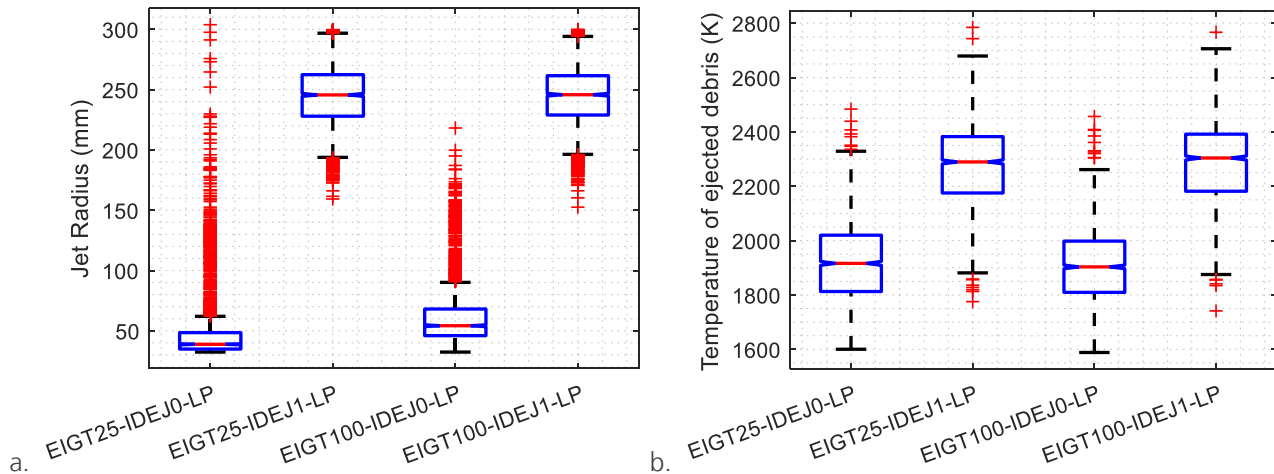
Figure 36. a) Mass averaged Jet Radius (mm); b) Mass averaged temperature of ejected debris (K).

Figure 37. Sensitivity of steam explosion impulse on pedestal wall (kPa*s) in EIGT100IDEJ1 scenario.
In case of IDEJ1 the results of coupled MEM-SEIM analysis are mostly affected by the pool depth (XPW), in-vessel particulate debris porosity (PDPor) and penetrations failure temperature (TPFAIL); which can be explained by the distributions of the jet radiuses (RPARN) and ejected debris temperatures (TPIN) predicted by MELCOR code in case of IDEJ1 (see Figure 36a and b). In case of large jet radiuses, the uncertainty in the results is mostly driven by the water pool depth, i.e. water pool depth defines system confinement and availability of volatile liquid available for interaction; thus, with reduction of pool depth steam explosion energetics deteriorate.

Figure 38 and 39 show the results of failure domain analysis in case of EIGT100-IDEJ1 in the domain of the most influential parameters identified in Figure 37. The results show that in the original design (Figure 38a, 39a), both possibility ($P_s = 1.e-3$) and necessity ($P_s = 0.999$) of failure is high, i.e. no matter the uncertainty in modelling parameters, the non-reinforced door will fail in case of EIGT100-IDEJ1 scenario (solid debris ejection – OFF).
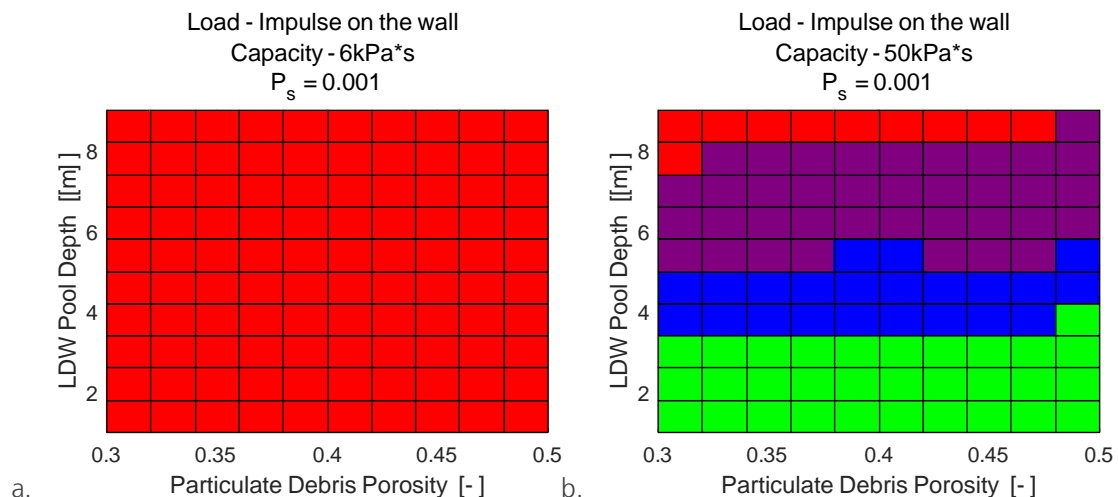
Figure 38. MEM-SEIM Failure domain analysis results in case EIGT100-IDEJ1 for a) domains (necessity of failure $P_s = 1 - 10^{-3}$) for (a) non-reinforced hatch door; (b) reinforced hatch door.
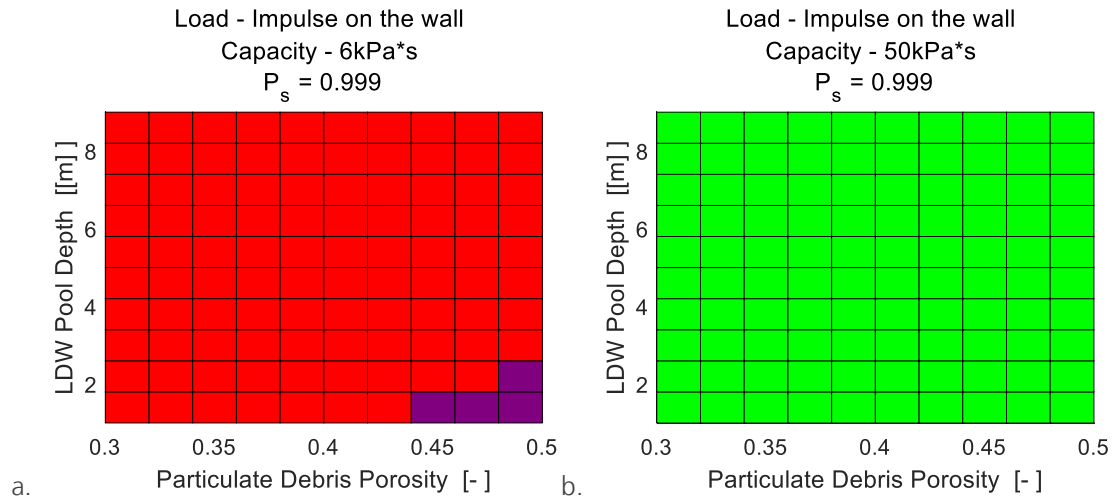
Figure 39. MEM-SEIM Failure domain analysis results in case EIGT100-IDEJ1 for a) domains (necessity of failure $P_s = 0.999$) for (a) non-reinforced hatch door; (b) reinforced hatch door.
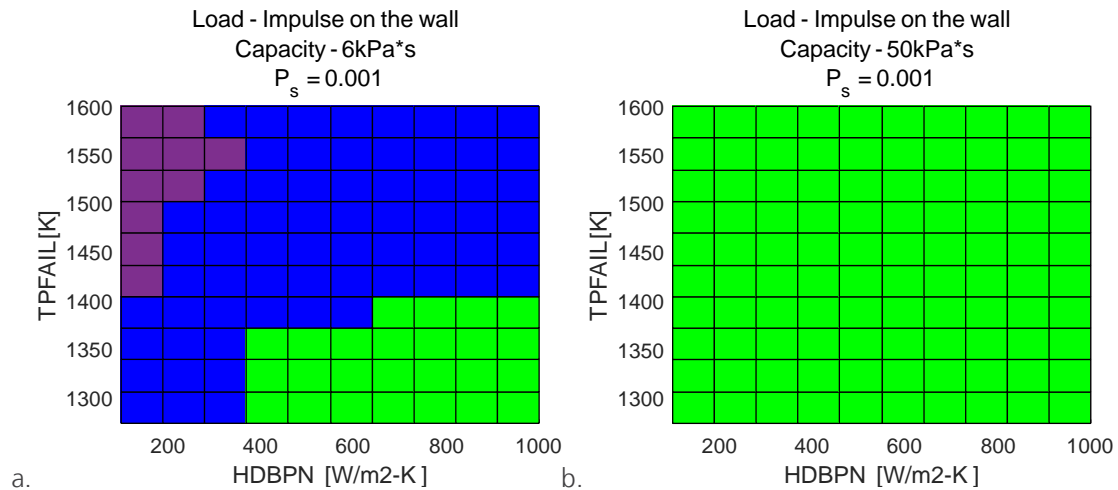

Figure 40. MEM-SEIM Failure domain analysis results in case EIGT100-IDEJ0 for a) domains (necessity of failure $P_s = 1 - 10^{-3}$) for (a) non-reinforced hatch door; (b) reinforced hatch door.

On the other hand, in case of EIGT100-IDEJ0 the results look completely different. For example, in the original design with non-reinforced hatch door, containment failure due to ex-vessel steam explosion can be considered as physically unreasonable (Figure 40a and 41a) in case of early failure of penetrations (IGTs), provided by large values of heat transfer coefficient between debris and penetration structures (HDBPN) and small values of penetrations failure temperature (TPFAIL). This effect can be explained by the amount of melt and melt superheat available at the time of penetrations failure, i.e. later time of penetrations failure can lead to increased amount of liquid melt and larger values of melt superheat that can affect ablation of the opening, and, thus, steam explosion energetics. In case modified design with reinforced hatch door (Figure 40b and 41b), containment failure due to ex-vessel steam explosion can be considered ash physically unreasonable for all combinations of the most influential parameters.
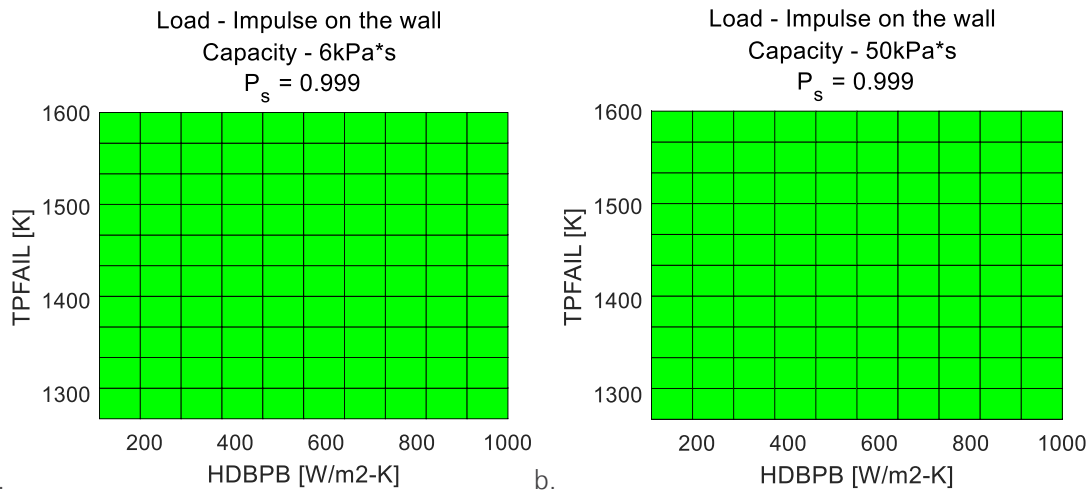
Figure 41. MEM-SEIM Failure domain analysis results in case EIGT100-IDEJ0 for a) domains (necessity of failure $P_s = 0.999$) for (a) non-reinforced hatch door; (b) reinforced hatch door.

4.2 Ex-vessel Debris Coolability

4.2.1 Risk Analysis Using Surrogate Model for Debris Coolability.

The analysis of the risk of containment failure due to ex-vessel debris coolability (formation of non-coolable debris configuration) has been performed using surrogate models for debris agglomeration (section 3.2.3.1) and coolability (section 3.2.3.2) in Nordic BWR. In the analysis four groups of parameters were considered for the load and capacity listed below:

(i)   Heat flux (HF) vs. dryout heat flux (DHF) (MW/m2), failure is declared when HF>DHF.

(ii)   Long term temperature of solid debris (TMAX) vs. debris oxidation temperature, failure is declared when TMAX>1200K.

(iii)   Long term temperature of solid debris (TMAX) vs. melting temperature of metallic debris, failure is declared when TMAX>1700K.

(iv)   Long term temperature of solid debris (TMAX) vs. melting temperature of oxidic debris, failure is declared when TMAX>2800K.

In the first step of the analysis we treat all parameters in debris agglomeration and coolability surrogate models (Table 6 and 8) as model intangible parameters, i.e. with incomplete probabilistic knowledge.

Using ROAAM+ probabilistic framework the complementary cumulative distribution of probability of failure $CCDF(P_F)$ can be obtained. Figure 42 illustrate $CCDF(P_F)$ obtained for different loads and fragility limits.

The results show that the screening probability P_s =1.e-3 which corresponds to "physically unreasonable" limit (see [5] for details) is exceeded in approximately 99% in all of the cases. If consider "necessity" of containment failure, i.e. the possibility that containment doesn't fail. For that we set the screening probability to $P_s = 0.999$. The fraction of scenarios where $P_F > P_s = 0.999$, is approximately ~0.468 for HF>DHF and ~0.253/0.252/0.252 for TMAX>1200/1700/2800K. The "necessity" of the containment failure due to ex-vessel debris coolability is high, but not sufficiently high to claim that the failure is unavoidable.
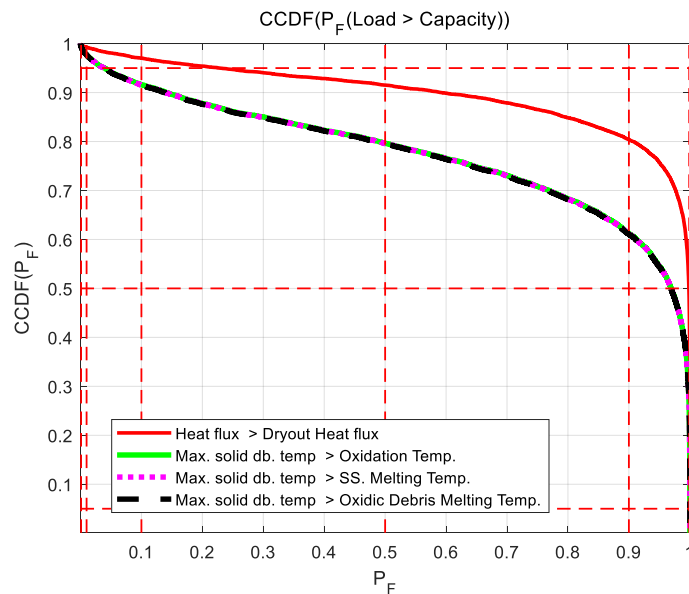
Figure 42. Complimentary CDF of conditional containment failure probability due to ex-vessel debris coolability: (red) HS>DHS (MW/m2); debris temperature > oxidation temperature (solid green); metallic debris remelting temperature (dashed purple); oxidic debris remelting temperature (dashed black).

Further reduction of uncertainty can be achieved through sensitivity and failure domain analysis. Figure 43 and 44 show the results of Morris [20] sensitivity analysis for the difference between heat flux and dryout heat flux (HF-DHF), and max. long term temperature of solid debris (TMAX).
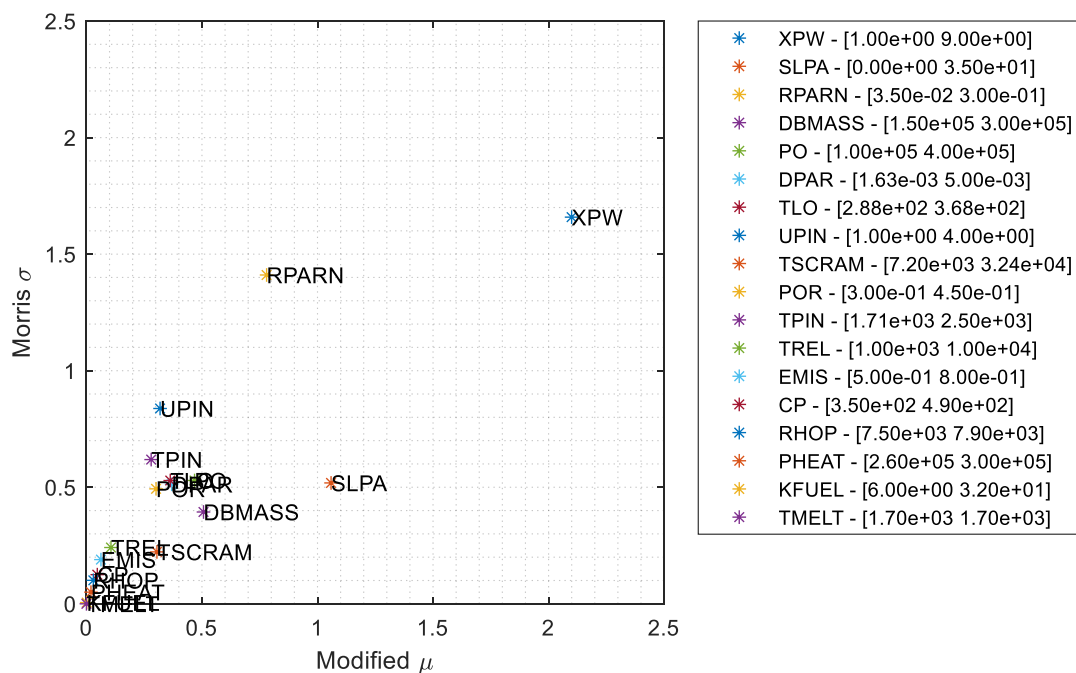
Figure 43. Sensitivity of the value of (HF-DHF) (MW/m²)
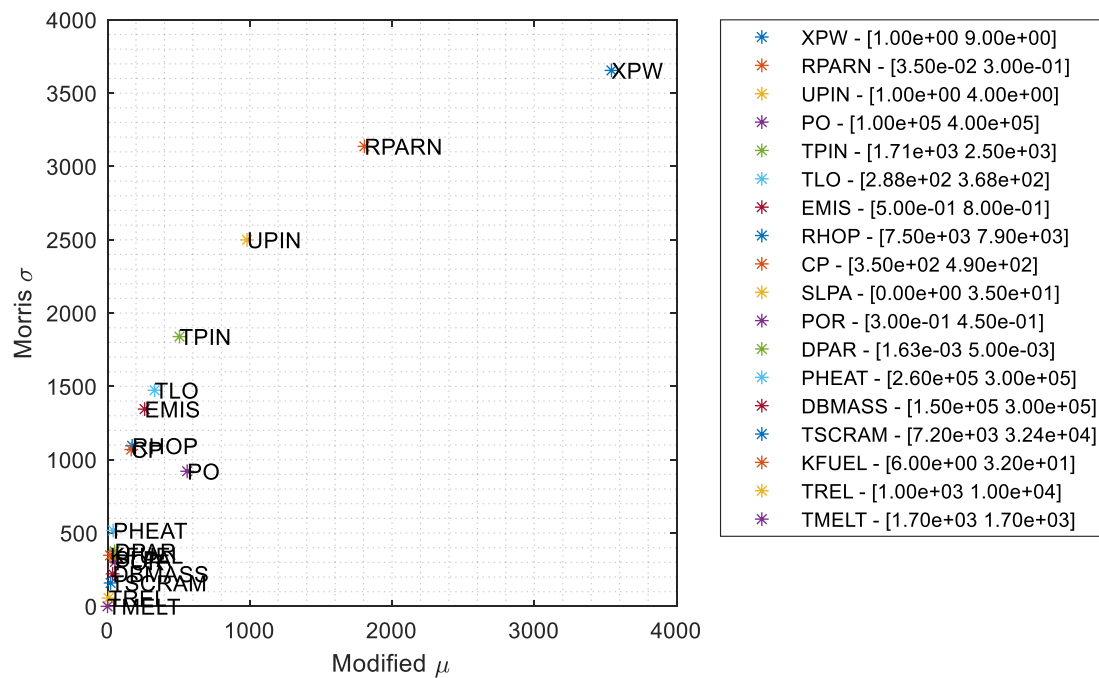
Figure 44. Sensitivity of the max. temperature of solid debris (K).

The results suggest that parameters that affect debris bed coolability are water pool depth (XPW), jet radius (RPARN), melt jet velocity (UPIN) and debris bed slope angle (SLPA).

The next step in ROAAM+ is failure domain analysis, performed to identify combinations of the most influential parameters that lead to failure (or success). Failure domain analysis is performed using probabilistic framework, where respective complementary cumulative distributions of probability of failure $CCDF(P_F)$ are obtained in the space of the influential parameters. In failure domains every $CCDF(P_F)$ is color coded with respect to the exceedance frequency of screening probability level P_s, as shown in Figure 11.

Figure 45 show the results of failure domain analysis for ex-vessel debris coolability. The results suggest that probability of HF>DHF (Figure 45a) and TMAX>Debris oxidation temperature (Figure 45b) cannot be considered as physically unreasonable for all combinations of jet radiuses (RPARN) and water pool depths (XPW). Furthermore, the results suggest that probability of containment failure due to formation of non-coolable debris configuration significantly decreases with increase of water pool depth (XPW) and decrease of jet radiuses (RPARN).
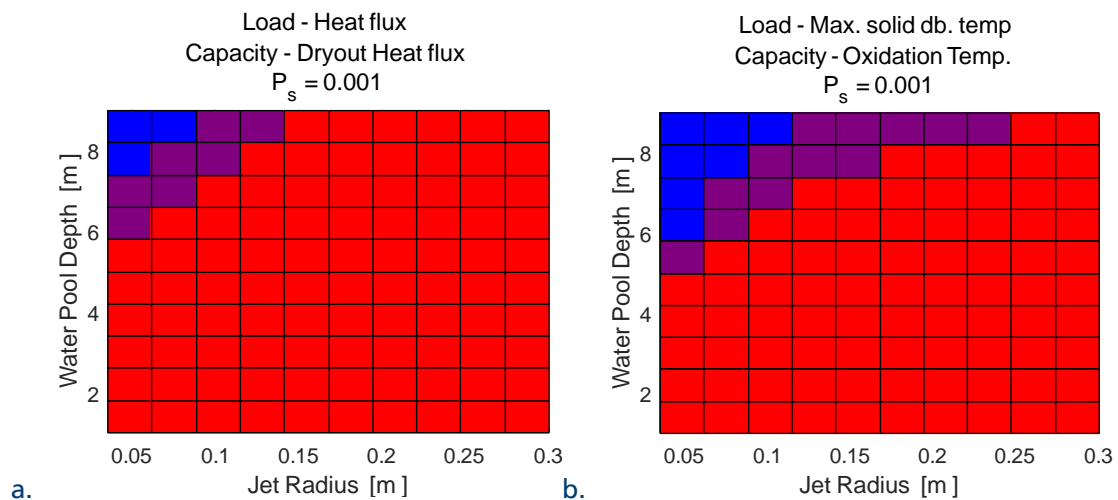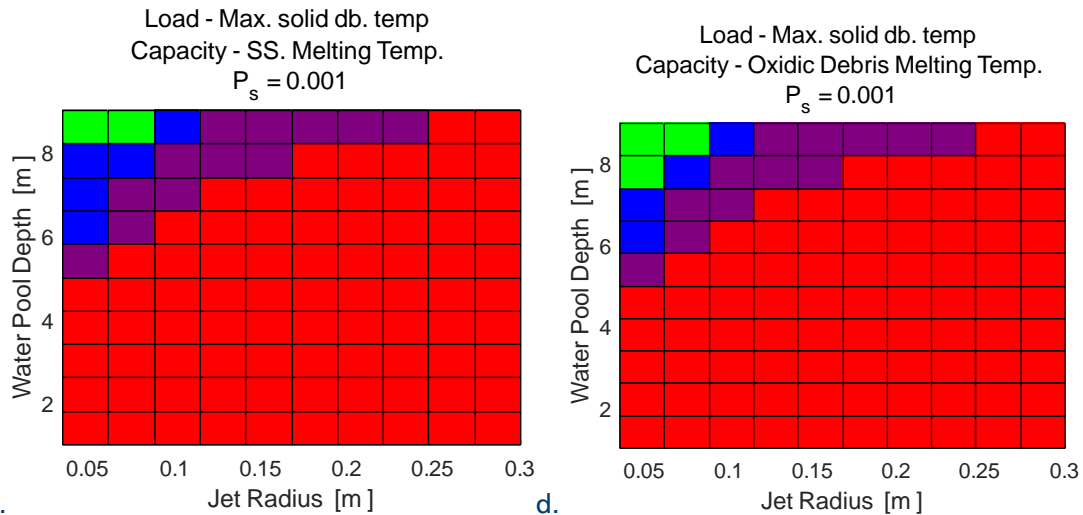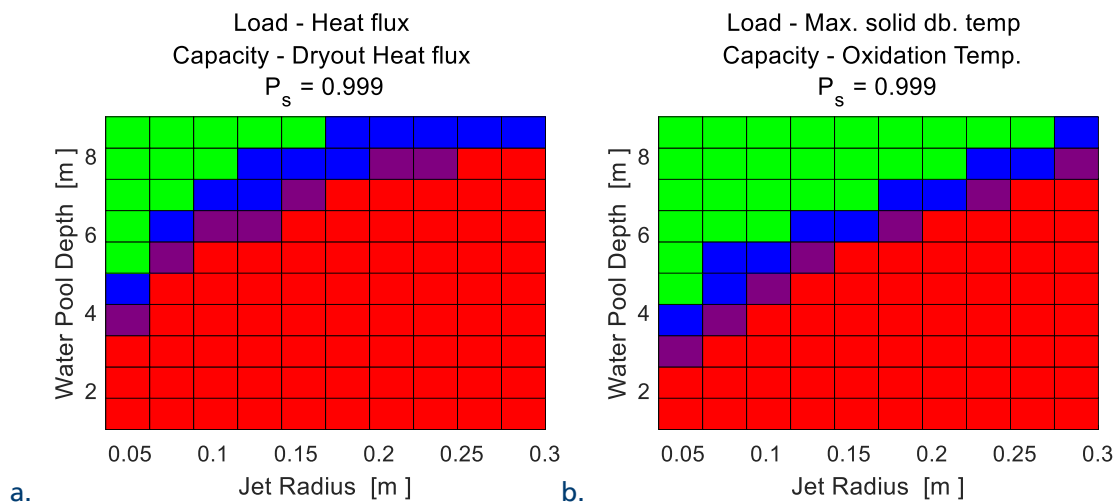
Figure 45. AGGDECO Failure domain analysis results (Possibility $P_s = 1.e-3$) for (a) HF>DHF [W/m2-K], (b) Debris temperature>Oxidation temperature (K), (c) Debris temperature>melting temperature of metallic debris (K), (d) melting temperature of oxidic debris (K).

Furthermore, if we consider melting temperature of metallic or oxidic debris (1700 and 2800K respectively) as a failure criterion, then failure due to formation of non-coolable debris configuration can be considered as physically unreasonable for deep pools (above 8.5m) and jet radiuses up to ~0.1m (slightly IGT size break).

Figure 46 show the results for "necessity" of failure, which suggest that containment failure can be considered as imminent (regardless uncertainty) in case of water pool depth below ~2-3.5m, and it strongly depends on the size of the break, e.g. in case of CRGT size break – failure is imminent if the pool depth is below ~6-7m (which is a typical depth of LWD pool under SA conditions in Nordic BWR, as demonstrated in [21][32]).
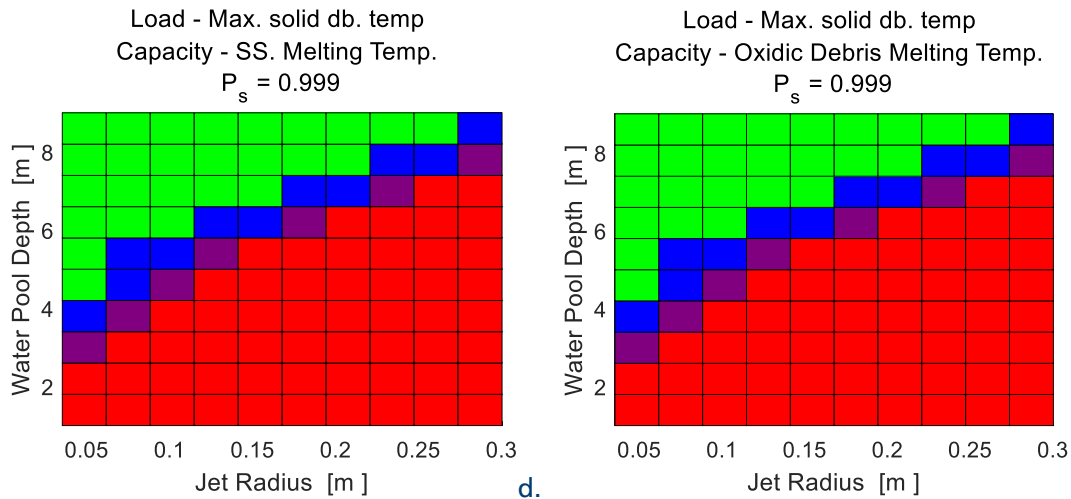
Figure 46. AGGDECO Failure domain analysis results (Necessity $P_s = 0.999$) for (a) HF>DHF [W/m2-K], (b) Debris temperature>Oxidation temperature (K), (c) Debris temperature>melting temperature of metallic debris (K), (d) melting temperature of oxidic debris (K).

4.2.2 Risk Analysis of Ex-vessel Debris Coolability Using Complete Framework.

The results of sensitivity (Figure 43 and 44) and failure domain analysis (Figure 45 and 46) performed for ex-vessel debris coolability surrogate models (AGG-DECO) demonstrated that the success of SAM strategy strongly depends on melt release characteristics (e.g. jet radius) and pool conditions (e.g. water pool depth), which depend on in-vessel phase of SA progression, vessel failure mode and melt release – which is predicted by melt ejection surrogate model (MEM SM).

In the following, a coupled analysis has been performed using complete ROAAM+ framework for Nordic BWR (MEM-AGG-DECO SMs).

The results of integral analysis of probability of failure are illustrated in the Figure 47a for EIGT100-IDEJ0 scenario, and in Figure 47b for EIGT100-IDEJ1 scenario.
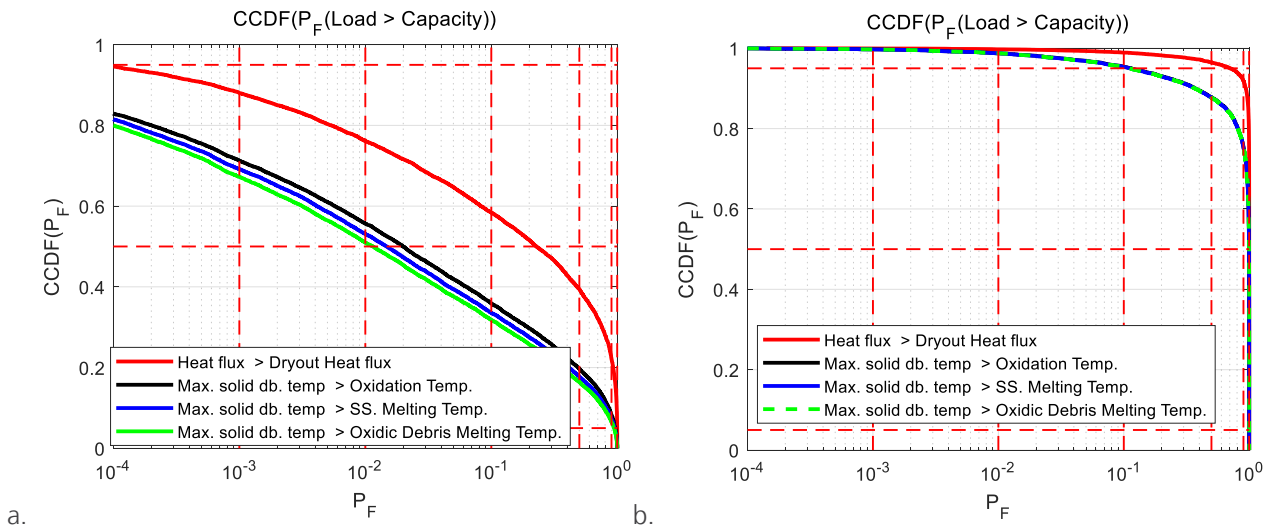

Figure 47. Complimentary CDF of probability of failure due to ex-vessel debris coolability for (a) EIGT100-IDEJ0;(b) EIGT100-IDEJ1.

Based on the results, the major contributor to the uncertainty in probability of containment failure due to formation of non-coolable debris bed is the mode of debris ejection from the vessel (IDEJ0 vs. IDEJ1) – which represented by two phenomenological splinters. Further reduction of uncertainty can be achieved by performing sensitivity and failure domain analyses, in order to identify the list of parameters that contribute the most to the uncertainty in these splinter scenarios and ranges of these parameters, where we can observe a transition from success failure.
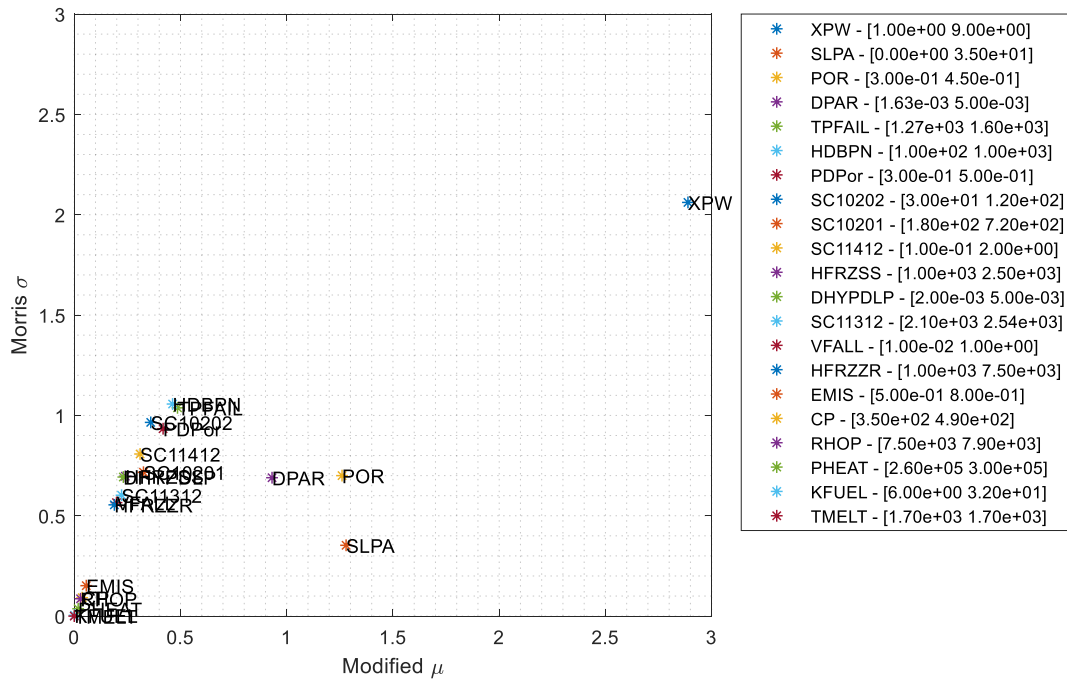
Figure 48. Sensitivity of the value of (HF-DHF) (MW/m²) in EIGT100IDEJ0 scenario.
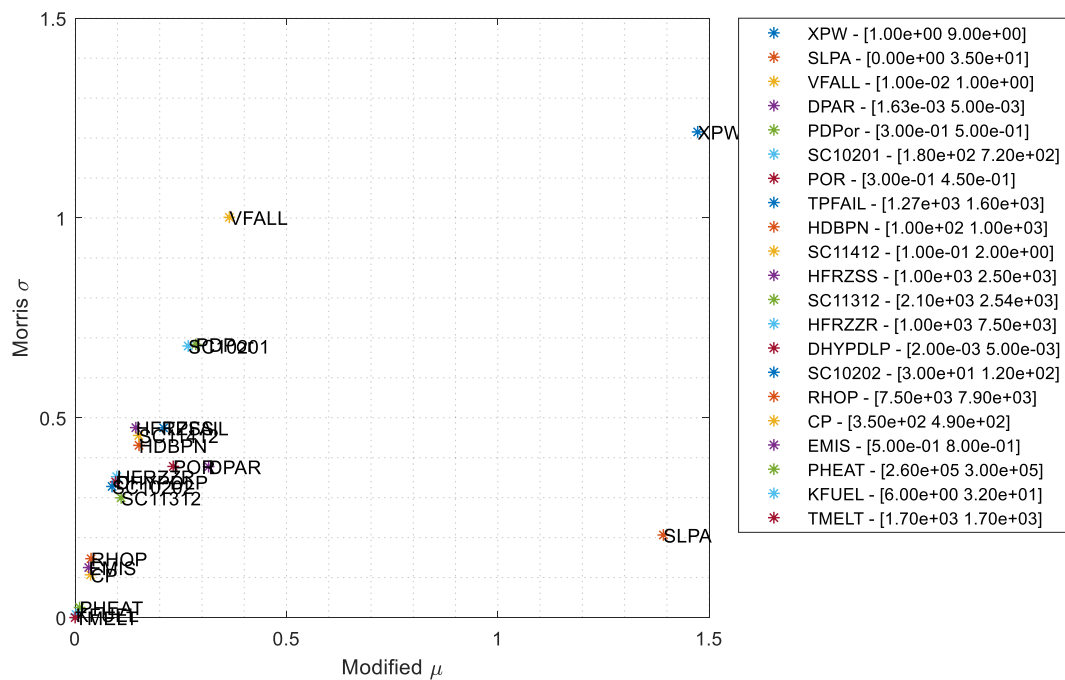

Figure 49. Sensitivity of the value of (HF-DHF) (MW/m²) in EIGT100IDEJ1 scenario.

The sensitivity analysis results of the relationship between heat flux and dry-out heat flux (HF vs. DHF, (see section 3.2.3.2 for details)) are presented in Figure 48 for EIGT100-IDEJ0 scenario, and in Figure 49 for EIGT100-IDEJ1 scenario. Based on the results, the most influential parameters are: water pool depth (XPW), debris bed slope angle (SLPA).
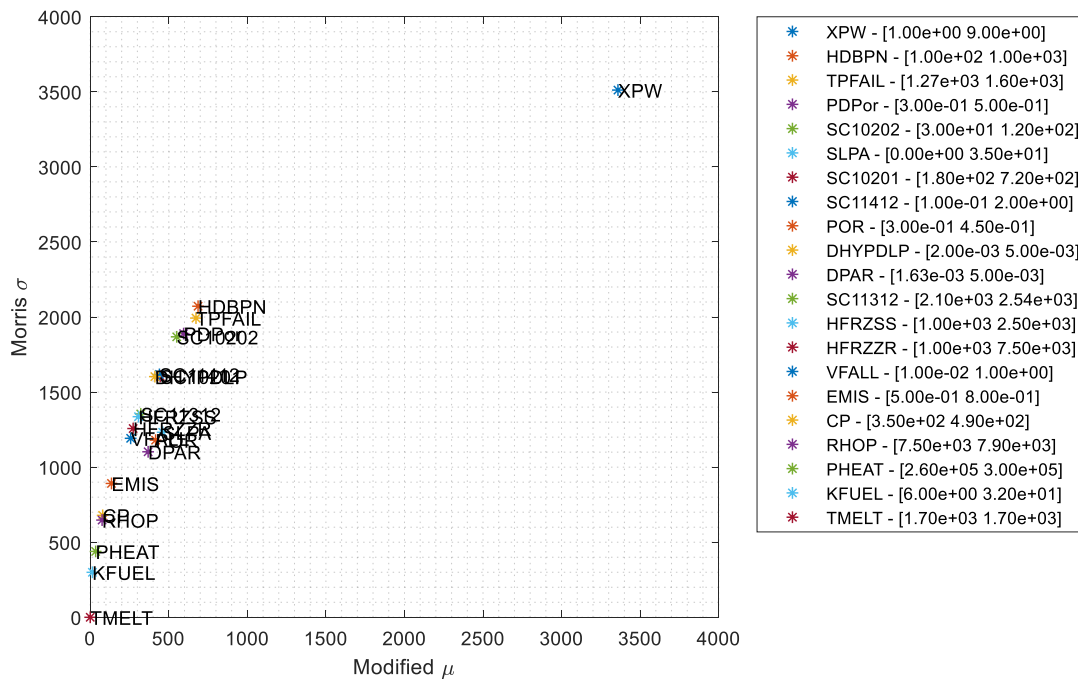
Figure 50. Sensitivity of the max. temperature of solid debris (K) in EIGT100IDEJ0 scenario.
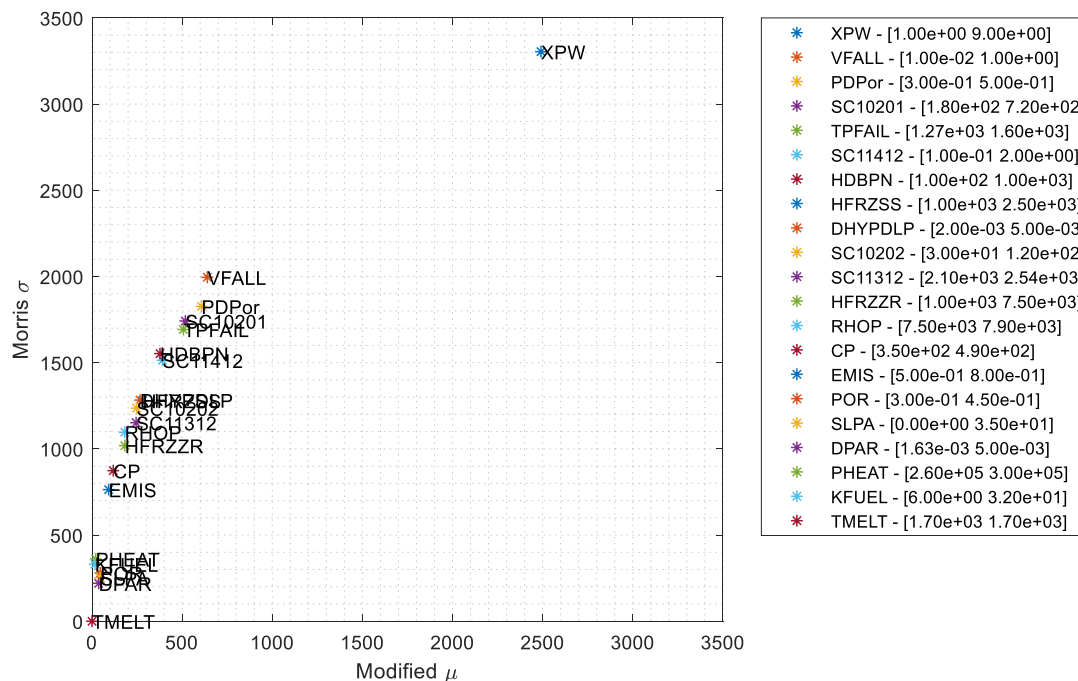

Figure 51. Sensitivity of the max. temperature of solid debris (K) in EIGT100IDEJ1 scenario.

Sensitivity of the maximum long-term temperature (see section 3.2.3.2 for details) of solid debris is illustrated in Figure 50 for EIGT100-IDEJ0 scenario, and in Figure 51 for EIGT100-IDEJ1 scenario. Based on the results, the most influential parameter (by a large margin) is the depth of LDW pool (XPW) and parameters that contribute the most to the uncertainty in MEM SM, such as HDBPN and TPFAIL in case of IDEJ0, and VFALL and PDPor in case of IDEJ1. In case of IDEJ0 these results can be explained by the effect of these parameters (HDBPN and TPFAIL) on the size of the jet (RPARN) which was demonstrated in [32][33], which is among the most influential parameters in AGG-DECO SMs (Figure 43 and 44). The effect of VFALL (velocity of falling debris in MELCOR code) and PDPor (initial particulate debris porosity in MELCOR code) on the results is yet to be explained.

Failure domain analysis results (Figure 52) for EIGT100-IDEJ0 scenario show that probability of containment failure due to formation of non-coolable debris configuration strongly depends on the depth of the pool (XPW) and debris

bed slope angle (SLPA). If we consider dry-out as a failure criterion, then failure can be considered as physically unreasonable only for deep pools (above 6m) and relatively flat debris bed shape, with slope angle below ~7.5 degrees. On the other hand, "no dry-out" failure criterion might be considered as too conservative. After dry-out, particle temperature rises above the saturation temperature, however, a small dry zone can be coolable by steam flow. Therefore, if we consider less conservative criteria, such as long term temperature of solid debris is below (i) debris oxidation temperature (Figure 52b); (ii) metallic debris remelting temperature (Figure 52c) or (iii) oxidic debris remelting temperature (Figure 52d), we see significantly larger domain of parameters where failure can be considered as physically unreasonable. In particular, the minimum depth of the pool should be above ~5m and the maximum allowed slope angle can be up to ~15 degrees (~up to 20-25 degrees for pool depths above 8m). Furthermore, based on the results, the difference between the failure domains (Figure 52b,c,d) obtained for oxidation temperature, melting temperature of metals and oxides is relatively small, and results look qualitatively similar.

If we consider necessity of failure ($P_s = 0.999$), i.e. "the possibility that containment doesn't fail". The results suggest that failure can be considered as unavoidable (i.e. over 95% of the cases exceed $P_s = 0.999$) only in case of "no dry-out" criterion and in case of very shallow pool (below 2m) and debris bed slope angle above 7.5 degrees, as illustrated in Figure 53a. For other criteria, based on long term debris bed temperature (Figure 53b,c,d) P_f exceed $P_s = 0.999$ in more than 5% of the cases only when the pool depth is below 2m.
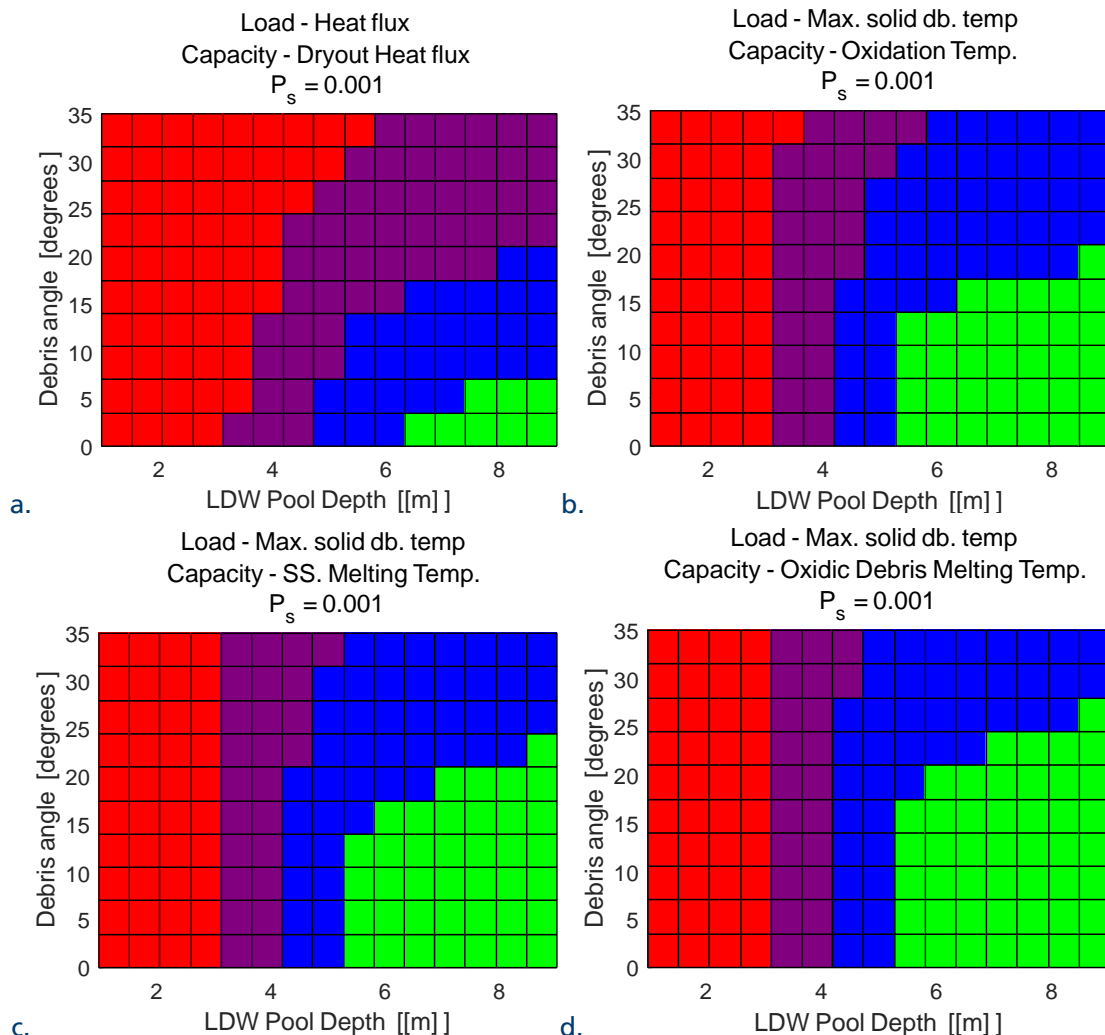

Figure 52. COR-AGGDECO Failure domain results (Possibility $P_s = 1.e - 3$) for EIGT100-IDEJ0 scenario for (a) HF>DHF [W/m2-K], Debris temperature> (b) oxidation temperature (c) melting temperature of metallic debris (d) melting temperature of oxidic debris (K).

Figure 53. COR-AGGDECO Failure domain results (Necessity $P_s = 0.999$) for EIGT100-IDEJ0 scenario for (a) HF>DHF [W/m2-K], Debris temperature> (b) oxidation temperature (c) melting temperature of metallic debris (d) melting temperature of oxidic debris (K).
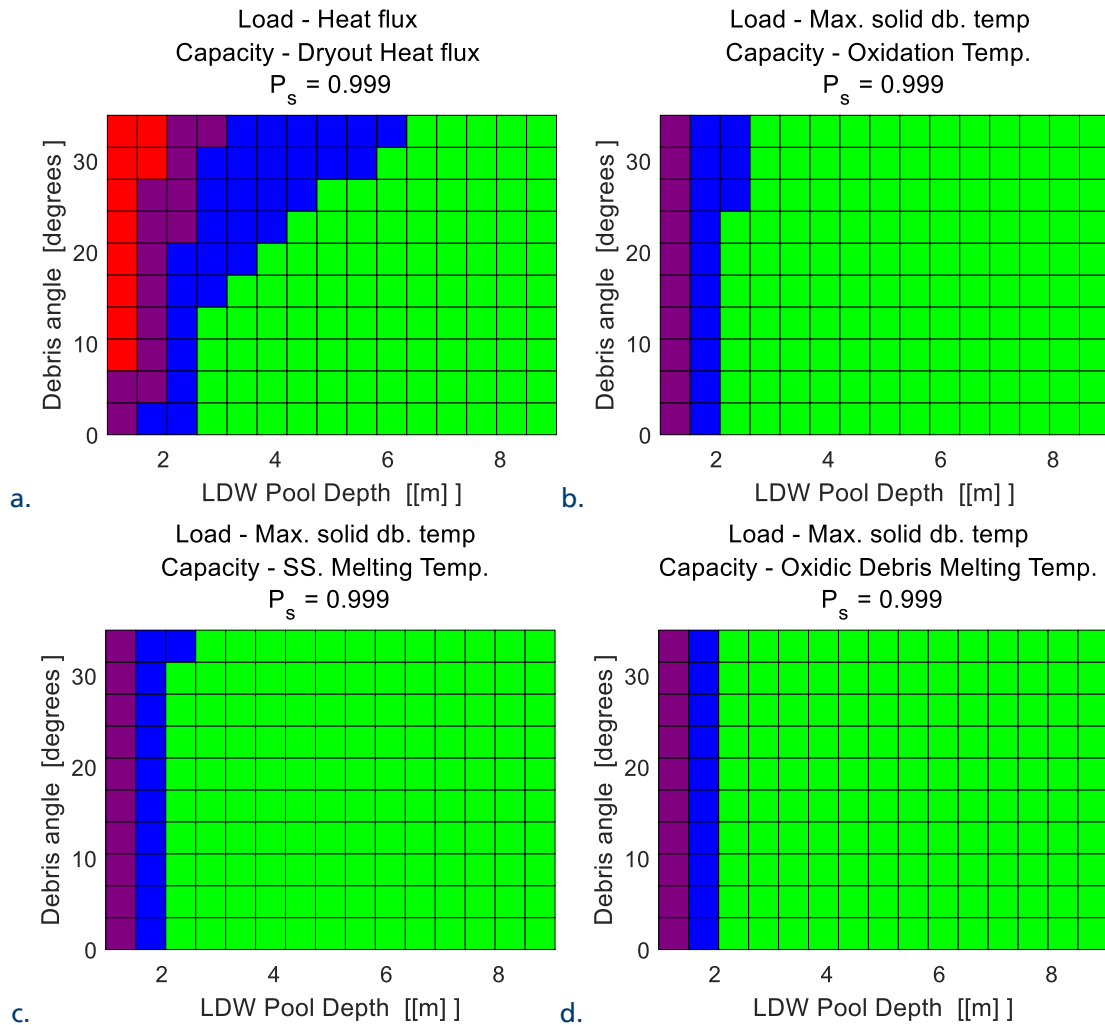
Figure 54 presents failure domain analysis results for EIGT100-IDEJ1 scenario. Based on the results, failure can be considered as physically unreasonable ($P_f < P_s = 10^{-3}$, in over 95% of the cases) only when melting temperature of metals (Figure 54c) or oxides (Figure 54d) was considered as a failure criterion and very deep pool depth (above 8m) and very small values of velocity of failing debris (VFALL<0.1m/s). It is important to note that the value of VFALL=0.01m/s is recommended by the MELCOR code best practices guidelines [64]. However,

This value is recommended for falling debris quench model, which is triggered by a failure of core support plate in one of the radial rings. On the other hand, the same value is used for axial debris relocation in "stationary" debris mode, which, as a results, give quite significant contribution to debris ejection rate in case of gross failure of vessel LH wall, which was identified in [32][33] and illustrated in Figure 56. Thus, the effect of this parameter and respective MELCOR modelling of phenomena of debris ejection form the vessel require further investigation.
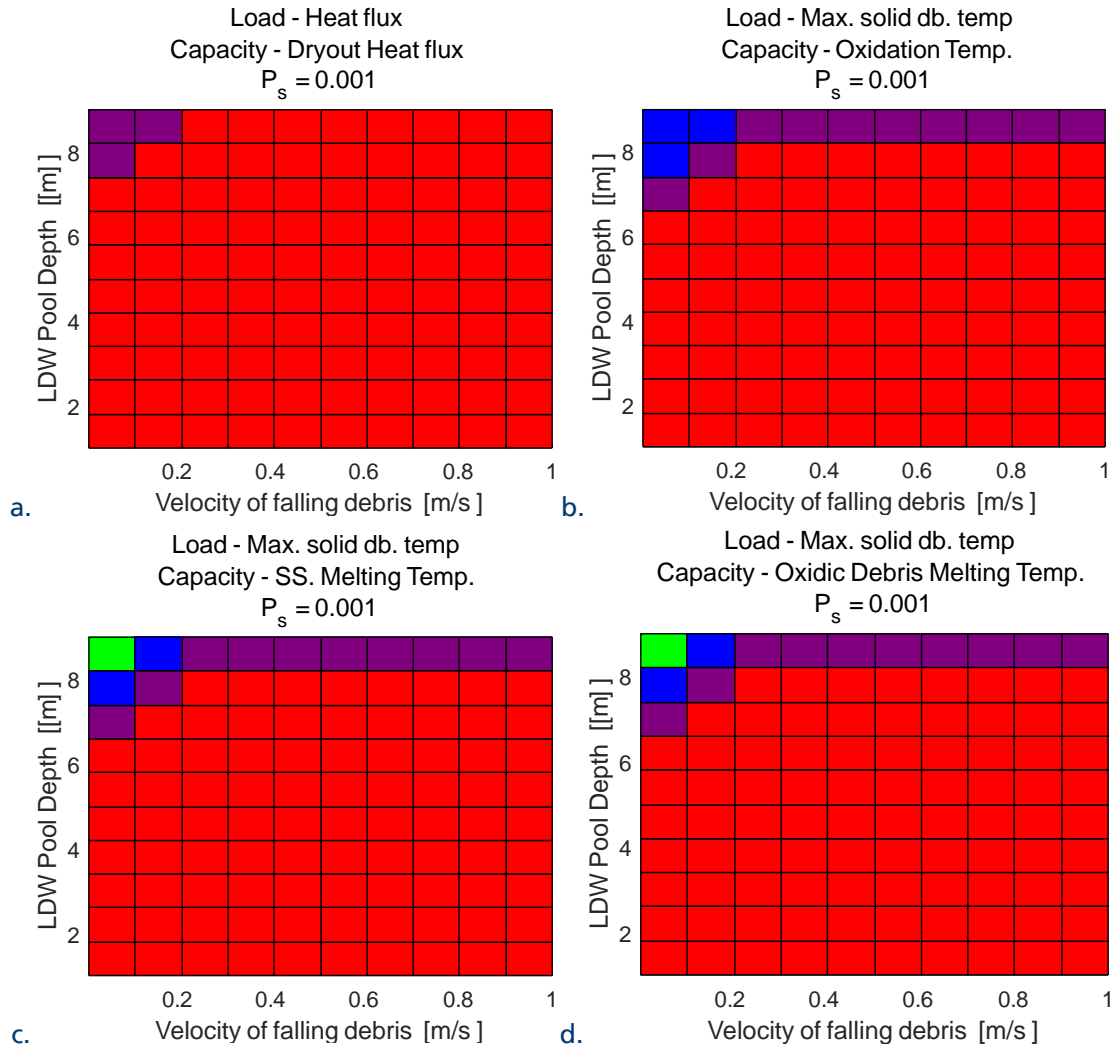
Figure 54. COR-AGGDECO Failure domain results (Possibility $P_s = 1.e - 3$) for EIGT100-IDEJ1 scenario for (a) HF>DHF [W/m2-K], Debris temperature> (b) oxidation temperature (c) melting temperature of metallic debris (d) melting temperature of oxidic debris (K).

If we consider necessity of failure ($P_s = 0.999$), then the failure can be considered as unavoidable ($P_f > P_s$ with 95% confidence) for EIGT100-IDEJ1 scenario for all failure criteria, if the water pool depth is below ~6m. For the pool depths above ~8m, the necessity of failure is small only in cases where long term temperature of solid debris is considered as a failure criterion (Figure 55b,c,d).
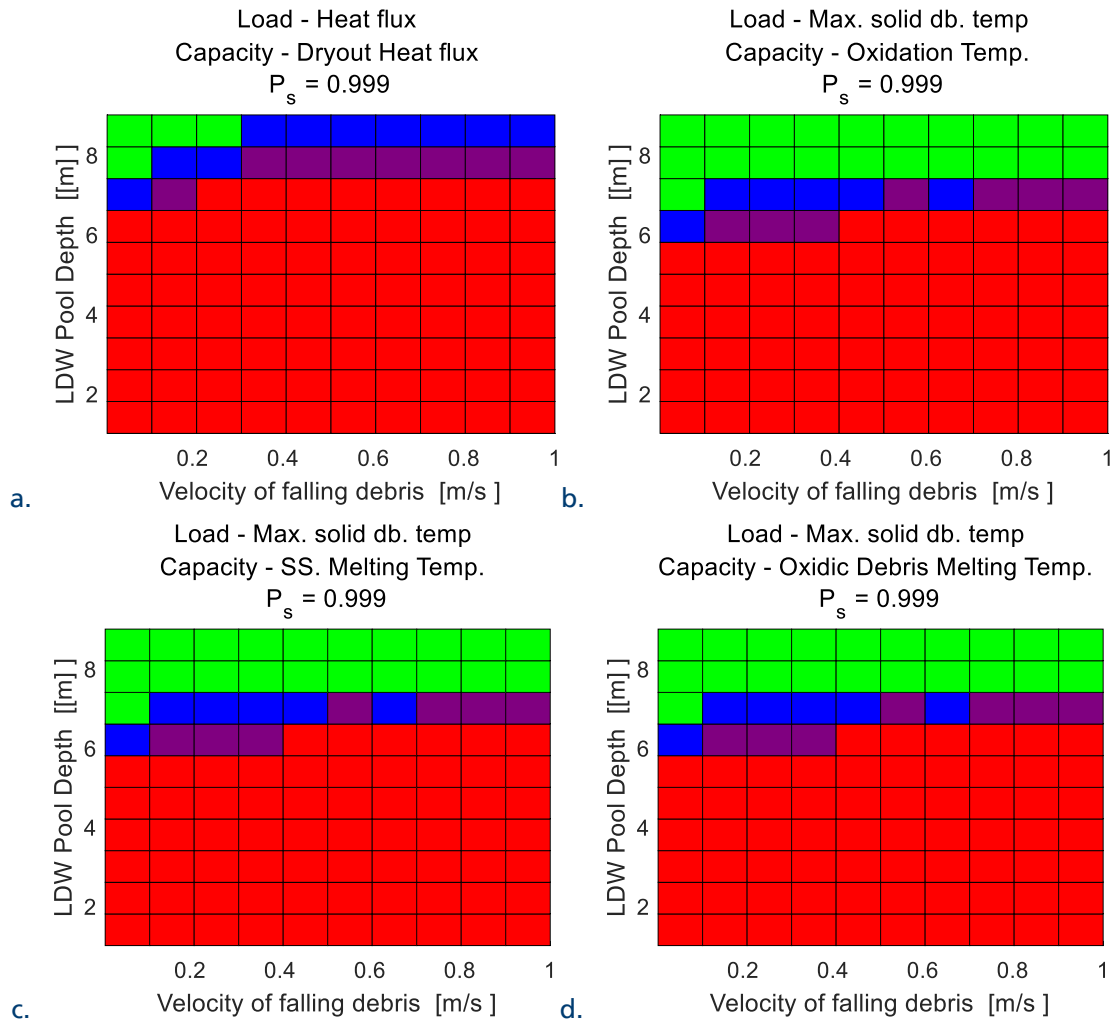
Figure 55. COR-AGGDECO Failure domain results (Necessity $P_s = 0.999$) for EIGT100-IDEJ1 scenario for (a) HF>DHF [W/m2-K], Debris temperature> (b) oxidation temperature (c) melting temperature of metallic debris (d) melting temperature of oxidic debris (K).
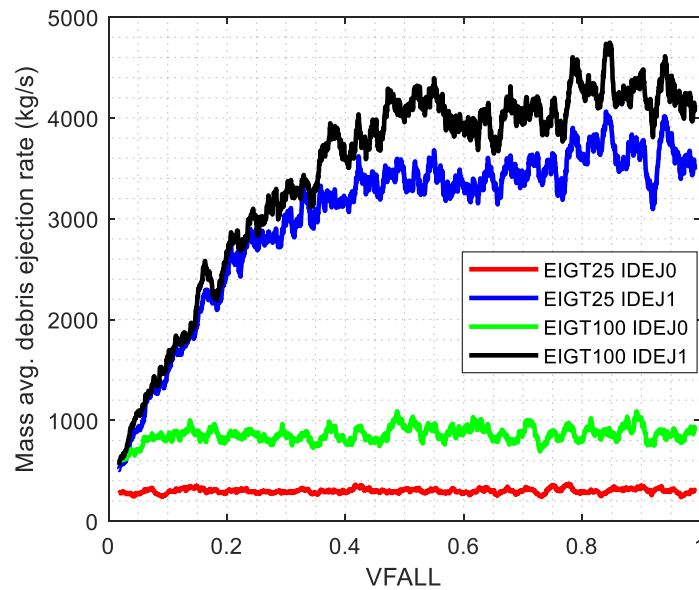

Figure 56. Moving average of mass averaged debris ejection rate (kg/s) as a function of VFALL (m/s)[32].

5   Pilot study for fully informed uncertainty analysis.

In a standard PSA, the output of PSA Level 1 is typically core damage (possibly separated in a few sub-categories). These core damage sequences are then divided into a number of sub-categories representing the important features for Level 2 progression.

The link between PSA L1 and L2 is the plant damage states. The plant damage states describe not only the core damage state but also the conditions of the primary system and the containment. There are normally around 20-40 Plant Damage States (PDS) defined in the interface between Level 1 and 2.

For the generic Nordic BWR PSA model studied here, there are 27 PDSs for power operation and low power operating modes. The attributes that are considered relevant for modelling of the continued process are:

- Core damage state (failure of shutdown, core cooling or residual heat removal).

- Initiating event (transient or LOCA).

- Time of core melt (early, late).

- Reactor pressure (low, high).

- Containment atmosphere (inert, air).

- Containment spray system status.

- Containment pressure relief status (activated, not activated).

- Filtered containment venting status (activated, not yet activated, failed).

- Bypass of containment (bypass, intact).

- Suppression pool temperature (warm if pool cooling fails, else cool).

The events that are represented in a PSA Level 2 are those that may change the conditions for retaining of releases within the RPV or the containment. Hence, if the coolability in the RPV is different in different scenarios – then this is vital information. If the sequences are affecting the phenomena that can occur, then this is also vital information. For each of the PDS, a subsequent containment event tree (CET) is defined, modelling the continued accident progression.

The accident progression sequences are influenced by various physical phenomena. The types of phenomena that are usually accounted for in a PSA are:

- Re-criticality (in the core, in lower plenum, in containment).
- Hydrogen burn (deflagration and detonation).
- In-vessel steam explosion.
- Ex-vessel steam explosion.
- Direct containment heating.
- Rocket mode.
- Melt concrete interaction (basemat penetration).
- Steam generator tube rupture (only for PWR).

The effect of the phenomena can be:

- Containment rupture.
- Different types of containment bypass.
- Activation of filtered containment venting.

The effect most focused on in the following is containment rupture. The sequences in the CET end at the release categories (RC) and there are normally around 15-40 of such. The RCs can be defined in different ways, for example by release size or type of sequence. The normal approach is to use the sequence type, because then only a limited

amount of verifying deterministic calculations are considered to be required. For the sequence type approach, the characterization is for example based on;

- Release path (containment bypass, containment rupture, filtered release, leakage).
- Timing of release (early, late).
- Initiator (pipe rupture, transient).
- Sprinkling of containment established (yes/no).

In a generic PSA model for Nordic BWR, which is used as reference case in this report, each phenomenon, for example steam explosion or debris bed coolability, is modelled with one fixed probability per binning sequence (if relevant). The reference case provides information to the deterministic analysis about which phenomena and parameters that are currently analyzed and is used in the binning of sequences and consequences.

Two important phenomena occurring at or after reactor vessel melt-through are steam explosion and debris bed coolability. To be able to study how these phenomena depend on different parameters, a dynamic approach can be used. The parameters that may influence the phenomena are physical parameters such as pressure, temperature and water depth in different parts of the plant which depend on accident scenario. Furthermore, assessment of the magnitude of phenomena is subject to epistemic uncertainty which can significantly affect level 2 PSA analysis results.

In the following chapters we present a reference PSA model of Nordic BWR and enhanced PSA model, which use information generated by ROAAM+ framework, taking into account both aleatory and epistemic sources of uncertainty.

5.1 Reference PSA model

The reference PSA model is a generic full-scale PSA for a Nordic BWR. In the reference PSA model, the accident progression for PSA level 2 is modelled in a containment event tree, CET. In the CET there is no explicit modelling of phenomena. Instead, there is a function event where all the phenomena are treated in a common fault tree.

The probabilities for steam explosion resulting in containment failure are:

- 1E-3 - for low pressure melt through.
- 3E-3 - for high pressure melt through.

These values are always applied even if the lower drywell (LDW) flooding system fails. The rationale for this modelling is that no positive credit should be taken for system failures. Furthermore, there may be enough water for a steam explosion to occur but not enough to avoid melt through of the penetrations in the LDW floor. The probabilities for melt through of the penetrations in the LDW floor are:

- 1E-3 - for successful LDW flooding.
- 1.0 - for failure of the LDW flooding system.

The studied PDSs in this study are:

- HS2-TH1. This is a plant damage state where the initiating event is a transient or a CCI, core cooling has failed and the reactor vessel pressure is still high (the automatic depressurization system, ADS, has failed).
- HS2-TL4. This is a plant damage state where the initiating event is a transient or a CCI, core cooling has failed, and the reactor vessel pressure is low.
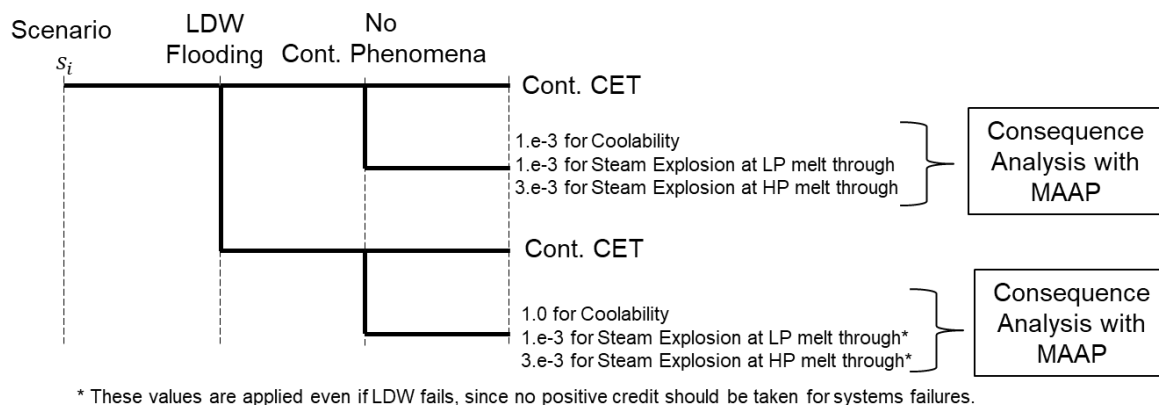
Figure 57. Treatment of containment phenomena in reference PSA model of Nordic BWR.

It is important to note that in current PSA-L2 approach, epistemic uncertainty in the outcomes of the phenomena is represented by a single probability number that containment can be damaged by ex-vessel steam explosion, or by non-coolable debris. The number can be based on expert judgment combined with some sort of uncertainty quantification. This number is sometimes perceived as frequency, e.g. frequency of occurrence of explosion or non-coolable debris. However, it is essentially a measure of confidence in prediction. Furthermore, consequences of containment damage are often point estimates (e.g. using a few MAAP calculations) for given accident sequences, without quantification of modelling uncertainty in the magnitude of the release.

5.2   Enhanced PSA model

The reference PSA model containment event trees for the plant damage states HS2-TH1 and HS2-TL4 were modified to consider the depth of the water pool in lower drywell (LDW) and respective ex-vessel phenomena, such as ex-vessel debris coolability (COOL) and ex-vessel steam explosion (STEX).

The water depth alternatives are (i) Deep water pool in LDW; (ii) Shallow water pool in LDW; (iii) No water in LDW.

Figure 58 shows an example of the sequences with explicit modelling of ex-vessel steam explosion and debris coolability (dashed red). For each end state in the CET there is a specific probability distribution generated with ROAAM+ framework for Nordic BWR (see Chapter 5.3.1).
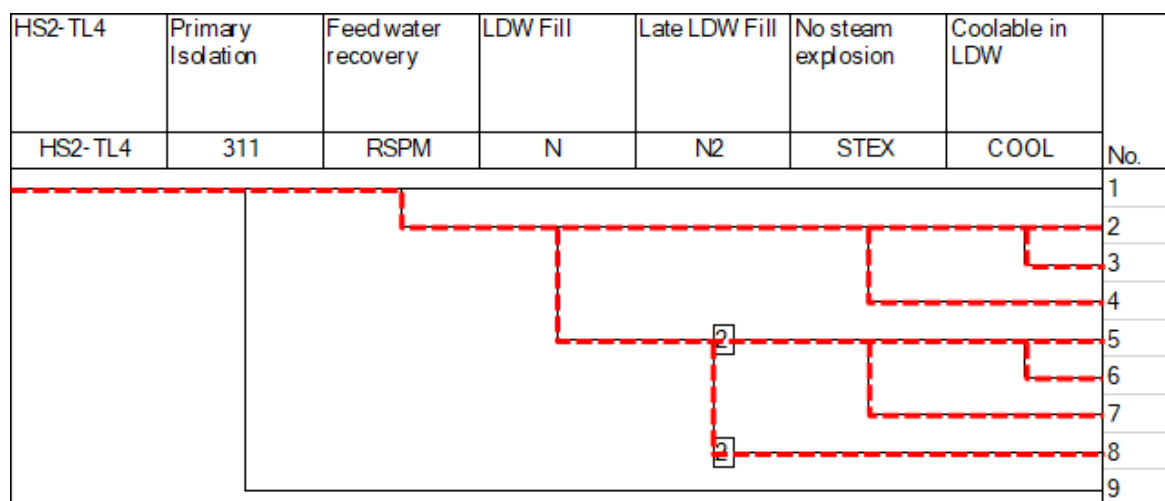

Figure 58. Containment event tree sequences in enhanced PSA model of Nordic BWR with explicit modelling of containment phenomena (dashed red).

In the complete CET there are also function events and sequences for isolation, long term residual heat removal etc. As seen in Figure 58 there is one common function event for steam explosion and one common function event for coolability. For each sequence, however there is a unique basic event used for each phenomenon depending on the sequence (i.e. the combination of depth and melt flow).

5.3 Enhanced Model Results

5.3.1 ROAAM+ Input to Enhanced PSA model

From the initial sequences in the PSA Level 1, all events that are leading to a certain PDS are then treated in the same manner in the continued sequence (however, dependencies are treated logically correct if the failure should affect systems in PSA Level 2). It is however obvious that it will be different scenarios from a deterministic standpoint if there is an initial loss of offsite power and no start of the diesels, compared to a scenario where the diesels would stop after some hours.

The purpose with the improved integrated link between the PSA and deterministic analyses is hence to be able to judge if, for example, these scenarios need to be treated differently in the PSA context. The approach chosen in this work was to identify some sequences from the PSA Level 1 and to use ROAAM+ framework to evaluate the progress of these sequences and correspondent conditional containment failure probability for different severe accident scenario.

Based on the ROAAM+ analysis results, presented in the chapter 4, the risk of containment failure due to ex-vessel steam explosion and ex-vessel debris coolability is mostly affected by the uncertainty in the water pool depth, which can be reflected in enhanced PSA modelling. Other parameters that have high contribution to the results (e.g. debris slope angle, velocity of falling debris, heat transfer coefficients between debris and IGTs, etc.) are epistemic modelling parameters and cannot be considered in ET/FT analysis. On the other hand, such parameters as (IDEJ1/IDEJ0) mode of debris ejection from the vessel are considered as phenomenological splinters, i.e. phenomenological scenarios where relevant epistemic uncertainties are beyond the reach of any reasonably verifiable quantification. These splinters will be treated in PSA analysis in the same manner as in ROAAM+ framework.

Figure 59, 60, 61 and 62 show the resulting distributions of probability of failure obtained from failure domain analysis for ex-vessel debris coolability and steam explosion, presented in section 4.1 and 4.2.

It is important to note that in the previous phase of SPARC project [66], the correlation between steam explosion and debris coolability was not taken into account due to the format of results compilation from ROAAM+ analysis. In the current implementation the analysis was performed for ex-vessel debris coolability and steam explosion simultaneously, i.e. the same set of respective input and deterministic\intangible parameters and probability distributions was used in risk assessment, and respective results are directly exported from ROAAM+ GUI (see section 3.1.9 and Figure 16) to RiskSpectrum PSA as user defined simulation values (i.e. the data is correlated correctly between these two events).

Furthermore, water depth at "deep pool" is related to system functionality and can be calculated with deterministic models or even with simple hand calculations. If the LDW flooding system works, there will always be about 7-8 m of water in LDW. Thus, for the "deep pool" analysis cases in ROAAM+ framework MELCOR code predictions of the pool depth were used [32]. The water depth for shallow pool conditions is much more uncertain since this completely depends on the sequence, therefore in current implementation it was considered as intangible parameter on specified range.

Additionally, in this work we address the effect of possible design modification (reinforcement of the containment hatch door) on unacceptable release frequency estimated by RiskSpectrum PSA using the data generated by ROAAM+.
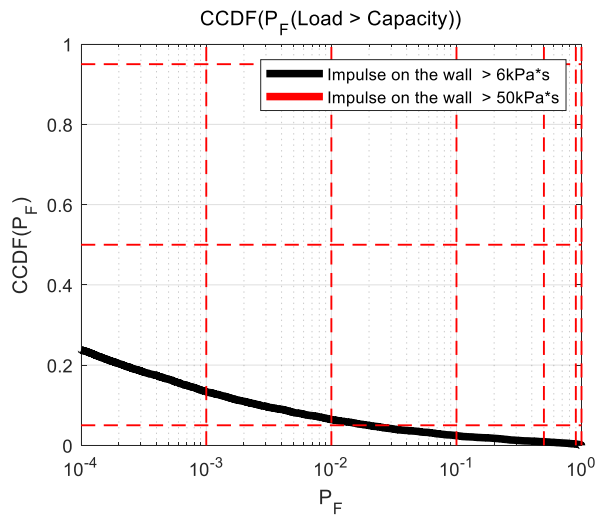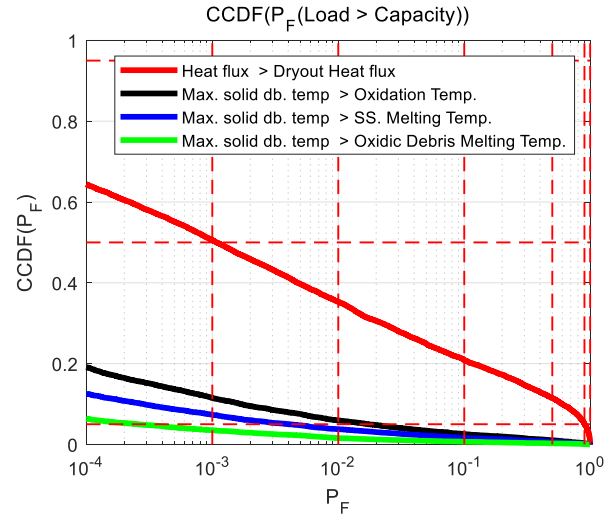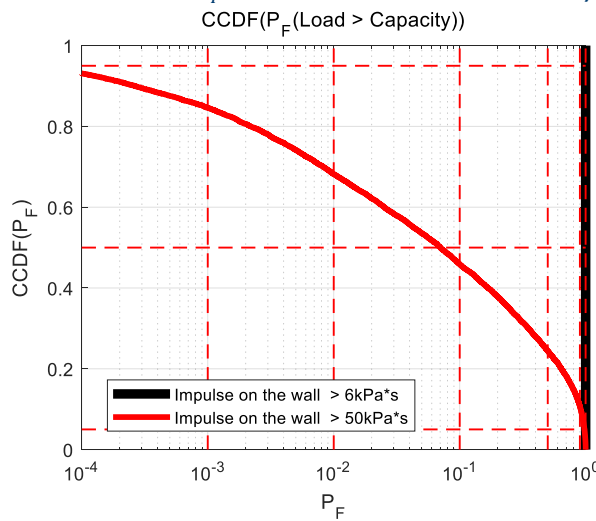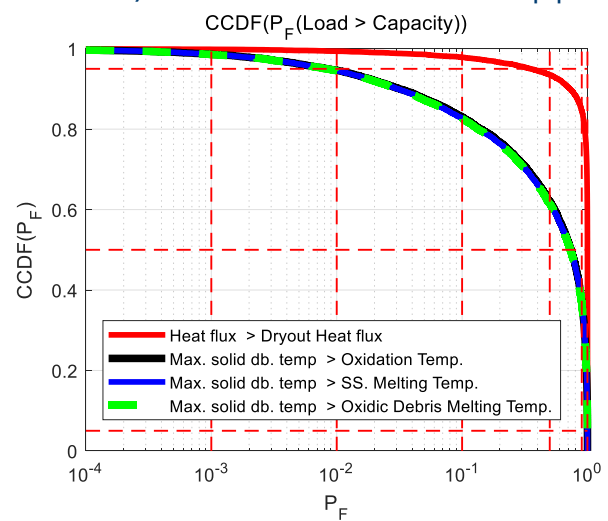
Figure 59. CCDF of P_F for EIGT100-IDEJ0 scenario a) MEM-SEIM b) MEM-AGGDECO in case of deep pool.
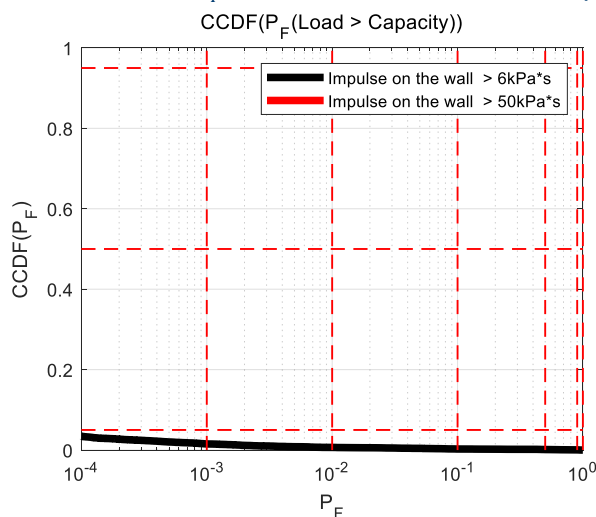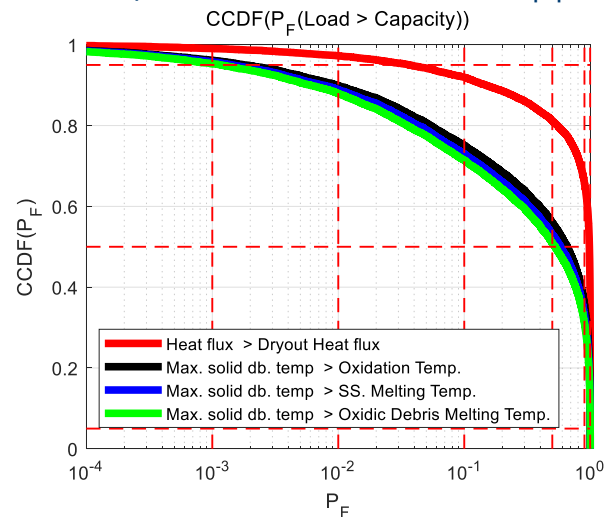

Figure 60. CCDF of P_F for EIGT100-IDEJ1 scenario a) MEM-SEIM b) MEM-AGGDECO in case of deep pool.
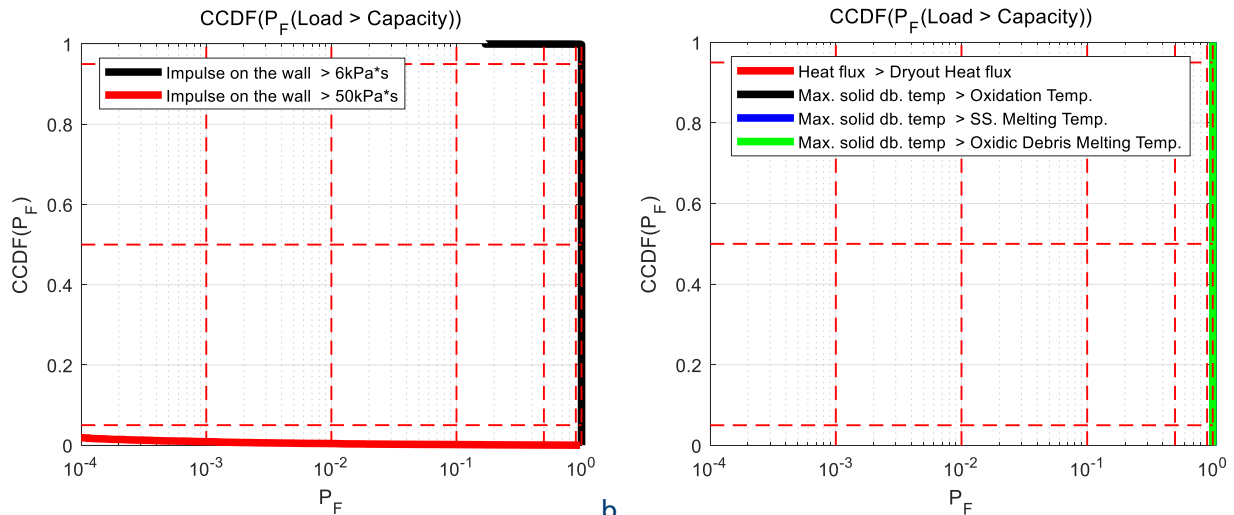

Figure 61. CCDF of P_F for EIGT100-IDEJ0 scenario a) MEM-SEIM b) MEM-AGGDECO in case of shallow pool.

a.   b.

Figure 62. CCDF of P_F for EIGT100-IDEJ1 scenario a) MEM-SEIM b) MEM-AGGDECO in case of shallow pool.

Table 10 show the summary of the results presented in the Figure 59, 60, 61 and 62 and to be used in RiskSpectrum PSA analysis using enhanced model.

Table 10. RiskSpectrum PSA simulation matrix.

Description	Debris ejection mode (splinter)	
	EIGT100-IDEJ1	EIGT100-IDEJ0
Deep pool (M)[1], Steam explosion load vs. fragility (Non-reinforced door).	CASEID_001D Mean: 1.0[2]	CASEID_001D: Mean: 1.236e-2
Deep pool (M)[1], Steam explosion load vs. fragility (Reinforced door).	CASEID_002D Mean: 2.697e-1	CASEID_002D Mean: 0.0
Deep pool (M)[1], Debris non-coolable if max. temperature exceed 1700K (SS melting temperature).	CASEID_003D Mean: 6.047e-1	CASEID_003D Mean: 8.547e-3
Shallow pool (1-4m)[3], Steam explosion load vs. fragility (Non-reinforced door).	CASEID_001S Mean: 9.98e-1	CASEID_001S Mean: 1.647e-3
Shallow pool (1-4m)[3], Steam explosion load vs. fragility (Reinforced door).	CASEID_002S Mean: 7.144-e4	CASEID_002S Mean: 0.0
Shallow pool (1-4m)[3], Debris non-coolable if max. temperature exceed 1700K (SS melting temperature).	CASEID_003S Mean: 1.0	CASEID_003S Mean: 5.312e-1

Note that two fragility limits will be used for ex-vessel steam explosion, in order to evaluate the effect of design modification of PSA analysis results:

- Non-reinforced hatch door, that can withstand 6kPa*s explosion impulses (original design).
- Reinforced hatch door, that can withstand 50kPa*s explosion impulses (modified design).

---

[1]. LDW water pool depth (XPW) for "Deep pool" was predicted by MELCOR code (MEM SM).

[2]. Mean values are obtained from respective distributions of probability of failure (P_F) illustrated in Figure 59-62.

[3]. LDW water pool depth (XPW) for "Shallow pool" was considered as intangible parameter on the range from [1-4m].

In case of ex-vessel debris coolability – remelting of metallic debris (debris bed temperature exceeding stainless steel melting temperature (1700K)) was considered as a failure criterion.

5.3.2 Analysis and Comparison between Reference Case Model and Enhanced Model

All transients and CCIs leading to the plant damage states HS2-TH1 and HS2-TL4 (core damage due to inadequate coolant inventory make-up) were analysed for all level 2 release categories. Release categories leading to release frequencies over 0.1% of the core inventory of an 1800 MW BWR are grouped as non-acceptable. Furthermore, in the analyses presented in earlier phases of the SPARC project [65], the release category "basemat melt-through" was, according to industry standard, presented individually. Those results were excluded from the group of non-acceptable releases. It can, however, be argued that basemat melt-through cases could represent large releases e.g. after the standard analysis period of 72 h. To account for this possibility, the former non-acceptable release group is, in the current analysis, merged with the basemat melt-through group to form a group named "non-contained release".

The normalized results for medium values of non-contained release frequency per type of initiating event are shown in Figure 63 and 64. The normalization is done with respect to the frequency for non-contained release due to Loss of offsite power. The results show that the non-contained release frequency in most of the cases (i) increases in the enhanced model in case of EIGT100-IDEJ1, and (ii) decreases in case of EIGT100-IDEJ0. This behavior can be explained by the effect of the mode of debris ejection from the vessel on melt release conditions predicted by MELCOR code (MEM SM). It is clear from these results the high sensitivity of the non-contained release frequency to the mode of debris ejection from the vessel (IDEJ0 vs. IDEJ1).

It can be noted that the initiating event group spurious M-isolation is much more affected by the enhanced modelling compared to the other initiating event types studied. To explain the reason for this, it can first be noted that the group of non-acceptable releases, for a BWR, to a relatively large extent contains so-called bypass sequences, in which closure (isolation) of the containment fails and the release path occurs through e.g. through open steam-lines. Such sequences will not be affected by the ROAAM+ approach since they are not created by the studied containment rupture phenomena. M-isolation, or IM-isolation, refers to a specific function of the reactor protection system, which initiates closing of isolation valves in the feedwater lines. The effect of the initiating event is thereby at first sight similar to that of the loss of feedwater transient. However, in the generic Nordic BWR plant design represented by the PSA model used in this study, M-isolation automatically activates another isolation function that initiates closure of the steam lines. This implies that for sequences starting with spurious M-isolation, bypass sequences through open steam lines are directly excluded (apart from cases with mechanical errors in the MSIVs) and this category of initiating events becomes the only category where the ROAAM+ methodology will influence all the resulting accident sequences. In contrast, e.g. the loss of feedwater initiating event category has a relatively low frequency, which implies that together with the event probabilities prescribed by the ROAAM+ methodology, sequences affected by ROAAM+ to a large extent end up below the cut-off frequency of the PSA analysis, leaving almost only bypass sequences above it. In summary, loss of feedwater sequences will in this model be minimally affected by ROAAM+ while the inverse is true for spurious M-isolation sequences, thereby creating a large difference between these seemingly similar initiating event families [66].
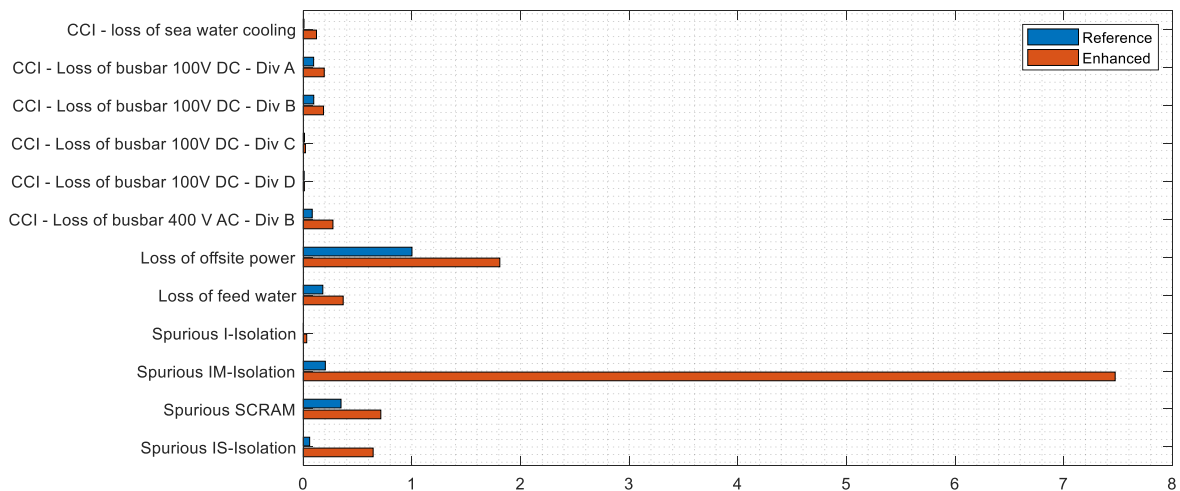
Figure 63. Comparison of normalized non-contained release frequencies between the reference and the enhanced models for EIGT100-IDEJ1 scenario with non-reinforced hatch door.
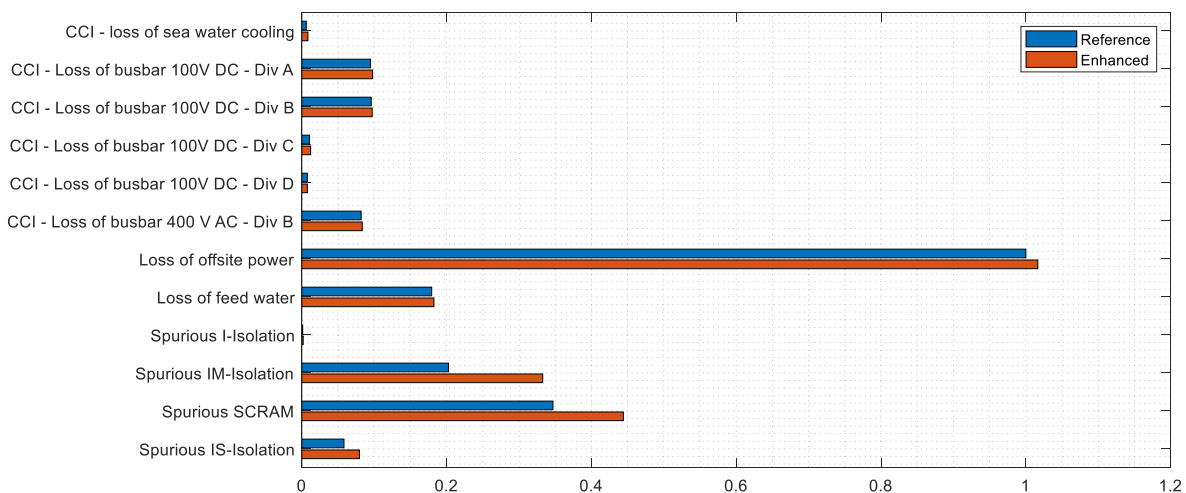

Figure 64. Comparison of normalized non-contained release frequencies between the reference and the enhanced models for EIGT100-IDEJ0 scenario with non-reinforced hatch door.

Figure 65 and 66 show the results of uncertainty analysis using ROAAM+ generated values of probability of containment failure due to ex-vessel debris coolability and steam explosion (see Figure 59, 60, 61 and 62). The results show that the uncertainty in the results depends on the mode of debris ejection from the vessel. For example, in case of IDEJ1 (solid debris ejection – OFF) the resultant distributions are concentrated around its expected values, which can be explained by the probability distribution of conditional containment failure probability due to ex-vessel steam explosion with non-reinforced hatch door (Figure 60a (deep) and Figure 62a (shallow)), which mean that the results of PSA analysis will not be significantly affected by probability distributions for ex-vessel debris coolability, with exception to some scenarios with shallow pool conditions.

In case of IDEJ0 (Figure 66) the resultant distributions are very narrow; however, the right tails of the distributions can span over several orders of magnitude for some accident scenarios.

Furthermore, figures 65 and 66 show the values of normalized non-contained release frequencies obtained with reference PSA model of Nordic BWR (marked with black "●"). The results indicate that in case of IDEJ1 (Figure 65), the reference values lie outside the range of respective distributions generated with enhanced model.

In case of IDEJ0 (Figure 66) the reference values give very good estimates of non-contained release frequencies (e.g. judging by 0.25, 0.5, 0.75 quantiles of the distributions) in all initiating event groups.
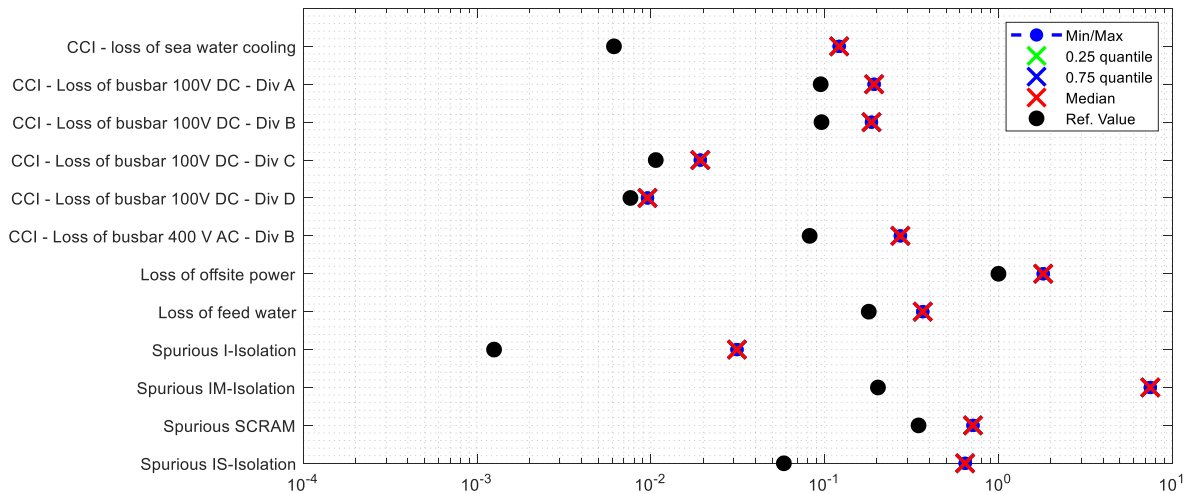
Figure 65. Uncertainty analysis results of normalized non-contained release frequencies using enhanced model for EIGT100-IDEJ1 scenario with non-reinforced hatch door.
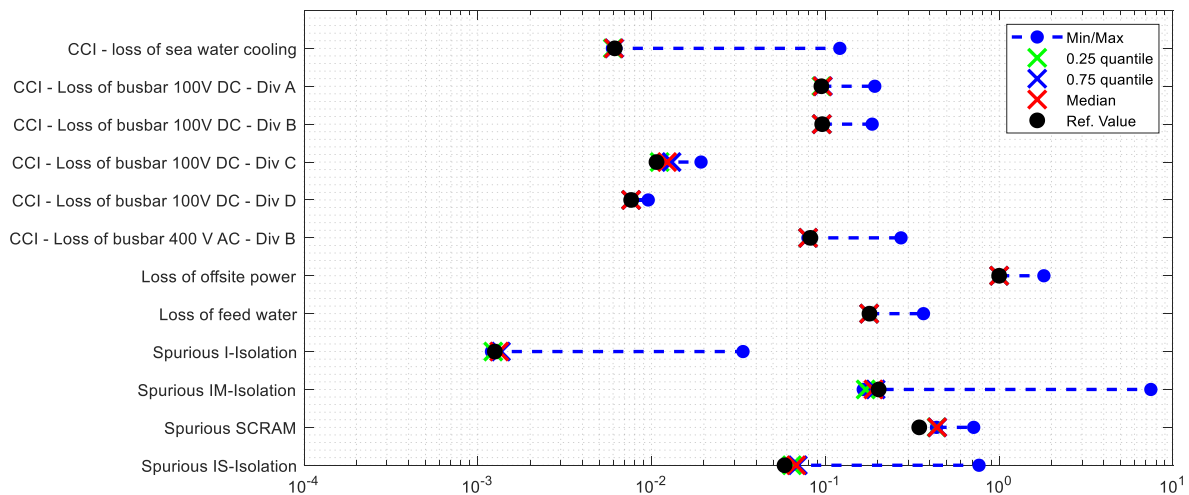

Figure 66. Uncertainty analysis results of normalized non-contained release frequencies using enhanced model for EIGT100-IDEJ0 scenario with non-reinforced hatch door.

5.3.2.1 Comparison with previous results

In this section a comparison with results obtained in the previous phase of NKS-SPARC project [66] is performed.

The normalized results for non-contained release per type of initiating event, obtained during the previous phase of NKS-SPARC project were calculated for (i) large (Figure 67) (ii) medium (Figure 68) and (iii) small (dripping) (Figure 69) melt flow rates from the vessel at vessel lower head failure. The normalization was done with respect to the frequency for non-contained release due to Loss of offsite power in the reference PSA model.

It is important to note that the melt flow at reactor vessel lower head failure was determined based on the size of the jet, i.e., melt flow sizes were defined by the following diameters of the melt jet:

- $d_{jet} < 0.075$ m   Dripping flow (corresponds to IGT size break).
- $0,075 < d_{jet} < 0.150$ m   Medium Flow (corresponds to ablated IGT to CRGT size break).
- $d_{jet} > 0.150$ m   Large Flow (significantly ablated CRGT or vessel wall segment failure).
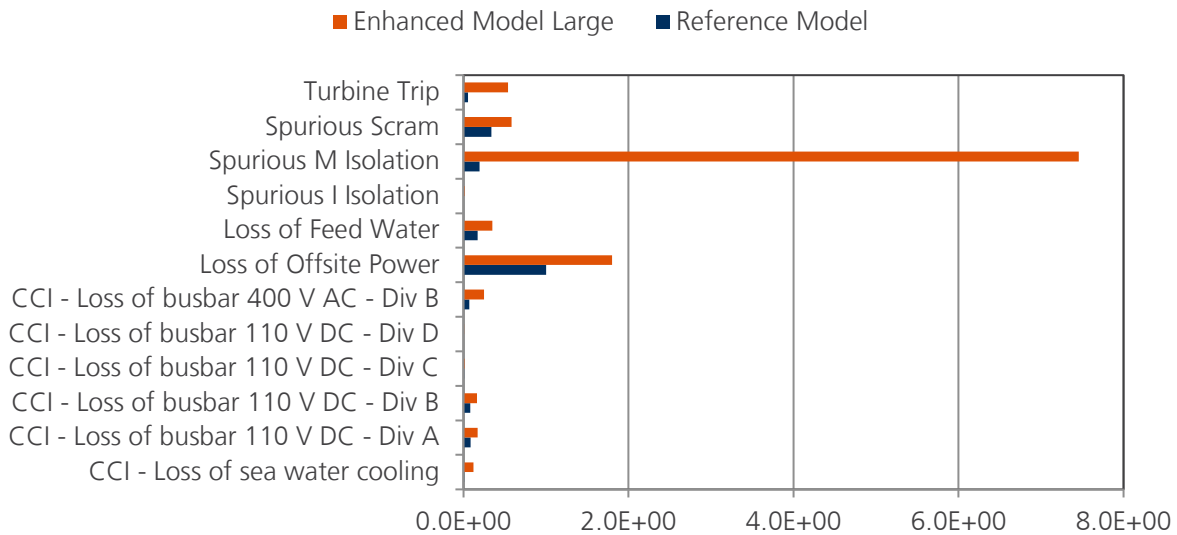
Figure 67: Comparison of normalized frequencies for non-contained release between the reference case and the enhanced model using large flow at melt-through.
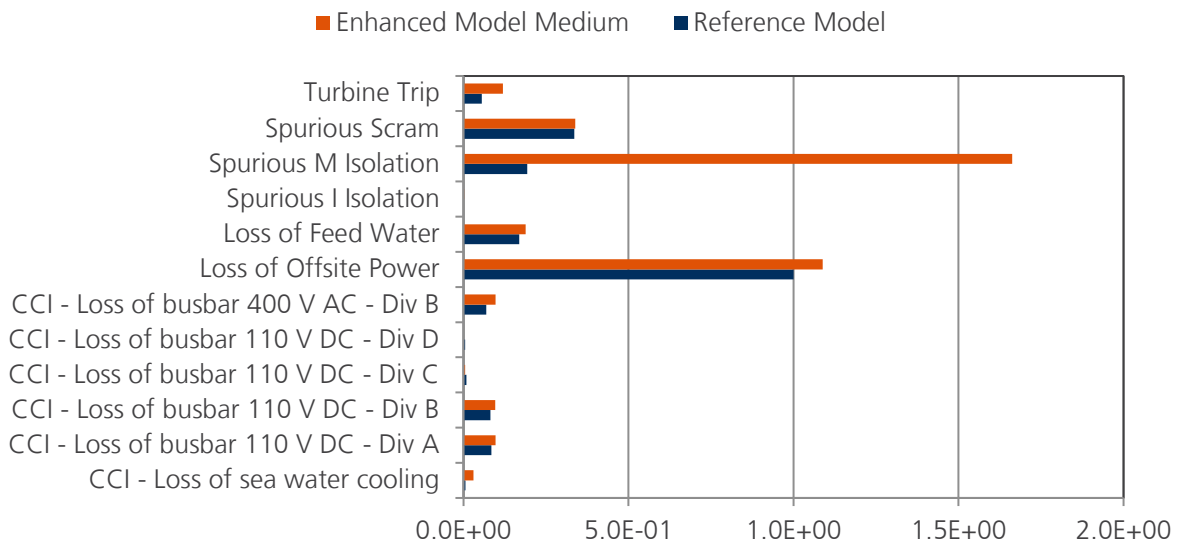

Figure 68: Comparison of normalized non-contained release frequencies between the reference case and the enhanced model using medium flow at melt-through.
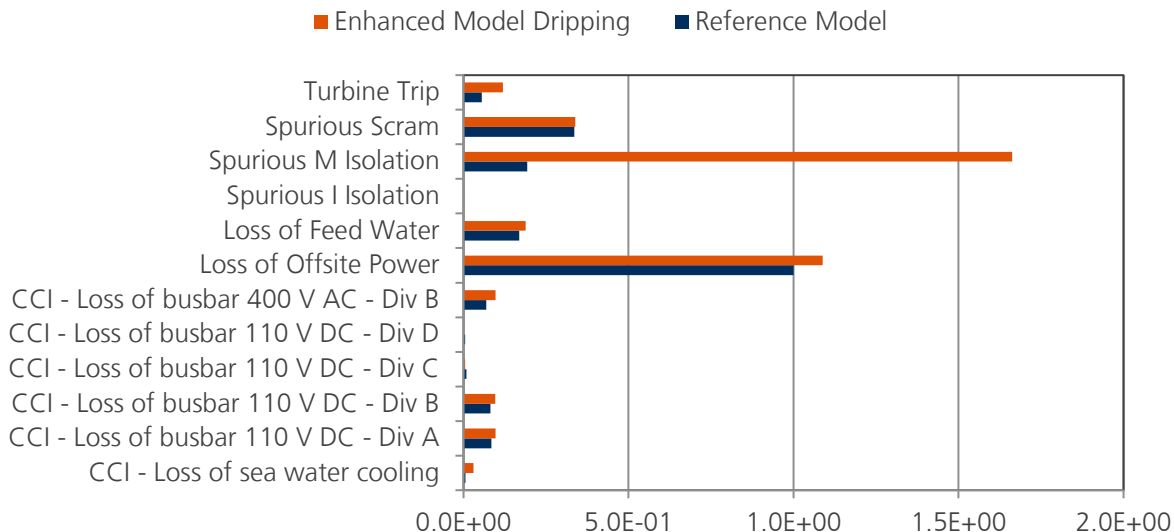
Figure 69: Comparison of normalized non-contained release frequencies between the reference case and the enhanced model using dripping flow at melt-through.

In case of dripping flow at vessel lower head failure, the results obtained in the previous phase of NKS-SPARC project are comparable with the results obtained in scenario with solid debris ejection – on (EIGT100-IDEJ0) presented in the Figure 64. Which can be explained by rather small values of jet radiuses and gradual melt and debris ejection rates in the case of IDEJ0, as demonstrated in the Figure 36a and b. The remaining difference can be explained by the improved modelling of ex-vessel debris coolability (see section 3.2.3).

On the other hand, EIGT100-IDEJ1 case, with solid debris ejection – off, in most of the cases results in large jet sizes and debris ejection rates (Figure 36a and b), which leads to significant loads on the containment due to both ex-vessel steam explosion and debris coolability. Therefore, the results for the large melt release (Figure 67) are comparable to the results obtained for EIGT100-IDEJ1 scenario, presented in the Figure 63.

5.3.3 The effect of design modification.

Analysis of the effect of possible design modification (reinforcement of hatch door) on PSA analysis results using ROAAM+ generated data has been performed. Based on ROAAM+ analysis results, reinforcement of the containment hatch door, located in the LDW, can significantly reduce the risk of containment failure due to ex-vessel steam explosion, as demonstrated in the Chapter 4.1.

Figure 70 and 71 show the comparison of PSA analysis results for the original and modified designs (reinforced vs. non-reinforced hatch door) and reference cases (non-reinforced). Note that the results presented in Figure 70, 71, 72 and 73 – are normalized with respect to the frequency for non-contained release due to Loss of offsite power in the reference PSA model.

The results suggest that in case of IDEJ1 (that typically results in large melt release rates and jet sizes, and, hence significant ex-vessel consequences), the design modification results in reduction of non-contained release frequency, however the effect is not very significant.

In case of IDEJ0 (that typically results in rather small jet sizes and release rates) the difference between non-reinforced, reinforced and reference cases is relatively small in all initiating event groups. The remaining difference can be explained by contribution from ex-vessel debris coolability, which is not affected by containment hatch door reinforcement and very sensitive to the pool depth (e.g expected value of P_f in case of IDEJ0 and deep pool is 8.547e-3, while in case of shallow pool it is 5.312e-1).

Figure 70: Comparison of normalized non-contained release frequencies (expected value) obtained with enhanced model for reinforced and non-reinforced hatch door in EIGT100-IDEJ1 scenario.
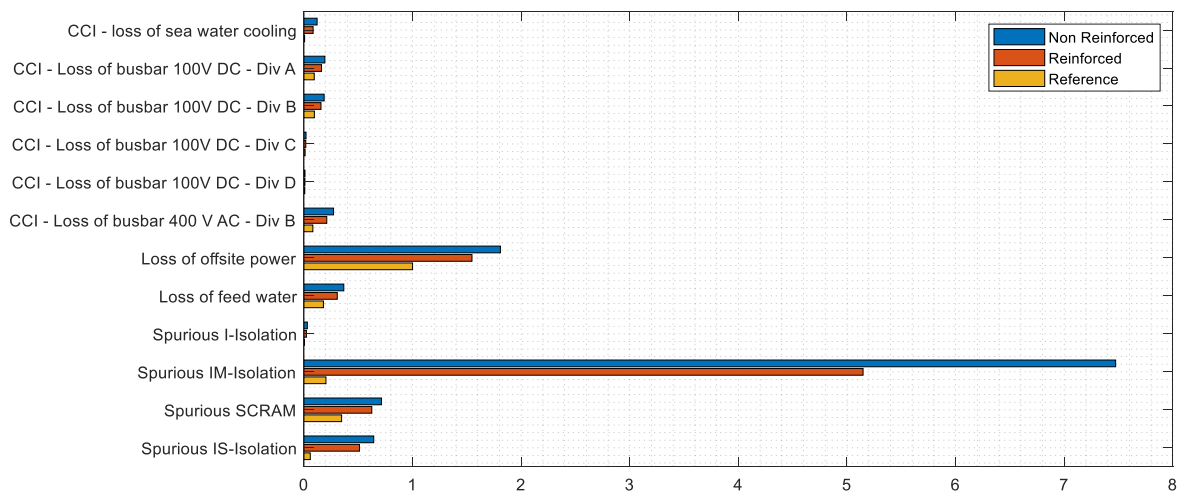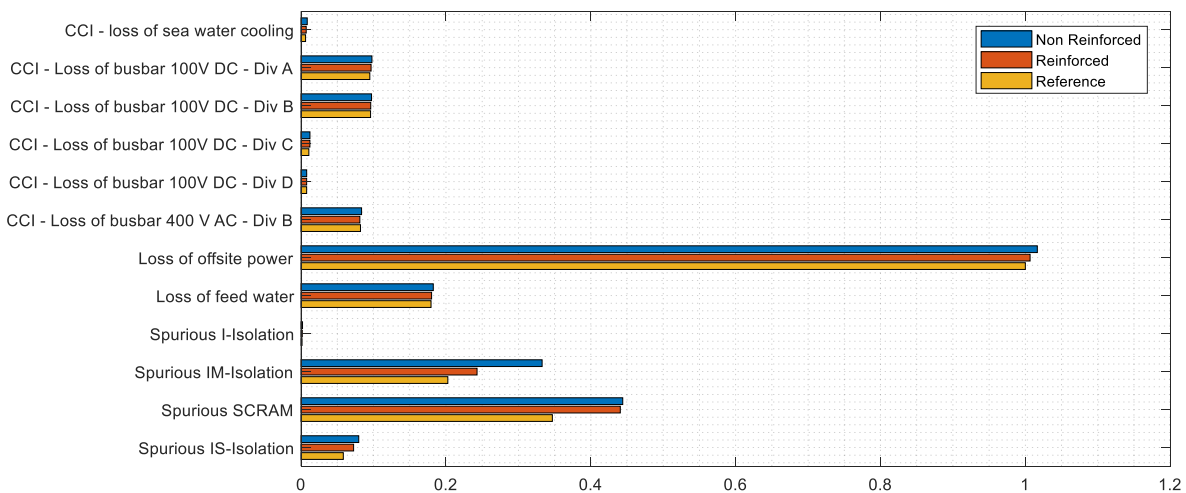

Figure 71: Comparison of normalized non-contained release frequencies (expected value) obtained with enhanced model for reinforced and non-reinforced hatch door in EIGT100-IDEJ0 scenario.

Figure 72 and 73 show the results of uncertainty analysis, that give better perspective regarding the effect of design modification on ranges and distributions of the non-contained release frequencies.

In case of IDEJ1 (Figure 72), reinforcement of the hatch door results in reduction of the non-contained release frequency in over 25% of the cases, however the major part of the distribution is concentrated around the values obtained with non-reinforced hatch door. It can be explained by the effect of the distribution of probability of failure due to ex-vessel debris coolability (Figure 60b, blue curve), which is not affected by design modification. If we compare the contribution from the sequences that lead to basemat melt-through in the reinforced (Figure A.2) and non-reinforced (Figure A.4) designs, presented in Appendix A., the contribution from these sequences in case of the non-reinforced design is relatively small, compared to its contribution in the reinforced design, which is due to the large values of probability of failure (Pf = 1) due to ex-vessel steam explosion in the non-reinforced design (i.e. in case of very large values of probability of ex-vessel steam explosion, the frequency of the sequences that lead to ex-vessel debris coolability in the CET (Figure 58) will be affected by success probability of steam explosion (i.e. no steam explosion), e.g. $(1 - Q_{SE})$, where Q_{SE} – is probability of failure due to ex-vessel steam explosion generated by ROAAM+ analysis, this value of success probability in turn is applied to all further events in the sequence [67]).

In case of IDEJ0 (Figure 73) reinforcement of the hatch door does significantly affect the results, which can be explained by relatively small values of probability of failure due to both ex-vessel debris coolability (Figure 59b) and steam explosion (Figure 59a).

It should be noted however that different modes of containment failure can potentially lead to different paths and consequences in terms of fission products release. Therefore, current analysis implementation should be extended

further, to take into account the effect of SA progression and containment phenomena on the magnitude, path and the timing of the release. Furthermore, proper consideration of different sources of uncertainty on the path and magnitude of potential releases is necessary (e.g. scrubbing, deposition on complex structures, mechanical resuspension, etc.)
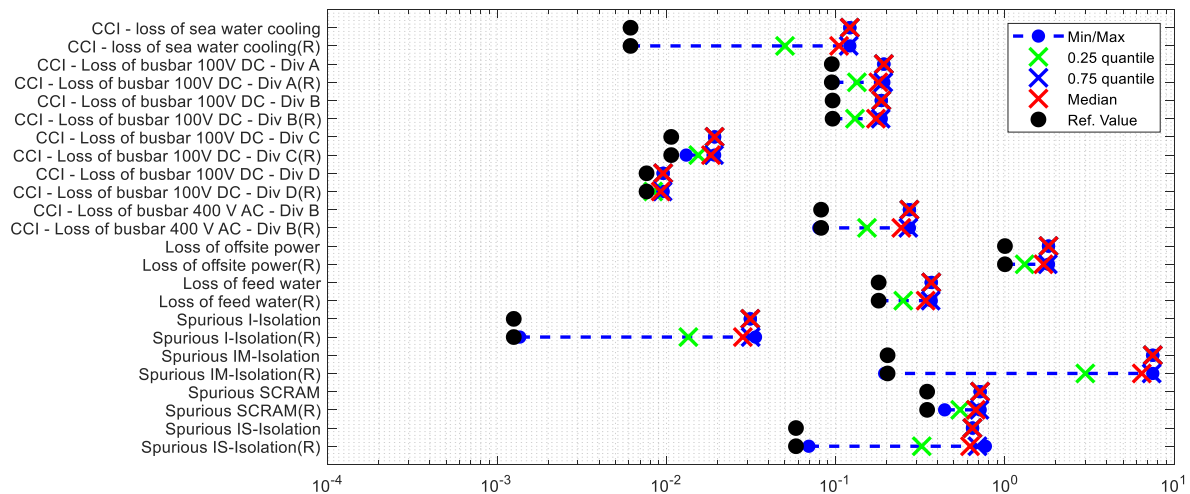
Figure 72: Comparison of distributions of normalized non-contained release frequencies obtained with enhanced model for reinforced (R) and non-reinforced hatch door in EIGT100-IDEJ1 scenario.
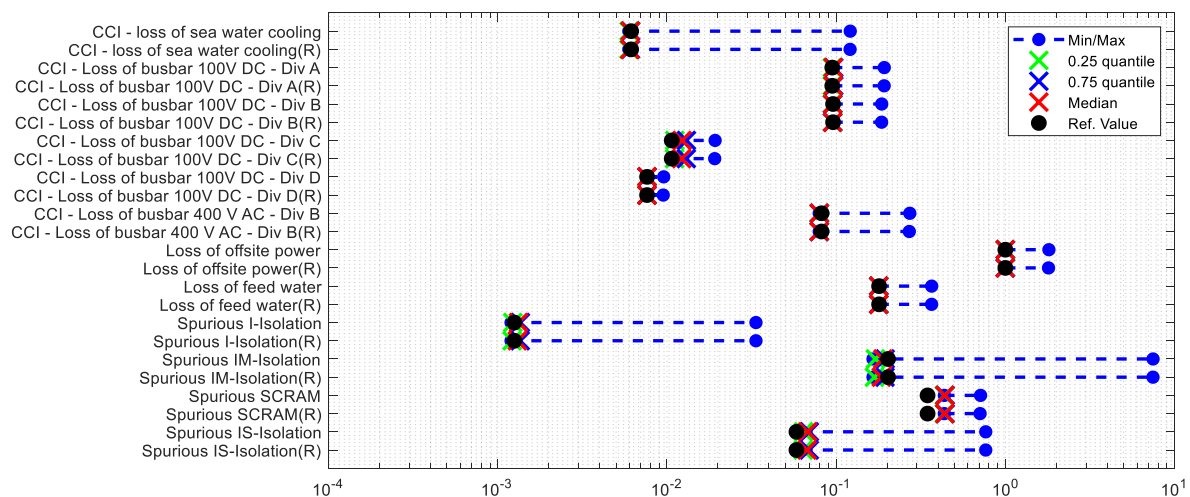
Figure 73: Comparison of distributions of normalized non-contained release frequencies obtained with enhanced model for reinforced (R) and non-reinforced hatch door in EIGT100-IDEJ0 scenario.

5.3.4 Summary of the Results

Figure 74 and 75 summarize the results showed in the previous chapters as normalized non-contained release frequency for HS2-TL4/TH1 plant damage states for all previously mentioned initiating event groups (i.e. all transients and CCIs leading to these plant damage states). The obtained non-contained release frequencies were normalized against the values obtained with the reference PSA model of Nordic BWR.

The results are presented for combinations of 2 phenomenological splinter scenarios (IDEJ1 vs. IDEJ0) and possible effect of design modification ($IDEJ1_R$ and $IDEJ0_R$).

Figure 74: Expected value of Normalized Non-contained Release Frequency.

The results show that in case of IDEJ0 (solid debris ejection – ON, typically results in gradual melt & debris ejection with relatively small sizes of the jet) the frequency of non-contained release increases by approximately 13% when compared with reference value. In case of IDEJ1 (solid debris ejection – OFF, ty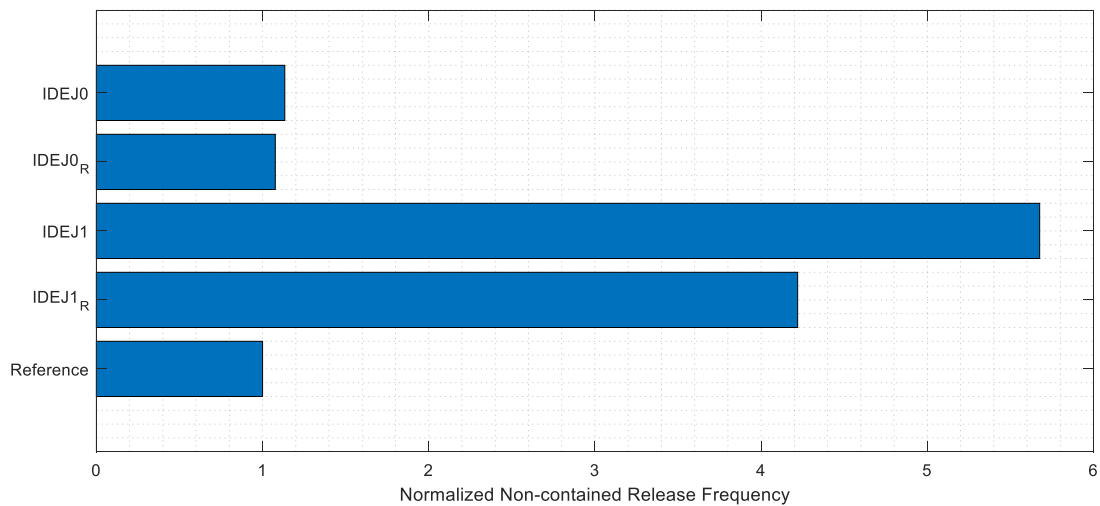pically leads to massive melt & debris ejection from the vessel with large sizes of the jet) the frequency on non-contained release is increased by a factor of ~5.6, when compared to the reference value. The effect of design reinforcement has relatively small impact on the results in case of IDEJ0 (see $IDEJ0$ vs. $IDEJ0_R$), since design modification does not affect ex-vessel debris coolability, however in case of IDEJ1 (see $IDEJ1$ vs. $IDEJ1_R$) it results in quite significant reduction of the frequency of non-contained release, from ~5.6 to 4.2, however these values are still above the values obtained with reference model.

Figure 75 show the results of uncertainty analysis. The resultant distributions of non-contained release frequency have quite significant spread in most of the cases, with exception to IDE1. On the other hand, in case of IDEJ0 and IDEJ0$_R$ the major part of the distribution is concentrated very close to the minimum value, however there are parameter combinations in deterministic models that can lead significantly large sizes of the jet and large values of non-contained release frequency. In case of IDEJ1$_R$ the distribution of non-contained release frequency is skewed to the right, however in ~50% of the cases it is below 5 times the reference value, and in ~25% of the cases it is below ~2.85 times the reference value, and for some deterministic models parameters combinations it can be very close to the values obtained with reference model.
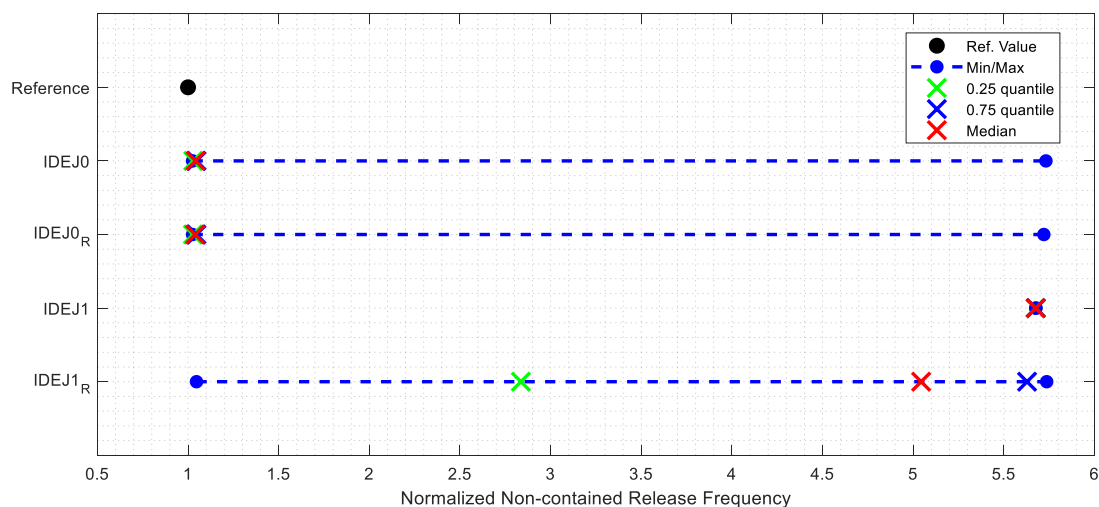

Figure 75: Uncertainty Analysis of Normalized Non-contained Release Frequency.

5.3.5 Influence of Limitations in Enhanced PSA model

In the present report it was attempted to minimize the effect of assumption and limitations that were made in the previous phase of NKS-SPARC project [66]. In particular, the following issues were addressed:

- Melt jet diameter: now predicted by MEM SM, based on MELCOR code results (Section 3.2.1). This parameter is crucial for the results since steam explosion energetics and probability of formation of non-coolable debris configuration strongly depend on the mode of debris ejection from the vessel (size of the jet, and ejected debris temperature in particular). It should be noted however, that the uncertainty in MELCOR predictions of the size of the jet is significant and dominated by the IDEJ parameter – mode of debris ejection from the vessel (see section 3.2.1, and Figure 20). In case of IDEJ=1 (solid debris ejection – OFF) – 100% cases result in creep-rupture of the LH wall and significant sizes of the melt jets. On the other hand, in case of IDEJ=0 (solid debris ejection – ON), the sizes of the jet are limited to IGT-slightly ablated IGT sizes, and rather gradual melt and debris releases from the vessel.

- Failure criteria: in this work 2 failure criteria were considered for ex-vessel steam explosion, in particular, we considered 6kPa*s – that represent original (current) design, although it should be mentioned that this value is based on expert judgement; and 50kPa*s – that represent possible design modification (hatch door reinforcement). In case of debris bed coolability, the models (section 3.2.3) used for this analysis were significantly improved, which allows use of less conservative criteria in risk assessment, i.e. onset of remelting of metallic or oxidic debris.

- Water depth for deep/shallow pool: The water pool depth is related to system functionality and can be calculated by deterministic codes (e.g. MELCOR or MAAP). If the LDW flooding system works, there will always be about 8 m of water in LDW. The water depth for shallow pool is much more uncertain since this completely depends on the sequence. In this work water pool depth in case of deep pool (successful activation of LDW flooding) the depth of the pool was predicted by MELCOR code. In case of shallow pool conditions, the pool depth was considered as an intangible parameter (see section 3.1.5 for details). However, a more realistic modeling could be developed to calculate the depth of the pool in case of late recovery of LDW flooding system.

Due to very large uncertainty in MELCOR predictions of vessel LH failure mode and melt release conditions the quantitative results should, therefore, be seen as indicative.

6 Discussion and conclusions.

This report presents an example of application of dynamic approached (such as ROAAM+) in PSA. In this approach the PSA was used as a basis to select important initiating events and sequences in the severe accident progression. These scenarios are then analyzed with deterministic models, yielding information about which parameters that are of the highest importance for the development of the accident progression. The results from the deterministic analysis are used in the PSA to improve sequence definition as well as improve the estimation of phenomena depending on the sequence and the varied parameters. Furthermore, ROAAM+ framework provides an assessment of the effect of epistemic (knowledge) uncertainty on the results employing "knowledge-based treatment" of epistemic uncertain parameters, i.e. no probability distributions of epistemic uncertain parameters are assumed if there is no available knowledge about them.

In particular, probability of containment failure due to ex-vessel steam explosion and ex-vessel debris coolability strongly depends on debris ejection mode from the vessel (Solid debris ejection option – IDEJ1 vs IDEJ0). In case of solid debris ejection – off (IDEJ1) containment failure due to ex-vessel phenomena cannot be considered as physically unreasonable (for both threats). In case of solid debris ejection – on (IDEJ0), containment failure due to ex-vessel steam explosion can be considered as physically unreasonable only in case of modified design (with reinforced hatch door)). On the other hand, containment hatch door reinforcement does not affect the probability of containment failure due to basemat melt-through and this threat cannot be considered as physically unreasonable in case of IDEJ0. ROAAM+ analysis results show that the probability of phenomena damaging the containment significantly depend on the depth of the pool in the lower drywell, e.g. coolability increases with the depth of the pool, however opposite is true for steam explosion (i.e. higher energetics in the deep pool), this information was used in enhanced PSA modelling.

The results obtained with the enhanced PSA model suggest that the non-contained release frequency depends on the mode of debris ejection from the vessel (IDEJ). In case of IDEJ1, it results in ~5.6 times larger value of non-contained release frequency when compared to the results obtained with reference model. Reinforcement of the hatch door in case of IDEJ1 results in reduction of the non-contained release frequency from ~5.6 to 4.2 times the value obtained with the reference PSA model. In case of IDEJ0 (both reinforced and non-reinforced design) enhanced PSA modelling results show relatively low increase of non-contained release frequency, from ~8 to 13% for non-reinforced and reinforced hatch door respectively.

Overall results show that the values of probabilities of phenomena damaging the containment used in the reference PSA model can be underestimated, judged by the respective values predicted by ROAAM+ framework. On the other hand, if it can be demonstrated that the vessel LH failure will be limited to IGTs failure and ablation of the opening will be limited, then the reference PSA model values of probabilities of phenomena damaging the containment can be considered as valid.

Present results show the dominant effect of the mode of debris ejection (IDEJ) on the results. However, given current state of knowledge about these phenomena, it should be treated as "phenomenological splinters" scenarios in PSA, that is, it should be demonstrated that non-contained release frequency is below regulatory requirements for all splinter scenarios considered.

It should be noted that current modelling approaches used in MELCOR code, for prediction of penetrations failure and melt and debris ejection, might be over-simplified in some aspects and lack necessary validation database. Furthermore, resent evidences from the Fukushima Daiichi Unit 2 and 3 primary containment vessel investigation [69], provided evidences that challenge ability of existing severe accident analysis tools to adequately predict transition of SA progression from in-vessel to ex-vessel phases in BWRs. Therefore, the results presented in this report should be considered as bounding estimates.

From a PSA stand point, the project has demonstrated that:

- It is both possible, achievable and desirable to increase the interaction between the deterministic and probabilistic assessment with regard to especially PSA level 2.
- Probabilities for phenomena can be estimated using the physical models in the thermal-hydraulic codes.
- The uncertainty can be assessed, and correlation between phenomena can be managed.
- There is room for improvement in current modelling in PSA level 2 (sequence parameters).

The implementation made in a large scale PSA model shows that the integration of the ROAAM+ results in the PSA model is not only feasible, but could potentially lead to a considerable change of the frequency for non-acceptable release. The results show that the parameters indicated by the ROAAM+ approach as being of high importance to the quantitative results. It also emphasizes the need to distinguish between different probabilities of phenomena depending on different scenario, physical and intangible parameters (e.g. pool depth, that significantly affect coolability and steam explosion).

The approach has demonstrated that the vision, to develop the sequence from core melting, and to understand what are the important factors, is possible to meet. The integrated approach will have the ability to give a more comprehensive estimation of the uncertainty compared to the standard approach. The uncertainty related to phenomena will consider the interdependency between phenomena (all the way back to relevant deterministic and intangible, boundary conditions and scenario parameters.

The dynamic approach used in the project requires extensive work regarding building the deterministic model. Once built, this model can however be modified to evaluate different initiating events and sequences. The changes in the enhanced PSA-model on the other hand are limited and easy to implement.

The integrated approach requires improvement in especially scenario definition, which practically leads to more plant damage states. The PDS should consider all necessary scenario parameters, that may affect the calculation of phenomena and hence consider also the system availability normally represented within CETs.

7   Outlook.

The work presented in this report can be extended further along several directions. Possible improvements can be subdivided into two main categories related to: (i) ROAAM+ probabilistic framework and deterministic modelling; (ii) related to aspects of application of ROAAM+ results in PSA.

Current ROAAM+ results show the dominant effect of the mode of multi-component debris ejection (IDEJ) on the results. The mode of debris ejection from the vessel is controlled through the user-defined switch (IDEJ=0 i.e. solid and liquid can be released vs. IDEJ=1 only liquid can be released). Development of a more mechanistic modeling approach would be needed in order to address this source of uncertainty.

ROAAM+ probabilistic framework employs sampling in the space of possible probability distributions of model intangible parameters (i.e. incomplete or partial probabilistic knowledge is available). In this work the sampling was performed using truncated normal distribution, where parameters that define the shape of distributions are selected by the user. An approach has been proposed [70] to overcome these limitations in risk analysis, and it is being implemented in ROAAM+.

Further reduction of the uncertainty can be achieved through refinement of existing melt ejection full and surrogate models. It can be achieved through refinement of the data base of MELCOR code solutions that account for the numerical effects of the maximum time step on the results. Currently the MEM SM does not predict material properties of the ejected debris from the vessel (e.g. density, thermal conductivity, etc.). These properties can be added to the MEM SM in the future, based on MELCOR analysis results. Furthermore, current treatment of debris ejection from the vessel implemented in MEM SM assumes uniform distribution of the ejected debris through the number of failed penetrations. An approach can be developed for non-uniform debris ejection from the vessel, depending on localized properties of the debris in the lower plenum and locations of failed penetrations.

Current implementations of melt ejection mode, ex-vessel steam explosion and ex-vessel debris coolability surrogate models are designed to predict respective melt release characteristics and containment loads per single jet, without taking into account interdependencies (e.g. interactions between several melt jets during melt fragmentation, etc.). More realistic approach is under development. It would affect both, steam explosion energetics as well as fraction of debris agglomerated and shape of the debris bed – which can affect significantly the risk of formation of non-coolable debris configuration.

With regards to the user-defined mode of melt release (IDEJ) one has to resolve a number of interacting relevant phenomena such as formation and accumulation of melt, gravity driven drainage of molten materials through the porous debris bed, resolidification of molten materials and formation of crusts in colder regions of the debris bed, that prevent further material drainage, which can result in either slow dripping of the melt from the vessel or accumulation of significant amounts of superheated metallic melt above the crust, which will be released upon crust remelting/failure. Crust formation can facilitate interaction of significant amounts of debris at high temperature with the vessel lower head wall, and significant mechanical load on the structure. This can lead to creep-rupture failure of the vessel lower head and massive ejection of debris from the vessel. Reduction of the uncertainty in the mode of ejection of multi-component mixture of solid and liquid debris, melt filtration through the porous debris, and crust formation is a necessary step for modelling of severe accident transition from in-vessel to ex-vessel phases, which is important for assessment of the loads on containment due to ex-vessel steam explosion and formation of non-coolable debris bed in the lower drywell of Nordic BWR design. Another important aspect of SA progression in BWRs is interaction of ejected debris and molten materials with the structures located under the vessel (such as CRD support, etc.) – which can significantly affect melt release conditions (e.g. vessel failure mode, or by jet breaking-up during interaction with the structures).

Current analysis has been performed only for one plant damage state. In the future other accident scenarios and possible recovery actions should be considered in the analysis. For example, analysis performed in [62] suggest that in case of mitigated SBO scenario in Nordic BWR, with recovery of ECCS after 2h after initiating event results in significant change in the mode of the vessel lower head failure (e.g. probability of the LH creep-to-failure increases from ~22% (in unmitigated case) to ~40% (in mitigated case) in case of IDEJ0, and decreases from 100% to ~80% in case of IDEJ=1 for unmitigated and mitigated scenarios respectively). This information can significantly affect risk analysis results in ROAAM+ framework and PSA. Furthermore, this information can provide more accurate and refined definition of available times for different operating actions and thus provide a better

basis material for the HRA. It might also indicate that the current assumptions regarding available time for recovery needs to be updated.

Current ROAAM+ framework for Nordic BWR considers conditional containment failure probability as an indicator of SAM effectiveness. Conditional containment failure probability obtained in ROAAM+ was used to calculate the frequency of non-contained release (or unacceptable release frequency) in PSA, which include contributions from bypass sequences, containment rupture due to steam explosion and basemat melt-through. However, different modes of containment failure can potentially lead to different consequences in terms of fission products release and environmental impact. For example, fission product release due to e.g. containment bypass, containment rupture due to energetic phenomena or basemat melt-through are completely different from each other in terms of (i) time scale, (ii) phenomena that can affect the magnitude of the fission product release, such as deposition on different surfaces, gravitational settling, chemical interactions, etc.; and, ultimately, (iii) offsite consequences in terms of release path and magnitude, e.g. directly to the environment in case of containment rupture or through auxiliary building or reactor building in case of containment bypass; ground water contamination in case of basemat melt-through.

Further complications that needs to be addressed in both PSA and deterministic modelling are the potential occurrence of major secondary sources of aerosol materials due to containment phenomena, e.g. steam explosion can lead to aerosol resuspension or revaporization of the deposited materials, molten core–concrete interaction (MCCI) on the other hand, result in significant diversification of suspended aerosol composition due to the addition of a large amount of largely nonactive aerosol material in the size range of the existing aerosols, which would act to promote agglomeration and accelerate depletion of activity suspended in the containment atmosphere [74].

Therefore, current framework implementation should be extended further, to take into account the effect of SA progression and containment phenomena on the path and magnitude of the release, which in turn should be reflected in enhanced PSA modelling.

From a PSA perspective it is relevant to discuss how the information from the ROAAM+ analysis shall be used and especially considering how to improve sequence definitions and treatment of uncertainties. Of especial interest is to discuss how parameters like the phenomenological splinters shall be treated. This also affects the existing PSA level 2 analyses, where the project has demonstrated that the probabilities used are closer to the IDEJ0 parameter. Uncertainty analysis and the impact of it on the evaluation for PSA level 2 should also be discussed – considering that the uncertainty can be quantified to a higher degree of realism than before.

References

[1] P. Kudinov, S, Galushin, S. Yakush, W. Villanueva, V.-A. Phung, D. Grishchenko, N. Dinh, "A Framework for Assessment of Severe Accident Management Effectiveness in Nordic BWR Plants," Probabilistic Safety Assessment and Management PSAM 12, June 22-27, 2014, Honolulu, Hawaii, Paper 154, 2014.

[2] Strålsäkerhetsmyndigheten (SSM) - Swedish National Action Plan Response to ENSREG's request within the European Stress Tests, revision 1, December (2014).

[3] S. Galushin, "Development of Risk Oriented Accident Analysis Methodology for Assessment of Effectiveness of Severe Accident Management Strategy in Nordic BWR", PhD Thesis, TRITA-SCI-FOU 2019:08, ISBN: 978-91-7873-103-9, (2019).

[4] P. Kudinov, S. Galushin, D. Grishchenko, S. Yakush, S. Basso, A. Konovalenko, M. Davydov, "Application of Integrated Deterministic-Probabilistic Safety Analysis to Assessment of Severe Accident Management Effectiveness in Nordic BWRs," The 17th International Topical Meeting on Nuclear Reactor Thermal Hydraulics (NURETH-17) Paper: 21590, Qujiang Int'l Conference Center, Xi'an, China，September 3-8, 2017.

[5] T. G. Theofanous, "On Proper Formulation of Safety Goals and Assessment of Safety Margins for Rare and High-Consequence Hazards," Reliability Engineering and System Safety, 54, pp.243-257, (1996).

[6] T. G. Theofanous and T.-N. Dinh, "Integration of multiphase Science and Technology with Risk Management in Nuclear Power reactors: Application of the Risk-Oriented Accident Analysis Methodology to the Economic, Simplified Boiling Water Reactor Design," Multiphase Science and Technology, V20(2), 2008, Pages 81-211.

[7] G. Apostolakis, M. Cunningham, C. Lui, C. Pangburn, W. Reckley, "A Proposed Risk Management Regulatory Framework," U.S. Nuclear Regulatory Commission, NUREG-2150, Washington, DC, April 2012.

[8] T. G. Theofanous, W. W. Yuen, "The probability of alpha-mode containment failure", Nuclear Engineering and Design 155, 459-473, 1995.

[9] M. M. Pilch, H. Yan, T. G. Theofanous, "The probability of containment failure by direct containment heating in Zion", Engineering and Design 164, 1-36, 1996.

[10] O. Kymäläinen, H. Tuomisto, T. G. Theofanous, "In-vessel retention of corium at the Loviisa plant", Nuclear Engineering and Design 169, 109-130, 1997.

[11] T. G. Theofanous, H. Yan, M. Z. Podowski, "The Probability of Mark-I Containment Failure by Meltattack of the Liner", NUREG/CR-6025 Report, 1993.

[12] S. Kaplan. and B. J. Garrick, "*On the Quantitative Definition of Risk*," Risk Analysis, 1: pp.11–27, (1981).

[13] H. Tuomisto, "ROAAM Methodology and its Application to the SAM Strategy Development at the Loviisa Plant" APRI 6 – Seminarium Svåra haverier & Haverihantering, Lejondal, Sweden, 22-23 January (2009).

[14] S.O. Hansson, "An Overview of Decision Theory", SKN Report 41, (1990).

[15] T. M. Mitchell, Machine Learning, Mcgraw-Hill Series in Computer Science, McGraw-Hill, New York, NY, USA, 1997.

[16] S. Galushin, D. Grishchenko, P. Kudinov, "Implementation of Probabilistic Framework of Risk Analysis Framework for Assessment of Severe Accident Management Effectiveness in Nordic BWR", (Submitted).

[17] J.C Helton, J.D. Johnson, W.L Oberkampf, C.J. Sallaberry, "Representation of analysis results involving aleatory and epistemic uncertainty," International Journal of General Systems, Vol.39(6), pp.605-646, (2010).

[18] Liao, W.-K., Liu, Y., and Choudhary A., "A Grid-based Clustering Algorithm using Adaptive Mesh Refinement," In proceedings of the 7thWorkshop on Mining Scientific and Engineering Datasets, 2004.

[19] Galushin S. and Kudinov P., "An Approach to Grouping and Classification of Scenarios in Integrated Deterministic-Probabilistic Safety Analysis," Science and Technology of Nuclear Installations, Article ID 278638, 13 pages, 2015.

[20] Saltelli A., Tarantola S., Campolongo F., Ratto M., Sensitivity Analysis in Practice, John Wiley & Sons Ltd, p. 94, 2004.

[21] S. Galushin, D. Grishchenko, P. Kudinov, "Surrogate Model Development for Prediction of Vessel Failure Mode and Melt Release Conditions in Nordic BWR based on MELCOR code", ICONE-27, 27th International Conference on Nuclear Engineering, Ibaraki, Japan, May 19-24, 2019.

[22] S. Galushin, D. Grishchenko, P. Kudinov, "The Effect of the Uncertainty in Prediction of Vessel Failure Mode and Melt Release Conditions on Risk of Containment Failure due to Ex-Vessel Steam Explosion in Nordic BWR", ICONE-27, 27th International Conference on Nuclear Engineering, Tsukuba, Ibaraki, Japan, May 19-24, 2019.

[23] Burkardt J., "The Truncated Normal Distribution", Department of Scientific Computing, Florida State University, 2014.

[24] Morris H. DeGroot, Mark J. Schervish, "Probability and Statistics (4th Edition) 4th Edition. Pearson Education.

[25] Sergey Galushin and Pavel Kudinov, "Analysis of the Effect of Severe Accident Scenario on Debris Properties in Lower Plenum of Nordic BWR Using Different Versions of MELCOR Code," Science and Technology of Nuclear Installations, vol. 2019, Article ID 5310808, 18 pages, 2019. https://doi.org/10.1155/2019/5310808.

[26] Niederreiter, H., Random number generation and quasi-Monte Carlo methods, SIAM, p. 29, ISBN 0-89871-295-5, (1992).

[27] Christoph Schlier, "On scrambled Halton sequences", Applied Numerical Mathematics, Volume 58, Issue 10, 2008.

[28] G. Ökten, "Random Sampling from Low-Discrepancy Sequences: Applications to Option Pricing", Mathematical and Computer Modelling 35 (2002).

[29] J. Shortle and P. L'Ecuyer, "Introduction to rare-event simulation," in Wiley Encyclopedia of Operations Research and Management Science, Wiley, 2010.

[30] Eric C. Anderson, "Monte Carlo Methods and Importance Sampling", Lecture Notes for Statistical Genetics, 1999.

[31] Galushin S., Ranlöf L., Bäckström O., Adolfsson Y., Grishchenko D., Kudinov P., Marklund A., "Joint Application of Risk Oriented Accident Analysis Methodology and PSA Level 2 to Severe Accident Issues in Nordic BWR", Probabilistic Safety Assessment and Management PSAM 14, September 2018, Los Angeles, CA. (2018).

[32] Galushin, S, and P Kudinov. "Uncertainty Analysis of Vessel Failure Mode and Melt Release in Station Blackout Scenario in Nordic BWR Using MELCOR Code." 18th International Topical Meeting on Nuclear Reactor Thermal Hydraulics (NURETH-18), no. Portland, OR, USA, August 18-22, 2019.

[33] Galushin, S., and P. Kudinov. "Sensitivity and Uncertainty Analysis of the Vessel Lower Head Failure Mode and Melt Release Conditions in Nordic BWR Using MELCOR Code." Annals of Nuclear Energy, Volume 135, 2020, ISSN 0306-4549.

[34] Humphries, L. L., R. K. Cole, D. L. Louie, V.G. Figueroa, and M.F. Young. 2015a. "MELCOR Computer Code Manuals." Vol. 2: Reference Manuals Version 2.1.6840, no. SAND2015–6692 R.

[35] Humphries, L.L., R. K. Cole, D. L. Louie, V.G. Figueroa, and M.F. Young. 2015b. "MELCOR Computer Code Manuals." Vol. 1: Primer and User's Guide Version 2.1.6840, SAND2015-6691 R.

[36] Magallon, D. 2012. "SERENA Programme Reactor Exercise: Synthesis of Calculations."

[37] Grishchenko, D., S. Basso, and P. Kudinov. 2016. "Development of a Surrogate Model for Analysis of Ex-Vessel Steam Explosion in Nordic Type BWRs." *Nuclear Engineering and Design, Volume 310, 15 December 2016, Pages 311-327*.

[38] D. Grishchenko, S. Basso, S. Galushin and P. Kudinov, Development of Texas-V code surrogate model for assessment of steam explosion impact in Nordic BWR, the 16th International Topical Meeting on Nuclear Reactor Thermal Hydraulics (NURETH-16), Chicago, IL, USA, August 30-September 4, paper 13937, (2015).

[39] D. Grishchenko, S. Galushin, Pavel Kudinov, "Failure domain analysis and uncertainty quantification using surrogate models for steam explosion in a Nordic type BWR", Nuclear Engineering and Design, Volume 343, 2019, Pages 63-75, ISSN 0029-5493, (2019).

[40] D. Grishchenko, P. Kudinov, "Development and Validation of a Full Model for the Analysis of Ex-Vessel Steam Explosion in LWRs", 18th International Topical Meeting on Nuclear Reactor Thermal Hydraulics (NURETH-18), no. Portland, OR, USA, August 18-22, 2019.

[41] Corradini, M.L., et al., Users' manual for Texas-V: One dimensional transient fluid model for fuel-coolant interaction analysis. 2002, University of Wisconsin-Madison: Madison WI 53706.

[42] Kudinov, P. and Davydov, M., "Development of Ex-Vessel Debris Agglomeration Mode Map for a LWR Severe Accident Conditions," Proceedings of the 17th International Conference on Nuclear Engineering, July 12-16, 2009, Brussels, Belgium, Paper ICONE17-75080.

[43] Kudinov, P. and Davydov, M., "Approach to Prediction of Melt Debris Agglomeration Modes in a LWR Severe Accident," Proceedings of ISAMM-2009, Böttstein, Switzerland, October 26 - 28, 2009.

[44] P. Kudinov, S. Galushin, M. Davydov, "Analysis of the Risk of Formation of Agglomerated Debris in Nordic BWRs", NUTHOS11, Gyeongju, South Korea, October 9-13, (2016).

[45] Yakush S. E., and Kudinov P., "Melt Agglomeration Influence on Ex-vessel Debris Bed Coolability" The 17th International Topical Meeting on Nuclear Reactor Thermal Hydraulics (NURETH-17), Paper: 21455, Qujiang Int'l Conference Center, Xi'an, China，September 3-8, 2017.

[46] S. E. Yakush, A. Konovalenko, S. Basso, P. Kudinov," Validation of DECOSIM Code Against Experiments on Particle Spreading by Two-Phase Flows in Water Pool", NUTHOS-11: The 11th International Topical Meeting on Nuclear Reactor Thermal Hydraulics, Operation and Safety, Gyeongju, Korea, October 9-13, 2016.

[47] Strålsäkerhetsmyndigheten (SSM). "APRI 9 – Accident Phenomena of Risk Importance, En lägesrapport om forskningen inom området svåra haverier under åren 2015-2017", June 2018.

[48] Kudinov, P., Karbojian, A., Ma, W., and Dinh, T.-N. "The DEFOR-S Experimental Study of Debris Formation with Corium Simulant Materials," Nuclear Technology, 170(1), April 2010, pp. 219-230, 2010.

[49] Magallon, D., Huhtiniemi, I., Hohmann, H., "Lessons Learnt from FARO/TERMOS Corium Melt Quenching Experiments," In: Proceedings of the OECD/CSNI Specialists Meeting on Fuel-Coolant Interactions, Tokai-Mura, Japan, NEA/CSNI/R(97)26, Part II, 1997, pp.431-446.

[50] Spencer, B.W., Wang K., Blomquist, C.A., McUmber, L.M., and Schneider, J.P., "Fragmentation and Quench Behaviour of Corium Melt Streams in Water," NUREG/CR-6133 ANL-93/32, Argonne National Laboratory. 1994.

[51] Karbojian, A., Ma, W., Kudinov, P., and Dinh, T.-N., "A Scoping Study of Debris Bed Formation in the DEFOR Test Facility", Nuclear Engineering and Design, 239, 2009, 1653-1659.

[52] Kudinov, P., Karbojian, A., Ma, W., and Dinh, T.-N. "The DEFOR-S Experimental Study of Debris Formation with Corium Simulant Materials," Nuclear Technology, 170(1), April 2010, pp. 219-230, 2010.

[53] Kudinov, P., Karbojian, A., and Tran, C.-T., "Experimental Investigation of Melt Debris Agglomeration with High Melting Temperature Simulant Materials," Proceedings of ISAMM-2009, Böttstein, Switzerland, October 26 - 28, 2009.

[54] Kudinov, P., Karbojian, A., Tran, C.-T., and Villanueva, W., "The DEFOR-A Experiment on Fraction of Agglomerated Debris as a Function of Water Pool Depth," The 8th International Topical Meeting on Nuclear Thermal-Hydraulics, Operation and Safety (NUTHOS-8), Shanghai, China, October 10-14, N8P0296, 2010.

[55] Kudinov, P., Karbojian, A., Tran, C.-T., Villanueva, W., "Experimental Data on Fraction of Agglomerated Debris Obtained in the DEFOR-A Melt-Coolant Interaction Tests with High Melting Temperature Simulant Materials," Nuclear Engineering and Design, 263, October 2013, Pages 284-295, 2013.

[56] Davydov, M.V., "Mathematical modeling of the process of interaction between high temperature melt and coolant in severe accident at NPP with water cooled reactor installation," PhD thesis: 05.14.03. 2010. 197p. (in Russian).

[57] Kolev N., Multiphase Flow Dynamics, Vol. 2, Ch. 2, Springer, Berlin, Heidelberg, NY (2005).

[58] S. E. Yakush and P. Kudinov. Coolablity and post-dryout behavior of a porous debris bed with distributed agglomerates. In Proc. 12th International Topical Meeting on Reactor Thermal-Hydraulics, Operation, and Safety (NUTHOS-12), pages 1–13. Chinese Nuclear Society (CNS) Quindao, China, 2018.

[59] Billone, M.C., Chung H.M. and Yan Y., "Steam Oxidation Kinetics of Zirconium Alloys", Argonne National Laboratory (ANL), 2002.

[60] Pär Lindahl, "Utbildningsmaterial - Att genomföra reaktorsäkerhetsteknisk värdering", OKG Report 2015-13703 (2015).

[61] M. L. Ang, N. E. Buttery, "An approach to the application of subjective probabilities in level 2 PSAs", Reliability Engineering and System Safety, Vol 58, pp.145-156. (1997).

[62] S. Galushin, P. Kudinov, "Comparison of Vessel Failure Model and Melt Release Conditions in Mitigated and Unmitigated Station Blackout Scenarios in Nordic BWR Using MELCOR code", ICONE-27, 27th International Conference on Nuclear Engineering, Tsukuba, Ibaraki, Japan, May 19-24, 2019.

[63] Sergey Galushin, Pavel Kudinov, Analysis of the effect of MELCOR modelling parameters on in-vessel accident progression in Nordic BWR, Nuclear Engineering and Design, Volume 350, 2019, Pages 243-258, ISSN 0029-5493, https://doi.org/10.1016/j.nucengdes.2019.04.040.

[64] K. Ross, J. Phillips, R.O. Gauntt, K.C. Wagner, MELCOR Best Practices as Applied in the State-of-the-Art Reactor Consequence Analyses (SOARCA) Project, NUREG/CR-7008, 2014.

[65] Pavel Kudinov, Sergey Galushin, Dmitry Grishchenko, Sergey Yakush, Yvonne Adolfsson, Lisa Ranlöf, Ola Bäckström, Anders Enerholm, "Scenarios and Phenomena Affecting Risk of Containment Failure and Release Characteristics," SPARC Project, NKS-395 22 Aug 2017, 2017.

[66] Pavel Kudinov, Sergey Galushin, Dmitry Grishchenko, Sergey Yakush, Anders Riber Marklund, Ola Bäckström, "Scenarios and Phenomena Affecting Risk of Containment Failure and Release Characteristics", NKS-410, ISBN 978-87-7893-499-4, (2018).

[67] "Theory Manual, RiskSpectrum Analysis Tools", Lloyd's Register Consulting – Energy AB, Version 3.3.0.

[68] R.O. Gauntt and N. Andrews, Insights on Fukushima Damage Progression based on PCV Inspections and Implications for Decommissioning Data Collection and Code Model Refinement, Sandia National Laboratories, SAND2018-11687R.

[69] "3-D Rendering of Images obtained during the Fukushima Daiichi Nuclear Power Station Unit 3 Primary Containment Vessel (PCV) Internal Investigation", TEPCO, April 26, 2018.

[70] S. Galushin, D. Grishchenko, P. Kudinov, "Quantification of the Uncertainty Due to State-Of-Knowledge Using ROAAM+ Framework for Nordic BWRs", 16th International Topical Meeting on Probabilistic Safety Assessment and Analysis, Charleston, South Carolina USA, April 28-May 3, (2019).

[71] Sandia National Laboratories, "NUREG/CR-5582: Lower Head Failure Experiments and Analyses," 1998.

[72] C. T. Martin, "Coupled 3D Thermomechanical Analysis of Nordic BWR Lower Head Failure" Master Thesis, Royal Institute of Technology, Stockholm, 2013.

[73] Gauntt, R. O. and Humphries, L. L., "Final Results of the XR2-1 BWR Metallic Melt Relocation Experiment", NUREG/CR-6527, SAND97-1039, (1997).

[74] Sehgal, B.R. "Nuclear Safety in Light Water Reactors", Academic Press, Pages 519-588, ISBN 9780123884466, 2012.

[75] Kudinov P., Galushin S., Grishchenko D., Yakush S., Davydov M., "ROAAM+ Analysis Results for Nordic BWRs". Accident Phenomena of Risk Importance (APRI-10) Report, 2019.

Appendix A.

Figure A.1-A.8 show the results of comparison between reference and enhanced PSA models, for different initiating events groups, where sequences marked (M) – are sequences that lead to basemat melt-through, and sequences marked (U) lead to non-contained release (including bypass, basemat melt-through and containment break due to ex-vessel steam explosion).
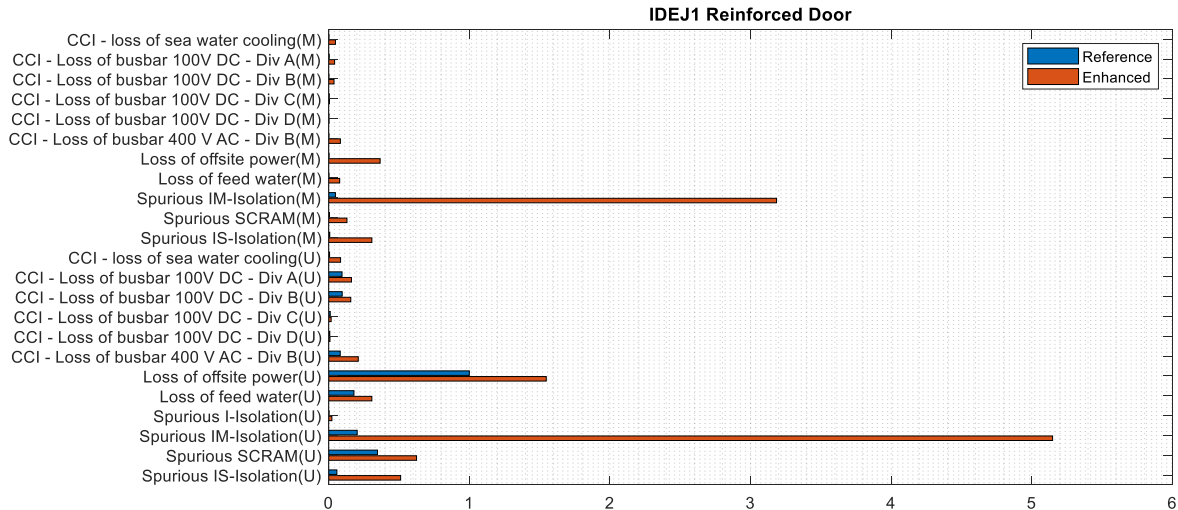

Figure A.1. Comparison of normalized non-contained release frequencies between the reference and the enhanced models for EIGT100-IDEJ1 scenario with reinforced hatch door, due to (M) basemat melt-through, (U) overall non-contained release (including basemat melt-though and bypass sequences).
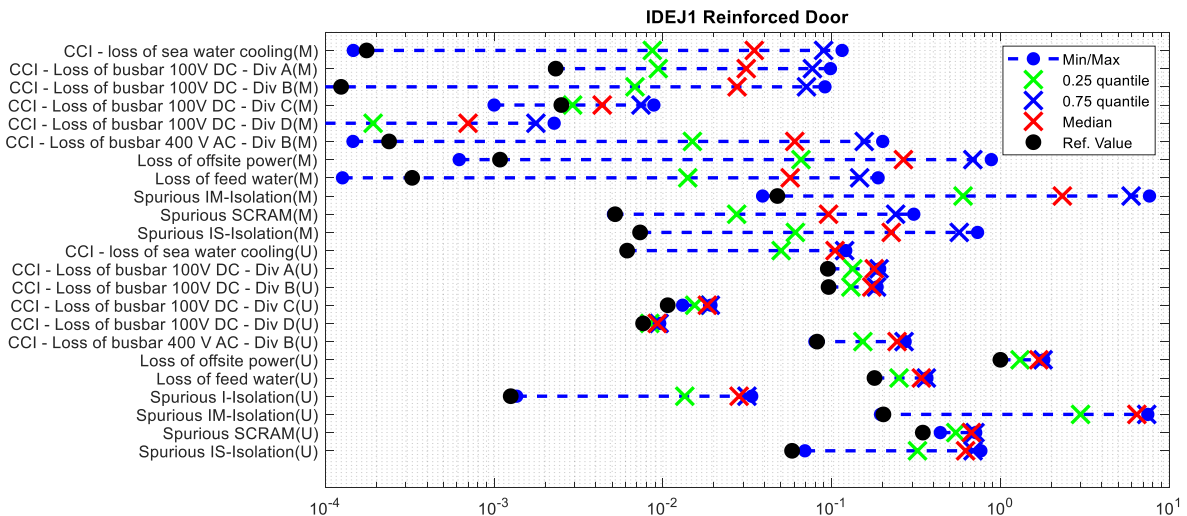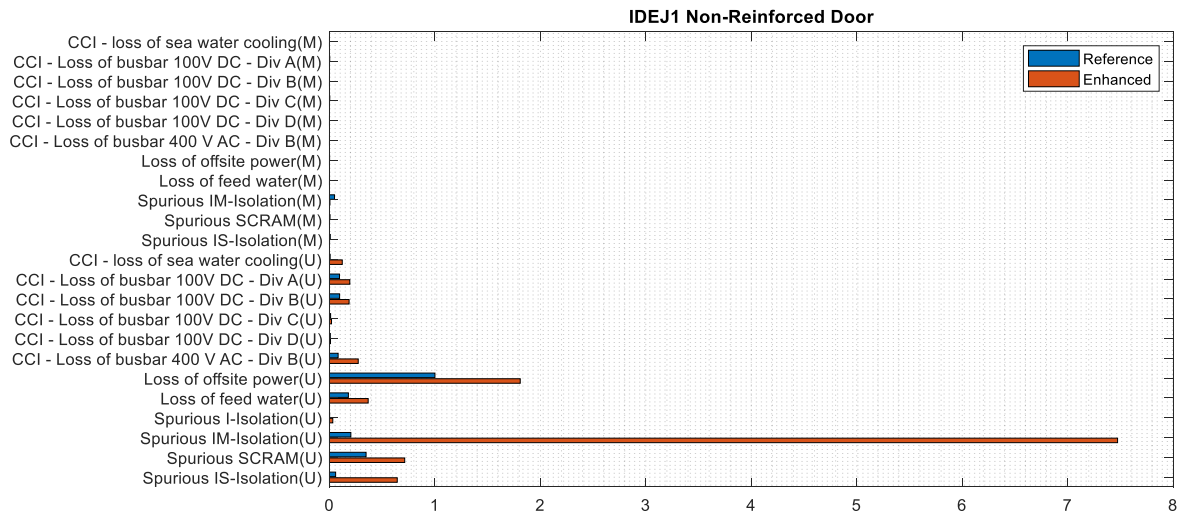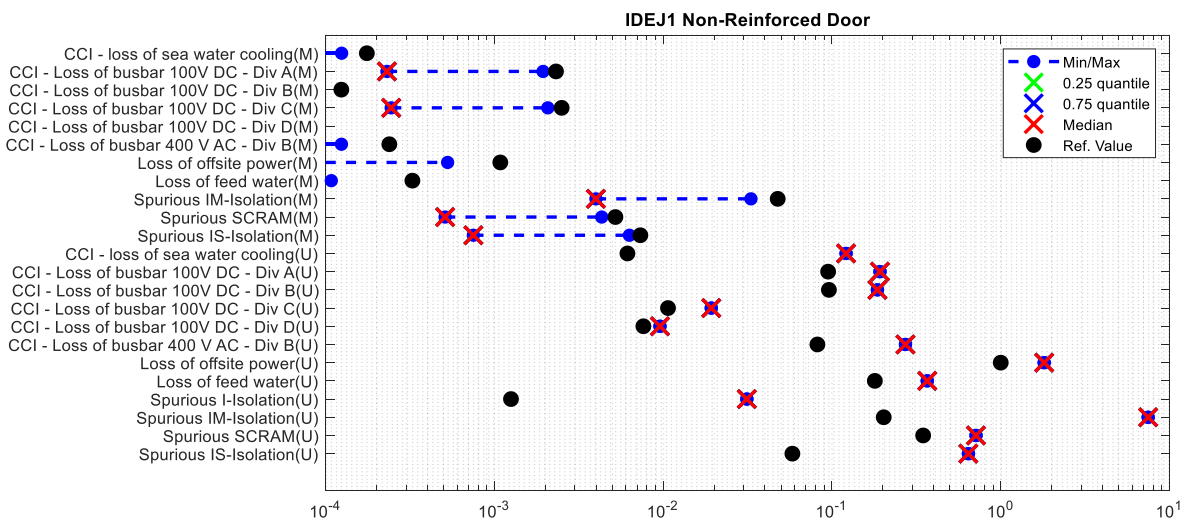

Figure A.2. Uncertainty analysis results of normalized non-contained release frequencies using enhanced model for EIGT100-IDEJ1 scenario with reinforced hatch door, due to (M) basemat melt-through, (U) overall non-contained release (including basemat melt-though and bypass sequences).

Figure A.3. Comparison of normalized non-contained release frequencies between the reference and the enhanced models for EIGT100-IDEJ1 scenario with non-reinforced hatch door, due to (M) basemat melt-through, (U) overall non-contained release (including basemat melt-though and bypass sequences).
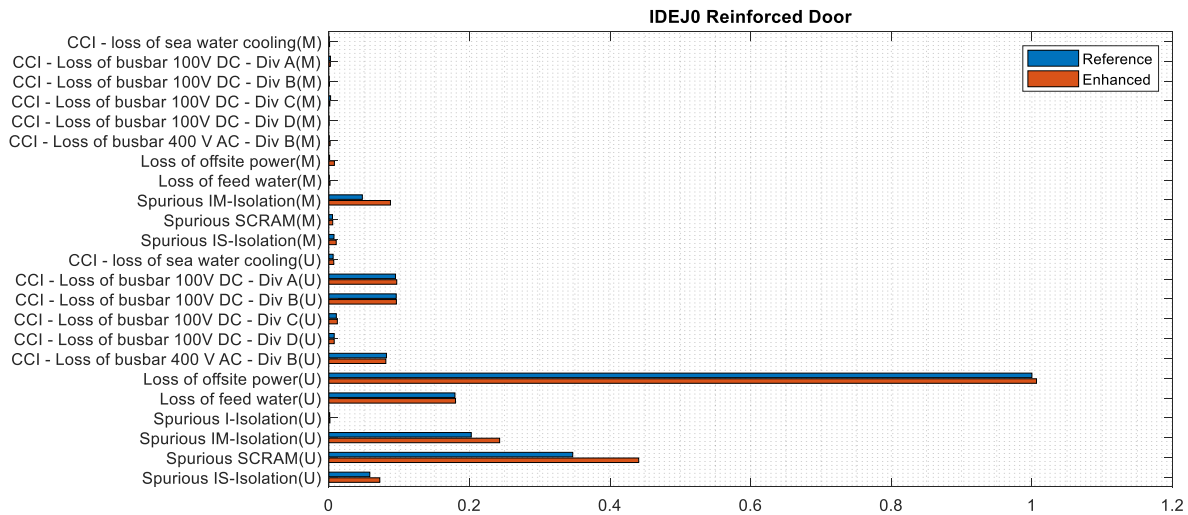

Figure A.4. Uncertainty analysis results of normalized non-contained release frequencies using enhanced model for EIGT100-IDEJ1 scenario with non-reinforced hatch door, due to (M) basemat melt-through, (U) overall non-contained release (including basemat melt-though and bypass sequences).
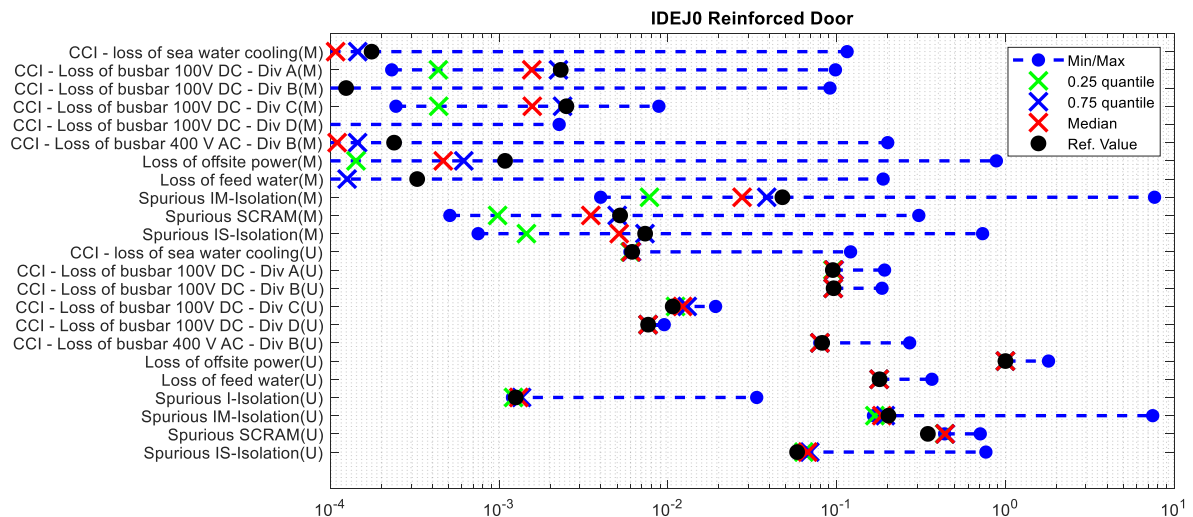
Figure A.5. Comparison of normalized non-contained release frequencies between the reference and the enhanced models for EIGT100-IDEJ0 scenario with reinforced hatch door, due to (M) basemat melt-through, (U) overall non-contained release (including basemat melt-though and bypass sequences).
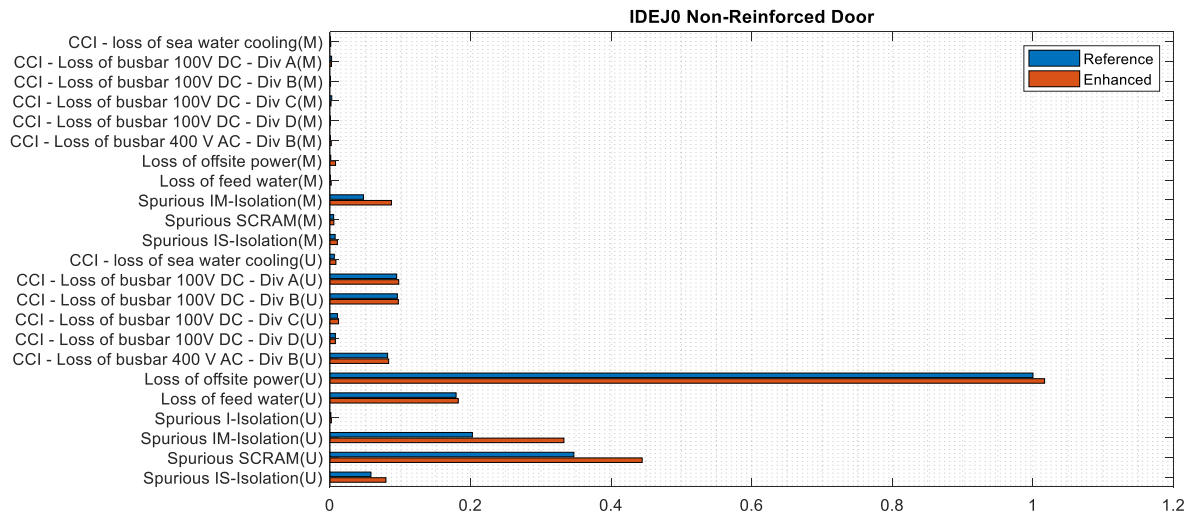

Figure A.6. Uncertainty analysis results of normalized non-contained release frequencies using enhanced model for EIGT100-IDEJ0 scenario with reinforced hatch door, due to (M) basemat melt-through, (U) overall non-contained release (including basemat melt-though and bypass sequences).

Figure A.7. Comparison of normalized non-contained release frequencies between the reference and the enhanced models for EIGT100-IDEJ0 scenario with non-reinforced hatch door, due to (M) basemat melt-through, (U) overall non-contained release (including basemat melt-though and bypass sequences).
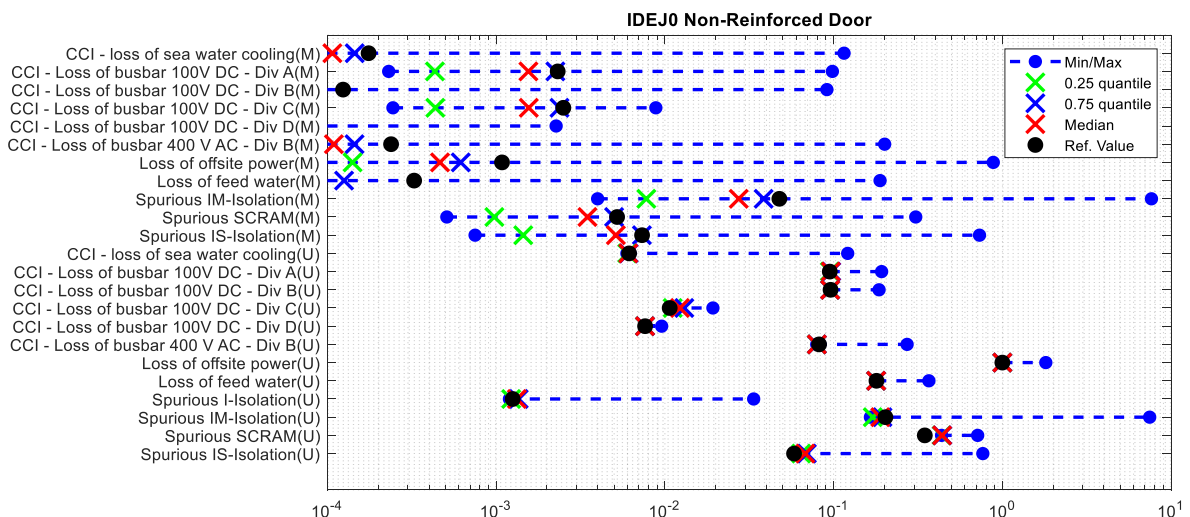

Figure A.8. Uncertainty analysis results of normalized non-contained release frequencies using enhanced model for EIGT100-IDEJ0 scenario with non-reinforced hatch door, due to (M) basemat melt-through, (U) overall non-contained release (including basemat melt-though and bypass sequences).

Bibliographic Data Sheet   NKS-428

Author(s)	Weimin Ma[1], Walter Villanueva[1], Sevostian Bechta[1], Qiang Guo[1], Andrei Komlev[1], Mohsen Hoseyni[1], Peng Yu[1]
	Anna Korpinen[2], Veikko Taivassalo[2], Tero Tyrväinen[2], Ilkka Karanta
	Anders Riber Marklund[3], Sergey Galushin[3], Ola Bäckström[3]

Affiliation(s)	[1]Royal Institute of Technology (KTH) [2]Technical Research Centre of Finland Ltd (VTT) [3]Lloyd´s Register Consulting Energy AB (LRC)

Abstract max. 2000 characters	Objective of the project "Scenarios and Phenomena Affecting Risk of Containment Failure and Release Characteristics", dubbed SPARC, is to produce new data, and to develop models and methodologies for addressing severe accident scenarios and phenomena which are important to assess the risk of containment failure and radioactivity release in a postulated severe accident of Nordic nuclear power plants.
	During 2018 substantial advances in experimental and analytical capabilities as well new insights into physical mechanisms were gained at KTH, VTT and LRC for: (i) development of experimental facilities of SIMECO-2, MRSPOD and POMECO-Q for studies of melt pool convection as well as remelting and quenching of debris beds; (ii) validation of the MEWA code for coolability analysis of particulate beds, and its applications to reactor-scale debris beds; (iii) experimental investigations on quenching of a hot sphere in a seawater pool and single molten droplet steam explosion in sea water; (iv) modeling of melt infiltration through particulate beds, and its validation against the REMCOD experiment; (v) coupled thermal-mechanical analysis approach and its validation against the FOREVER-EC2 experiment; (vi) study of a dynamic containment

event tree modelling particularly focusing on the modelling of timings of events and uncertainty analysis; (vii) the comparison of MEWA and DECOSIM simulations for the post-dryout conditions of the same idealized particulate beds; and (viii) the application of a dynamic approach (such as ROAAM+) to PSA for an enhanced probabilistic risk analysis.